Crustal carbonate assimilation limits and CO_2 production within arc magmas - The Jurassic Bonanza arc, Vancouver Island, Canada

by

Rebecca Anne Morris
B.Sc. (Hons), University of Calgary, 2010
M.Sc., Western Washington University, 2017

A Dissertation Submitted in Partial Fulfillment
of the Requirements for the Degree of

DOCTOR OF PHILOSOPHY

in the School of Earth and Ocean Sciences

We acknowledge and respect the lək̓ʷəŋən peoples on whose traditional territory the university stands and the Songhees, Esquimalt and W̱SÁNEĆ peoples whose historical relationships with the land continue to this day.

Supervisory Committee

Crustal carbonate assimilation limits and CO_2 production within arc magmas – The Jurassic Bonanza arc, Vancouver Island, Canada

by

Rebecca Anne Morris
B.Sc. (Hons), University of Calgary, 2010
M.Sc., Western Washington University, 2017

Supervisory Committee

Dr. Dante Canil (School of Earth and Ocean Sciences)
Supervisor

Dr. Jon Husson (School of Earth and Ocean Sciences)
Departmental Member

Dr. Kathy Gillis (School of Earth and Ocean Sciences)
Departmental Member

Dr. Arthur Blackburn (Department of Physics and Astronomy)
Outside Member

Abstract

Supervisory Committee
Dr. Dante Canil (School of Earth and Ocean Sciences)
Supervisor
Dr. Jon Husson (School of Earth and Ocean Sciences)
Departmental Member
Dr. Kathy Gillis (School of Earth and Ocean Sciences)
Departmental Member
Dr. Arthur Blackburn (Department of Physics and Astronomy)
Outside Member

The contribution of crustal-derived CO_2 into arc magmas is controversial. Traditional views assume most CO_2 outgassed at arc volcanoes is slab-derived, but recent studies show that active and ancient systems where arc magmas intrude carbonate may contribute significant crustal CO_2. Quantifying CO_2 from magma-carbonate reactions within the crust is important as it has implications on how we understand the long-term C cycle. In addition, the mechanism of carbonate assimilation into arc magmas is understudied, especially in the form of well-constrained field exposures that provide in situ reactions. Within this thesis, I document carbonate assimilation limits, CO_2 production, and the mechanisms that drive assimilation for different scales of well-exposed magma bodies (m-scale dikes and sills, km-scale pluton) that intrude limestone within the Jurassic Bonanza arc, on Vancouver Island, Canada.

Magma-carbonate reactions preserved in m-scale dikes is observed in two forms: 1) as unique orbicular dikes that outcrop above the level of stratigraphy of basalt-limestone reactions, and 2) as reacted margins (or 'boundary melts') preserved at basalt-limestone contacts in dikes and sills. Orbicular dikes consist of segregated Ca-rich microcrystalline orbicules, where orbicule compositions are similar to hybrid melts produced from basalt-limestone experiments. Binary mixing models of limestone into basalt confirms the orbicules form from assimilating up to 25 wt.% limestone into basalt, and are capable of producing up to 11 wt.% CO_2. I interpret that orbicules formed from basalt-limestone reactions at depth, where produced calcic melts were transported upwards from recharging magma feeding the dikes in the lower section. Rapid cooling within the dikes preserved these segregated calcic melts in situ, where homogenization with the host melt was limited due to their varying viscosities.

Reacted margins at basalt-limestone contacts in dikes and sills document boundary melts that are distinctly lighter in colour and texturally unique (glassy ± orbicules). Boundary melt

compositions show unique Ca, U, and Sr enrichments, Si depletion, and $^{87}Sr/^{86}Sr$ that approaches host limestone values. Binary mixing models indicate the boundary melts form from ~20 wt.% limestone assimilation into basalt, suggesting that these reacted margins which make up to 4% of dike and sill volumes are capable of producing ~10 wt.% CO_2. Contrasting viscosities between the boundary and interior melts appears to promote uphill diffusion of elements more enriched in the wallrock (U, Sr), and is preserved in these reacted margins that likely cooled in minutes. Extreme Sr enrichment (up to 5500 ppm) far above typical basalt concentrations (~400 ppm) in dike and sill interiors is surmised to occur from meltback of channel walls, where Sr-enriched boundary melts may remelt and concentrate in dike interiors where flow velocities are greatest.

Magma-carbonate reactions from a km-scale gabbro pluton that intrudes limestone shows limited carbonate interaction, with the exception of a thin (<2 m) gabbroic chilled margin with elevated U, Sr, REEs, and $^{87}Sr/^{86}Sr$ ratios. This chilled margin is also in contact with a wide (~50 – 150 m) metamorphic aureole. Modeling of assimilation + concurrent fractional crystallization (AFC) indicates the chilled margin chemistry and mineralogy can be obtained from the uptake of 20 wt.% limestone into gabbro, suggesting this thin reacted veneer is capable of producing ~10 wt.% CO_2. A lack of enriched $^{87}Sr/^{86}Sr$ ratios shows no indication of crustal enrichment from ~10 to >1000 m from the contact, which further constrains that any reaction with carbonate is limited to the outer ~10 m margin of the pluton, accounting for <1% of the total pluton volume.

Results indicate that an enhanced extent of magma-carbonate reaction and CO_2 production is via a network of shallow m-scale dikes and sills versus deeper km-scale plutons. Additional estimates on CO_2 produced within the metamorphic aureole indicate that >89% of crustal-derived CO_2 is liberated via wallrock decarbonation and <11% is liberated by magma from carbonate assimilation. Estimates of CO_2 were extrapolated to calculate a flux for the Jurassic Bonanza arc that is notably lower than some present-day fluxes from arc volcanoes intersecting carbonate-rich lithologies (i.e., Etna, Popocatépetl). These lower estimates are likely due to thinner (<1 km) carbonate sequences in the Bonanza arc crustal substrate. Nonetheless, this work details the limited extent to which plutons assimilate limestone and caution any historical flux estimate where a consistent mass fraction of carbonate was assimilated into plutons. Experimental data from others further indicates that assimilation into km-scale magma bodies in thick transcrustal sections is limited with depth. The results from this study ultimately provide realistic and quantitative limits on arc-derived CO_2 from upper crustal wallrock sources.

Table of Contents

List of Tables

List of Figures

Chapter 1 Figures

Chapter 2 Figures

Chapter 3 Figures

Chapter 4 Figures

Appendix A – Chapter 2 Supplemental Figures

Appendix C – Chapter 4 Supplemental Figures

Acknowledgments

It has been an honour to learn and work with Dante Canil over these past few years. Thank you Dante for your creativity, patience, support, and guidance throughout the project. You are an endless think tank of ideas, and have been a great teacher of writing with simplicity and elegance. I truly enjoyed each paper I wrote with you. Thank you for the opportunity and space to deviate from my dissertation for other interests, such as teaching and helping piece together Bonanza arc geochronology - both very much highlights during my time here. My mini Bonanza arc crustal section will also be a forever treasured gift.

Thank you to Jody Spence, for your assistance and patience with analytical work, and for your continued moral support over the years. I am grateful to each of my committee members: Jon Husson, for your big picture questions and reminding me that the carbon cycle lives beyond the subduction zone; Kathy Gillis, for your mentorship and support, both in teaching and research; Arthur Blackburn, for your enthusiastic questions and coming onto the project late; and to my external, Jade Star Lackey, for your 'magma adjacent' and skarn knowledge.

Thank you to the many graduate students and staff, especially the friendships and support from Katie Withrow, Xin Qiao, Michaela Maier, Julia Horne, Siobhan McGoldrick, Alex Geen, CJ Smith, and Catherine Duncan. Thank you to all of the wonderful students I instructed, you were truly a pocket of joy in my years at SEOS – and especially to the EOS 316 class of Fall 2022, who saw me through my first term of teaching <3, thank you for your patience and sharing your love of rocks with me. I am grateful for my online petrology group: Luan Heywood (UW), and Thi Truong – UCI), for all of the listening, paper sharing (and finding!), element ratio ideas, and insight. Thank you to Gosia, I am so grateful for each of our chats over the years.

And of course, a most heartfelt thanks to Simon, (Jack), Owen, and Lewis for reminding me there is a limit to how much one should talk about rocks (truly), and for your love, support, cheering, and balance outside of work.

Chapter 1
Introduction

1.1 An overview of the long-term C cycle

Carbon (C) inputs from the solid Earth (crust, mantle) to the ocean-atmosphere-biosphere is fundamental for sustainable life and regulates Earth's long-term (>1 Myr) climate variability. The long-term C cycle is defined as the flux of C over millions of years, between the atmosphere, oceans, and biosphere (herein referred to as the exogenic system) with the crust and mantle (herein referred to as the endogenic system). This continuous exchange of C is what controls atmospheric carbon dioxide (CO_2) levels on million-year timescales, and in turn, Earth's surface temperature that allows for a habitable climate (Berner, 2004; Hayes and Waldbauer, 2006).

Increasing levels of modern atmospheric CO_2 and subsequent warming has motivated recent studies to better understand the long-term C cycle and warming (or 'greenhouse') events in Earth's history. Increased atmospheric CO_2 levels are generally thought to be the result of an increased CO_2 flux to the exogenic system, where the primary mechanism of CO_2 delivery to Earth's atmosphere is by volcanic degassing and metamorphic reactions, and to a lesser extent, the weathering of carbonates and organic carbon (Figure 1.1) (Kerrick and Caldeira, 1998; Berner, 2004; Lee et al., 2019; Werner et al., 2019). Other potential mechanisms of atmospheric warming could include decreased efficiencies in removal of exogenic CO_2, such as decreased weathering of silicate crust (oceanic and continental) (Lee et al., 2019; Isson et al., 2020).

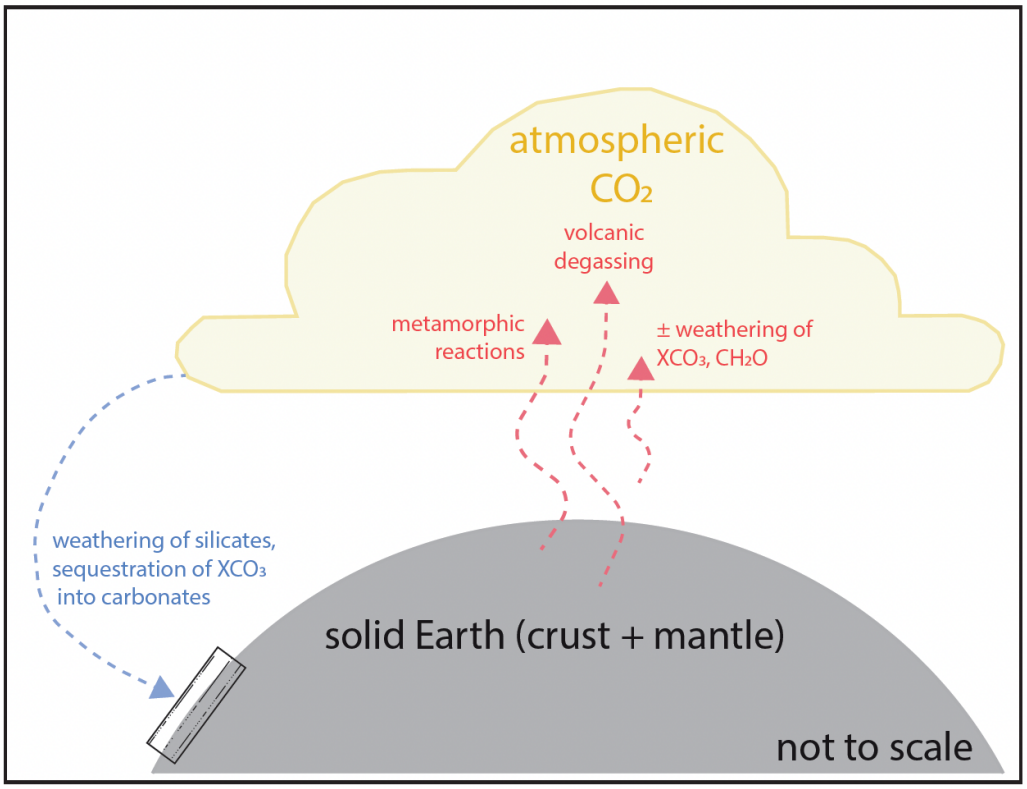

Figure 1.1: A highly simplified schematic of C fluxes controlling long-term (>1 Myr) atmospheric CO_2 levels. Outputs of CO_2 to the exogenic system (atmosphere, oceans, biosphere) primarily occurs from volcanic degassing, metamorphic reactions, and less significantly by weathering of carbonates (XCO_3) and organic (CH_2O) material. Inputs back into the endogenic system (crust, mantle) occurs by weathering of silicates and sequestration of carbonates, and possible subduction. Carbonate compositions (XCO_3) refers to an 'X' cation that is typically Ca^{2+}, Mg^{2+}, and to a lesser degree Fe^{2+}. The short-term C cycle is not shown nor described in this thesis.

Long-term climate regulation is considered to be largely dependent on negative feedback responses, where excess atmospheric CO_2 is removed by silicate weathering (Figure 1.1), as expressed by the following simplified Urey equation (Urey, 1952; further simplified in Isson et al., 2020):

$$CO_2 + XSiO_3 = XCO_3 + SiO_2$$

This removal of atmospheric CO_2 sequesters C back into the crust and mantle, either directly by deep burial of crustal C in the continents or oceans, or indirectly by subduction of C on or within the slab that is then transferred to the mantle (Galvez and Pubellier, 2019; Lee et al., 2019; Isson et al., 2020).

As mentioned, a primary mechanism for delivery of atmospheric CO_2 is from volcanic degassing (Hayes and Waldbauer, 2006), however the magnitude of CO_2 contributions from different volcanic settings (e.g., arcs, rifts, hot-spots) varies (Wong et al., 2019). Numerous studies have suggested that increased volcanic degassing drove past greenhouse events, (Caldeira and Rampino, 1990; Larson, 1991; Lee et al., 2013; Lee and Lackey, 2015; McKenzie et al., 2016; Brune et al., 2017), but the type of volcanism is often debated. For example studies suggest past greenhouse events were driven by ridge or rift volcanism (Brune et al., 2017), while others suggest they were driven by arc volcanism (Lee et al., 2013; McKenzie et al., 2016). The latter, arc dominanted, has been the subject of recent attention because of the various sources of C with the arc system (slab, mantle, ± overlying crust) and their potential CO_2 contributions.

1.2 Subduction zones – complex C cycling

CO_2 contributions from arc settings are complex because of the multiple C sources (slab, mantle, overlying crust) and the behaviour of C in each. In a subduction zone, C is brought into the mantle on or within the slab, where C is either released and recycled back to the atmosphere from volcanic degassing, or is carried to the deep mantle on the slab. The fate of recycled C, whether it is recycled to the surface or transferred to the deep mantle varies between subduction zones and is dependent on numerous factors, such as 1) the C type (i.e., organic vs inorganic, marine sediments vs altered oceanic crust); 2) the pressure-temperature-time path of the slab; 3) slab composition and degree of alteration; and 4) the involvement of other fluids (i.e., H_2O).

Traditional (Kerrick and Connolly, 2001; Shaw et al., 2003; Wallace, 2005) and recent (Chen et al., 2023) estimates suggest that most subducted C (50 – 87%) survives decarbonation and melting reactions, for both warm and cold slabs. Other studies have indicated a large range

(and therefore uncertainty) of C that is recycled back to the surface (20 – 80% from Dasgupta and Hirschmann, 2010; 18 – 70% from Johnston et al., 2011; and 27 (+23) (-16)% from Plank and Manning, 2019.

Regardless of C proportions recycled, all estimates agree that subducted slabs undergo some degree of metamorphic decarbonation reactions (Kerrick and Connolly, 2001; Johnston et al., 2011; Gonzalez et al., 2015) and/or potential melting of C (Skora et al., 2015; Poli, 2015), where both decarbonation and melting reactions are enhanced in the presence of H_2O (Ague and Nicolescu, 2014; Skora et al., 2015; Poli, 2015). Decarbonation and melting of C within the slab transfers C to the mantle, either as a fluid phase or as CO_2-bearing liquids, which inevitably fluxes as diffuse or direct CO_2 to the surface. Direct degassing of CO_2 from gas plumes at or nearby the main magmatic arc (Figure 1.2a) is dominantly sourced from exsolution of CO_2 in magmas ascending the crust, whereas diffuse degassing of CO_2 occurs from non-structurally bound C that is mobilized in the crust along grain boundaries and fractures from low temperature (<450°) hydrothermal fluids (Shinohara, 2013; Auippa et al., 2017; Werner et al., 2019). Diffuse degassing is thought to be an underestimated factor for global C flux, as significant and unmeasured CO_2 degassing likely occurs distally (>km's away) from the main arc edifice along faults and fractures (Kerrick, 2001; Tamburello et al., 2018). Diffuse degassing is also common in the forearc and accretionary wedge (Figure 1.2a), especially in subduction zones with particularly warm geotherms and clay-rich C sediments on the slab (Kerrick and Connolly, 2001).

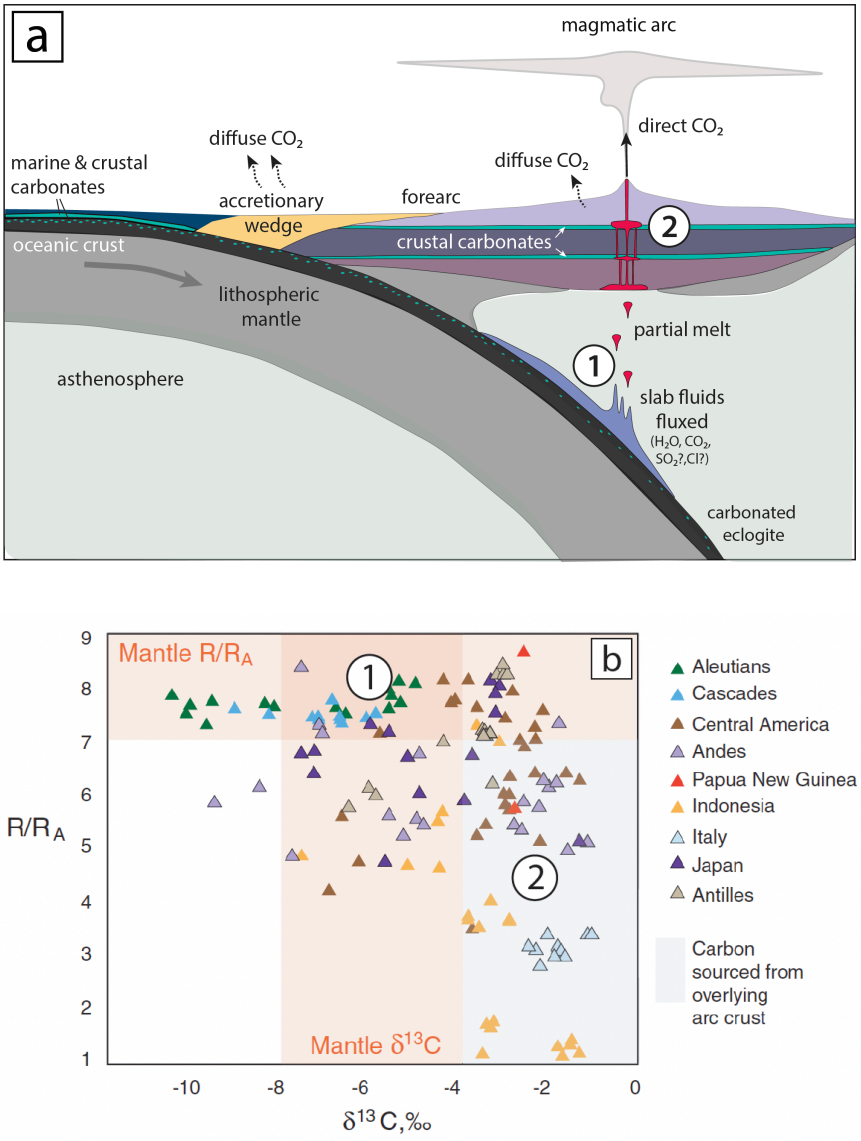

Figure 1.2: **(a)** Cross-section schematic of an arc with crustal carbonates. Outgassed CO_2 at arcs is sourced from decarbonation and/or melting reactions fluxed from (1) the downgoing slab, ± (2) magma-carbonate reactions within the overlying arc crust. **(b)** Figure from Mason et al. (2017) displaying volcanic gas He ($^3He/^4He$ normalized to air = R/R_a) versus $\delta^{13}C$ from various arc volcanoes. Gases with enriched $\delta^{13}C$ and lower R/R_a are interpreted to be sourced from mantle-derived (1) versus crustal carbonates (2).

1.3 Arc volcanism and crustal-derived C

Traditional views assume that most of the CO_2 emitted from arc volcanoes is slab-derived (Plank and Manning, 2019). However, numerous studies have demonstrated evidence of reactions between magmas and the crustal carbonates they intersect during ascent through the overlying plate – at both active (Del Moro et al., 2001; Whitley et al., 2020) and ancient (Barnes et al., 2005; Dyer et al., 2011; Lee et al., 2013; Ramos et al., 2020) arcs. Arc magmas reacting with crustal carbonates has implications for the C cycle, because these interactions have potential to produce substantial CO_2. A simplification of this reaction is as follows, where a silicate melt (dominantly SiO_2) reacting with carbonate ($CaCO_3$) produces a silicate melt more enriched in calcium (or eventually phases) + CO_2, and due to the low solubility of CO_2 in arc magmas, most CO_2 produced is degassed:

$$CaCO_{3(s)} + SiO_{2(l)} = CaSiO_{3(l)} + CO_{2(g)}$$

Quantifying the CO_2 produced from these reactions is difficult and requires detailed studies on both active and ancient systems, in addition to supporting experimental work. The extent to which magma-carbonate interactions occurs from natural studies (active and ancient arcs) is debated. Some view these reactions as very localized where magma is dominantly isolated from continued wallrock reaction (Del Moro et al., 2001), yet others suggest wholesale assimilation of carbonate into magma occurs to produce prodigious amounts of CO_2 over the lifetime of a pluton or an entire arc (Lee et al., 2013).

At active arcs, magma-carbonate reactions are evident in the chemistry of emitted gases and erupted minerals and xenoliths. Recent work by Mason et al. (2017) documents enriched $\delta^{13}C$ and lower $^{3}He/^{4}He$ relative to mantle values in gases emitted at arcs that are built upon a carbonate substrate, such as in Indonesia (Sunda arc) and in Italy (Campanian arc). This work

interprets that mantle-derived magmas with lower $\delta^{13}C$ values (~ –5‰ $\delta^{13}C$) react with enriched $\delta^{13}C$ crustal carbonates (~ 0‰ $\delta^{13}C$), producing a volcanic gas that is enriched in $\delta^{13}C$ (> –5‰ $\delta^{13}C$, Figure 1.2b). A study by Auippa et al. (2017) supports this interpretation, where evidence of magma-carbonate interactions was observed in notably higher (~4) CO_2/S_T (S_T = total sulfur) to mean global ratios (~2.5) at many of the same arc volcanoes (Italy + Indonesia). Both the Auippa et al. (2017) and Mason et al. (2017) studies suggest magma-carbonate reactions are an important source of emitted CO_2 at arcs, where Auippa et al. (2017) estimate ~20 – 30% of active arc CO_2 emissions are derived from these interactions.

Further confirmation of magma-carbonate reactions occurring at depth in active arcs where magmas intersect crustal carbonates (i.e., Indonesia, Italy) is evident in calc-silicate xenoliths that are erupted in lavas (Del Moro et al., 2001; Whitley et al., 2020). These xenoliths are rich in skarn mineralization (typically garnet + pyroxene), which is a distinct product of metamorphic decarbonation at magma-carbonate contacts (Meinert et al., 2005). In addition, minerals in erupted lavas from Indonesian arc volcanoes show evidence of carbonate interactions from enriched isotopic signatures ($^{87}Sr/^{86}Sr$ in plagioclase – Chadwick et al., 2007; $\delta^{18}O$ in clinopyroxene – Deegan et al., 2021).

Exposed ancient arcs also document magma-carbonate reactions and provide an opportunity to view these interactions at depth. This work however has been largely limited to exposed plutons where entrained xenoliths of reacted carbonate, now converted to skarn mineralization or marble, provide as evidence of magma-carbonate interactions (Barnes et al., 2005; Barnes et al., 2009; Lee et al., 2013; Ramos et al., 2020). Cretaceous crustal xenoliths of skarn mineralization with preserved plutonic textures in erupted Quaternary volcanic rocks also provide as evidence of past reactions, where these xenoliths are interpreted to represent the

contact of magma-carbonate reactions between Cretaceous magmas with older (Paleozoic) carbonates in the Sierra Nevada Batholith (Dyer et al., 2011). Studies on ancient systems estimate both significant (Barnes et al., 2005; Barnes et al., 2009; Lee et al., 2013) and localized (Dyer et al., 2011) assimilation of carbonate within plutons and/or batholiths. However, quantifying the amount of wallrock assimilation into plutons from entrained or erupted xenoliths is difficult, as spatial context from field relationships is generally lost (Glazner and Bartley, 2006).

Approaches to understand the extent and limits of magma-carbonate reactions have also been completed experimentally. In general, these experiments show that magma-carbonate reactions are nearly instantaneous, occurring in seconds to minutes, and that these reactions can be further progressed if the magma is hydrous, as in arc systems (Deegan et al., 2010; Jolis et al., 2013). For example, extensive assimilation of carbonate (up to 48 wt.%) into basalt occurs in <24 h (Carter and Dasgupta, 2015). Products from these experiments have included geochemically unique Ca-rich and isotopically enriched ($^{87}Sr/^{86}Sr$) melts (Deegan et al., 2010; Jolis et al., 2013), and in some cases pyroxene with a high aluminum (or Ca-Tschermacks) component (~15 – 20 wt.% Al_2O_5) (Jolis et al., 2013; Carter and Dasgupta, 2015). Ultimately, these experiments represent unrealistic upper bounds for natural assimilation, because they take place within a closed system where many parameters are controlled (pressure, time, ± oxygen fugacity) and where temperature (heat) is limitless. The controlled conditions of experiments fail to account for the open system behavior of natural systems, where magmas lose temperature and pressure as they cool and/or ascend through the crust, and for physical reasons may or may not interact with the wallrock crust.

1.4 Outstanding questions

Although much experimental work has been done to progress our understanding of magma-carbonate reactions and the implications these interactions have on CO_2 degassing, many questions remain regarding the mechanisms that drive these reactions and the extent to which they occur in the natural case. Experiments prove that these reactions can be significant, but to what extent do such reactions progress in natural open systems, and at what depths? Erupted xenoliths of reacted carbonate (skarn) indicate magma-carbonate interactions have occurred, but exact sampling depths are difficult (if not impossible) to constrain and any context of reaction extent and direction is largely lost. In addition, xenoliths rich in skarn mineralization are dominantly metamorphic products from H_2O-rich magmatic fluids decarbonating and reacting with wallrock, limiting our understanding of magmatic processes. This latter evidence also begs to question if metamorphic processes to liberate CO_2 are dominant in these systems. If so, are the enriched $\delta^{13}C$ gases emitted at arc volcanoes dominantly recording metamorphic or magmatic CO_2? This is important because one assumption in long-term C cycle modeling asserts that $\delta^{13}C$ of volcanic gases has nearly constant mantle-derived values of – 5‰ $\delta^{13}C$, whereas contributions from crustal carbonates can shift that value upward, affecting C isotope mass balance, at least during periods where arc activity was emplaced on carbonate platforms (Mason et al., 2017).

Most importantly, outstanding questions remain as to whether magma-carbonate reactions are localized or more extensive throughout magma bodies, and how different scales of magma and timespans of magma-wallrock interactions influence reaction extents. A simplified view into the roots of an arc volcano can be seen as an extensive system of m-scale dikes and sills that transfer the magma vertically and horizontally, as well as km-scale reservoirs where magma stalls, convects, and cools (Figure 1.3). No study has yet documented and compared the

mechanisms of how carbonate assimilation might take place with these different scales of magma bodies (i.e., dikes versus plutons). This is an important gap of research to address because different scales and timespans of magma-wallrock reaction should have different efficiencies at assimilating carbonate. For example, quickly transiting m-scale dikes and sills that are common in the shallow (<0.2 GPa) arc crust should undergo different igneous processes in comparison to larger km-scale magma reservoirs that stall and cool over much longer periods of time (>kyrs). If m-scale dikes and sills assimilate carbonate on shorter timespans (minutes to days), dissolution or melting of carbonate should be evident from simple binary mixing of two end-member compositions (magma + wallrock). This is different from assimilation of carbonate within a long-lived pluton, where concurrent fractional crystallization can provide additional energy (latent heat of crystallization) for assimilation to proceed, a process known as “assimilation + fractional crystallization” or “AFC”. If the latter (AFC) occurs, this will be evident from geochemical modeling of both fractionation and assimilation processes.

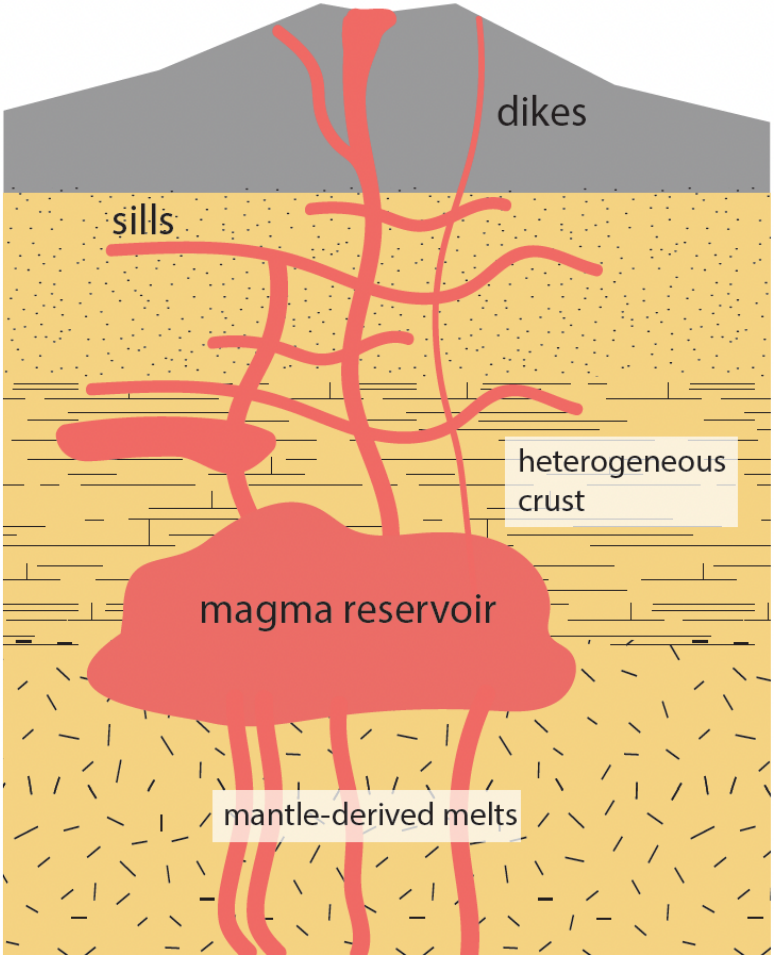

Figure 1.3: A schematic of the various scales of magma bodies that ascend and stall within heterogenous arc crust. The smaller and linear magma bodies are representative of dikes and sills, which transfer magma vertically (dikes) and horizontally (sills) in the crustal column, whereas larger 'magma reservoirs' are representative of plutons where the magmas stall, convect, and cool.

1.5 Research approaches

My research approach for this dissertation focuses on exposures of various scales of magmas (m-scale dikes and sills versus plutons) that have reacted with carbonate in the arc crust. Here, I use exposed magma-carbonate contacts with textures that indicate reactions took place within the Jurassic Bonanza arc on Vancouver Island, Canada, where Jurassic magmas reacted with a Triassic limestone platform (Quatsino Limestone) in the shallow (<5 km) arc substrate.

My in situ and detailed field approach to quantify limestone assimilation limits in arc magmas provides realistic estimates on the magmatic CO_2 that these interactions can produce.

In Chapter 2, I study the origin of unique orbicular dikes. Using detailed petrographic and mineral chemistry analyses, I determine the orbicules to be segregated Ca-rich melts (comprised of only calcic minerals) that differ from the surrounding host melt. Similar to the surrounding host melt, orbicules are crystalline and document identical grain sizes, proving they are igneous in origin. Using mineral chemistry combined with Monte Carlo simulations I provide a range in chemistry for orbicule compositions, and show they are geochemically similar to hybrid melts generated from basalt-limestone experiments by others. Through the use of major and trace element binary mixing models with basalt and limestone end-members I determine orbicules can be generated from the assimilation of 3 – 25 wt.% limestone into basalt, indicating the orbicules that make up to ~17% of dike volumes are capable of producing 11 wt.% CO_2. I use my values of CO_2 produced from orbicule generation to estimate a liberal flux of CO_2 from Bonanza arc magmas, which considers all magmas (plutonic and volcanic rocks) have assimilated the same amount of limestone. This study documents for the first time the formation of calcic orbicules in dikes from limestone assimilation, and as I know, the first time that experimental data (by others) is compiled to determine the effect of depth on carbonate assimilation limits.

In Chapter 3, I study detailed profiles of dikes in contact with limestone from two separate but stratigraphically equivalent regions within the Bonanza arc. I examine dike-limestone contacts petrographically, which reveal unique reacted margins (herein termed ‘boundary melts’) that are distinctly lighter in colour, holohyaline, and often display orbicular textures – much different from the crystalline and darker dike interiors. I further investigate these dike margins in geochemical detail, by micro-sampling ~5 mm intervals from the dike-limestone

contact inward and show that boundary melts display unique Ca, U and Sr enrichments, Si depletion, and $^{87}Sr/^{86}Sr$ that approaches host limestone values. Through the application of major and trace element binary mixing models, I estimate that boundary melts form from ~20 – 25 wt.% limestone assimilation into basalt, indicating the boundary melts that make up to 4% of dike and sill volumes are capable of producing ~9 – 11 wt.% CO_2. I also document possible uphill diffusion of Sr in natural melts preserved in quickly-cooling (minutes) reacted margins, where contrasting viscosities between boundary melts and interior magmas hindered mixing, but promoted super-enrichment of Sr far above typical igneous values. This work shows metal enrichments within magmas at magma-carbonate contacts, which may be of interest to those studying the formation of ore deposits, and sheds light on an overlooked area (magmatic margins) where attention is typically given to metal deposits within the wallrock (skarn).

In Chapter 4, I study in detail the pluton-wallrock contact, from both sampled outcrops and drillcore, the latter which ground truths the exact transition from limestone through a metamorphic aureole and into a pluton. Petrography from marginal pluton samples indicates a very fine-grained chilled margin of unique mineralogy (clinopyroxene + plagioclase) in contact with the metamorphic aureole. I analyze the chilled margin and more interior regions of the pluton (up to ~1.1 km inward) for major, trace, and isotope (Sr) chemistry, which indicates a geochemically unique chilled margin that is enriched in U, REEs, Sr, and $^{87}Sr/^{86}Sr$. Using AFC modeling, I determine the chilled margin can be produced from 20 wt.% limestone assimilated into gabbro, and that fractional crystallization alone can produce most plutonic rock compositions, as determined by thermodynamic modeling. I further prove that the majority of the pluton has not assimilated limestone by analyzing $\delta^{18}O$ values of clinopyroxene, a phase that is readily crystallized from limestone assimilation, and show that no pyroxene analyzed 10 m – 1.1

km from the margin is enriched in $\delta^{18}O$ from wallrock interactions, but depleted. I therefore surmise that the only record of any assimilation within the pluton must be restricted to a <10 m margin, indicating that <1% of the pluton is capable of producing ~10 wt.% CO_2 (assuming 20 wt.% limestone assimilation from modeling).

Chapter 4 also assesses a more regional view of CO_2 production, from dikes and sills (Chapter 2,3), a pluton (Chapter 4), and metamorphic aureole (Chapter 4) at my field site. I further extrapolate these estimates to calculate a realistic CO_2 flux from the Bonanza arc that considers magmatic and metamorphic CO_2 contributions. I show that some historical estimates from plutons (and batholiths) are likely over-estimated, and that unlike plutons, smaller-scale basaltic dikes and sills are a more efficient mechanism of producing magmatic crustal-derived CO_2.

1.6 Dissertation outline

This dissertation is organized into five chapters. Chapter 1 provides an overview of the motivation that drove this research, giving context to why this work is important and the necessary contributions it provides to current gaps in the field. I also provide a brief overview of the various research approaches I have used to quantify magma-carbonate reactions in arc crust. The proceeding chapters (2, 3, and 4) along with their accompanying appendices, represent separate manuscripts that have been published (Chapter 2) or submitted (Chapter 3, 4), all in which I am the first author on. My advisor, Dr. Dante Canil, is the second author on all three manuscripts, and Jody Spence who assisted with Sr-isotope methods and sample digestion techniques is a third author on the manuscript submitted for Chapter 3. Chapter 2 has been published in *Contributions to Mineralogy and Petrology* (Morris and Canil, 2022;

https://doi.org/10.1007/s00410-021-01852-y), Chapter 3 has been published in *GEOLOGY* (Morris et al., 2023; https://doi.org/10.1130/G51439.1) and Chapter 4 has been recently submitted to *Geochemistry, Geophysics, Geosystems*. Some minor editing to Chapter 2 and 3 was made post publication to satisfy a thesis-style document (i.e., unnecessary information in manuscript, such as spherulitic lava photomicrographs in Chapter 2, have been included here). I note that due to specific requirements for manuscript submissions (i.e., for Chapter 3 in *GEOLOGY* and Chapter 4 *Geochemistry, Geophysics, Geosystems*), data submission in open-access repositories is required. For this reason, large datasets for Chapter 3 and 4 are provided in the accompanying appendices, reflecting the organization of the submitted manuscript. To simplify user access to data, all tables included in this thesis are available for download here: https://doi.org/10.6084/m9.figshare.24884265.v1 (Morris, 2023). Finally, Chapter 5 concludes this dissertation with a brief summary of the work and also highlights outstanding questions and potential research avenues for continued work in this field.

Chapter 2

CO_2 transport at shallow depths in arc magmas: Evidence from unique orbicular dikes in the Jurassic Bonanza arc, Vancouver Island, Canada

2.1 Abstract

A growing body of evidence suggests the interaction between arc magmas and crustal carbonates may play a large role in outgassed CO_2 at arcs. To address this, I examined magma-carbonate interactions within the shallow (< 0.2 GPa) crust in the Jurassic Bonanza arc on Vancouver Island, a well-exposed island arc crustal section. Detailed mapping in the Merry Widow mountain area revealed unique, late-stage orbicular mafic dikes that only occur above the stratigraphic level of subsurface carbonates. The orbicular dikes are primitive, show physical and chemical evidence of interaction with limestone, including high CaO/SiO_2 and low REE (~10 – 20x chondrite) that correlate with orbicule abundance, and are geochemically discordant from other rocks of the Bonanza arc. The orbicules have identical intergranular textures to the host melt but markedly higher Ca/Si. Simple binary mixing and MELTs modeling indicates the orbicular dike compositions are a mixture of a primitive hydrous arc basalt with 3 – 25% limestone addition. Comparisons to published experimental data on basalt-calcite reaction suggest some of the dike compositions result from >25% calcite assimilation, producing up to 11 wt.% CO_2, orders of magnitude higher than the CO_2 solubility of the parent melt (0.11 wt.% CO_2). I interpret the orbicules as Ca-rich hybrid melts produced from limestone assimilation that did not homogenize with the host dike magma and underwent crystallization during rapid ascent, possibly propelled by the excess CO_2. These results inform on the amount and mechanism of CO_2 transport at low crustal pressures (<0.5 GPa) in island arcs built on carbonate platforms. I

estimate the CO_2 flux of the Jurassic Bonanza arc to have ranged from 0.14 to >1.16 Tg CO_2/year during its ~34 Myr lifespan.

2.2 Introduction

Earth's long-term (> 1 Myr) climate is controlled by the regulation of atmospheric CO_2 levels (Lee et al., 2013; Lee and Lackey 2015; Isson et al., 2020). Volcanic degassing, a primary mechanism for delivering CO_2 to the atmosphere, may have driven past greenhouse events, but the CO_2 contributions and sources from the various volcanic settings (e.g., arcs, rifts, hot-spots) are debated (Lee et al., 2013, Cao et al., 2017; Auippa et al., 2019; Ratschbacher et al., 2019; Werner et al., 2019; Isson et al., 2020). Constraining the CO_2 flux and its source is difficult in volcanic arcs, where outgassed CO_2 may be produced from decarbonation reactions within both the subducting slab or sub-arc crust (Wallace, 2005; Lee et al., 2013; Auippa et al., 2017; Auippa et al., 2019). It has traditionally been assumed that the CO_2 emitted at arcs is primarily sourced from the subducted slab (Wallace 2005). However, mounting evidence from the chemistry of erupted gases, melts, minerals, and xenoliths, suggests the interaction between arc magmas and crustal carbonates play a larger role (Del Moro et al., 2001; Fulignati et al., 2004; Piochi et al., 2006; Chadwick et al., 2007; Lee et al., 2013; Troll et al., 2013; Mason et al., 2017; Whitley et al., 2019; Whitley et al., 2020; Deegan et al., 2021).

Distinguishing whether crustal carbonates are a significant source of directly outgassed CO_2 in arc settings requires understanding the mechanisms and quantifying the extent of magma-carbonate reactions at all scales. As a complement to active arc studies, exhumed arc crustal sections provide a unique opportunity to examine and quantify such reactions at depth. For example, previous work by Barnes et al. (2003, 2005) examined magma-carbonate interactions

within the exposed Caledonian Hortavær complex (Norway), and showed arc magmas assimilated substantial amounts of crustal carbonate (20 – 60%). Other studies on arc magma-carbonate interactions have focused on decarbonated wallrock (skarn) xenoliths, such as km-scale limestone blocks (now skarn) stoped within the Cretaceous Sierra Nevada Batholith (Lee et al., 2013; Lee and Lackey 2015; Ramos et al., 2020).

The Jurassic Bonanza arc on Vancouver Island is a well-exposed island arc crustal section (DeBari et al., 1999; Canil et al., 2010; Canil et al., 2013). Magmas that fed this arc from ~202 – 168 Ma (Nixon and Orr 2007; Nixon et al., 2011) may have interacted with a basement containing Triassic and Permian carbonates. On northern Vancouver Island, the Merry Widow Mountain area is an ideal site to study these interactions, where historical mining provides remarkable exposures of magma-carbonate contacts (Lund 1966; Ray and Webster 1991), and drillcore logs provide their relationships at depth. Mapping revealed late-stage orbicular mafic dikes showing physical and chemical evidence of magmas that interacted with subsurface carbonate wallrock, and may represent a possible unexplored transport mechanism of CO_2. This study examines how basaltic dikes in arcs can assimilate substantial amounts of limestone, and transport the carbonate component (and excess CO_2) within shallow arc systems. I interpret the unique orbicular textures within these dikes to be fluid-saturated, Ca-rich melts produced from limestone assimilation, that were transported in primitive basaltic melts feeding the arc. Previous experiments on similar basalt-carbonate interactions support my findings and serve as a tool for estimating the carbonate consumed within the shallow arc crust (≤0.5 GPa) (Iacono-Marziano et al., 2007, 2008; Freda 2008; Deegan et al., 2010; Mollo et al., 2010; Carter and Dasgupta, 2015). I show that mafic diking during early magmatism of the Bonanza arc may have assimilated

>25% carbonate. My results help to inform on the amount and mechanism of CO_2 transport at active arc settings today.

2.3 Geologic setting & map units

The Jurassic Bonanza arc (Figure 2.1) is built on a basement of Devonian island arc rocks (Sicker Group), Mississippian to Permian siliciclastic and carbonate rocks (Buttle Lake Group), Middle to Late Triassic large igneous province rocks (Karmutsen Formation), Late Triassic carbonates (Quatsino Formation), and Late Triassic to Early Jurassic mixed carbonate and volcaniclastic rocks (Parson Bay Formation) (Muller 1977).

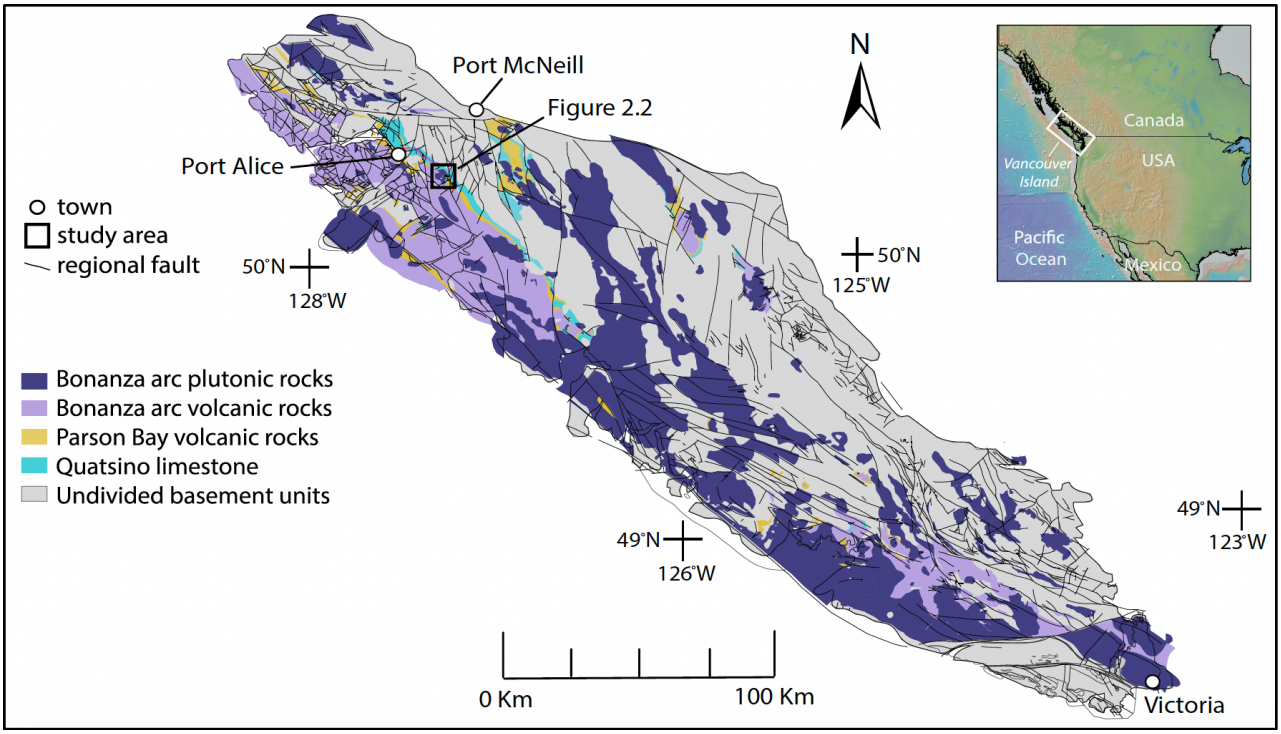

Figure 2.1: Regional geology of Vancouver Island showing only rocks of the Jurassic Bonanza arc and the underlying carbonate-bearing units of the Triassic Parson Bay calcareous rocks (carbonate and volcaniclastic rocks) and Quatsino limestone Formations (modified from Morris and Canil 2021). Geologic unit boundaries and faults are from the British Columbia Geological Survey (BCGS) MapPlace dataset (BC Geological Survey 2021). Inset from GeoMapApp (Ryan et al., 2009). The study area (Merry Widow Mountain) is outlined (black box).

Contacts between Bonanza arc rocks and the underlying Triassic carbonate substrate are well-exposed over a strike-parallel distance of ~6 km along the eastern slope of Merry Widow Mountain, where a section of up to ~2.5 km of paleo-vertical thickness can be traced (Figure 2.2a and 2.2b). The oldest and stratigraphically lowermost units within the study area are massive to bedded, grey to white micrite of the Triassic Quatsino Formation ('Quatsino limestone') which reaches up to ~1 km in thickness and regionally dips ~25 – 50° southwest (Lund, 1966; Ray and Webster, 1991). The limestone is cross-cut by various m-scale dikes and sills, as well as decameter-scale hypabyssal intrusions (Figure 2.2a). In some cases the limestone displays localized ductile folding near magma contacts (Figure A1).

Overlying and conformable with the Quatsino limestone is the late Triassic to early Jurassic Parson Bay Formation (Lund 1966; Nixon and Orr 2007). At Merry Widow, this stratified unit is <100 m thick, and is dominantly a crystal-poor, lithic tuff with a hypocrystalline groundmass (Morris and Canil 2020). Near-vertical bodies of polymictic breccia cross-cut the stratified tuff and include angular xenoliths (tuff, plagioclase-phyric basalt, and gabbro) within a flow-banded hypocrystalline groundmass (Figure A2). Although not exposed, volcanic breccia occurs along the pluton-limestone contact, and is documented in historical drillcore logs (Morris and Canil, 2021). Late-stage mafic dikes also cross-cut the stratified tuff (Figure 2.2a).

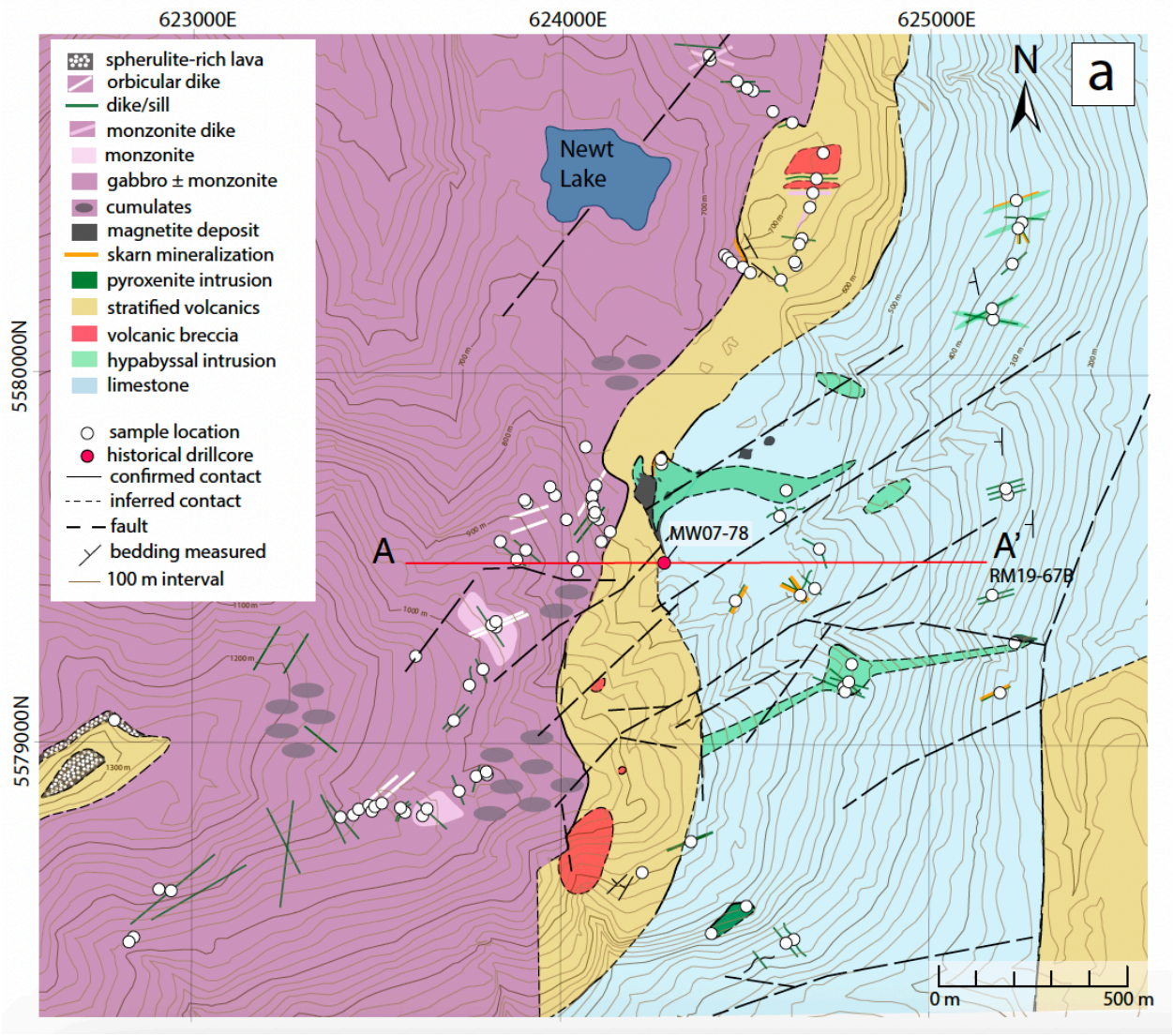
623000E
624000E
625000E
5580000N
5579000N
N
a
Newt Lake
spherulite-rich lava
orbicular dike
dike/sill
monzonite dike
monzonite
gabbro ± monzonite
cumulates
magnetite deposit
skarn mineralization
pyroxenite intrusion
stratified volcanics
volcanic breccia
hypabyssal intrusion
limestone
sample location
historical drillcore
confirmed contact
inferred contact
fault
bedding measured
100 m interval
A
A'
MW07-78
RM19-67B
0 m
500 m

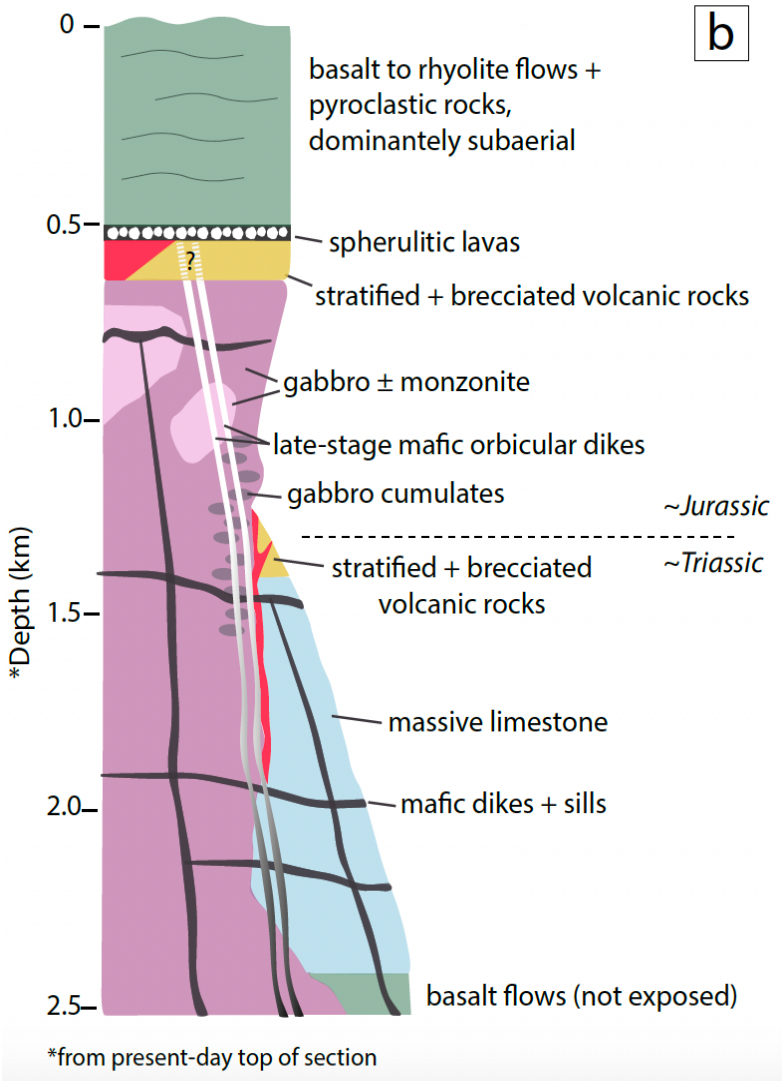

Figure 2.2: **(a)** Detailed bedrock geology of the Merry Widow Mountain area, modified after Sangster (1964), Lund (1966), Ray and Webster (1991), and Nixon et al. (2011). Outcrop sample locations are shown in white. Note sample location RM19-67B (labelled), which is the deepest dike sampled in the stratigraphic section. A cross-section of A-A' is provided in Figure A2, which displays the present-day orientation and dipping of units based on outcrop measurements and historical drillcore (Nicholson, 2006; Wesley and Nelson, 2008; Morris and Canil, 2021). **(b)** A simplified stratigraphic section for the Merry Widow area based on detailed mapping in (a) and drillcore data (Morris and Canil, 2021). Horizontal widths are not to scale, vertical thicknesses and depths are based on outcrop exposures. Thickness of overlying stratigraphic volcanic flows are estimated from previous mapping west of the Merry Widow summit (Nixon et al., 2011) and a conservative regional dip of ~30° southwest (Lund 1966; Ray and Webster 1991). Stratigraphic section is corrected to its assumed paleo-vertical orientation, based on undipping of (assumed) original near-horizontal deposited units (i.e., Parson Bay Formation, Quatsino Formation, and volcanic rocks).

The Merry Widow pluton cross-cuts the Quatsino limestone and Parson Bay Formation, and ranges from dominantly gabbro with pegmatitic mafic cumulates, to lesser occurrences of monzonite (Figure 2.2a). West of the study area, near the Merry Widow summit and stratigraphically higher in the section, monzonite is the more dominant plutonic rock (Ray and Webster 1991; Nixon et al., 2011). The gabbro and monzonite have U-Pb in zircon ages of >197.4 ± 0.5 and 197.1 ± 0.3 Ma, respectively, where ages are within error of an Ar-Ar age of 197.9 ± 1.3 Ma for phlogopite within skarn (Nixon et al., 2011), indicating the age of magma-limestone reactions within the Merry Widow area. Mapped pluton-wallrock exposures at the surface (Figure 2.2a) combined with depths of intersection based on drillhole trend and plunge data indicates the pluton margin has an orientation of ~340°/59° if generalized to be a planar structure (Morris and Canil, 2021).

Spherulite-rich lavas with interbedded crystal-poor tuff are exposed in the western and stratigraphically higher part of the section (Lund, 1966; Figure 2.2a and 2.2b). The lavas vary in thickness (>1 m to <10 cm), as well as in their spherulite diameters (>2 cm to <3 mm) and abundances (>80% to ~20% of rock). Banding of spherulite-rich and spherulite-poor zones is common. The spherulites are dominantly albite and display partial to full replacement of secondary minerals (epidote, oxides, chlorite, albite) (Figure A3).

Mafic dikes and sills intrude the limestone in the lower part of the exposed section and the plutonic rocks within the upper section (Figure 2.2a and 2.2b). The dikes and sills range in width from ~0.25 – 2 m, with most ~1 – 2 m wide, and display chilled margins that are distinctly lighter in colour when in contact with limestone (Figure 2.3). Thin (mm – cm scale) skarn mineralization (grt-ep-mag-ccp-py-bn) and recrystallized calcite are also common at the contact of dikes and sills with limestone. One set of mafic dikes and sills are dominantly plagioclase-

phyric to aphyric and occur throughout the section. A second set of clinopyroxene ± plagioclase phyric dikes contain orbicules that are distinctly lighter in colour than the surrounding host melt, where orbicules can reach >5 mm in diameter (Figure 2.4). These dikes are herein referred to as '*orbicular dikes'*. The orbicular dikes show channelized flow with orbicules that coarsen and increase in abundance towards dike interiors, where margins show <5% orbicules and dike interiors contain up to ~20% orbicules (Figure 2.4). The amalgamation of orbicules is also common (Figure A4). The orbicular dikes outcrop only above the stratigraphic level of the carbonates, where they cross-cut both the gabbro pluton and earlier plagioclase-phyric mafic dikes (Figure A5), and are interpreted to be the youngest magmatic unit within the study area. The unique textures and chemistry of the orbicular dikes are the focus of this study.

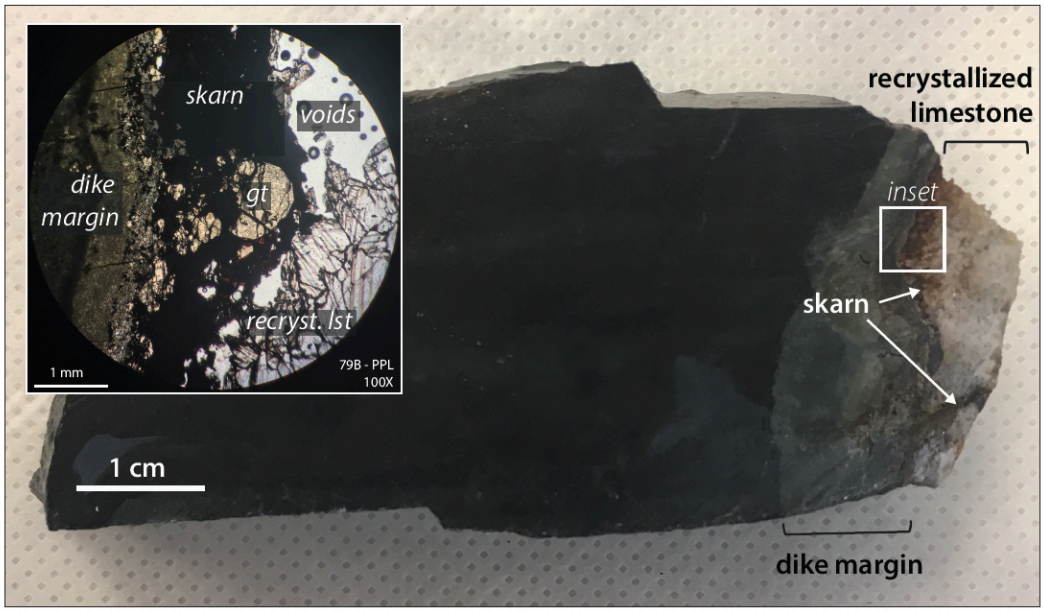

Figure 2.3: Hand sample and photomicrograph across a basaltic dike (RM19-79B) in contact with limestone wallrock. Dikes and sills in contact with limestone are stratigraphically lower in the section, plagioclase-phyric, and commonly show chilled dikes margins that are distinctly lighter in colour. Skarn mineralization (grt-ep-mag-ccp-py-bn) and recrystallized calcite are also common at the contact.

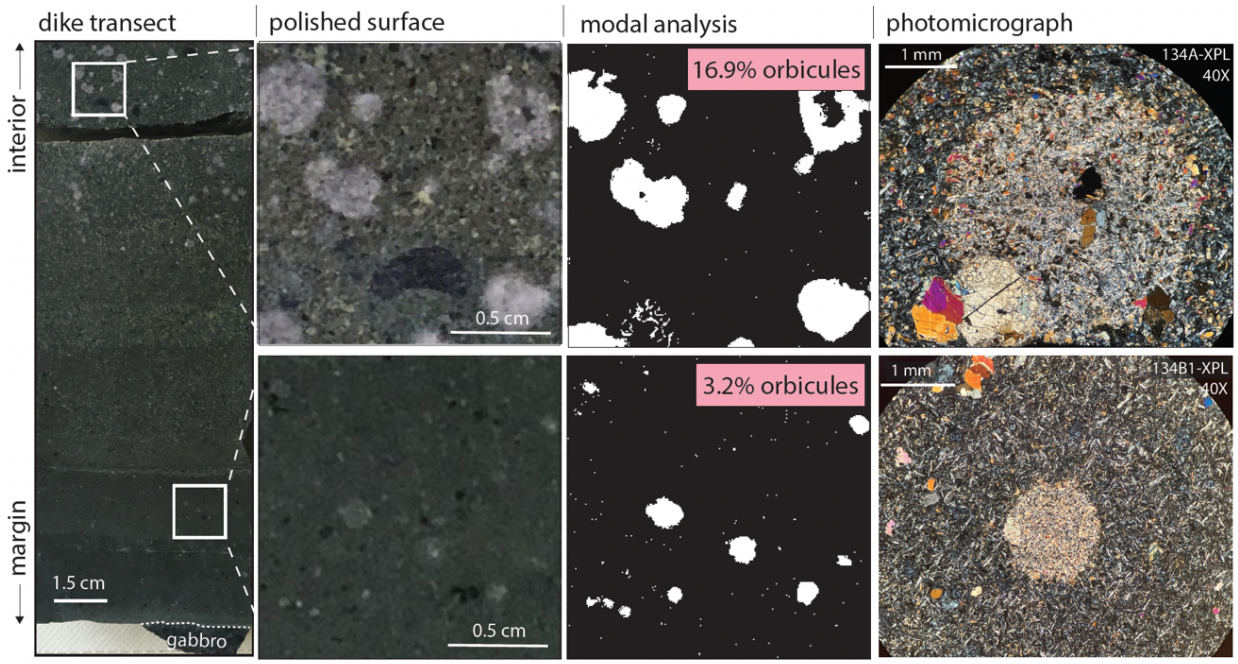

Figure 2.4: Detailed overview of hand sample and photomicrograph across an orbicular dike (RM19-134). Slabbed hand sample photo displays flow texture. Note increasing orbicule concentration from the margin (<5%) to the interior (~17%). Modal analysis was completed using Fiji (trainable weka segmentation plugin v3.2.34 – Schindelin et al., 2012). Modal analysis was 16.9% ± 0.7% for RM19-134A and 3.2% ± 0.1% for RM19-134B1. These estimates are considered qualitative and approximate, as light-coloured alteration phases (i.e., chlorite) similar to the light-colour shade of the orbicules is picked up in modal analysis (i.e., small white spots in black groundmass). The photomicrographs (in cross polarized light - XPL) contrasts the mineralogical differences of orbicules and the surrounding host melt.

2.4 Methods

2.4.1 Sampling and whole-rock geochemistry

Samples from mafic dikes and sills were collected from interiors (sample 'A') and margins (sample 'B'). A transect from dike margin to interior of one orbicular dike (134) was sampled at cm-scale intervals to capture a detailed transition between the orbicule-rich and orbicule-poor regions. All samples collected for geochemistry were from intact and in-situ exposures.

Major element compositions for whole-rock analyses of 21 samples (19 dike and sill samples, 2 limestones) were obtained via inductively coupled plasma optical emission spectrometry (ICP-OES) by Activation Laboratories Ltd (Actlabs). Samples were prepared by powdering fresh rock chips in a planetary agate ball mill. Analyses by ICP-OES measured 10 major element oxides (SiO_2, TiO_2, Al_2O_3, $Fe_2O_{3(T)}$, MnO, MgO, CaO, Na_2O, K_2O, and P_2O5) (Table 2.1). Data accuracy was estimated by Actlabs by comparison of measured differences (wt.%) between known values of certified reference materials (DNC-1, GBW 07113, W-2A, SY-4, and BIR-1A). Measured differences were <2.5% or within 0.1% (i.e., for trace amounts of MnO, K_2O, P_2O_5), with the exception of two $Fe_2O_{3(T)}$ measured differences of 4.7% (DNC-1) and 3.2% (W-2A). Precision estimates measured by Actlabs between repeat samples (RM19-61 and RM19-79B) were <3.7% (Table B1 – Chapter 3).

Trace element compositions of whole-rock analyses of 17 dikes and sills were obtained by solution nebulisation inductively coupled plasma mass spectrometry (ICP-MS) using an Agilent 8800 ICP-MS at the University of Victoria (Table 2.1). Certified reference materials (BCR-2, BHVO-2, BIR-1A, DNC-1, JP-1, and SY-4) were analysed along with samples. Samples were prepared by digesting ~100 mg of whole-rock powder in concentrated acids (5 ml of 50% HF and 0.5 ml of 16N/70% HNO_3) at 120°C for 24 hrs. Digested solutions were uncapped and dried at 150°C for 4 hrs until a gel state was reached. A second acid digestion (4 ml of 8N HNO_3) at 120°C for 12 hrs was completed, dried down, followed by third and final acid digestion (2 ml of 8N HNO_3) that was also dried down. Final solutions were prepared by diluting digested samples with ~125 ml of deionized water. Analyses by ICP-MS measured 14 rare earth elements (REE), as well as Li, P, Ca, Sc, Ti, V, Cr, Mn, Fe, Ni, Cu, Zn, W, Pb, Th, U, Rb, Sr, Y, Zr, Nb, Mo, Cd, Sn, Sb, Cs, Ba, Hf, and Ta. Data correction methods followed Eggins

et al. (1997), using ^{115}In as an internal standard. The corrected data was converted from counts per second (CPS) to concentration by calibration with analyzed standards. Precision for certified reference materials was <3.5% for all analyzed elements. No drift correction was required, as indicated by drift samples measured every 6 samples.

Table 2.1 Whole-rock major element (wt.%) and trace element (ppm) composition

	Plagioclase-phyric dikes and sills										
	RM19-61	RM19-67B	RM19-70B	RM19-79B	RM19-80B	RM19-89B	RM19-95	RM19-102	RM19-113	RM19-151	RM19-161B
Latitude (°N)	50.34835°	50.35359°	50.34505°	50.35359°	50.35472°	50.34756°	50.34914°	50.35469°	50.35142°	50.36380°	50.35556°
Longitude (°W)	-127.26392°	-127.24006°	-127.24796°	-127.24742°	-127.24660°	-127.25168°	-127.25991°	-127.25801°	-127.24559°	-127.24683°	-127.24823°
SiO_2	57.8	49.9	52.7	53.0	51.0	56.1	48.3	50.1	49.7	53.6	50.5
TiO_2	1.24	1.01	1.99	1.78	2.07	1.85	1.47	1.89	1.92	1.98	1.68
Al_2O_3	14.9	18.5	16.9	16.1	14.2	15.0	14.2	14.1	16.1	16.3	14.5
FeO*	7.85	6.58	7.19	9.08	10.08	6.87	10.05	12.67	9.92	8.56	8.24
MnO	0.22	0.14	0.15	0.16	0.17	0.13	0.21	0.21	0.18	0.08	0.18
MgO	1.65	6.06	3.11	3.36	4.20	2.30	3.97	3.91	4.75	3.31	3.78
CaO	4.36	12.89	8.40	7.64	9.54	7.45	8.53	6.32	10.97	7.92	12.89
Na_2O	5.43	2.65	4.72	5.05	3.57	4.83	4.07	3.50	3.13	4.88	4.95
K_2O	1.29	0.28	0.89	0.75	1.72	2.60	0.23	0.91	0.92	1.13	0.69
P_2O_5	0.44	0.17	0.69	0.34	0.31	0.63	0.18	0.21	0.27	0.68	0.27
LOI	3.78	1.73	2.02	1.77	1.39	2.06	7.85	4.33	1.61	1.22	1.92
Total	99.0	99.9	98.7	99.1	98.2	99.8	99.0	98.1	99.5	99.7	99.6
Mg#	14.0	41.7	25.1	22.3	24.4	20.6	23.5	19.3	27.1	23.1	26.2
Cs	0.10	0.92	0.64	0.16	1.22	0.21	0.15	0.18	0.51	0.92	4.06
Rb	28.3	4.9	19.5	12.8	39.8	43.4	5.6	24.1	20.5	20.4	4.1
Sr	252	439	2624	1472	4159	895	252	270	442	606	645
Zr	202	58	113	61	98	182	91	97	97	78	67
Ba	277	86	223	229	439	600	55	410	283	261	99
Sc	17	32	24	29	44	28	36	39	38	27	37
V	30	227	125	183	399	84	284	371	349	119	329
Cr	2	82	4	2	24	4	24	1	22	2	17
Ni	0	29	4	1	12	1	11	4	18	2	5
Cu	9	12	6	19	63	109	57	13	28	13	16
Co	10	18	6	23	27	24	31	36	22	12	18
Zn	96	46	47	82	193	48	96	122	47	38	63
Ga	23	15	21	20	26	34	15	28	23	22	16
Y	53	18	51	36	40	61	32	33	34	42	28
Nb	7.28	2.09	8.44	5.71	5.03	10.37	3.50	3.49	4.20	7.09	3.58
Ta	0.46	0.13	0.53	0.35	0.32	0.64	0.22	0.22	0.26	0.44	0.22
La	13.8	4.3	12.3	11.0	8.6	17.3	6.8	6.5	7.9	13.7	7.1
Ce	33.7	10.5	29.4	25.5	21.9	44.6	16.8	16.2	20.1	29.8	17.1
Pr	5.19	1.53	4.62	4.01	3.55	7.16	2.68	2.70	3.30	4.65	2.64
Nd	23.9	7.1	22.1	18.2	16.8	32.6	12.7	13.1	15.5	22.0	12.3
Sm	6.94	2.13	6.82	5.12	5.09	9.05	3.90	4.13	4.57	6.38	3.64
Eu	2.31	0.86	2.55	1.78	1.59	2.67	1.48	1.34	2.04	2.43	1.40
Gd	7.97	2.56	8.14	5.79	5.91	9.96	4.62	4.92	5.26	7.27	4.24
Tb	1.38	0.45	1.43	0.98	1.03	1.66	0.82	0.88	0.91	1.20	0.73
Dy	8.92	2.94	9.08	6.20	6.71	10.41	5.31	5.71	5.83	7.51	4.73
Ho	1.88	0.62	1.85	1.28	1.41	2.18	1.12	1.20	1.23	1.54	0.99
Er	5.56	1.82	5.10	3.65	4.12	6.30	3.24	3.49	3.57	4.35	2.88
Tm	0.84	0.28	0.72	0.53	0.61	0.93	0.48	0.52	0.53	0.63	0.43
Yb	5.44	1.78	4.41	3.29	3.88	5.90	3.02	3.26	3.35	3.90	2.77
Lu	0.84	0.28	0.64	0.47	0.58	0.89	0.45	0.49	0.50	0.58	0.42
Hf	5.30	1.55	3.13	1.79	2.71	4.86	2.48	2.66	2.64	2.19	1.97
Pb	4.52	0.49	0.96	1.12	10.54	2.62	2.26	1.57	1.34	1.43	1.38
Th	1.66	0.67	1.34	0.90	1.27	2.24	0.64	0.66	0.71	1.06	0.92
U	0.86	0.33	0.66	0.41	0.81	0.97	0.34	0.35	0.39	0.50	0.52

Major elements total includes LOI value. FeO is total FeO, calculated from Fe2O3(total)*0.8995. Data accuracy was estimated between known values of certified reference materials (DNC-1, GBW 07113, W-2A, SY-4, and BIR-1A). Measured differences were <2.5% for all oxides or within 0.1% for trace amounts of MnO, K2O, P2O5, with the exception of two Fe2O3(total) measured differences of 4.7% (DNC-1) and 3.2% (W-2A). Precision estimates between repeat samples (RM19-61 and RM19-79B) were <3.7%. Relative precision for certified reference materials (BCR-2, BHVO-2, BIR-1A, DNC-1, JP-1, and SY-4) was <3.5% for all trace elements. Results for repeat samples and certified reference materials provided in Table B1 (Chapter 3). Em dash (–) indicates element not analyzed.*

Table 2.1 Whole-rock major element (wt.%) and trace element (ppm) composition

	Orbicular dikes - margins				*Orbicular dikes - interiors*				*Carbonates*	
	RM19-120B	RM19-99B	RM19-134B1	RM19-134B2	RM19-120A	RM19-99A	RM19-134A	RM19-134B3	RM19- 30	RM19- 34
Latitude (°N)	50.34833°	50.35289°	50.35620°	50.35620°	50.34833°	50.35289°	50.35620°	50.35620°	48.52923°	48.53106°
Longitude (°W)	-127.26445°	-127.25917°	-127.25536°	-127.25536°	-127.26445°	-127.25917°	-127.25536°	-127.25536°	-123.36542°	-123.36580°
SiO_2	46.1	47.3	47.9	46.7	47.0	45.8	44.8	47.2	4.00	1.24
TiO_2	0.88	0.92	0.85	0.87	0.83	0.79	0.74	0.87	<0.01	<0.01
Al_2O_3	14.9	15.6	16.3	16.7	15.4	16.4	16.3	16.6	0.18	0.02
FeO*	9.42	9.35	9.95	9.87	8.77	8.64	8.19	9.58	0.32	0.10
MnO	0.18	0.17	0.16	0.17	0.17	0.17	0.15	0.16	0.09	0.03
MgO	7.71	7.43	7.94	7.82	7.15	6.91	6.48	7.43	0.29	0.13
CaO	9.39	7.80	7.87	9.18	11.82	13.21	15.40	10.23	53.6	55.0
Na_2O	2.48	2.99	3.96	3.47	2.09	2.20	2.26	3.39	< 0.01	< 0.01
K_2O	1.37	1.50	0.03	0.06	1.36	0.72	0.01	0.02	< 0.01	< 0.01
P_2O_5	0.15	0.14	0.14	0.14	0.14	0.12	0.11	0.14	0.12	0.02
LOI	4.72	4.40	4.27	4.17	4.64	4.89	4.65	3.97	41.7	43.2
Total	97.3	97.6	99.3	99.1	99.4	99.8	99.1	99.5	100.3	99.7
Mg#	38.8	38.1	38.2	38.1	38.7	38.3	38.0	37.6	–	–
Cs	–	0.08	0.02	0.01	–	0.03	0.01	0.01	–	–
Rb	–	35.3	0.4	1.1	–	14.0	0.3	0.2	<2	<2
Sr	311	311	302	567	195	107	360	645	287	210
Zr	43	43	40	42	40	38	36	42	<2	<2
Ba	339	666	9	13	267	89	3	5	6	3
Sc	37	38	34	35	36	37	37	37	<1	<1
V	296	296	272	284	279	271	259	279	<5	<5
Cr	–	139	90	132	–	152	187	139	<20	<20
Ni	–	53	42	52	–	56	58	56	<20	<20
Cu	–	103	94	141	–	128	36	143	10	30
Co	–	42	44	43	–	38	33	40	<1	<1
Zn	–	96	70	69	–	71	45	61	<30	<30
Ga	–	30	10	12	–	15	14	12	<1	<1
Y	12	15	14	15	12	13	13	15	4	<1
Nb	–	2.51	2.29	2.43	–	2.13	1.99	2.41	<1	<1
Ta	–	0.15	0.14	0.15	–	0.13	0.12	0.15	<0.1	<0.1
La	–	5.3	4.8	5.2	–	4.3	4.4	5.1	1.0	0.3
Ce	–	12.9	11.7	12.5	–	10.9	10.7	12.4	1.5	0.4
Pr	–	1.89	1.69	1.82	–	1.59	1.56	1.80	0.24	0.06
Nd	–	8.5	7.6	8.1	–	7.2	7.1	8.1	1.1	0.3
Sm	–	2.25	2.03	2.17	–	1.92	1.90	2.16	0.30	<0.1
Eu	–	0.88	0.73	0.97	–	0.73	0.76	0.90	0.08	<0.05
Gd	–	2.52	2.22	2.42	–	2.12	2.14	2.41	0.40	0.10
Tb	–	0.42	0.37	0.40	–	0.35	0.35	0.40	<0.1	<0.1
Dy	–	2.59	2.29	2.49	–	2.21	2.21	2.48	0.40	0.10
Ho	–	0.53	0.47	0.51	–	0.46	0.46	0.51	<0.1	<0.1
Er	–	1.53	1.35	1.47	–	1.31	1.30	1.46	0.20	<0.1
Tm	–	0.22	0.20	0.21	–	0.19	0.19	0.21	<0.05	<0.05
Yb	–	1.42	1.25	1.36	–	1.21	1.21	1.36	0.20	<0.1
Lu	–	0.21	0.19	0.21	–	0.19	0.18	0.20	0.03	<0.01
Hf	–	1.19	1.09	1.14	–	1.04	0.98	1.13	<0.2	<0.2
Pb	–	1.75	1.48	1.10	–	1.77	3.27	2.48	<5	<5
Th	–	0.36	0.33	0.34	–	0.31	0.29	0.34	<0.1	<0.1
U	–	0.18	0.16	0.17	–	0.15	0.14	0.17	0.9	0.7

Major elements total includes LOI value. FeO is total FeO, calculated from Fe2O3(total)*0.8995. Data accuracy was estimated between known values of certified reference materials (DNC-1, GBW 07113, W-2A, SY-4, and BIR-1A). Measured differences were <2.5% for all oxides or within 0.1% for trace amounts of MnO, K2O, P2O5, with the exception of two Fe2O3(total) measured differences of 4.7% (DNC-1) and 3.2% (W-2A). Precision estimates between repeat samples (RM19-61 and RM19-79B) were <3.7%. Relative precision for certified reference materials (BCR-2, BHVO-2, BIR-1A, DNC-1, JP-1, and SY-4) was <3.5% for all trace elements. Results for repeat samples and certified reference materials provided in Table B1 (Chapter 3). Em dash (–) indicates element not analyzed.*

2.4.2 Mineral chemistry

Minerals in the orbicular dikes were analyzed for major element chemistry by electron probe micro analysis (EMPA) using a five-wavelength spectrometer Cameca SX-100 at the University of Alberta (Table A1 – A6). All minerals were measured using a 20 kV accelerating potential and a 30 nA beam current. A focused beam diameter of <1μm was set for pyroxene, oxides, titanite and prehnite. Analysis of epidote (2 μm), plagioclase (10 μm), chlorite (10 μm), and calcite (10 μm) employed a larger beam diameter for better stability under the electron bombardment. Element peaks and backgrounds were counted at 20 s for all elements. Analytical uncertainty was calculated from standard deviations of repeat (4 times) measured standards: Si <0.14%; Al <0.09%; Ca <0.16%; Fe <0.18%; Mg <0.06%; Na <0.15%; K <0.03%; Ti <0.33%; Cr <0.1%, and Mn <0.06%.

2.5 Results

2.5.1 Petrography

Triassic and younger units on Vancouver Island have experienced prehnite-pumpellyite facies burial metamorphism (Stewart and Page, 1973; Kuniyoshi and Liou, 1976). In the descriptions below: igneous clinopyroxene is fresh; plagioclase is variably albitized, or pseudomorphed by prehnite; glass is replaced by prehnite, pumpellyite or chlorite; and Fe-Ti oxides have been variably replaced by titanite.

I examined nine dikes and sills which were either plagioclase-phyric or clinopyroxene ± plagioclase phyric and orbicule-rich (‘orbicular dikes’). Plagioclase-phyric dike and sills have plagioclase laths (~0.2 – 1 cm) that are sieved and/or sericitized within a groundmass of intergranular clinopyroxene, plagioclase, and secondary minerals (±chl, ±ttn, ±ep, ±act).

The orbicular dikes contain segregated orbicules that are distinctly lighter in colour compared to the surrounding host melt (Figure 2.4). The orbicules and host melt are hypocrystalline, with remarkably identical grain sizes and textures of intergranular clinopyroxene, plagioclase, and glass (Figure 2.5). The modal mineralogy of the orbicules and host melt differ significantly. The host melt consists of albitized plagioclase (30 – 58%), clinopyroxene (20 – 40%), chlorite (20 – 36%), epidote (< 3%), and titanite (< 3%); whereas the orbicules consist of plagioclase and glass (pseudmorphed by prehnite) (35 – 80%), clinopyroxene (20 – 62%) and titanite (<5%) (Figure 2.5). Both the orbicules and host melt are fine-grained at dike margins and coarsen inward. Clinopyroxene phenocrysts are euhedral and occur within the host melt, in orbicules, and along the orbicule-host melt interface. Rare primary calcite inclusions occur within some clinopyroxene phenocrysts (Figure A6). The orbicular dikes also contain small (<1 cm) angular gabbroic xenoliths of granoblastic clinopyroxene and euhedral plagioclase (now albitized), similar in texture and mineralogy to the gabbro of the pluton margin. Rare plagioclase phenocrysts within orbicular dikes are also albitized.

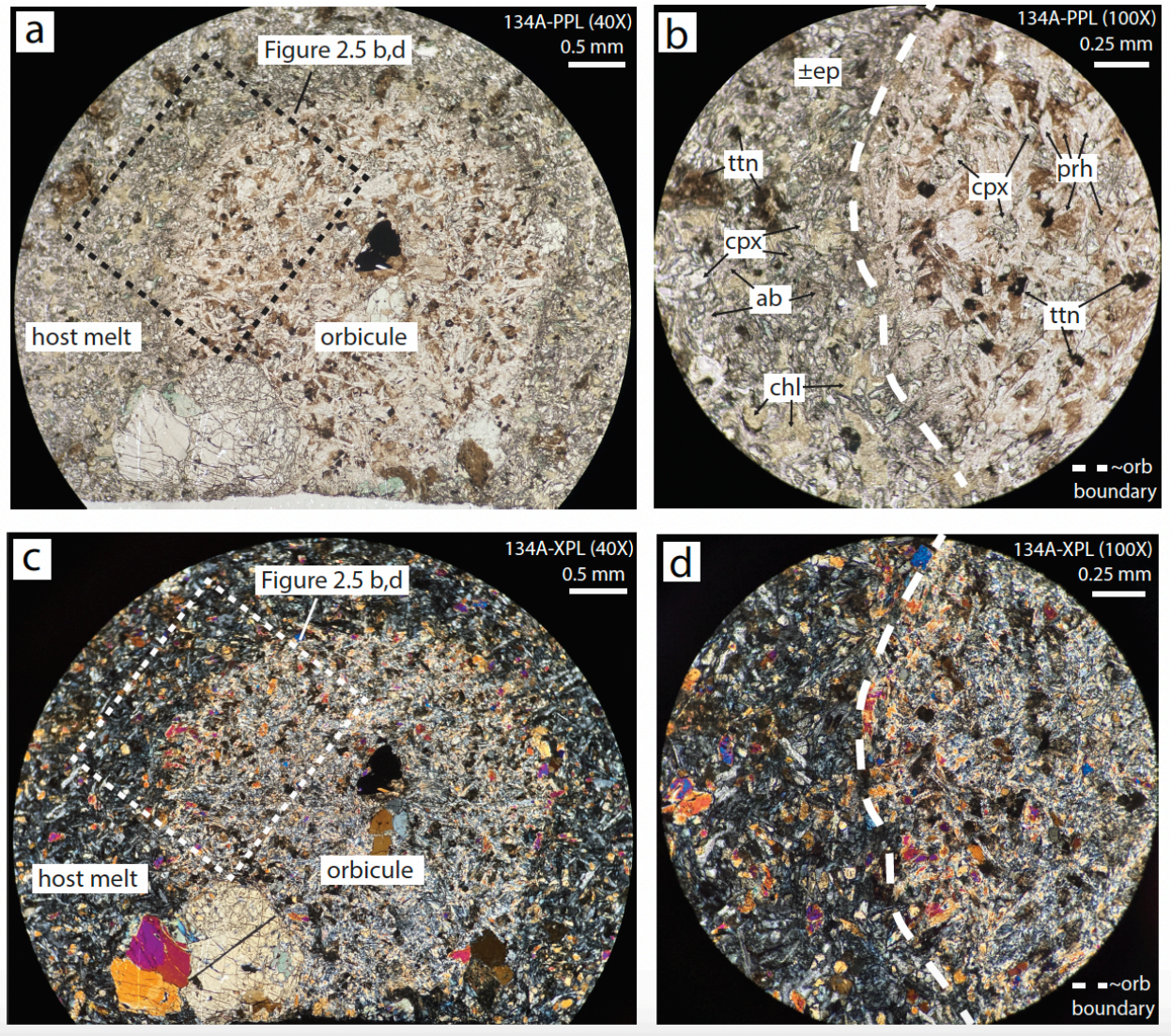

Figure 2.5: Photomicrograph of an orbicule ~4 mm in diameter from orbicule dike interior RM19-134A in plane polarized light (a,b) and cross polarized light (c,d). The host melt consists of albitized plagioclase (30 – 58%), clinopyroxene (20 – 40%), chlorite (20 – 36%), titanite (<3%), and ± epidote (<3%). The orbicules consist of plagioclase and glass (pseudmorphed by prehnite) (35 – 80%), clinopyroxene (20 – 62%) and titanite (<5%). Clinopyroxene phenocrysts are euhedral and occur within the host melt, orbicules, and along the orbicule-host melt interface. A close-up of the clinopyroxene with a calcite inclusion along the host melt – orbicule boundary in the lower left corner of Figure 2.5c is provided in Figure A6. The host melt and orbicules display identical grain sizes, crystallinity, and intergranular texture, indicating they coexisted as liquids and cooled contemporaneously.

2.5.2 Mineral chemistry

Clinopyroxene occurs as phenocrysts or is intergranular within both the host melt and orbicules in orbicular dikes, and is dominantly diopside in composition (Table A1). Intergranular clinopyroxene in the host melt overlaps in composition with that found in the orbicules (Figure 2.6). Clinopyroxene phenocrysts within the host melt and orbicules are similar in composition (Figure 2.6) with elevated Mg# (~0.85) and Cr_2O_3 wt.% (>0.35) in comparison to intergranular clinopyroxene. Mineral compositions of secondary phases that pseudomorph plagioclase, glass or Fe-Ti oxides (prh, ttn, ab, chl, ep) within the host melt or the orbicules are provided in Tables A2 to A6.

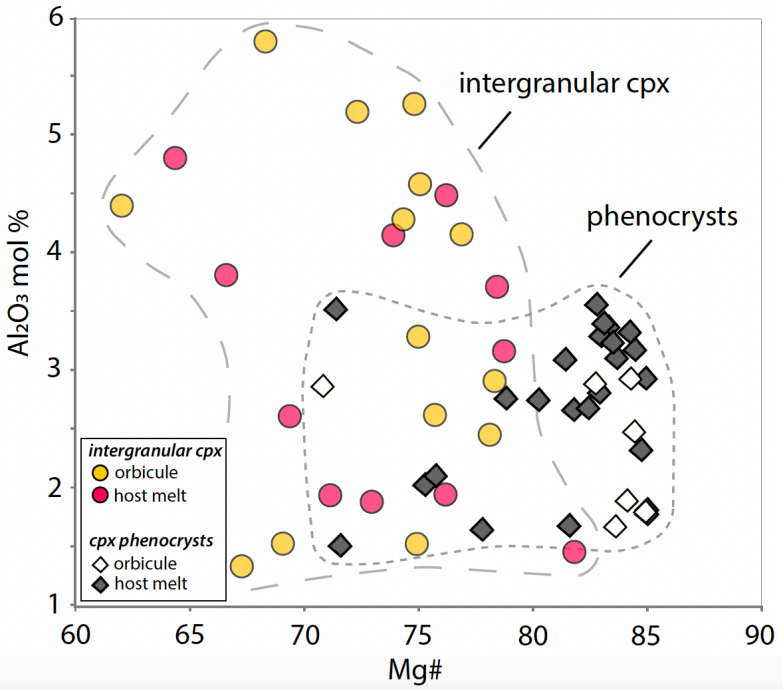

Figure 2.6: Mineral chemistry of primary clinopyroxene preserved within orbicular dikes. Clinopyroxene phenocrysts have a higher Mg#, indicating they are less evolved than the later intergranular clinopyroxene that surrounds them in the dikes. Intergranular and phenocryst clinopyroxene in the orbicules overlap in composition with those in the host melt.

2.5.3 Whole-rock geochemistry

The plagioclase-phyric dikes and sills range from 48 – 58 wt.% SiO_2 and show lower MgO, and Al_2O_3, and higher CaO, FeO*, TiO_2, Na_2O, and P_2O_5 in comparison to other Bonanza arc rocks (Figure 2.7, Table 2.1). Plagioclase-phyric dikes and sills show large ion lithophile enrichment (LILE) and high field strength element (HFSE) depletion, typical of arc settings (Pearce and Peate 1995). Samples have a negative Nb-Ta anomaly, where most display a slight enrichment relative to MORB.

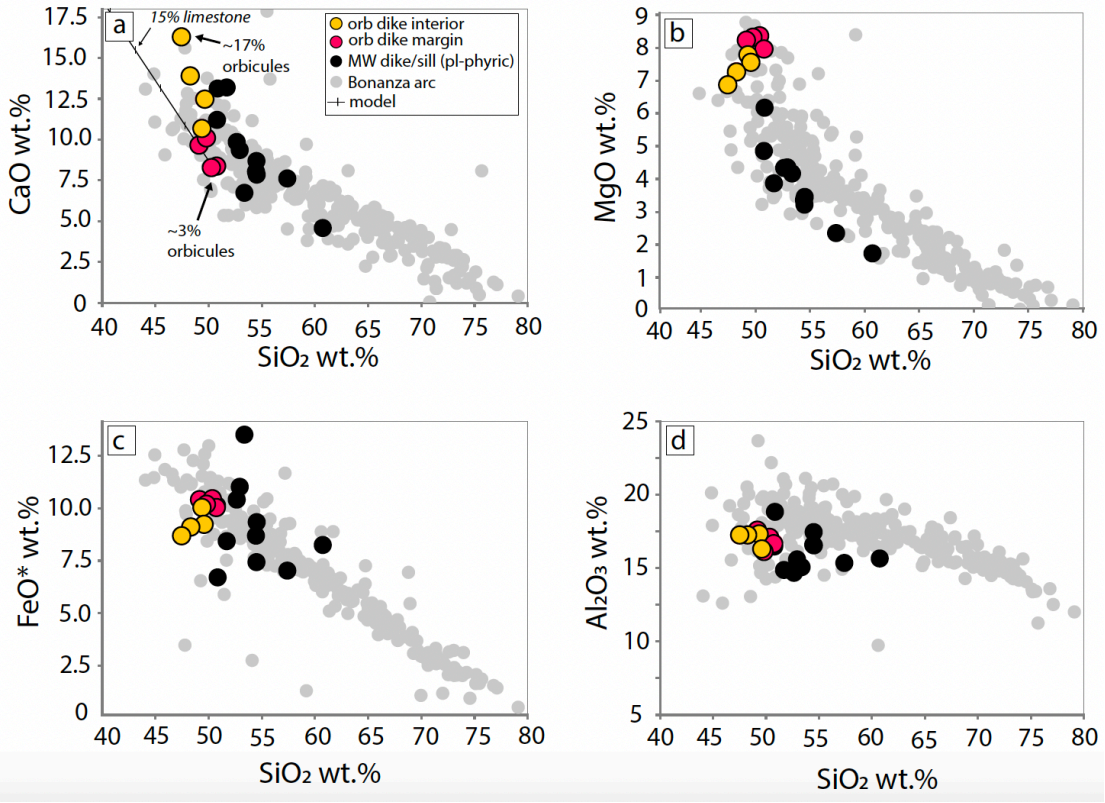

Figure 2.7: Harker diagrams of Merry Widow samples in comparison to Bonanza arc plutonic and volcanic rocks (data from Andrew et al., 1991; Massey 1995a-c; DeBari et al., 1999; Larocque 2008; Fecova 2009; Larocque and Canil, 2010; D'Souza et al., 2016). Orbicular dikes margins are shown as red circles and dike interiors as yellow circles. Plagioclase-phyric dikes and sills are shown as black circles. Merry Widow samples have higher CaO, FeO*, TiO_2, Na_2O, and P_2O_5, and lower MgO and Al_2O_3 in comparison to the trend of other Bonanza arc rocks. Orbicular dikes display a unique discordant geochemical trend from the other arc rocks by having higher CaO and lower MgO, FeO* and TiO_2 with decreasing SiO_2 projecting to a Ca-rich and Si-poor composition, such as limestone (a). Major element oxides have been normalized to 100% on a volatile-free basis.

The orbicular dikes are primitive (45 – 48 wt.% SiO_2, ~0.6 Mg#, 90 – 187 ppm Cr, and 42 – 58 ppm Ni) (Table 2.1), but display strikingly unique geochemical trends, such as markedly increasing CaO with decreasing SiO_2 (Figure 2.7a). In particular, the orbicular dikes transition from calc-alkaline margins to tholeiitic interiors due to a decrease in SiO_2 at relatively constant FeO*/ MgO. Orbicular dikes and one plagioclase-phyric dike from the lower stratigraphic section (RM19-67B – Figure 2.2a) have no Nb-Ta anomaly relative to MORB (~1), higher La_N/Yb_N ~ 2.5 – 2.8, exclusively positive Eu anomalies (Eu/Eu* = 1.1 – 1.3) and strikingly low bulk REE (~10 – 20x chondrite) (Figure 2.8a). These unique REE patterns are nearly identical to other '*primitive*' dikes identified in previous studies of the Bonanza arc (DeBari et al., 1999; Larocque, 2008; D'Souza et al., 2016).

The geochemical transects within the orbicular dikes show that REE abundances markedly decrease with increasing orbicule proportion (Figure 2.8b). The orbicular dikes plot on or near a mixing trend with the Quatsino limestone (Figure 2.7a, 2.9). The latter is nearly pure calcite (>97% $CaCO_3$) and has significantly low REE (<1x chondrite), in some cases below detection limits (Table 2.1).

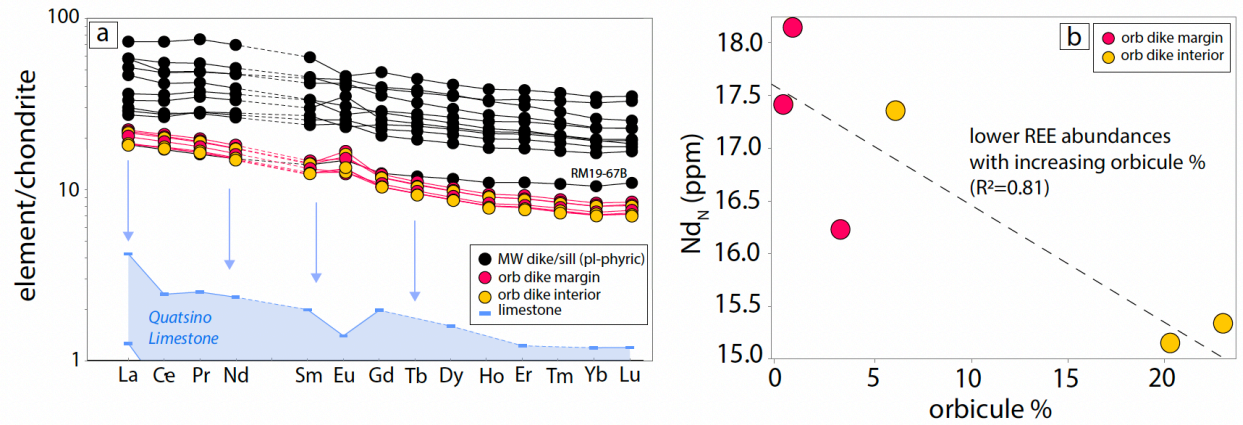

Figure 2.8: **(a)** Whole-rock rare earth element (REE) patterns of the Merry Widow dikes and sills. Orbicular dikes display slight light-REE enrichments (La_N/Yb_N ~ 2.5 – 2.8) and lower REE abundance (10 – 20x chondrite) compared to the plagioclase-phyric dikes and sills (La_N/Yb_N ~ 1.5 – 2.5). **(b)** Orbicular dikes show a decrease in REE concentration with increasing orbicule proportion from margins to interiors.

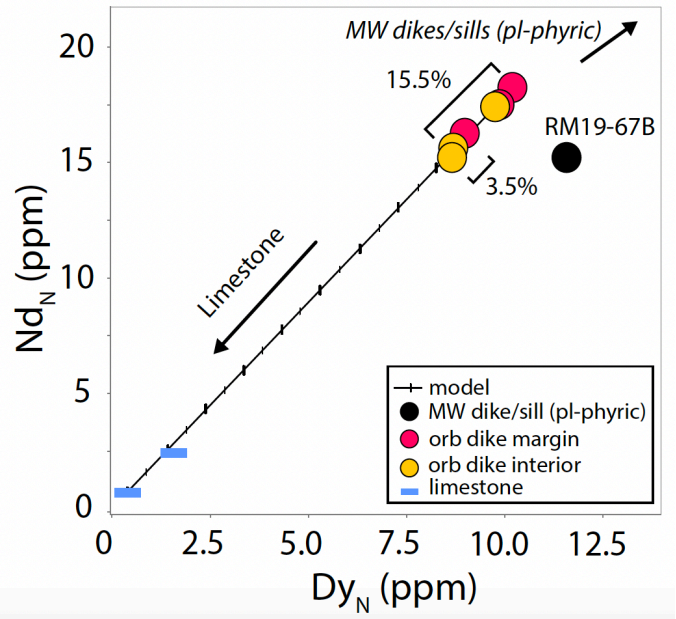

Figure 2.9: Covariation of chondrite- normalized (Nd_N) vs (Dy_N) in the orbicular dikes, one plagioclase-phyric dike with similar REE abundances (RM19-67B – Figure 2.8a), and the Quatsino limestone wallrock. Trends from orbicular dike margins to interiors display a decrease in REE abundance. A conservative simple binary mixing model shows the orbicular dike interior compositions can be achieved by mixing 3.5 – 15.5 wt.% of Quatsino limestone with orbicule dike margin compositions.

2.6 Discussion

2.6.1 Element mobility

I first address the textural and chemical distinction of the orbicules from their host melt, followed by the evidence and extent that they assimilated limestone wallrock. Although all rocks of the Bonanza arc experienced prehnite-pumpellyite facies burial metamorphism, previous studies show they preserve primary igneous trends and $^{87}Sr/^{86}Sr$ ratios, despite the fact that Rb and Sr can be mobile during metamorphism (Andrew et al., 1991; D'Souza et al., 2016).

Nevertheless, I used Pearce element ratio diagrams (Pearce, 1968; Nicholls and Russell, 2016) to test for the effects of low-grade metamorphism on element mobility and geochemical trends in the dike samples specific to this study. The presence of clinopyroxene and/or plagioclase phenocrysts in the mafic dikes at Merry Widow suggest the control of these phases on the bulk chemistry of the dikes. Assuming the dikes differentiated by clinopyroxene ± plagioclase ± olivine control, which is typical of many basalts, the major elements in the rocks should plot along Pearce element ratios for this assemblage (Pearce, 1968; Nicholls and Russell, 2016). Using Nb or K as the conservative element, the Pearce element ratios involving Ca, Mg, Fe, Si, Na in the stoichiometry for the sorting of olivine + plagioclase + clinopyroxene for all mafic dikes plot on slopes of ~ 1, indicating that the abundances of these elements in the rocks are consistent with this hypothesis (Figure A7). The disposition of orbicular dikes on a slope differing from 1 could reflect that they are part of a separate chemical system (i.e., open-system assimilation). For the purposes of testing element mobility, I therefore consider that igneous concentrations of Ca, Mg, Fe, Si, and Na are retained within the dike samples despite prehnite-pumpellyite metamorphism. Any metamorphism that has albitized primary plagioclase, or

replaced mafic glass or other phases with chlorite or prehnite, has not disturbed element systematics at a scale beyond the hand sample or outcrop.

2.6.2 Orbicule and host melt compositions

The orbicular dikes consist of two main components – the orbicules and host melt. I interpret these two components as primary and of igneous origin given that primary intergranular igneous pyroxenes are indistinguishable in composition both within and outside the orbicules (Figure 2.6). The intergranular clinopyroxene is more evolved (lower Mg#) than clinopyroxene phenocrysts either within or outside of the orbicules. Thus, the orbicules and host melt are interpreted to have crystallized around clinopyroxene phenocrysts that were an earlier liquidus phase in the dikes. Although the intergranular clinopyroxene (cpx) compositions in the orbicules and host melt are similar, the melts that they crystallized from are vastly different mineralogically. This difference is shown petrographically by the pseudomorphs in the orbicules (prehnite – 'prh' + titanite – 'ttn') contrasting to those within the host melt (albite – 'ab' + chlorite – 'chl' + titanite – 'ttn' + epidote – 'ep') (Figure 2.5).

The bulk compositions of the orbicules (cpx + prh + ttn) and host melt (cpx + chl + ab + ttn + ep) can be made by combining mineral modes and compositions in Monte Carlo simulations (1000x) to calculate the mean $\pm 1\sigma$ and full range of possible compositions for each oxide component (Table 2.2). Range of modes in orbicules (n=20) are: cpx (20% – 62%), prh (35% – 80%), ttn (<5%), whereas range of modes in host melt (n=20) are: ab (30 – 58%), cpx (20 – 40%), chl (20% – 36%), ep (<3%), ttn (<3%). Mean compositions and standard deviations for phases in orbicules and host melt used in Monte Carlo simulations are provided in Table A7. Stark chemical differences between the orbicules and host melt are well-preserved (Figure 2.10)

even though the samples suffered low-grade burial metamorphism. Calculated host melt compositions surrounding the orbicules are slightly offset from other Bonanza arc rocks, by having elevated Mg, Fe, and Na, and lower Ti (Figure 2.10 – Ti and Na not shown). The presence of a primary igneous intergranular texture and Ca-rich bulk composition (Figure 2.10) indicates that the orbicules crystallized from a Ca-rich melt.

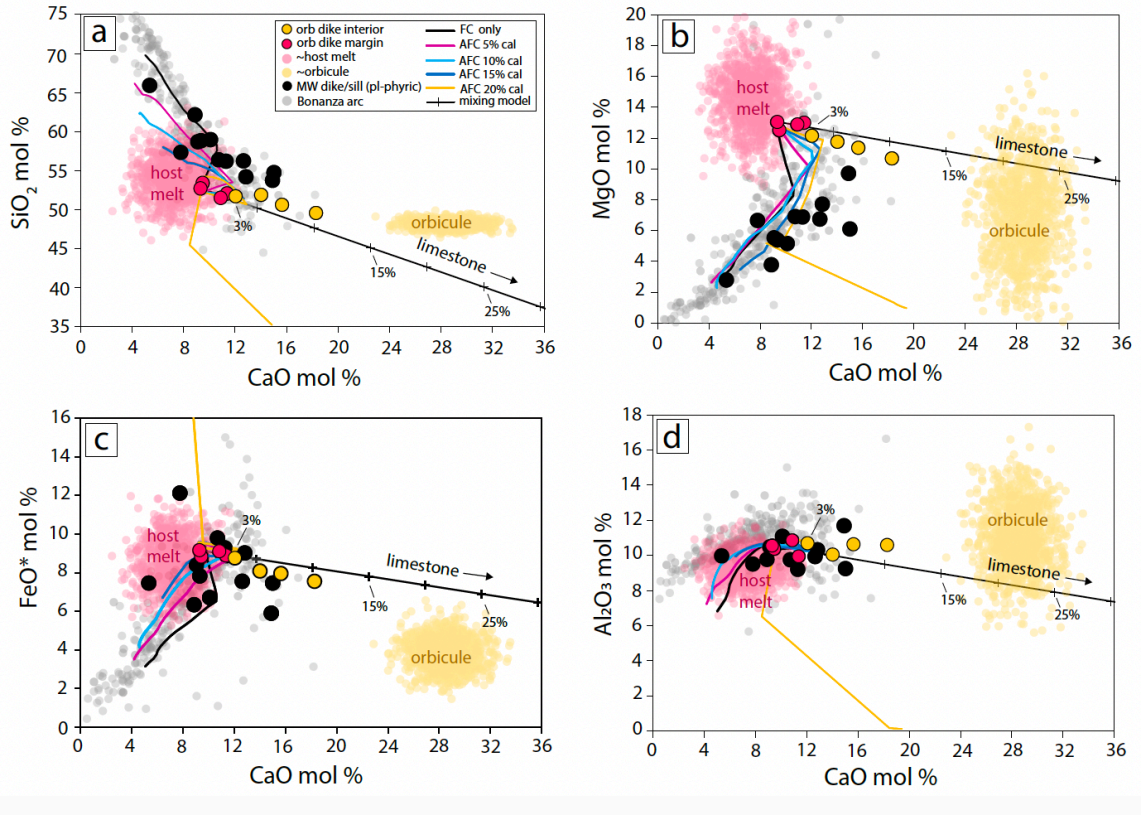

Figure 2.10: Plot showing compositions of Bonanza arc igneous rocks (grey circles), Merry Widow plagioclase-phyric dikes and sills (black circles), and orbicule dikes (red and yellow circles). Light yellow and pink regions display the range of host melt and orbicule compositions derived using mineral compositions and modal data in Monte Carlo simulations (Table 2.2). Coloured lines are MELTS models (Gualda et al., 2012) at 0.2 GPa (isobaric), fO_2 of NNO+1, and initial H_2O of 5 wt.% for fractional crystallization only (FC – black line) and assimilation + fractional crystallization (AFC – coloured lines). For AFC models, 5, 10, 15, or 20% of pure calcite was added at a starting melt liquidus temperature of 1140°C. Models for 5 and 10% calcite assimilation ran to completion with a final melt fraction (F) of < 0.05. Models for 15 and 20% calcite assimilation did not evolve past F ~0.20. MELTs models cannot achieve the most Ca-rich orbicule dike compositions (interiors), nor any of the estimated orbicule compositions. Also shown are simple binary mixing models (black lines with tick marks) that indicate an addition of 3.0 – 10.3% limestone (RM19-34) to orbicule dike margins (RM19-134B1) can produce the orbicule dike interiors.

Table 2.2 Mean Orbicule and Host Melt Compositions (wt.%)

	SiO_2	CaO	Al_2O_3	FeO*	MgO	TiO_2	Cr_2O_3	MnO	Na_2O	K_2O	TOTAL
orbicule	44.85	24.45	16.52	4.55	4.95	1.48	0.04	0.07	0.07	–	96.97
1σ	*0.84*	*0.81*	*2.56*	*1.03*	*2.03*	*0.49*	*0.02*	*0.03*	*0.03*	–	*n.a*
host melt	50.58	6.96	15.21	9.18	9.07	0.77	0.04	0.06	4.60	0.05	96.52
1σ	*2.34*	*1.44*	*0.96*	*1.24*	*1.23*	*0.29*	*0.01*	*0.01*	*0.90*	*0.01*	*n.a*

Compositions calculated based on modal ranges (cpx = clinopyroxene, prh = prehnite, ttn = titanite, ab = albite, chl = chlorite, ep = epidote and phase compositions (ESM Table 1-6) from orbicule and host melt thin section locations

Range of modes in orbicules (n=20): cpx (20-62), prh (35-80), ttn (<5)

Range of modes in host melt (n=20): ab (30-58), cpx (20-40), chl (20-36), ep (<3), ttn (<3)

FeO is total FeO. Em dash (–) indicates oxide not analyzed in any phases. n.a indicates not applicable.*

2.6.3 Models of mixing and assimilation of carbonate

The decrease in REE abundance with increased orbicule proportions (Figure 2.8b) suggest that the orbicule compositions represent an interaction of the parental magma in the dikes with an REE-depleted lithology such as limestone (Figure 2.8a, 2.9). Dikes lower in the section are in direct contact with limestone (Figure 2.3), where some show geochemical similarities to orbicular dikes higher in section (i.e., RM19-67B in Figure 2.8a, 2.9). Given this connection, and that orbicular dike margins and limestone lie on a mixing trend on major and trace element bivariate plots (Figure 2.7a, 2.8a, 2.9), I explore if the Ca-rich orbicules arise from the dissolution of limestone wallrock .

A simple binary mixing model was used to derive the amount of limestone addition needed to achieve the compositions of dike interiors. The model input used orbicule-poor dike margins as the starting melt composition, as they represent the first quenched melt within the dike channel. The model assumes no fractional crystallization occurred during flow in dikes, and considers only the removal of melt at the expense of any added wallrock material. The mixing model therefore maintains mass balance, where the relationship between the element in the parental melt (C_P), the added wallrock (C_A), and the resultant melt (C_R) is:

$$C_R = [F \times C_P] + [(1 - F) \times C_A]$$

In this equation, C is the concentration (mol % or ppm) of the element of interest, and F is the parent melt fraction. Increments of 5% Quatsino limestone (Table 2.1) were added to each step (Figure 2.9 and 2.10), where 5% of the parent melt (dike margin) was subsequently removed from the system. A total of six models were performed, which included testing the dike margin of three orbicule dikes (RM19-134B1, RM19-120B, and RM19-99B) with two Quatsino limestone samples (RM19-30 and RM19-34) (Table 2.1).

The most conservative binary mixing model is one that mixes an orbicule-poor dike margin (RM19-134B1, Table 2.1) with the most Ca-rich and REE-depleted limestone (RM19-34, Table 2.1). Binary mixing results using major elements indicates 3.0 – 10.3 wt.% limestone addition to orbicular dike margins can produce their dike interiors (Figure 2.10). Results using trace elements require 3.5 – 15.5 wt.% limestone addition (Figure 2.9). To obtain the estimated orbicule compositions would require an addition of ~20 – 25 wt.% limestone (Figure 2.10). The amount of added limestone generally correlates with the abundance of orbicules for major element models, but not for trace elements. My mixing calculations suggest ~1.3 – 11.0 wt.% CO_2 could be produced from digested wallrock in the dikes given the Quatsino limestone is nearly pure calcite with 44 wt.% CO_2.

Thermodynamic modeling of major element compositions via the software package rhyolite-MELTS version 1.2.0 (Ghiorso and Gualda 2015) was used to test if it is possible to assimilate the amount of limestone derived in the simple binary mixing models. Starting melt compositions were identical to those used in the mixing models and the assimilant was pure calcite (starting melt composition: RM19-134B1; assimilant: RM19-34). The following model input parameters were used as input: 0.2 GPa (isobaric), starting temperature of 1140ºC for both melt and assimilant, oxygen fugacity (fO_2) buffered to NNO+1, 5% H_2O in the starting melt

composition, and varying additions of calcite assimilant (0, 5%, 10%, 15%, and 20%). A isobaric pressure of 0.2 GPa was based off of an assumed melt emplacement depth of <6 km, estimated from the ~0.5 km of preserved volcanic stratigraphy at the site (Figure 2.2b), which is known to reach maximum thicknesses of 3 km (Canil and Morris, 2023). A starting melt water content of 5 wt.% H_2O was input, similar to hydrous arc melts by others (Wallace, 2005; Plank et al., 2013; Nandedkar et al., 2014). The liquidus temperature of 1140ºC was used as an input starting melt temperature (based on a hydrous composition with 5 wt.% H_2O).

The calcite-free MELTS model provides as a baseline where the starting melt only evolves within a closed-system undergoing fractional crystallization (Figure 2.10). This model follows the liquid line of descent of Bonanza arc rocks until more felsic compositions are reached. For the remaining models with calcite added, the system not only assimilates the calcite, but simultaneously fractionates phases, and hence is commonly referred to as '*assimilation + fractional crystallization'* or AFC modeling. In AFC modeling, the required energy for assimilation to proceed within the system is provided by the latent heat of crystallization (Spera and Bohrson, 2002). Models for 5 and 10% calcite assimilation ran to completion with a final melt fraction (F) of <0.05, whereas those for 15 and 20% calcite assimilation did not evolve past F ~ 0.20. Modeling carbonate assimilation via MELTS is limited by the CO_2 solubility within the melt (~0.5 wt.% CO_2 for MELTS – Ghiorso and Gualda, 2015), and a lack of thermodynamic data available for this process (Heinonen et al., 2021). The addition of 10 – 20% calcite in the models can achieve the compositions of some orbicular dike interiors, but not the most calcic ones furthest displaced from the Bonanza arc liquid line of descent (Figure 2.10). It should be noted that incremental calcite additions generally produce slightly elevated FeO* in the melt, due to earlier fractionation of clinopyroxene and plagioclase, with no early phases removing FeO*

(i.e., magnetite). The addition of 20% calcite also produces an odd dog-leg trend towards Ca-rich compositions, with low Si, Al, Mg and high Fe (Figure 2.10). Adjustments to model input such as increased or decreased pressure (0.1 – 0.3 GPa) and water contents (2 – 7 H_2O wt.%) were also tested, but could not attain the most calcic orbicular dike compositions. I therefore conclude that AFC cannot produce the orbicular dike compositions.

2.6.4 Application of carbonate assimilation experiments

Given the chemical evidence for limestone assimilation and mixing (Figure 2.9, 2.10), I further tested if orbicule and dike compositions fall within the composition space of hybrid melts produced by experiments in which basalt reacts with, and is oversaturated in, pure calcite (Deegan et al., 2010; Carter and Dasgupta, 2015). The compositional spectrum of orbicular dikes lie on the same trend of hybrid basalt-limestone melts (Figure 2.11). In particular, the compositions for orbicules match those of hybrid melts in the short duration (<5 minute) limestone assimilation experiments at 1200ºC and 0.5 GPa (Figure 2.11) (Deegan et al., 2010).

I further apply these experimental data to quantify the amount of calcite assimilated to produce the dike and orbicule compositions. Using mass balance of the modes and compositions of phases reported in basalt-limestone reaction experiments, I calculate the difference in molar CaO/SiO_2 (dCa/Si) between original starting and final hybrid melt as a function of the amount of calcite consumed. More calcite consumption increases the dCa/Si of the hybrid melts in the run products (Figure 2.12). Applying the relation for experiments at ≥0.5 GPa (blue dashed line – Figure 2.12) to the dike compositions, the change in dCa/Si from orbicule dike margins to their interiors would correspond to ~2.4% calcite consumption. A change in composition from host melt to those of the orbicules requires ~5.7% calcite consumption (Figure 2.12).

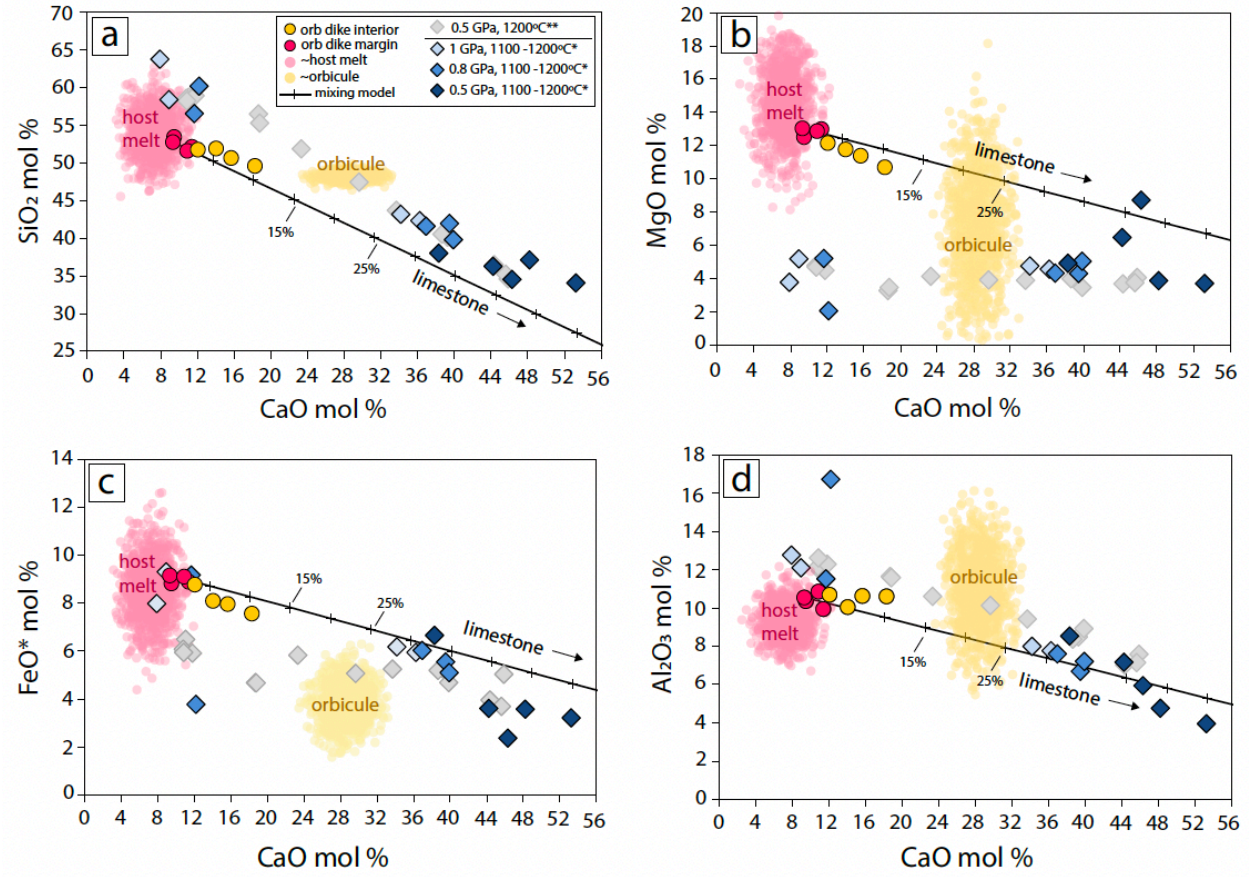

Figure 2.11: Plot comparing the compositions of Merry Widow orbicular dikes (red and yellow circles), and estimates of orbicule (light yellow region) and host melt (light pink region) composition to hybrid melts produced in basalt-calcite reaction experiments (grey and blue diamonds). Blue diamonds – experiments used a hydrous low-K tholeiite (4 wt.% H_2O) at 1100 to 1200ºC, 0.5 to 1 GPa, FMQ -0.5 to FMQ +3, for 16 to 72 hrs (Carter and Dasgupta 2015); grey diamonds – experiments used a hydrous tholeiitic basaltic-andesite (2.2 wt.% H_2O) at 1200ºC, 0.5 GPa, fO_2 NNO+2, for 0 to 5 minutes (Deegan et al., 2010). The trends of hybrid melts generated from experiments are similar to those of the orbicular dikes, and fall on a mixing line between their starting melt and limestone (~pure calcite). The orbicule compositions in the dikes are most similar to hybrid melts from short duration experiments of basalt-calcite reaction (0 – 5 mins) from Deegan et al. (2010).

The relationship above used experiments at ≥0.5 GPa, which is higher than inferred for the Merry Widow setting (Figure 2.2b) and most of the Bonanza arc (<0.2 GPa – Canil et al., 2010). Lower pressure (≤0.5 GPa) basalt-limestone reaction experiments at similar temperatures

(1050 – 1300ºC) (Iacono-Marziano et al., 2007, 2008; Freda 2008; Mollo et al., 2010) are more representative of the arc section at Merry Widow and show systematically higher calcite consumption. Using a best-fit trend to experiments at ≤0.5 GPa (black dashed line – Figure 2.12) the change in dCa/Si from orbicule dike margins to their interiors amounts to ~9.5 % calcite consumption. A change in composition from host melt to those of the orbicule requires >25% calcite consumption (orange dashed line does not intersect with black dashed line – Figure 2.12). The exhaustion of calcite in the lower pressure (i.e., calcite-undersaturated) experiments means they serve as a *minimum* for calcite consumption, whereas the higher pressure experiments having residual carbonate are a conservative estimate of carbonate consumed for <1 GPa.

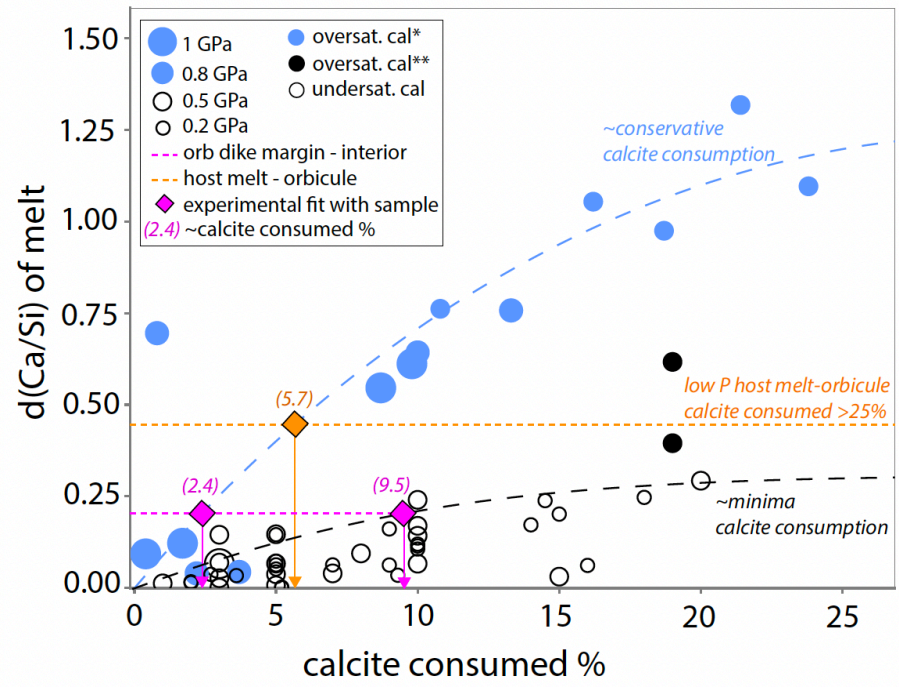

Figure 2.12: Plot showing the change in molar CaO/SiO_2 (dCa/Si) from the starting material to the final hybrid melt (glass) with the amount of calcite consumed in basalt-limestone assimilation experiments. Calcite consumed is calculated by mass balance using modal and chemical data from phases in the experiments. Blue circles are data for a tholeiitic hydrous basalt with excess (50%) limestone where melts are oversaturated in calcite (*Carter and Dasgupta, 2015). Open black circles are experiments using hydrous high-K and shoshonitic basalts (Iacono-Marziano et al., 2007, 2008; Freda et al.. 2008; Mollo et al., 2010) having complete exhaustion of calcite added (≤20%) in all but two cases (filled black circles – **Mollo et al., 2010). The exhaustion of calcite in the latter low pressure experiments indicates the calculated amount of carbonate consumed is a *minima*. The low pressure experiments potentially serve as a minimum for calcite consumption within the shallow crust. The horizontal lines are the maximum d(Ca/Si) observed in the orbicular dikes assuming the starting and end melt compositions are the dike margin and interior (pink line), or host melt with orbicule (orange line).

2.6.5 Liberation of excess CO_2

The simple binary mixing model and the comparison of orbicular dike compositions with experimental data indicates these unique dikes can be produced by 2.4 to > 25 wt.% calcite consumption, which would liberate 1.1 to > 11.0 wt.% CO_2. These levels of CO_2 are far greater than the solubility in hydrous basalts within the shallow arc crust (Edmonds et al., 2020). Due to the hydrous nature of arc basalt, I calculated the maximum volatile saturations of both CO_2 and

H_2O using the thermodynamic model MagmaSat (Ghiorso and Gualda, 2015) over the range of pressures that the dikes experience as they transit the crust observed at Merry Widow (<0.2 GPa). The maximum CO_2 solubility within orbicular dike margins and/or host melt cannot exceed 0.11 wt.% CO_2, negligible in comparison to the CO_2 added by carbonate wall rock assimilation (1.1 to >11%). I surmise nearly all of the CO_2 added from the wallrock (1.1 to >11.0 wt.% CO_2) would be degassed immediately, leaving behind a residual Ca-rich melt now preserved as an orbicule. Excess CO_2 may have also enhanced buoyancy of the Ca-rich melt.

2.6.6 Orbicules from liquid immiscibility or incomplete mixing?

The two phase meniscus (Figure 2.5) between the host melt and orbicules suggests they coexisted, cooled, and crystallized from two separate liquids. One possibility is the Ca-rich orbicules are a conjugate liquid exsolved from an original single phase by liquid immiscibility. Comparison of the compositions of the host melt, orbicules, and orbicule dike margins and interiors to experimentally derived two-liquid solvi, however, show they fall within the one-liquid field for several systems: SiO_2–CaO–Al_2O_3 (Charlier and Grove 2012); Na_2O+K_2O+P_2O_5+TiO_2–CaO–Al_2O_3 (Charlier and Grove 2012); Na_2O–SiO_2+Al_2O_3–CaO–CO_2 (Brooker and Kjarsgaard 2011); and FeO+MnO+TiO_2+CaO+P_2O_5–Al_2O_3+MgO+K_2O+Na_2O–SiO_2 (Roedder 1951, Philpotts 1982) (Figure A8). More interestingly, the orbicule-rich dike interiors trend away from two-liquid fields for all systems with the exception of FeO+MnO+TiO_2+CaO+P_2O_5–Al_2O_3+MgO+K_2O+Na_2O–SiO_2 (Roedder 1951, Philpotts 1982). These systems are H_2O-free, and addition of H_2O is known to expand the two-liquid field (Lester et al., 2013), especially in the presence of CO_2 (Brooker and Kjarsgaard 2011), but likely not to the degree needed to intersect the dike compositions.

An alternative hypothesis is that the host melt + orbicules preserved in the dikes were two liquids unable to homogenize due to rapid crystallization and supercooling (McCarthy and Müntener, 2016; Zhang and Lee, 2021). In this way the Ca-rich orbicules could represent the remnants of limestone dissolution with insufficient time for complete mixing into the recharging host melt within the dikes. I note the orbicules are close in composition to hybrid melts in disequilibrium, short duration (< 5 min) limestone dissolution experiments (Figure 2.11). Furthermore, using typical diffusion rates for Ca, Mg, and Fe cations in a basaltic melt at 1200ºC (1.3×10^{-11} to 1.5×10^{-12} m^2/s – Zhang et al., 2010) I calculate diffusion distances of 0.4 to 1.8 mm over a timescale of 24 to 72 hours for simple conductive cooling of 1 to 2 m wide dikes. These length scales are far shorter than the radii of the orbicules (1.5 to 2.5 mm), consistent with a lack of homogenization if the orbicules were produced by dissolution and subsequent the transport time was short.

The removal of CO_2 also affects reaction progress and how the two liquids may be unable to homogenize after limestone dissolution. Experiments by Blythe et al. (2015) show bubble accumulation at the magma-carbonate reaction site can retard carbonate dissolution into the melt, until fluid pressure exceeds the confining pressure and a 'bubble blowout' occurs. Within active arc systems, this build-up of CO_2 can be described as 'CO_2 flushing', where exsolved gas from carbonate wallrock dissolution will increase the volume of the magma, likely leading to over-pressurization and fluids degassing and/or volcanic eruptions occurring (Caricchi et al., 2018). Irregular contacts at some basalt-limestone contacts lower in the stratigraphic section may be localized regions of carbonate dissolution (Figure A9), where CO_2 may have preferentially degassed along the contact. In addition to the orbicular dikes at the field site, units such as polymict hypocrystalline volcanic breccias (Morris and Canil 2020) and spherulitic lavas suggest

a fluid-rich environment where ‘bubble blowouts’ and/or ‘CO_2 flushing’ may have occurred. The compositions and field relationships suggest that a combination of supersaturation in CO_2 with bubble accumulation and/or blowouts, in addition to rapid cooling soon after limestone dissolution, would have caused the discrete segregated textures between orbicules and host melt observed in these unique dikes.

In view of the apparent two-liquid textures, I also investigated the difference in viscosity and liquidus temperatures between orbicules and host melt to further understand their physical behaviour in the dikes. If the orbicular dikes formed by limestone assimilation, the excess CO_2 calculated above will reduce the viscosity of a melt (Lester et al., 2013). Because the original fluid contents (H_2O + CO_2) in neither the parental host melt nor the orbicules can be quantified, I calculated the viscosities using anhydrous compositions (Table 2.2). Using the method of Giordano et al. (2008) at 1100ºC, my calculations show the host melt is nearly three times more viscous (290 ± 2 Pa·s) than the orbicules (110 ± 2 Pa·s). Ultimately an input temperature of 1100ºC and 0 wt.% H2O does not reflect the original magma temperature and water contents, however it is the difference in viscosity values, not absolute values, that matters for these calculations. This difference in viscosity would enhance the amalgamation of orbicules as observed in outcrop (Figure A4). This interpretation is supported by magma-carbonate experiments, where lower viscosity Ca-rich melts ‘piled up’ against a rheological barrier that formed along the boundary with Ca-normal host melt (Deegan et al., 2010).

Rhyolite-MELTS version 1.2.0 (Ghiorso and Gualda 2015) was used to calculate potential liquidus temperatures for orbicule and host melt compositions at fO_2 of NNO+1 and 0.2 GPa. The anhydrous liquidus temperatures of host melt and orbicule compositions (Table 2.2) are 1280ºC and 1290ºC, respectively. The similar liquidus temperatures in the host melt and

orbicules would suggest they crystallized at the same temperature and time, and explain their identical intergranular textures and grain sizes.

2.6.7 Orbicule formation by limestone assimilation in hydrous arc basalts

The following model for the formation of orbicular dikes within primitive hydrous arc basalts at Merry Widow uses textural observations, geochemical trends, modeling, and comparisons to experimental data. The plutonic rocks, dikes, and sills at Merry Widow represent some of the earliest magmatic events (~197 Ma) within a young Jurassic Bonanza arc (~202 – 168 Ma). The immature stages of arc construction would have resulted in significant magma-carbonate interactions, where incipient arc formation was built on a stratigraphy comprising ~1 km thick Triassic Quatsino limestone. Assimilation of the cold limestone wallrock would have been difficult during the early stages of arc building, but continued magmatism would have heated the surrounding limestone in direct proximity to the intrusion to near basalt liquidus temperatures (~1140ºC). Progressive heating of the wallrock likely resulted in the ductile nature I observed in cm- to m-scale folds in limestone near magma contacts (Figure A1).

Late-stage mafic dikes are common in the final stages of arc flare-up events, where the arc relaxes, undergoes extension, and subsequent diking occurs (Busby et al., 2006). Earlier sills that intrude the limestone at Merry Widow are boudinaged (Figure A1b) and further support an extensional setting. Field relationships indicate that after emplacement of the ~50 km^3 dominantly gabbroic pluton, co-magmatic dikes transited the crust that included an earlier swarm of plagioclase-phyric basaltic dikes, followed by a later swarm of orbicular basaltic dikes (Figure A5). Being the latest phase of magmatism, the orbicular dikes preserve the final more mature state of magma-carbonate reactions that occurred within the system. Their composition indicates

they are primitive arc melts, similar to others identified within the Bonanza arc (DeBari et al., 1999; Larocque, 2008; D'Souza et al., 2016).

The orbicular dikes started as hydrous melts at >1100ºC that assimilated limestone wallrock, producing a Ca-rich hybrid melt (Figure 2.13). These Ca-rich melts would enter the dikes lower in the crustal section and get transported upwards from recharge melts feeding the dikes. Geochemical modeling and application of published experimental data indicates over 11 wt.% CO_2 may have been added from the host limestone into the magma, and due to the low CO_2 solubility (<0.11 wt.%), most would exist as a separate fluid phase. The buoyant excess CO_2 would rapidly escape upwards from the system, concentrating in the dike interior where flow velocities are greatest, and suspending the unmixed Ca-rich hybrid melt now represented as an orbicule (Figure 2.13). This unique magma-carbonate interaction and CO_2 transport within the orbicular dikes would have continued to occur as long as 1) sufficient heat and magma recharge was supplied; 2) wallrock reactants were available; and 3) the reaction products, such as CO_2, were continuously removed (Barnes et al., 2003, 2005; Blythe et al., 2015).

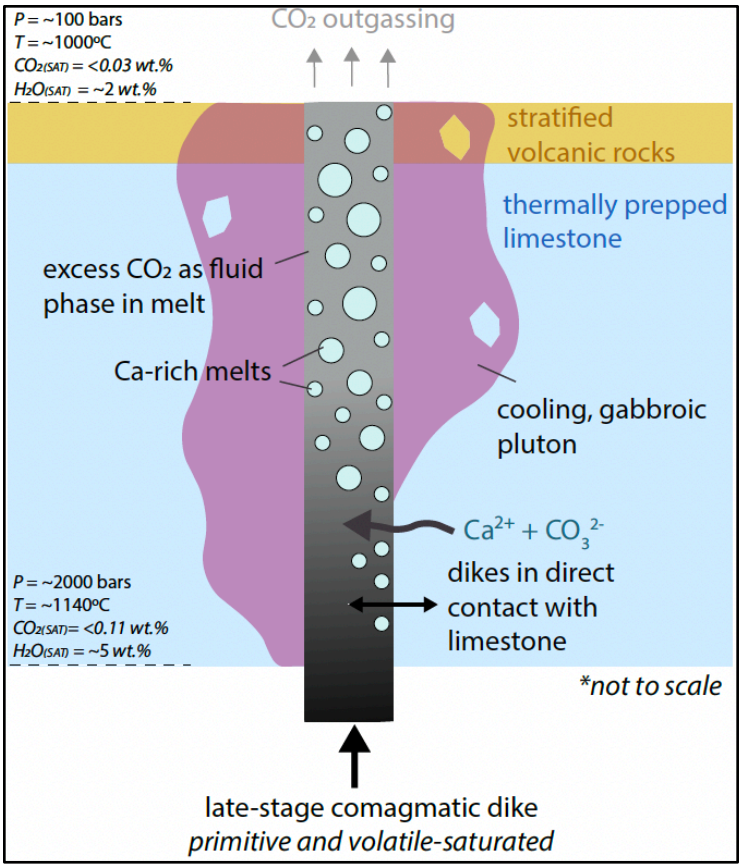

Figure 2.13: A schematic of a proposed model for orbicule formation within late-stage primitive basalts at Merry Widow. Orbicules are interpreted to be a result of Ca-rich melts produced from limestone dissolution, which is unable to homogenize with the primitive, hydrous basalt transiting the crust and in contact with the limestone. The excess CO_2 produced from reaction with limestone is outgassed, leaving behind a residual lower viscosity Ca-rich hybrid melt that quickly cools as a segregated orbicule in the host dike melt.

2.6.8 CO_2 flux by the orbicule mechanism

I estimated the CO_2 flux by the proposed assimilation and transport mechanism preserved in the orbicular dikes in the Jurassic Bonanza arc. The total mass of magma is determined by combining the aerial extent of Bonanza arc volcanic and plutonic rocks, with their estimated thicknesses (~2.5 km and ~12 km, respectively, Canil et al., 2010; Canil et al., 2013) and an assumed magma density of 2900 kg/m^3. When magma mass is integrated over the timespan of the arc (34 Myr – Nixon and Orr 2007; Nixon et al., 2011), with 1.1 to 11 wt.% CO_2 from

carbonate assimilation, respectively, I calculated CO_2 fluxes of the Bonanza arc of 0.14 – 1.16 Tg CO_2/yr . These estimated fluxes are similar to those derived by Auippa et al. (2019) for active modern arc volcanoes built on carbonate substrates, such as at Etna (3.01 ± 1.27 Tg CO_2/yr), Merapi (0.03 ± 0.05 Tg CO_2/yr), Bromo + Semeru (0.72 ± 0.3 Tg CO_2/yr), and Popocatepétl (3.09 ± 3.12 Tg CO_2/yr). I note that my flux estimates for the Bonanza arc likely portray a 'maximum' flux, as they assume that all erupted volcanic rocks underwent the same assimilation process observed in the orbicular dikes and that stalled magmas now preserved as plutons interacted with the carbonate wallrock to the same extent. Given the rarity of orbicules (documented as a first time in this study), it is unlikely that all erupted volcanic rock from the Bonanza arc assimilated limestone. In addition, entire plutons likely do not assimilate mass fractions of limestone (Glazner and Bartley, 2006). Conversely, some volume of eroded magmatic rocks is not preserved in the exposed arc section, lowering these estimates. The arc may have also pulsed, erupting magma at two dominant periods, rather than continuously over 34 Myr. More precise estimates on the thickness and ages of Bonanza arc intrusive rocks would help constrain the CO_2 flux in the arc.

2.7 Conclusions

The Merry Widow area is a multi-stage magmatic system within the nascent Jurassic Bonanza arc showing textural and compositional evidence of magma-carbonate interactions documented in late-stage orbicular dikes. The orbicular dikes have unique geochemical trends, discordant to liquid lines of descent within the Bonanza arc, but that can be achieved through simple binary mixing of 3 – 25 wt.% limestone in arc basalt.

When compared with hybrid melts produced in experiments by others on basalt-limestone reaction at similar crustal pressures, the orbicule compositions require >25% calcite assimilation, liberating >11 wt.% CO_2. Such high CO_2 amounts would be insoluble in the dikes, exsolve and preferentially escape to the surface, leaving behind a residual Ca-rich melt, now represented as an orbicule. I interpret the orbicular dikes to be a mixture of two liquids not in equilibrium – a host melt and a hybrid melt from limestone assimilation. The orbicules generated by limestone assimilation contaminated the host dike melt, but due to the rapid cooling possibly by ascent and CO_2 liberation, homogenization was incomplete and segregation textures of the two liquids were quenched, crystallized, and uniquely preserved.

This model from an exposed and in-situ example of carbonate reactions with basalt in the shallow arc crust (<0.2 GPa) reveals the mechanisms and possible prodigious amounts of CO_2 that can be produced. Using the present-day footprint of exposed magmatic rocks, emplaced over a timespan of ~34 Myr, I calculate CO_2 flux estimates of the Bonanza arc to have ranged from 0.14 to >1.16 Tg CO_2/year.

Chapter 3

Magma-carbonate interactions drive CO_2 production and metal enrichment in shallow dikes and sills at volcanic arcs

3.1 Abstract

The contribution of CO_2 from crustal carbonates into arc magmas is debated, as is its role in the long-term C cycle. To better understand the contributions and mechanisms that drive CO_2 production in arc magmas, I examined in detail basaltic dike and sill contacts with carbonate in the Jurassic Bonanza arc on Vancouver Island, Canada. I discovered discrete boundary melts that form along dike and sill margins in contact with limestone, and display unique Ca, U and Sr enrichments, Si depletion, and $^{87}Sr/^{86}Sr$ that approaches host limestone values (~0.708). Binary mixing modeling indicates 20 – 25 wt.% limestone assimilation into basalt forms the boundary melts. Contrasting viscosities between boundary and interior melts hinder mixing and chemical homogenization but appear to promote uphill diffusion phenomena and metal enrichment within systems that cool in minutes to days. While shallow dikes and sills may be volumetrically minor in an arc magma system, the open flow of magma and large surface area in channels greatly enhances magma-carbonate interactions, and ultimately CO_2 production, likely over that of more common and voluminous plutons.

3.2 Introduction

The contribution of crustal-derived CO_2 into arc magmas is controversial. Traditional views assume most CO_2 outgassed at arc volcanoes is slab-derived (Plank and Manning, 2019), however studies on active and ancient systems indicate arc volcanoes built on carbonate may contribute significant crustal CO_2 (Deegan et al., 2010; 2023; Iacono et al., 2009; Auippa et al.,

2017) and have been considered a driver of past greenhouse events (Lee et al., 2013). Evidence of magma-carbonate reaction has been well-documented from mineral and rock scale studies in volcanic and plutonic rocks (Barnes et al., 2003, 2005; Chadwick et al., 2007; Lee et al., 2013; Ramos et al., 2020; Whitley et al., 2020; Deegan et al., 2021), and in isotopic signatures of volcanic gases (Mason et al., 2017). Less clear are the mechanisms and extent to which magma-carbonate reactions are sustained within arc magmas. Experiments on such reactions (Iacono-Marziano et al., 2007, 2008; Freda et al., 2008; Deegan et al., 2010; Carter and Dasgupta, 2015) show they are most efficient at <0.5 GPa (c.f. Figure 2.12 – Chapter 2 where low pressure experiments exhaust calcite). Predictably, enhanced magma-carbonate interaction may be recognized in networks of dikes and sills that feed arc systems in the shallow crust, where the open melt channels endure continuous flow of magma along an extensive surface area for reaction, in contrast to scenarios involving deeper, stalled plutons. Here, I test this idea by examining and quantifying the extent of limestone assimilation within m-scale basaltic dikes and sills in direct contact with carbonate.

3.3 Geological setting & samples

The Jurassic Bonanza arc on Vancouver Island, British Columbia, Canada is ideal for studying magma-carbonate interactions, given the abundance of exposures of magma in contact with limestone of the underlying Triassic Quatsino Formation (Figure 3.1). I investigated in detail the Merry Widow locality (Figure B1), where interactions between early and primitive arc magmas with a ~1 km limestone platform are preserved in an extensive network of shallow m-scale dikes and sills. A second locality (Quinsam area) of central Vancouver Island that is stratigraphically equivalent to Merry Widow was sampled for comparison (Figure 3.1 –

Quinsam). Volcanic strata overlying the limestone at both sites is <3 km thick, implying dikes and sills are emplaced at <0.2 GPa (Canil and Morris, 2023). Dike and sill margins from both localities were studied in petrographic (Figure 3.2a-h) and geochemical (Figure 3.2a-l) detail.

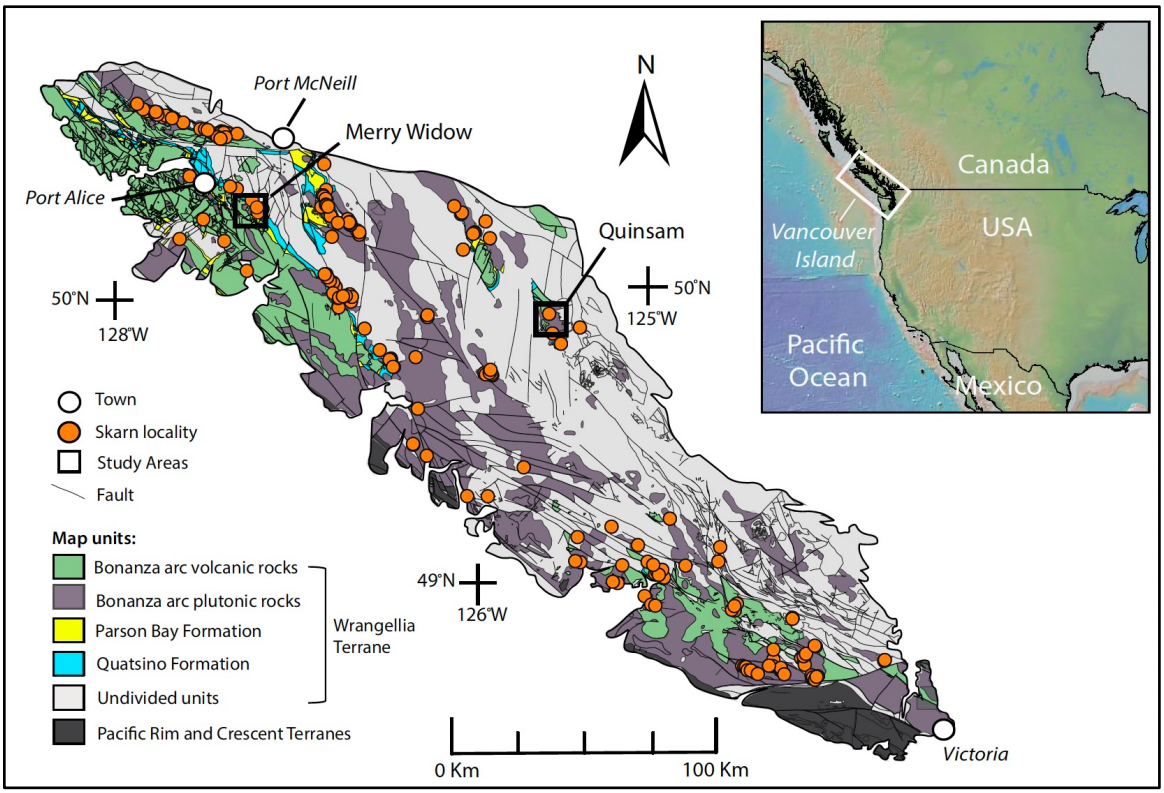

Figure 3.1: Regional geology of Vancouver Island displaying Jurassic Bonanza arc rocks and underlying carbonate-bearing units of the Triassic Parson Bay and Quatsino limestone Formations. Skarn localities indicate where magma-carbonate reactions are documented. Other Wrangellia Terrane lithologies (undivided) occur as dominantly older and deeper basement units. Unit boundaries and skarn locations are from the British Columbia Geological Survey (BCGS) MapPlace dataset (BC Geological Survey 2023a) and MINFILE Mineral Inventory (BC Geological Survey 2023b). Inset from GeoMapApp (Ryan et al., 2009).

Dikes and sills (dominantly 1 – 2 m wide) are dominantly mafic, microcrystalline, aphyric to plagioclase-phyric, and at limestone contacts, show a thin (<2 cm) light-coloured reacted margin (herein termed 'boundary melt') that is holohyaline and often displays orbicules (Figure 3.2d,e,h), The orbicules have been discussed previously (Chapter 2 – Morris and Canil,

2022). The boundary melt transitions across a visible meniscus to a microcrystalline dike interior (Figure 3.2cd). Skarn mineralization occurs at contacts (Figure 3.2f-h). Both sites indicate that the boundary melts can comprise up to 4% of the total dike or sill volume.

Bulk rock samples for geochemical analyses (Table B1) were collected from: limestone; dikes and sills in contact with limestone (‘dike-in-limestone’ or ‘sill-in-limestone’) sampled at margins (‘B’) and interiors (‘A’); dikes that cross-cut a nearby pluton (dike-in-pluton), and dikes that cross-cut stratified tuff or earlier dikes (‘dike-in-other’) (Figure B1). Dike-in-limestone margins from both localities were sampled at mm-scale increments from a visible limestone contact inwards through a boundary melt to the dike interior, and are herein referred to as ‘dike profiles’ (Figure 3.3). Sample collection and analytical details are provided in Appendix B.

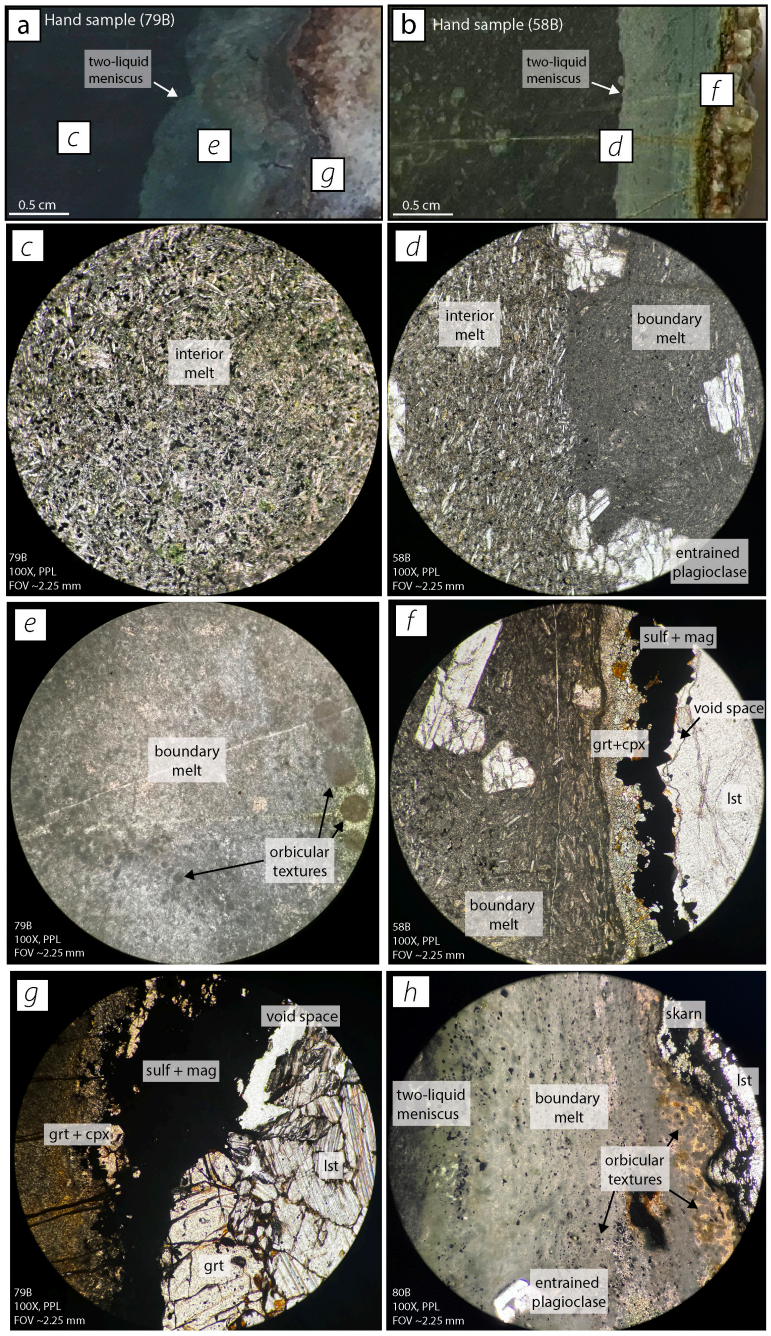

Figure 3.2: Cut rock slabs (a,b) from dike-limestone contacts with various locations (c-h) identified. Petrographic images (c-h) in plane polarized light show: I microcrystalline interior melt of plagioclase + clinopyroxene + oxides + glass (partially overprinted by chlorite, epidote, actinolite, albite); (d) two-liquid meniscus between meltI(e) distinctly lighter holohyaline boundary melt with orbicular textures proximal to contact; (f) boundary melt to skarn transition in 58B (dike); (g) skarn mineralization (garnet + clinopyroxene + sulfides + magnetite) at the contact in 79B (dike); and (h) orbicule- and oxide-rich boundary melt to skarn transition in 80B (sill). Void spaces (f,g) are not primary. Lst = limestone. Field photos of basalt-limestone contacts are provided in Chapter 2 (Figure A9).

3.5 Bulk rock geochemistry

Dike and sill samples range in composition from basalt to trachyandesite. Dike profiles show increasing SiO_2, Na_2O, K_2O and decreasing CaO trends away from the limestone contact (e.g., Figure 3.3a-d), where boundary melt samples have notably different compositions. Dike- and sill-in-limestone samples, and dike profiles, show Sr and U enrichments similar to or exceeding limestone values (Figure B2). Within the dike profiles, U and Sr are highest in the boundary melt (Figure 3.3e-h), and display variable concentration with distance from the limestone contact. Rare earth elements are generally diluted within the boundary melt (Figure 3.3ij). The highest initial $^{87}Sr/^{86}Sr$ ratios (~0.708 to 0.709) occur in limestone (Figure 3.4ab) (Table B2). Dike- and sill-in-limestone samples at Merry Widow vary from 0.705 to 0.708, where the most enriched values occur within a sill-in-limestone margin (80B) and interior (80A) (Figure 3.4b). Merry Widow dike profile samples have enriched values (~0.707), all within uncertainty of one another (±0.001, 2σ)(Figure 3.4b). Quinsam dike profile samples range from 0.704 to 0.706, with the most enriched ratios in the boundary melt (Figure 3.4a). Dike-in-other samples show slight enrichment (0.704 to 0.706), whereas dike-in-pluton samples (0.703 to 0.704) are similar to primary Bonanza arc magma values (Figure 3.4b) (D'Souza et al., 2016).

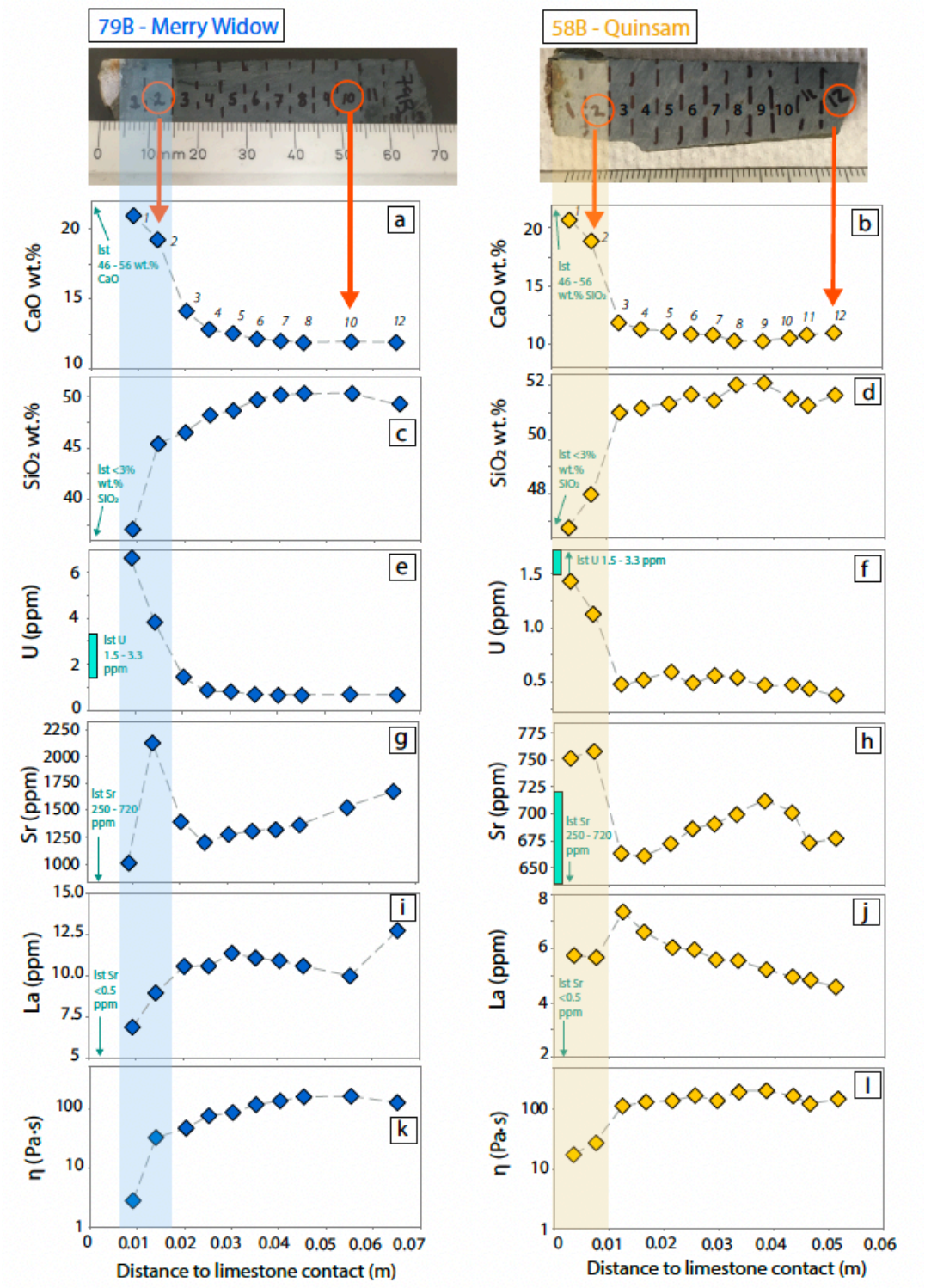

Figure 3.3: Select major element oxides (CaO, SiO_2) (a-d), trace elements (U, Sr, La) (e-j), and viscosity (k,l) versus distance from limestone contact for dike profiles 79B and 58B. Shaded regions (sample 1 and 2) represent the discrete 'boundary melt'. Viscosities (k,l) were calculated using the methods of Giordano et al. (2008) with uncertainties of ± 2 Pa·s.

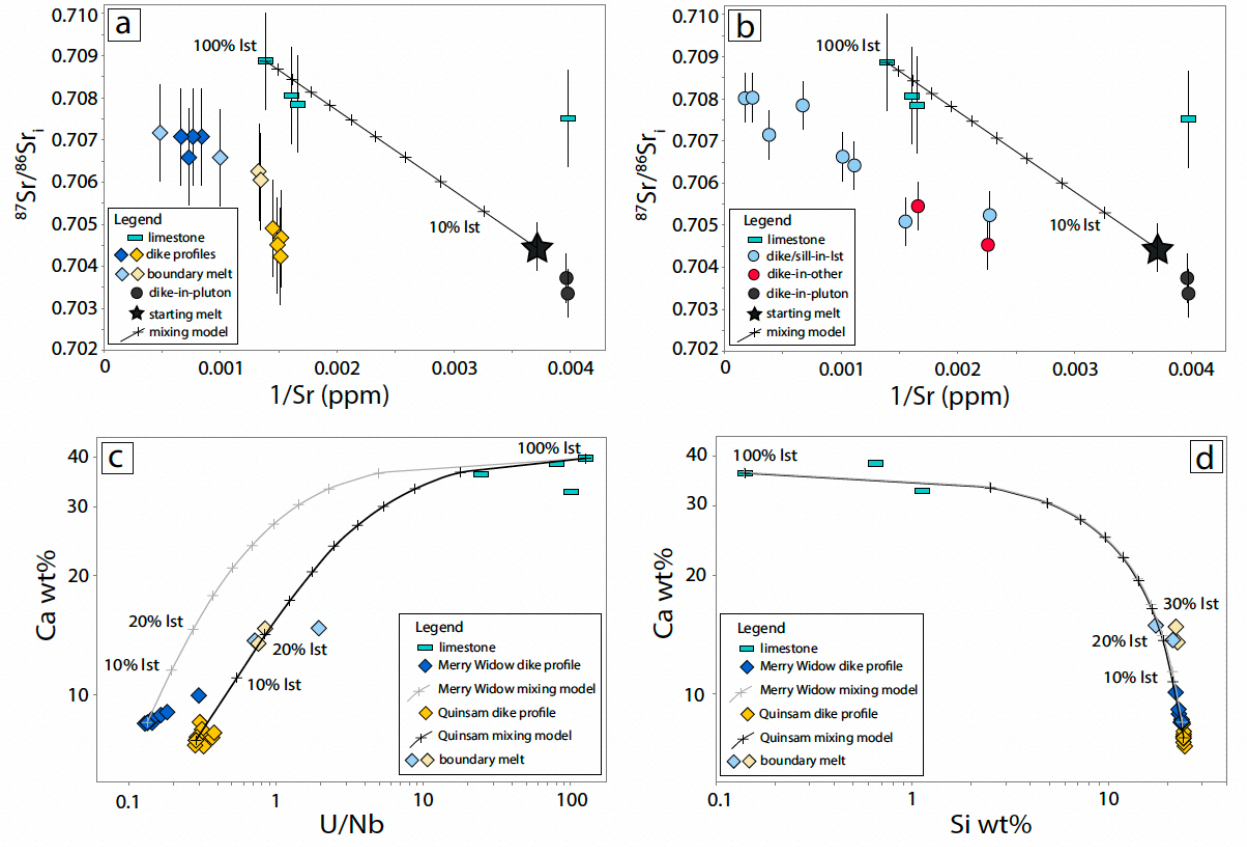

Figure 3.4: Initial $^{87}Sr/^{86}Sr$ isotopic ratios versus 1/Sr for (a) dike profiles; and (b) dike- and sill-limestone, dike-other, and dike-pluton samples. Binary mixing lines display 10% increments between model end-member compositions of a starting melt basalt (102) mixed with limestone (78D). Binary mixing models of Ca versus U/Nb (c) or versus Si (d) for Merry Widow (79B) and Quinsam (58B). Limestone with detectable Si (165D) used in (d).

3.6 Hindered magma mixing and 'super-enrichment' of Sr

Dike- and sill-in-limestone contacts show a clear meniscus between the boundary and interior melts (Figure 3.2ab). The presence of a meniscus, and lower SiO_2 in the boundary melt (Figure 3.3cd) suggests a contrasting rheology between itself and interior melts, which may have impeded mixing these liquids on the timescale of intrusion and cooling. Assuming anhydrous compositions at 1200°C, boundary melts have lower viscosities (<35 ± 2 Pa·s) than interior melts

(45 – 215 ± 2 Pa·s; Figure 3.3kl). Such differences would hinder mixing on the short timescales (<280 h) for conductive cooling of <2 m wide channels ($x = Dt^{1/2}$; x is the distance from dike center to margin (i.e., 1m in a 2m wide dike); D is the thermal diffusivity coefficient of $1x10^{-6}$ m^2/s, and t = time in seconds) . An analogue to this is observed in experiments where lower-viscosity Ca- and $^{87}Sr/^{86}Sr$ enriched melts 'pile up' against more viscous melts (Deegan et al., 2010).

Anomalous Sr enrichment above limestone concentrations is preserved in the boundary melts from dike profiles (Figure 3.3gh). This is unless original limestone Sr concentrations were far above present-day values, where high Sr (>7500 ppm) can precipitate in carbonates from aragonite seas (Kinsman, 1969). This interpretation would further suggest that lower present-day Sr values in the limestone reflect fluid mobilization of Sr within the nearly impermeable and recrystallized limestone adjacent to dikes and sills, but preserves enriched Sr values within the dike and sill margins. Strontium enrichment from aragonite seas also does not explain the 'super-Sr enrichment' observed in dike- and sill-in limestone interiors. For example, a dike (161) and sill (80) show Sr enrichments from margins to interiors of 645 – 981 ppm and 4159 – 5553 ppm, respectively (Table B1). These enrichments are far above typical arc basalt values, including previously studied mafic Bonanza arc dikes, where Sr is commonly <400 ppm (DeBari et al., 1999; D'Souza et al., 2016). Fluid mobile large ion lithophile elements (Sr, Rb, Ba, K) show no correlation with loss-on-ignition, so the enrichments are not from hydrothermal alteration. In addition, CO_2-rich fluids produced during limestone interactions would have low metal solubility impeding element transport or enrichment (van Hinsberg et al., 2016). Fractional crystallization of wallrock phases, which are present in the skarn mineralization (clinopyroxene and garnet) also cannot explain Sr enrichment, as this would concentrate some incompatible elements in

boundary melts which are instead diluted (i.e., La – Figure 3.3ij). Plagioclase accumulation can also not explain the anomalous Sr levels, as samples low in plagioclase phenocryst abundance (<5% – sample 80A and 80B) have the highest Sr (>4000 ppm). Therefore, another process must rationalize the anomalous Sr enrichment in dikes and sills.

These observations document how magma-carbonate interactions create a Ca-rich and Si-poor boundary melt juxtaposed with the initial magma, forming a two-liquid system (Figure 3.2ab). The dike profiles reveal an inflection in Sr concentrations at the transition of these two melts, also marked by a change in viscosity (Figure 3.3kl). This pattern of enrichment is similar to experiments in two-liquid systems that show enhancement of Sr concentrations by uphill diffusion, wherein Sr diffuses against its concentration gradient but from high to low chemical activity, due to variation in SiO_2 activity between the two coexisting liquids. This phenomena is observed for Sr in experiments in the simple K_2O-SrO-SiO_2 system (Varshneya and Cooper, 1972) and between basalt and rhyolite melts (Lesher 1990, 1994). Similar to Lesher's (1990) experiments, I document a natural system where $^{87}Sr/^{86}Sr$ isotopic equilibrium between basalt and carbonate can be obtained without chemical equilibrium, as is the case with the Merry Widow dike profile samples which retain a sharp chemical gradient in Sr (Figure 3.3g) yet have consistent $^{87}Sr/^{86}Sr$ ratios (~0.707) that approach limestone values (Figure 3.4a).

I surmise uphill diffusion has created anomalous Sr enrichments in natural samples, now preserved within cm-scale boundary melts at dike and sill margins. I suggest this phenomena has inflated Sr above limestone assimilant values (252 – 720 ppm) within the low-Si boundary melt at its interface with melts of higher Si and viscosity. The interface is preserved between melts which did not physically mix because of differing viscosities and a lack of time. The uphill diffusion profiles of Sr are preserved because the dike or sill cools faster than the rate at which Sr

can diffuse to erase the concentration gradient. For example, a <2 cm thick boundary melt would cool by conduction within 10 minutes, whereas the diffusion of Sr through the same thickness of a basaltic melt would take orders of magnitude longer (D_{Sr} = 3.8 x 10^{-11} m^2/s; Zhang et al., 2010). The release of exsolved CO_2 gas phase (now removed from the system) would cool the boundary melt even faster. While the phenomena of uphill diffusion is well-known in experiments, its preservation in natural silicate liquids has never been documented (González-Garcia et al., 2018).

Dike- and sill-in-limestone samples show the most remarkable super-enrichment of up to 5500 ppm Sr. It is possible these Sr rich intrusions did not have a single injection of melt that stagnated, but represent multiple injections with sustained flow, which juxtaposed Sr-enriched boundary melts with new melt introduced into the channel (as confirmed in field observations – Figure B3). Thermal considerations of dike and sill emplacement suggest that continual supply of heat in magma channels can exceed its loss to the country rock, causing 'meltback' of channel walls (Bruce and Huppert, 1989). In this way frozen Sr-enriched boundary melts upstream could re-melt and concentrate within channel interiors where flow velocities are greatest. Repeated intrusion, open flow, and uphill diffusion between new and older melts may have acted to compound and multiply the Sr enrichment to the phenomenal values I observe, far above those typical of igneous rocks.

3.7 Limestone assimilation and CO_2 production

Enriched $^{87}Sr/^{86}Sr$ and Sr provide geochemical evidence of limestone assimilation in basalt collected at or near contacts with limestone. Conventionally, binary mixing trends in $^{87}Sr/^{86}Sr$ versus 1/Sr space are used to quantify assimilation (Faure, 1998) (Figure 3.4ab), but my

results show anomalous trends given the profound Sr enrichment in nearly all dike and sill samples. I instead use binary mixing in Ca versus U/Nb space to quantify assimilation, as both Ca and U are enriched in boundary melts (Figure 3.3), and Nb is an immobile element (Figure 3.4c). For these models, as a conservative approach I use dike profile samples in direct contact with limestone, where the most interior melt (sample 12) is mixed with limestone (78D). For the Quinsam dike profile, boundary melt compositions fall on the model line, indicating ~22 wt.% limestone assimilation (Figure 3.4c). Due to U enrichment above limestone values, the mixing model was unsuccessful for the Merry Widow dike profile (79B), where U/Nb at a given Ca concentration is displaced from the model trend (Figure 3.4c). Similar to Sr, U is more enriched in the limestone than basalt and may also be affected by uphill diffusion within the Merry Widow boundary melt. Therefore, I provide a binary mixing model in Ca versus Si space, where neither element is affected by uphill diffusion (Figure 3.3a-d), indicating 20 – 24 wt.% limestone assimilation (Figure 4.4d). From these models, I estimate a 20 – 24 wt.% limestone was assimilated into basalt, generating the observed boundary melts. As the wallrock limestone contains ~44 wt.% CO_2, this suggests dikes and sills are capable of producing 9 – 11 wt.% CO_2 within the thin (<2 cm) boundary melt margins.

I note similar systems show bulk mixing between end-members that has gone to completion (Deegan et al., 2010). These may differ from the open-system case I present, where replenishing melts can juxtapose reacted boundary melts preserved on short timescales (minutes). The same open-system melt dynamics common in dikes and sills could also erase these boundary melts (i.e., by melting back dike margins), but retain evidence of bulk mixing between assimilant and melt in dikes, sills, or erupted products.

3.8 Summary & conclusions

Previous studies on magma-carbonate interactions have focused on plutons as the most prodigious CO_2 producer in arc systems (Barnes et al., 2009; Lee et al., 2013), but contributions from small-scale intrusions that are an important mechanism of magma transfer in the shallow crust have thus far been overlooked. I show that unlike plutons, where km-scale magma reservoirs stall and cool slowly, extensive m-scale channels of continuously replenished magma in dikes and sills can compound reactions with carbonate wallrock, as observed in enhanced CO_2 production and metal enrichments (Sr, U) at their margins. I document for the first time, possible uphill diffusion of Sr in natural melts that were quenched and preserved on the timescale of quickly-cooling (minutes) and thin (<2 cm) boundary melts, where contrasting viscosities between reacted margins and interior magmas hindered mixing, but promoted super-enrichment of Sr. My results indicate an efficient mechanism for producing crustal-derived CO_2 in arc magmas from carbonate wallrock is via a shallow network of dikes and sills, and might be more effective than deeper, voluminous plutons that build a large contact aureole preventing further reaction. In addition, the unique metal enrichment within smaller-scale and shallow intrusions will be of interest to those studying the formation of ore deposits associated with magma-carbonate contacts and builds on earlier hypotheses for the generation of low-viscosity melts and element partitioning in shallow skarn systems (e.g. Lentz, 1999).

Chapter 4

CO_2 production from plutons in carbonate wallrock is driven by shallow metamorphic decarbonation not magma assimilation

4.1 Abstract

Quantifying the contribution of CO_2 from arc magma-carbonate wallrock interactions in the crust is important for a better understanding of the long-term C cycle. Traditionally it is assumed that contributions of crustal CO_2 to volcanic emissions at arc settings are minor, but this requires well-constrained field studies to determine the location and extent of magma-carbonate wallrock reaction and the concomitant C released. The Jurassic Bonanza arc on Vancouver Island (Canada) was built on a Triassic limestone platform and makes for an ideal field setting to examine magma-carbonate reaction in detail beneath an island arc. Here, I examined how large-scale magma bodies might react with carbonate from a well-constrained and detailed study of a gabbro pluton that intrudes limestone. The pluton shows muted to nil carbonate interaction, with primary igneous values $^{87}Sr/^{86}Sr$ (~0.703) preserved, except in a thin (<2 m) chilled margin with elevated $^{87}Sr/^{86}Sr$ (~0.706) in contact with a decarbonized metamorphic aureole. A lack of $\delta^{18}O_{cpx}$ enrichment in gabbro ~10 to >1000 m from the contact further suggests that any reaction with limestone wallrock must be limited to at most the outer ~10 m of the pluton. More enhanced magma-carbonate interaction, and ultimately CO_2 production, occurs via a network of shallow dikes and sills (<0.2 GPa) when compared to deeper plutons. Published experimental data confirm reactions are more restricted in the deep (>0.5 GPa) crust. Plutons are an important heat source to release CO_2 from carbonate wallrock by contact metamorphism, where >90% of crustal-derived CO_2 is liberated via wallrock decarbonation, but only <10% is liberated by

magma that assimilated wallrock. This detailed study places more realistic and quantitative limits on arc-derived CO_2 from upper crustal sources than attested in previous work.

4.2 Introduction

Earth's long-term (>1 Myr) climate variability is controlled by the regulation of atmospheric carbon dioxide (CO_2) levels, of which volcanic degassing is a primary input (Berner, 2004). Arc volcanoes are of particular interest to study because of the various C sources within the slab, mantle, and/or overlying crust that can contribute to the emitted CO_2. Traditionally, it has been assumed that much of the outgassed CO_2 at arc volcanoes is slab-derived (Plank and Manning, 2019), yet recent studies indicate that active arc volcanoes built on carbonate platforms (i.e., Etna, Merapi, Popocatépetl) where magma-carbonate interactions are known to occur at depth, are significant volcanic CO_2 emitters today (Auippa et al., 2019). These volcanoes show crustal-like C and He isotopic signatures in emitted volcanic gases, further supporting the occurrence of magma-carbonate reactions (Mason et al., 2017). Magma-carbonate reactions have been well documented by others both experimentally and from natural systems (Iacono-Marziano et al., 2007; 2009; 2020; Deegan et al., 2010; Whitley et al., 2020; Deegan et al., 2023). Less clear is the mechanism and efficiencies by which crustal-derived CO_2 is produced and released by magma-carbonate interaction when considering different sizes and shapes of magma bodies.

Well-exposed ancient arcs can provide an in-situ view of magma-carbonate interactions. Previous studies document evidence of these reactions in the form of metamorphosed carbonate wallrock (i.e., marble, skarn) and/or entrained skarn pendants in plutons (Barnes et al., 2003; 2005; 2009; Lee et al., 2013; Lee and Lackey, 2015; Ramos et al., 2020). Some studies of these

systems have suggested that stalled magma reservoirs, now preserved as plutons, might assimilate significant (>10%) carbonate, producing enough CO_2 to drive past greenhouse climates (Lee et al., 2013; Lee and Lackey, 2015). In this way, CO_2 is fluxed to the atmosphere via two dominant pathways: transport within the magma, or via wallrock decarbonation in contact aureoles and reactive transport of hydrothermal fluids (Ramos et al., 2020). However, the extent to which magma-carbonate reactions continue over time within these systems is understudied. In a generalized view, plutons accumulate incrementally and cool slowly, building an outer carapace that over time presents thermal and spatial limitations for continued magma-wallrock interaction (Glazner, 2021).

Detailed studies on exposures of arc magma-carbonate contacts from ancient systems are required to quantify such reaction extents and understand the mechanisms driving these interactions. In this study, I used exposed and drilled contacts of a large (>50 km^3) gabbro pluton that intrudes a carbonate platform to quantify magma-carbonate interactions within shallow (<5 km) arc crust. My results show carbonate assimilation is only evident within a thin (m-scale) veneer along the pluton margin, indicating that crustal-derived magmatic CO_2 from this system is minimal. A comparison of my results from a pluton with small m-scale dikes and sills in contact with limestone (Chapter 3) shows crustal-derived magmatic CO_2 is more efficient in the latter case, where the surface area of magma in tabular bodies interacting with wallrock is collectively greater, and reaction progress is accelerated. Regardless, my detailed study at magma-carbonate contacts documents that the dominant production of CO_2 occurs from decarbonation of the wallrock adjacent to the pluton, with more than >90% of offgassed CO_2 being derived from the country rock, and <10% by the assimilating magma. I then scaled my results to provide

quantitative limits on arc-derived CO_2 from upper crustal sources for comparison with more general cases used in previous work.

4.3 Geological setting

The Jurassic Bonanza intraoceanic arc is part of the Wrangellia Terrane on Vancouver Island, British Columbia, Canada. Wrangellia consists of a heterogeneous basement from deepest to shallowest of: Devonian island arc rocks (Sicker Group), Mississippian to Permian siliciclastic and carbonate rocks (Buttle Lake Group), Middle to Late Triassic large igneous province rocks (Karmutsen Formation), Late Triassic carbonates (Quatsino Formation), and Late Triassic to Early Jurassic carbonate and volcaniclastic rocks (Parson Bay Formation) (Muller, 1977). The latter of these units, the Triassic Quatsino and Parson Bay Formations, immediately underlie erupted volcanics of the Jurassic Bonanza arc.

The mid- to upper- crust of the Bonanza arc is well-exposed in section and ideal for studying magma-carbonate interactions, given the abundance of exposures of arc magma in contact with limestone of the Quatsino Formation, typically represented as mappable aureoles and skarn mineralization (Chapter 3 – Figure 3.1). This study investigates the Merry Widow Mountain region in detail, where interactions between early and primitive arc magmas with a ~1 km thick limestone platform are well-preserved (Figure 4.1, Figure A2).

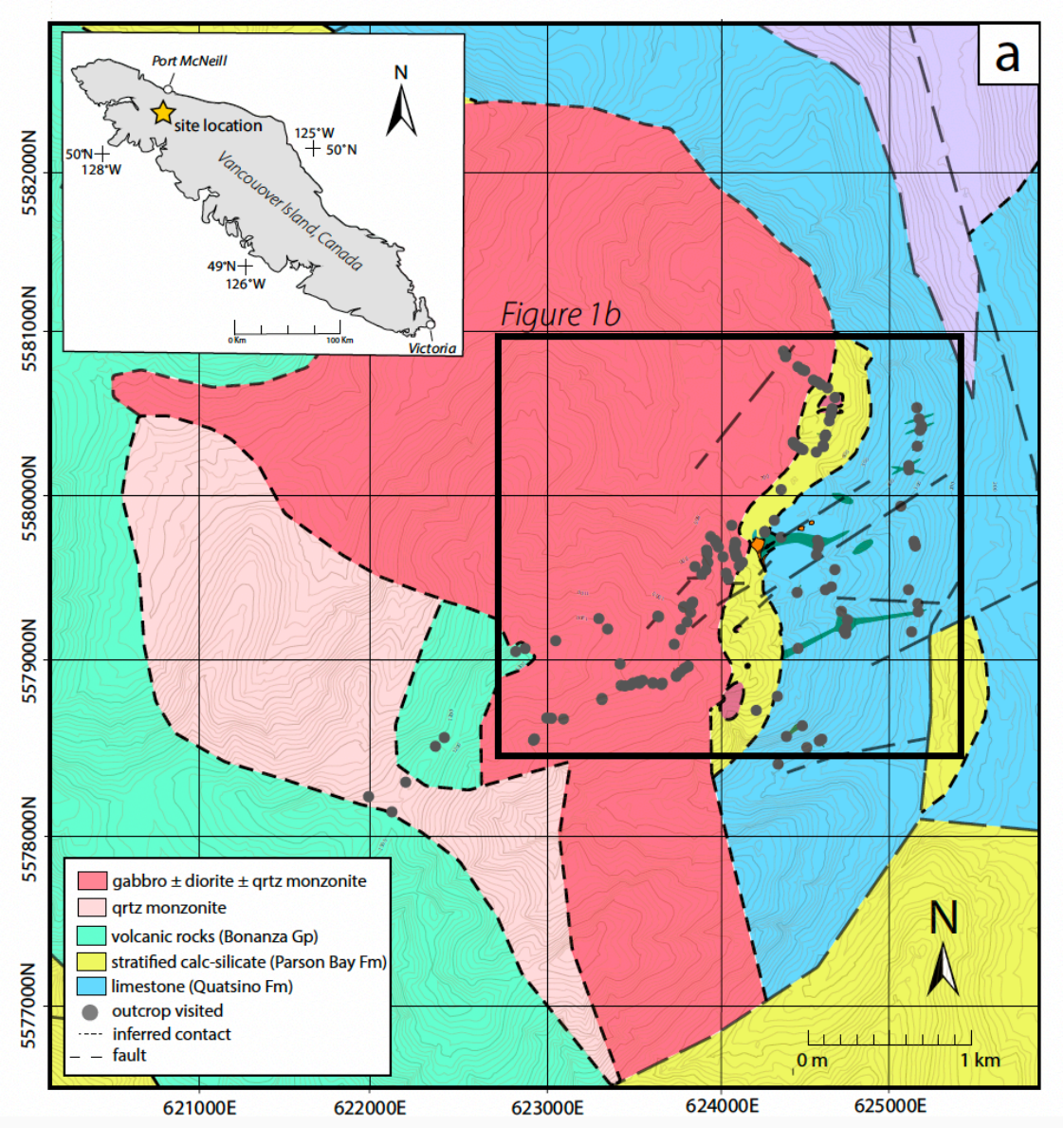
a
Port McNeill
site location
125°W
50°N
50°N
128°W
Vancouver Island, Canada
49°N
126°W
0 Km
100 Km
Victoria
N
Figure 1b
gabbro ± diorite ± qrtz monzonite
qrtz monzonite
volcanic rocks (Bonanza Gp)
stratified calc-silicate (Parson Bay Fm)
limestone (Quatsino Fm)
outcrop visited
inferred contact
fault
N
0 m
1 km
5582000N
5581000N
5580000N
5579000N
5578000N
5577000N
621000E
622000E
623000E
624000E
625000E

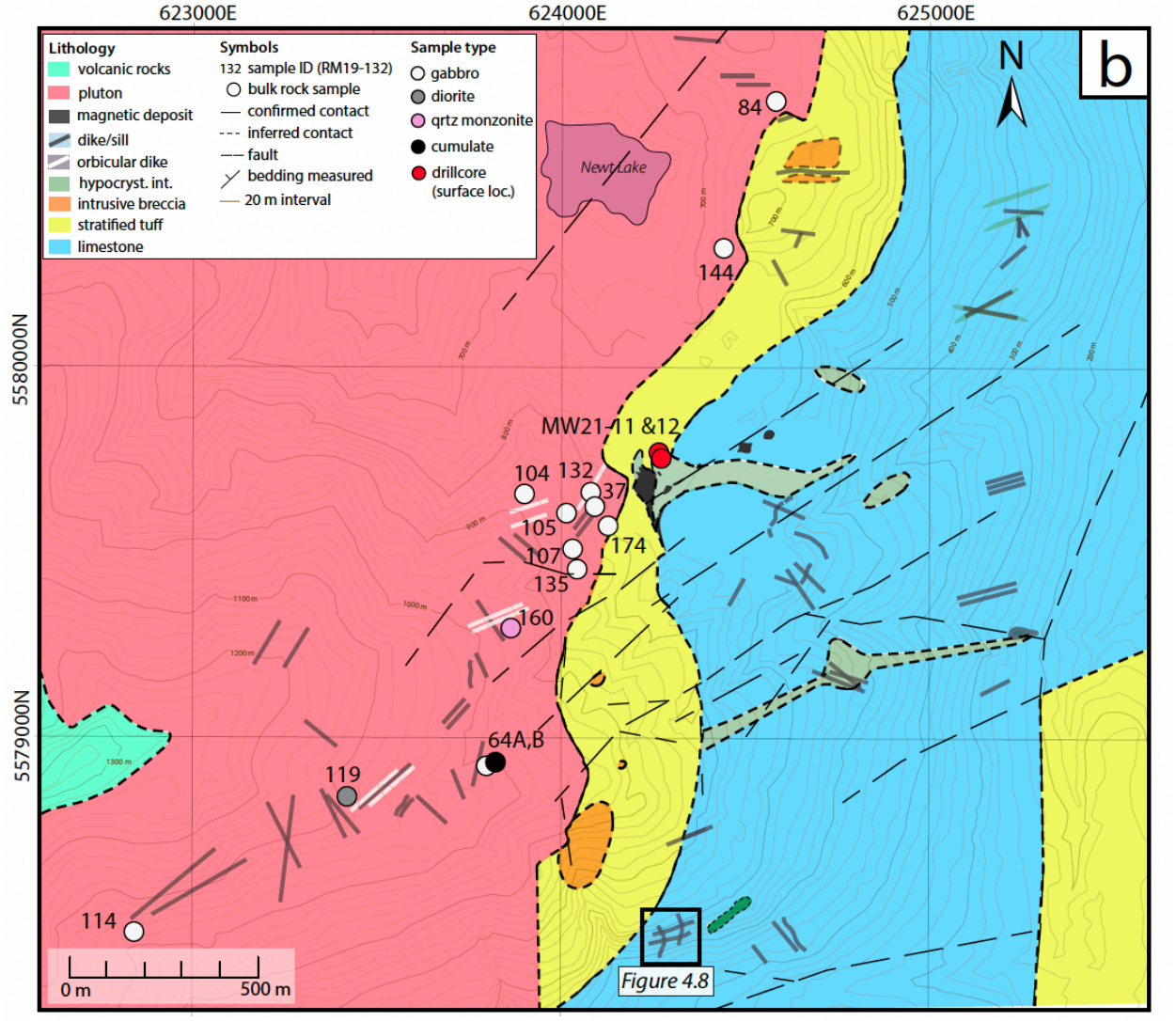

Figure 4.1: **(a)** Regional bedrock geology of the Merry Widow pluton and surrounding units, modified from Nixon et al. (2011). **(b)** Bedrock geology along the eastern Merry Widow pluton-wallrock contact is modified after Sangster (1964), Lund (1966), Ray and Webster (1991), showing sample locations collected for this study. See Figure A2 for field relationships at depth, including the relationship of the stratified tuff (Parson Bay Formation) and limestone (Quatsino Formation) with the Merry Widow pluton.

4.3.1 Merry Widow lithologies

4.3.1.1 Limestone and stratified tuff

Wallrock lithologies consist of ~1 km thick Late Triassic limestone (Quatsino Formation or 'Quatsino limestone') that is overlain by <100 m Late Triassic to Early Jurassic stratified tuff, siltstone and marl (Parson Bay Formation) (Figure 4.1, Ray and Webster, 1991; Morris and Canil, 2021). At the Merry Widow site and surrounding area, the Quatsino limestone reaches its greatest thickness (~1.1 km) documented on Vancouver Island (Figure C1). The limestone is the stratigraphically lowermost unit exposed (Figure 4.1b) consisting of massive grey to white micrite beds that regionally dip ~20 – 25º southwest (Lund 1966; Ray and Webster, 1991). The limestone is intruded by the Merry Widow pluton, as well as a dense network of dikes and sills (Figure 4.1b), and is locally folded or deformed within meters to magmatic intrusions (Morris and Canil, 2020). Stratified tuffs that overlie the limestone are dominantly crystal-poor and lithic rich with a hypocrystalline groundmass (Morris and Canil, 2020). The stratified tuff is also cross-cut by mafic dikes and near-vertical bodies of polymict breccia, the latter abundant in angular xenoliths (tuff, plagioclase-phyric basalt, and gabbro) within a flow-banded hypocrystalline groundmass (Morris and Canil, 2020), and often referred to as an 'intrusive breccia' (Figure 4.1b).

4.3.1.2 Merry Widow intrusive rocks

The Merry Widow pluton is dominantly gabbro with minor diorite and quartz monzonite. The pluton intrudes the Quatsino limestone and overlying calcareous rocks (tuffs + marls) of the Parson Bay Formation for a strike parallel distance of ~6 km along its eastern margin, where a section of up to ~2.5 km in thickness can be traced (Figure 4.1b). The gabbro and quartz

monzonite have U-Pb zircon ages of >197.4 ± 0.5 Ma and 197.1 ± 0.3 Ma, respectively (Nixon et al., 2011).

Over a ~100 m wide margin, the gabbro transitions from layers of fine-grained gabbro with distinct granoblastic clinopyroxene to coarse-grained gabbro with interstitial clinopyroxene, euhedral olivine, and minor apatite (<5%). This layering is observed on both the m-scale (outcrop and drillcore) and cm-scale (thin section – Figure 4.2a). In the gabbro, symplectites are observed between oxide-olivine contacts to form orthopyroxene, and plagioclase-oxide contacts forming amphibole (Figure 4.2b). Rare pegmatitic gabbro cumulates with unique spheroidal shapes in outcrop (10 – 30 cm wide) also occur proximal (<200 m) to the pluton-wallrock contact (Morris and Canil, 2021). These cumulates are similar in mineralogy to the coarse-grained gabbro, with more apatite (5 – 10%), amphibole (15 – 20%), and trace titanite (<1%).

Drillcore and historical logs indicate the pluton is in contact with a ~50 to 150 m wide heterogenous unit of skarn mineralization and various polymict breccias, herein referred to as the metamorphic aureole. From drillcore, a thin chilled margin (1.5 m wide) of very fine-grained (<100 μm) granoblastic gabbro consisting only of clinopyroxene (55 – 60%) and plagioclase (40 – 45%) is in contact with this aureole (Figure 4.2d,e). Massive quartz monzonite occurs in the stratigraphically higher and exposed interior regions of the pluton, west of the study area near the Merry Widow summit (Nixon et al., 2011). Field relationships indicate the quartz monzonite is a late-stage phase where cm- to m-scale apophyses intrude or mingle with the marginal gabbro, and intrude the proximal (<100 m) wallrock. For more petrographic details on the plutonic rocks see Appendix C (Supplementary Material Text). An extensive network of mafic dikes and sills cross-cut all units at the Merry Widow site (Figure 4.1b), and are described in detail in the previous chapters (Chapter 2 – Morris and Canil, 2022; Chapter 3).

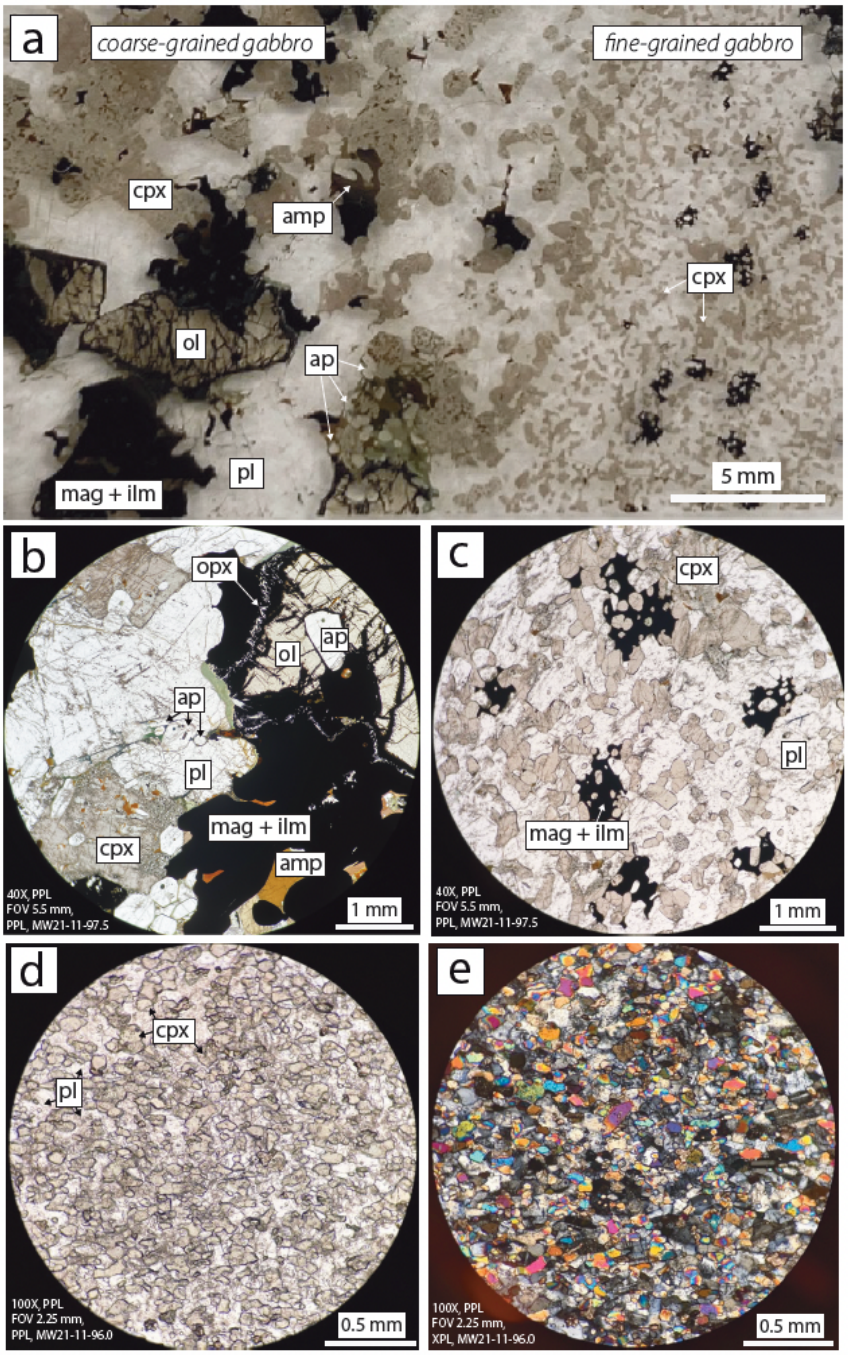

Figure 4.2: Gabbro petrography of the Merry Widow pluton, demonstrating **(a)** coarse- and fine-grained textures, where layered-like transitions between coarse- to fine-grained gabbro are common within the <100 m marginal gabbro in contact with wallrock. **(b)** Coarse-grained gabbro with clinopyroxene (cpx), plagioclase (pl), magnetite (mag), ilmenite (il), olivine (ol), amphibole (amp), apatite (ap), and orthopyroxene (opx). **(c)** Fine-grained gabbro with distinct granoblastic cpx texture, consisting of dominantly cpx, pl and ± mag, ilm. A very-fine grained chilled margin of the pluton in **(d)** plane-polarized and **(e)** cross-polarized light rich in clinopyroxene (55 – 60%) and plagioclase (40 – 45%) displaying granoblastic textures.

4.3.1.3 Mineralization

Mineralization at the Merry Widow site is a Fe ± Cu-Ag-Au-Co deposit localized at the top (Empire deposit) and base (Benson Lake deposit) of the Quatsino Limestone (Ray and Webster, 1991), as well as along the pluton-wallrock contact. Historical drillcore logs indicate that mineralization is disseminated within various intrusive breccias at the contact of the pluton with the limestone wallrock. These deposits are evidence that the entire thickness (~1 km) of the Quatsino limestone was subject to magma-carbonate interactions. Skarn mineralization at exposed contacts of the pluton with the tuffaceous Parson Bay Formation was minimal (<20 cm) and strictly localized to the contact (i.e., exposures near RM19-144, Figure 4.1b).

4.4 Sample collection

Major and trace element concentrations were determined in 20 plutonic rocks collected near the pluton margin, and along a transect to more interior regions of the pluton (Figure 4.1b). Plutonic rocks sampled included gabbro (13), and one quartz monzonite, diorite, and cumulate (Table C1 to C3). Plutonic rock samples were also collected from two drillcores oriented at 270°/–45° (See MW21-11 and MW21-12 in Figure 4.1b), which included four chilled margin samples (MW21-11 samples), one cumulate ~3 m from the margin (MW21-12-91), and one gabbro ~40 m from the margin (MW21-12-137) (Table C1 and C2). Four limestone samples with bulk rock and $^{87}Sr/^{86}Sr$ isotope analyses (Table B2 – Chapter 3) were also analyzed for $\delta^{18}O$ and $\delta^{13}C$ isotopes (Table C4). Major element analyses of clinopyroxene, plagioclase, olivine, magnetite, ilmenite, amphibole or biotite, and ± orthopyroxene were determined in two coarse-grained gabbros (RM19-107 and RM19-84) and one fine-grained gabbro (RM19-132) (Table C5). Trace elements on clinopyroxene, plagioclase, magnetite, ilmenite, and apatite (cumulate

only) were determined from three gabbros (RM19-132, RM19-144, RM19-64A) and one cumulate (RM19-64B) (Table C6). Not all phases were analyzed for trace elements, for example only magnetite, ilmenite, and apatite were analyzed in the cumulate sample (RM19-64B) due to alteration of clinopyroxene and plagioclase phases (Table C6). Detailed methods for bulk rock and mineral chemistry are provided in Appendix C (Supplementary Material Text).

4.5 Results

4.5.1 Bulk rock chemistry

Gabbro at Merry Widow contains 46 to 50 wt.% SiO_2 and 4.5 to 6.0 wt.% MgO. More evolved diorite to quartz monzonite compositions contain (57 – 62 wt.% SiO_2, <3 wt.% MgO) (Ray and Webster, 1991). Chilled margin samples most proximal to the wallrock contact (MW21-11-96.0 and MW21-11-96.3) have higher SiO_2 (53.7 to 54.3 wt.%), and CaO (>15 wt.%) relative to gabbro (<12 wt.% CaO) with similar MgO (~5 wt.%). Cumulates are lower in SiO_2 (40.9 to 42.2 wt.%) with notably higher TiO_2 (4.6 – 4.8 wt.%) and P_2O_5 (1.8 – 2.1 wt.%) than the host gabbro. Merry Widow plutonic rocks show tholeiitic character, similar to intrusive rocks at the site studied in the previous chapters (2,3) and by others (Ray and Webster, 1991), where mafic compositions (<52 SiO_2 wt.%) show FeO* enrichment relative to MgO (Figure C2). These plutonic rocks are overall more enriched in TiO_2, CaO, Na_2O, and ± P_2O_5, but lower in K_2O and ± Al_2O_3 in comparison to most Bonanza arc rocks (Figure C2).

Merry Widow plutonic rocks show large ion lithophile enrichment (LILE) and high field strength element (HFSE) depletion patterns typical of arc magmas (Pearce and Peate, 1995) (Figure 4.3a). Diorite and quartz monzonite have greater abundances in most trace elements in comparison to gabbro, with the exception of Sr, and Ti. Gabbro is generally enriched in U (0.3 –

4X NMORB) and Sr (3 – 5X NMORB) relative to NMORB, which are common signatures in arc rocks, however the chilled margin shows far more elevated U (15 – 17X NMORB) and Sr (8 – 9 X NMORB) values (Figure 4.3a). The chilled margin is also more notably abundant in HFSEs (excluding Ti) and rare earth elements (REEs), where samples most proximal to the wallrock contact (MW21-11-96.0 and MW21-11-96.3) shows a distinct LREE enrichment ($La/Yb_{(N)}$ 2.6 – 3.0) in comparison to the gabbro ($La/Yb_{(N)}$ <1.6) (Figure 4.3b). Cumulates, rich in apatite (5 – 10%), also show REE enrichment, with patterns similar to apatite analyzed in samples (enriched MREE, depleted Y, Yb, Lu) (Figure 4.3b, Figure C3). Fluid mobile large ion lithophile elements (Sr, Rb, Ba, K) show no correlation with LOI (R^2 value <0.4), which was <1.6 wt.% for all samples (Table C1).

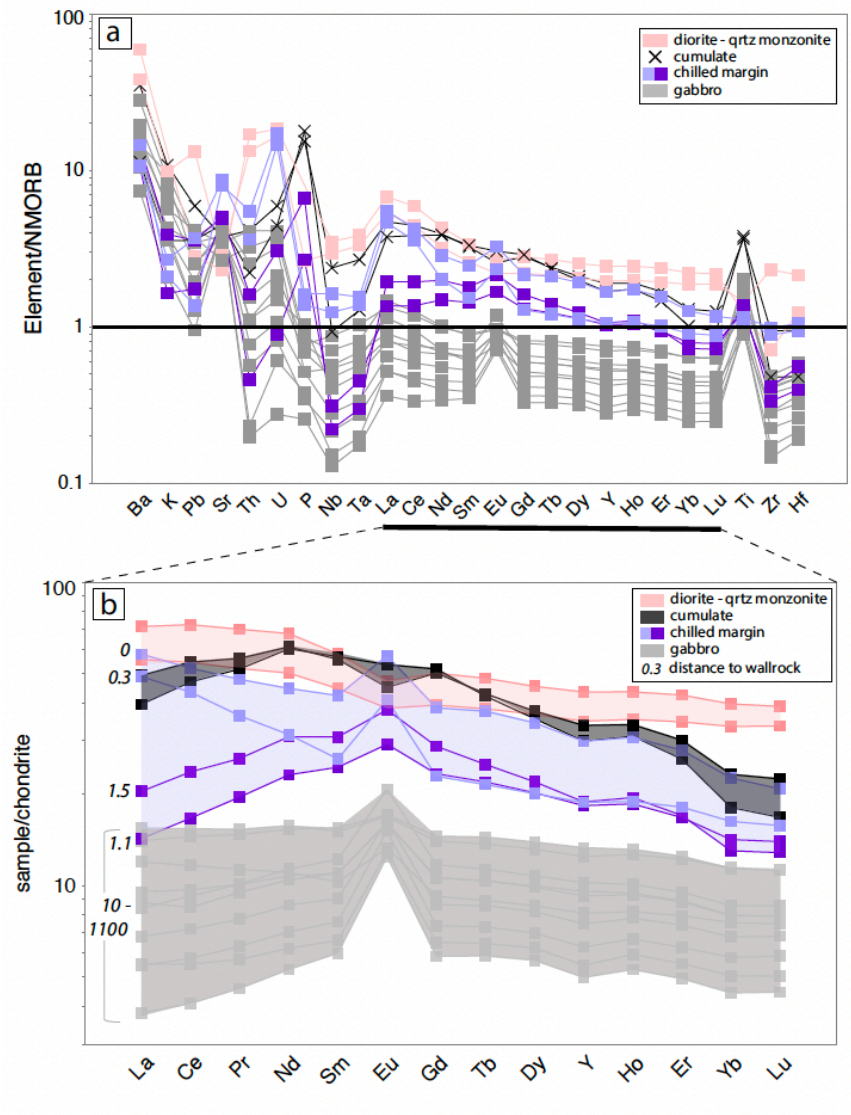

Figure 4.3: **(a)** Normal mid-ocean ridge (NMORB) normalized extended trace element diagram (Sun and McDonough, 1989) and **(b)** Chondrite normalized rare earth element (REE) plots (Sun and McDonough, 1989) for plutonic rocks at Merry Widow. Italicized numbers in (b) is distance to pluton-wallrock contact for gabbro and chilled margin samples. Chilled margin plutonic rocks (purple shades) have distinct Sr, U, and REE enrichments in comparison to more interior gabbro samples. Cumulate REE patterns in (b) resemble apatite patterns, likely due to their high modal (5 – 10%) apatite abundance. Plutonic rocks show Ti enrichments (a) except for more evolved diorite and quartz monzonite (qrtz monzonite) compositions.

4.5.2 Mineral chemistry

Mineral chemistry for major (clinopyroxene, orthopyroxene, olivine, plagioclase, magnetite, ilmenite, and amphibole) and trace (clinopyroxene, plagioclase, apatite, magnetite, and ilmenite) elements analyzed in gabbro and a cumulate (trace only) shows compositions typical for gabbro (Table C5 and C6). Clinopyroxene in both fine- and coarse-grained gabbro is dominantly augite, with compositions ranging from $Wo_{41-45}En_{17-20}Fs_{38-40}$ in granoblastic clinopyroxene and $Wo_{39-46}En_{15-19}Fs_{39-43}$ in coarse (anhedral) clinopyroxene, with low Al_2O_3 (<3 wt.%) (Table C5). Orthopyroxene analyzed from coarse-grained gabbro is enstatite with an average composition of $Wo_{2-3}En_{61-63}Fs_{34-36}$. Olivine compositions in coarse-grained gabbro range from Fo_{53-60}, and in fine-grained gabbro are slightly more evolved ranging from Fo_{49-52}. Plagioclase compositions from both fine- and coarse-grained gabbro span a range of An_{78-84} within cores, and An_{45-64} within rims. Ilmenite ranges from 49.0 – 51. 3 wt.% TiO_2 and 44.5 – 47.0 wt.% FeO, with notable MnO (up to 2.2 wt.%). Magnetite composition ranges from 77.8 – 86.8 wt.% FeO and 1.9 to 10.3 wt.% TiO_2, with notable Al_2O_3 (up to 4.9 wt.%). Minor amphibole (<10% abundance) is typically hastingsite and is primary (Table C5).

Plagioclase and clinopyroxene in gabbro, as well as apatite in cumulates display typical REE abundances and patterns for gabbro (Rollinson, 1993) such as high Eu anomalies for plagioclase, and enriched REE abundances in apatite (Figure C3). Rare earth element concentrations + Y (REE+Y) in apatite ranges from 1.0 to 1.6 wt.% (10,000 – 16,000 ppm). Trace element chemistry for magnetite and ilmenite analyzed in gabbro indicated notable V in

magnetite (0.6 – 1.7 wt.%). In addition ilmenite had detectable Nb (33 – 56 ppm), but was non-detect in magnetite.

4.5.3 $^{87}Sr/^{86}Sr$ isotopes

Sr isotope ratios ($^{87}Sr/^{86}Sr$) were calculated to initial values, based on an age of 197 Ma for plutonic rocks (Nixon et al., 2011). Gabbro collected along a trend from the pluton-wallrock contact to more interior regions (~1100 m) generally shows low $^{87}Sr/^{86}Sr$ and varies from 0.7022 to 0.7039 (± 0.001, 2σ), similar to primary MORB (~0.7027 from White and Hoffman, 1982). One exception is the chilled margin near the pluton-wallrock contact (0 – 0.3 m) with enriched $^{87}Sr/^{86}Sr$ of 0.7057 to 0.7061 (± 0.001, 2σ) (Table C2). The chilled margin is in contact with the metamorphic aureole, rich in skarn mineralization and calcite. Initial Sr ratios for the wallrock limestone vary from 0.7075 to 0.7079 (± 0.0006) (Table B2 – Chapter 3).

4.5.4 $\delta^{18}O$ isotopes in silicates

Bulk rock powders of Merry Widow plutonic rocks collected between 9 and 1070 m from the pluton-wallrock contact vary considerably for $\delta^{18}O_{VSMOW}$: gabbro 3.8 to 13.3‰, a cumulate 5.8‰, and a quartz monzonite 6.8‰ (Table C3, Figure 4.4). As noted in methods (Appendix C – Supplementary Material Text), four repeat analyses for $\delta^{18}O$ on fresh and unaltered gabbro (RM19-174) proximal (9 m) to the pluton-wallrock contact vary by ±3.7 ‰. The high sample variability suggests the $\delta^{18}O$ results on bulk rock powders should be considered with caution. In contrast, $\delta^{18}O$ on fresh and unaltered clinopyroxene grain separates in the gabbro (collected between 40 m to 1070 m from the pluton-wallrock contact), showed a narrower range from 2.3 to 5.5‰ ±0.8, slightly lower than mantle-like clinopyroxene values (5.2 – 6.0‰; Mattey et al.,

1994) (Table C3). A chloritized clinopyroxene from a cumulate (RM19-64B) gave values of 3.2 to 4.2 ‰ (±1.1). The $\delta^{18}O_{SMOW}$ on bulk rock powders and clinopyroxene separates generally show $\delta^{18}O$ depletion in comparison to mantle-derived basalt and clinopyroxene (Figure 4.4).

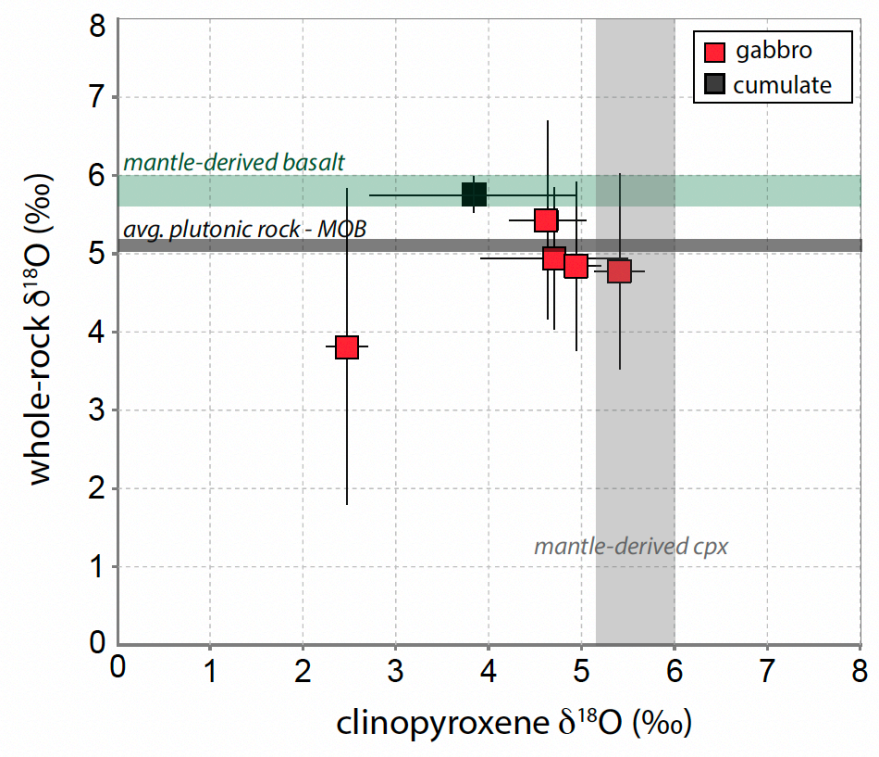

Figure 4.4: Oxygen isotope values ($\delta^{18}O_{VSMOW}$) for plutonic rock samples (gabbro and one cumulate) with corresponding whole-rock and clinopyroxene data. Samples generally plot below mantle-derived values for both whole-rock and clinopyroxene (Bindeman, 2008), indicating am overall depletion in $\delta^{18}O_{SMOW}$ values. Average plutonic rock values from the modern ocean basins (MOB) are also provided (Coogan et al., 2019).

4.5.5 $\delta^{13}C$ and $\delta^{18}O$ isotopes in carbonates

The Quatsino limestone at Merry Widow ranges from 3.2 to 4.3 ± 0.2‰ for $\delta^{13}C$, and from 19.5 to 23.5 ± 0.4‰ for $\delta^{18}O$ (Table C4). Both the most depleted (19.5‰) and enriched (23.5‰) $\delta^{18}O$ samples were collected ~1 m from contacts with a <2 m wide mafic dike that has a presumed mantle-derived $\delta^{18}O$ value of 5.5 – 5.9 ‰ (Bindeman, 2008).

4.6 Discussion

4.6.1 Geochemical modeling of plutonic rocks

Ultimately, a goal of this study is to quantify how much of the pluton has assimilated the limestone wallrock. Merry Widow geochemistry shows anomalous trends from other Bonanza arc magmas, such as tholeiitic character in most mafic plutonic rocks (<52 SiO_2 wt.%), and enriched Sr, U, REEs, and $^{87}Sr/^{86}Sr$ observed within the chilled margin. I therefore use various geochemical modeling techniques to examine if these geochemical differences can be explained by carbonate assimilation or other processes.

4.6.1.1 Thermodynamic modeling of open and closed system processes

To test whether limestone assimilation can generate the unique Fe-enriched trends in Merry Widow plutonic rocks, I use the thermodynamic software package rhyolite-MELTS v.1.2.0 (Ghiorso and Gualda, 2015) which generates liquid lines of descent from concurrent assimilation and fractionation crystallization (AFC) processes that occur within slowly (>1 kyr) cooling plutons. For AFC models, I assume a hydrous (5 wt.% H_2O) primitive basaltic melt from the Bonanza arc (JL06-027; Larocque and Canil, 2010) that cooled from 1200°C to 800°C at 2 kbar (isobaric), and assimilated between 0 to 20% calcite, also at 1200°C (Figure 4.5a). A water content of 5 wt.% H_2O is typical for primitive arc magma values (Wallace, 2005; Plank et al., 2013; Nandedkar et al., 2014). A temperature range of 1200°C to 800°C was modeled to obtain the liquid line of descent from above hydrous liquidus temperatures (~1140°C) where the system is 100% melt (melt fraction or 'F' of 1), down to 800°C where melt fractions are 15 – 20% (F=0.15 to 0.20) (Figure 4.5). Additions of >20% calcite causes the rhyolite-MELTS software to fail, as does cooler calcite temperatures (i.e., 600 – 700°C). For these models, I consider an open

system of oxygen exchange between the melt and assimilant, therefore no fO_2 buffer is fixed.

Modeled AFC trends, which represent liquid lines of descent (LLD) can generate most of the enriched Fe/Mg plutonic rocks at Merry Widow from 0 to 10% calcite assimilation (Figure 4.5a). However, and more importantly in plutonic rocks where melt fractions are low (<50% – Dufek and Bachmann, 2010), is that the mineral assemblages and their chemistry fractionated in the models, do not match what I observe. Model trends show an Fe-enrichment and Si-depletion with increasing calcite addition due to an increased removal of clinopyroxene at the expense of olivine and plagioclase (Figure C4). Clinopyroxene produced from the model AFC trends has notable Al_2O_3 (7 – 10 wt.%), which is not observed in gabbro clinopyroxenes (Al_2O_3 <2.8 wt.%) (Table C5). High Al_2O_3 (i.e., as Ca-Tschermacks component) is common in clinopyroxene generated from limestone assimilation. For example, 0.5 GPa experiments by Carter and Dasgupta (2015) produced even higher Al_2O_3 (~15 – 20 wt.%) in clinopyroxene compared to those generated by rhyolite-MELTS AFC models. In addition, model fractionates with increasing calcite assimilation are dominantly clinopyroxene + Fe-oxides (early aluminous spinel, late magnetite) with low plagioclase abundance (<17%) (Figure C4), which is not a mineral assemblage observed in any Merry Widow plutonic rocks. Rhyolite-MELTS can have limitations in carbonate-silicate systems, due to a lack of thermodynamic data (Heinonen et al., 2021), therefore fractionate compositions and modeled trends are limited in using this software.

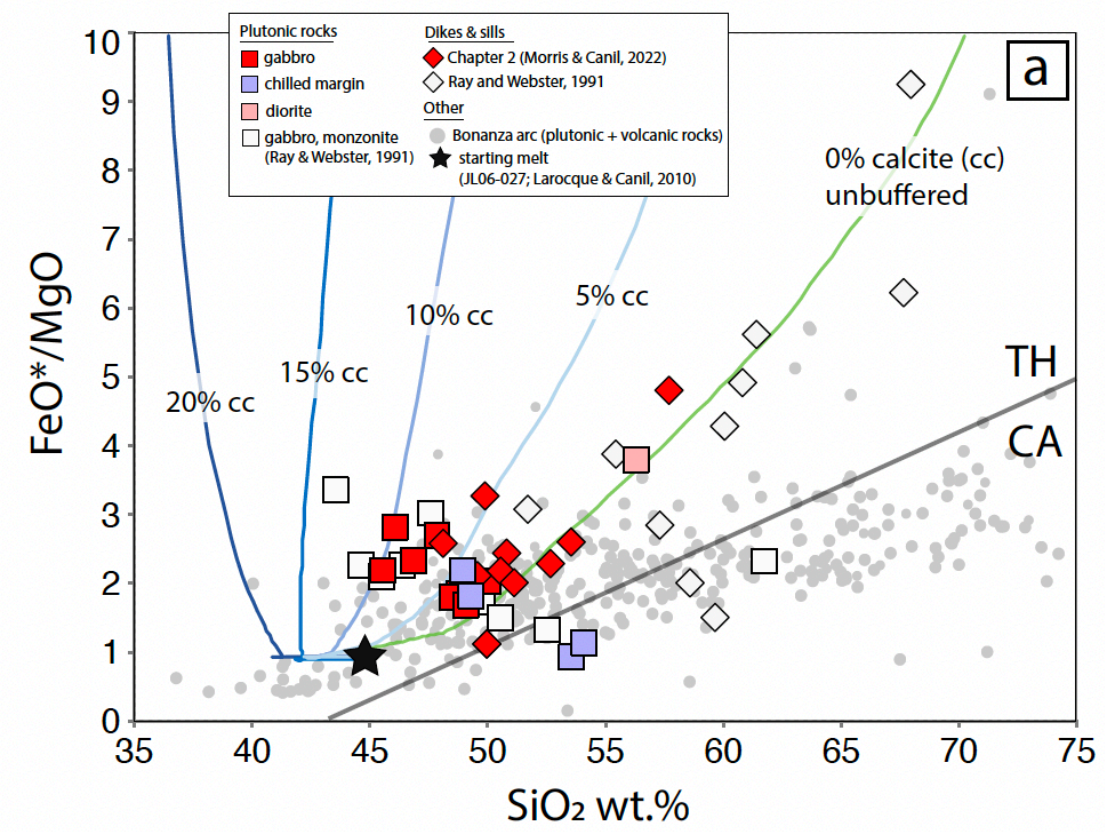
Plutonic rocks
gabbro
chilled margin
diorite
gabbro, monzonite (Ray & Webster, 1991)
Dikes & sills
Chapter 2 (Morris & Canil, 2022)
Ray and Webster, 1991
Other
Bonanza arc (plutonic + volcanic rocks)
starting melt (JL06-027; Larocque & Canil, 2010)
a
0% calcite (cc) unbuffered
5% cc
10% cc
15% cc
20% cc
TH
CA
FeO*/MgO
SiO2 wt.%
0
1
2
3
4
5
6
7
8
9
10
35
40
45
50
55
60
65
70
75

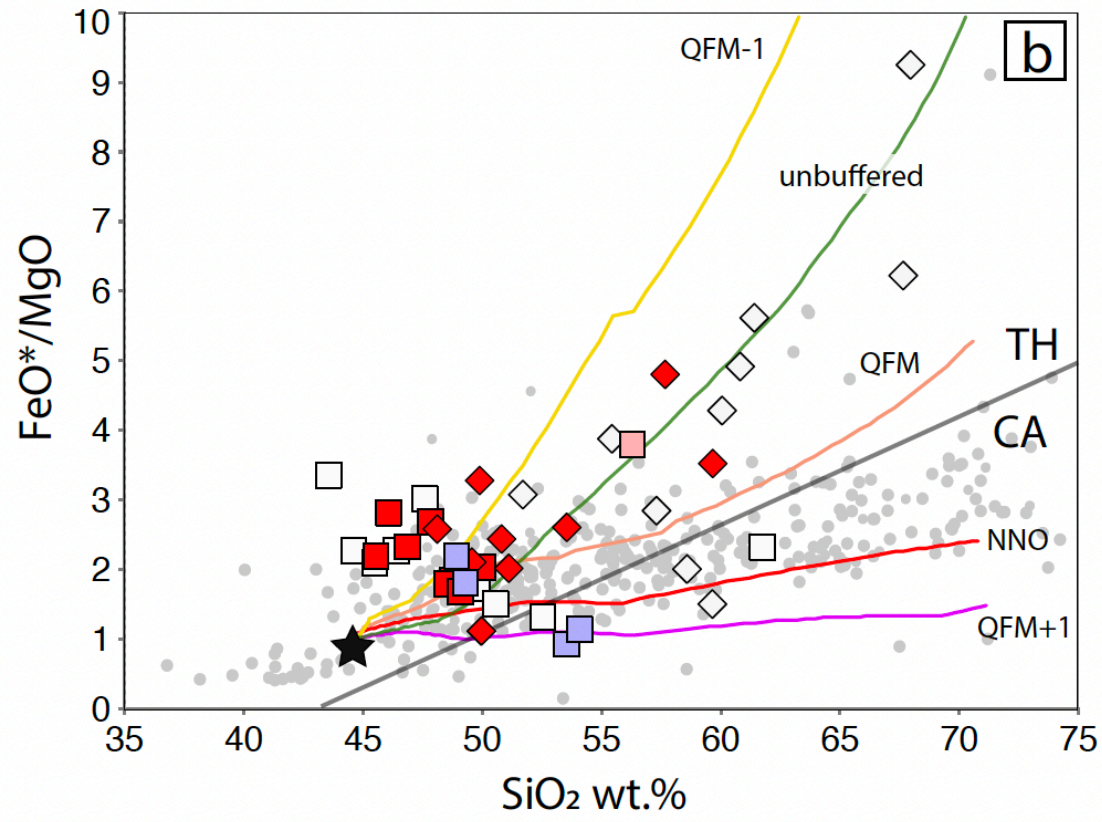

Figure 4.5: Major element bivariate diagrams of FeO*/MgO vs SiO_2 for Merry Widow non-cumulate plutonic rocks from this study and others (Ray and Webster, 1991), and comagmatic dikes and sills from others (non-orbicular dikes and sills – Chapter 2; Ray and Webster, 1991). Merry widow plutonic rocks and comagmatic dikes and sills show dominantly tholeiitic (TH) character defined by Miyashiro (1974). Modeled trends from rhyolite-MELTS v.1.2.0 (Ghiorso and Gualda, 2015) are **(a)** liquid lines of descent (LLD) for open-system assimilation + fractional crystallization (AFC) displaying trends from 0 – 20% calcite addition (model inputs: 1200°C to 800°C, 2 kbar, starting melt 5 wt.% H_2O, unbuffered, calcite input temperature 1200°C); and **(b)** for closed-system fractional crystallization with identical model inputs except at varying fixed and unfixed fO_2 buffers and no assimilation. Unbuffered runs in both (a) and (b) have initial melt at 0.2 Fe^{3+}/Fe_{total}. Modeled trends in both (a) and (b) display LLD from a starting melt fraction (F) of 1 to a final F of ~0.16 to 0.21.

The model AFC trends can also not explain the more evolved melt compositions from assumed comagmatic dikes and sills reported by others (Ray and Webster, 1991; Chapter 2 – Morris and Canil, 2022), that appear to instead follow the 0% calcite assimilation trend. I therefore test if fractional crystallization alone can produce the spectrum of Merry Widow compositions from plutonic rocks (gabbro to diorite) and comagmatic dikes and sills (basalt to trachydacite). To do so, I use rhyolite-MELTS v.1.2.0 (Ghiorso and Gualda, 2015) with the same primitive basaltic melt used in AFC modeling (JL06-027; Larocque and Canil, 2010), and identical input parameters (cooled 1200°C to 800°C, isobaric pressure held at 2 kbars, 5 wt.% H_2O), with the exception of no calcite added. In these models, I assume a closed system, where fO_2 is fixed to various oxygen buffers ranging from QFM-1 to QFM+1 (Figure 4.5b). A liquid line of descent generated with fO_2 unfixed (open system), with a starting melt Fe^{3+}/Fe_{total} of 0.2 is also included (Figure 4.5b). These modeled trends indicate that the enriched Fe/Mg compositions in plutonic rocks at Merry Widow can be generated via closed system fractional crystallization at lower fO_2 (<QFM) in comparison to most Bonanza arc magmas which follow the higher fO_2 NNO trend. This indicates limestone assimilation is not required and that the majority of Merry Widow plutonic rocks may have simply crystallized under more reducing conditions (Figure 4.5b). The only outliers from fractional crystallization processes in more reduced conditions (<QFM) are chilled margin samples collected most proximal (0 – 0.3 m) to the pluton-wallrock contact, suggesting the chilled margin crystallized at a higher fO_2 (i.e., ~QFM+1) or underwent some other process. Comagmatic dike and sill compositions, that are more representative of an evolved melt compositions also confirm that calcite assimilation is not needed to explain the tholeiitic trends. In fact, the dike and sill compositions are best fit along unbuffered 0% calcite assimilation trends (Figure 4.5a) or buffered FC trends between QFM to

QFM-1 (Figure 4.5b). In addition, dikes and sills that are known to have assimilated limestone, but via binary mixing processes (not AFC) are shown for completeness in Figure C5, where 10% calcite assimilation via AFC can produce compositions similar to orbicular dikes (Chapter 2 – Morris and Canil, 2022) and 20 wt.% calcite assimilation can produce compositions similar to boundary melts in dike-limestone profiles (Chapter 3).

4.6.1.2 Mass-balance modeling for magma-carbonate reactions

Enriched $^{87}Sr/^{86}Sr$ values and high Sr in the chilled margin of the pluton suggests evidence of limestone assimilation. I therefore test for limestone assimilation and concurrent fractional crystallization (AFC) within the chilled margin of the pluton using a mass-balanced geochemical model based on calculations by DePaolo (1981) and appropriate phases (and ranges) present. The model uses a starting melt composition of a gabbro (RM19-174) with $^{87}Sr/^{86}Sr$ (0.7034) and Sr concentrations (396 ppm) similar to mantle-derived values (Figure 4.6, Table C2), and an assimilant of Merry Widow limestone (RM19-78D) with the most enriched $^{87}Sr/^{86}Sr$ (0.7089 ± 0.0013) and Sr (720 ppm) (Table B2 – Chapter 3). Using the mass-balanced AFC model, I obtained the enriched $^{87}Sr/^{86}Sr$ and Sr concentrations observed in the chilled margin with representative modal percentages of phases observed (cpx = 60%, plagioclase = 40%; Figure 4.6) and partition coefficients of $D_{Sr} = 0.06$ and $D_{Sr} = 1.83$ for clinopyroxene and plagioclase, respectively (Rollinson, 1993 and references within). Chilled margin mineralogy (40 – 45% plagioclase, 55 – 60% cpx – Appendix C) supports this model. The best fit model obtains the $^{87}Sr/^{86}Sr$ and Sr concentrations of the margin with a ratio of mass assimilant added (Ma) versus mass of crystals removed (Mc) = 0.25, corresponding to 20 wt.% limestone assimilation (0.25/1.25 of total system volume), with a melt fraction of 25% (F=0.25) remaining (Figure 4.6).

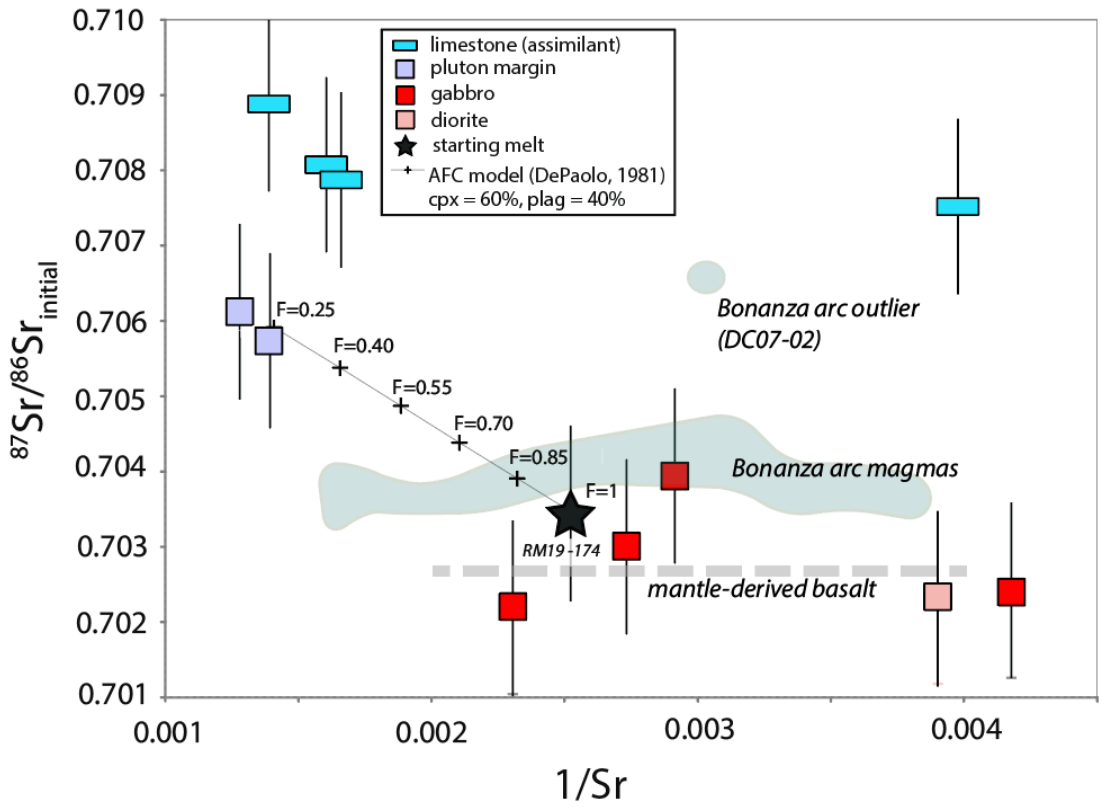

Figure 4.6: Initial $^{87}Sr/^{86}Sr$ isotopic ratios versus 1/Sr for plutonic rocks (gabbro, diorite, chilled margin) of the Merry Widow pluton, host wallrock limestone (Quatsino Formation), and regions displaying fields for Bonanza arc magmas (D'Souza et al., 2016). Assimilation + Fractional Crystallization (AFC) modeling as per the methods and calculations of DePaolo (1981) produces a best fit model when the ratio of mass assimilant (Ma) to mass fractionated (Mc) is 0.25:1 (Ma:Mc). Modal percentages of minerals within this model is from observed phase percentages in marginal samples (Figure 4.2d,e; cpx = 60%, plag = 40%). Partition coefficients (Sr = 0.06 in clinopyroxene, 1.83 in plagioclase) are based on mineral/melt partition coefficients from Rollinson, 1993 and references within.

Although the AFC modeling obtains the enriched $^{87}Sr/^{86}Sr$ in the pluton margin by assimilation of 20 wt.% limestone, the physical expression of this process is small, being observed over a <2 m width within a single drillcore sample (MW21-11). In concert with this muted physical evidence, is the lack of enriched $\delta^{18}O$ of clinopyroxene in gabbro (Figure 4.4), a mineral whose crystallization is accelerated by limestone assimilation (Figure C4). Assimilation

of $\delta^{18}O$ enriched crustal carbonates has been shown to enrich crystallizing clinopyroxene above mantle-derived clinopyroxene values (Deegan et al., 2021). The limestone country rock has $\delta^{18}O$ of > 19.5 ‰ but no $\delta^{18}O$ enrichment is observed in gabbro clinopyroxene nor bulk rock from ~10 to >1000 m from the wallrock contact (RM19-174 to RM19-114, Table C3). I interpret $\delta^{18}O$ depletion for both bulk rock and clinopyroxene (Figure 4.4) from typical mantle values to be a result of interaction with high temperature fluids (>500°C) (Bindeman, 2008). Nonetheless, a lack of enriched $^{87}Sr/^{86}Sr$ values within main phase gabbro samples collected ~10 to >1000 m from the wallrock contact (Table C2) indicates any reaction with the wallrock must be limited to at most the outer ~10 m of the pluton, as no samples collected between 0.3 to 9 m from the contact were analyzed for $^{87}Sr/^{86}Sr$ (Table C2). I therefore consider a reacted pluton margin that has assimilated 20 wt.% limestone and has a maximum thickness of 10 m within the Merry Widow pluton to be a liberal estimate.

4.6.2 Arc magmas and mechanisms driving crustal decarbonation

A goal of this study is to quantify the amount of CO_2 liberated from crustal carbonates assimilated into arc magmas, particularly from plutons. Ramos et al. (2020) shed light on various mechanisms that liberate crustal CO_2 from carbonate-bearing lithologies within arc crust including: (1) magma-hosted CO_2, where CO_2 from assimilated carbonates is transported within the magma, which also carries primary mantle-derived CO_2; (2) CO_2 release by decarbonation in the metamorphic aureole; and (3) metamorphic decarbonation from reactive transport of hydrothermal fluids. Herein, I focus on the mechanism of magma-hosted CO_2 transport (1),

comparing estimates of liberated CO_2 from the pluton with that from dikes and sills (Chapter 3). Calculations for CO_2 mass and fluxes for section 4.6 are provided in Table C7.

4.6.2.1 Quantifying CO_2 sourced from a pluton in carbonate versus shallow dikes and sills

I estimate the crustal-derived magmatic CO_2 produced from limestone assimilation into arc magmas based on AFC (pluton – this study) and binary mixing (dikes and sills – Chapter 3) modeling, and compare CO_2 volumes via two mechanisms of arc magmas interacting with carbonate: a km-scale pluton versus m-scale dikes and sills. For CO_2 flux estimates, I first consider the Merry Widow case (~1 km thick limestone) and further extrapolate to the entire Bonanza arc on Vancouver Island where the Quatsino limestone is on average 0.5 km in thickness (Nixon and Orr, 2008). Assimilation of the overlying calcareous sediments (Parson Bay Formation) is not considered, as decarbonation (skarn) was minimal (<20 cm) at its exposed contacts of the Merry Widow pluton. To quantify CO_2 sourced from limestone assimilation into the pluton, I use evidence from a lack of enriched $^{87}Sr/^{86}Sr$ isotopic ratios indicating no limestone assimilation at distances >10 m from the wallrock contact has occurred. I then calculate a reacted pluton volume for an (at most) 10 m thick reacted veneer of the pluton margin that assimilated 20 wt.% limestone.

The Merry Widow pluton covers an aerial extent of ~27 km^2 (4.5 km E-W x 6 km N-S) and intrudes a maximum thickness of ~1 km of Quatsino limestone, giving a total volume of 27 km^3 of magma that potentially interacts with the limestone. Considering a uniform 10 m wide pluton margin reacts with 1 km of limestone, this produces a volume of 0.21 km^3 of reacted magma (27 km^3 - 26.8 km^3 unreacted = 0.21 km^3 reacted margin), meaning only 0.8% of the Merry Widow pluton may have assimilated limestone along its margin. Assuming a basaltic

magma density of 2900 kg/m^3, I calculate a mass of the reacted pluton margin to be 608 Tg (Table C7). If I consider this mass of reacted magma to have assimilated 20 wt.% limestone producing 9 wt.% CO_2, this would indicate the reacted margin could have produced up to a maximum of 55 Tg CO_2 (Table 4.1, Figure 4.7).

Lithologic unit	Unit volume	Volume reacted/assimilated	Limestone assimilated	CO_2 produced	CO_2 transport media
	(km^3)	*(%)*	*(wt.%)*	*(Tg CO_2)*	
pluton	27	< 1	20	**<55**	magma
dikes & sills	7.3	< 4	20 - 25	**74 - 93**	magma
orbicular dikes	0.3	17	<25 %	**<15**	magma
skarn	1.1 – 3.2	100	n/a	**1307 – 3802**	fluids

Table 4.1: *CO_2 production from Merry Widow lithologies. See Table C7 for calculations.*

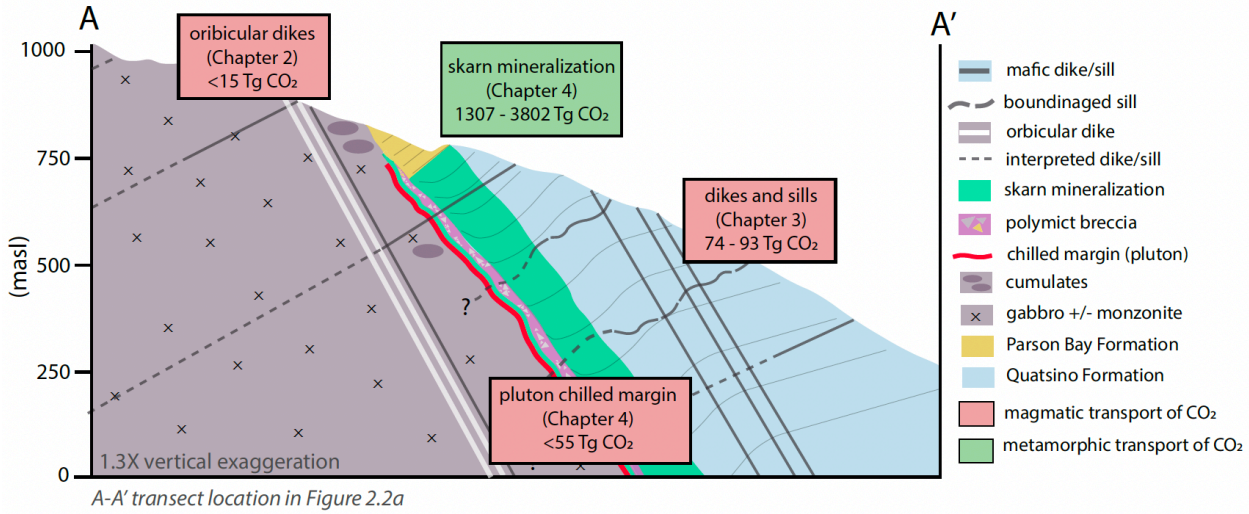

Figure 4.7: Modified figure A2 displaying magmatic and metamorphic (skarn mineralization) CO_2 contributions from the Merry Widow site. CO_2 contributions are also provided in Table 4.1 and calculations provided in Table C7.

The amount of produced CO_2 from limestone assimilation in the pluton is clearly dependent on the width of the reacted pluton margin, which ranges from nearly negligible (<2 m) to potentially slightly thicker (10 m) widths, where the latter and more liberal value is used to estimate a maximum CO_2 production. I emphasize this observation because previous studies on CO_2 liberated from magma-carbonate interactions from arc plutons (Lee et al., 2013) suggest >10% assimilation of carbonate into the entire pluton volumes , such as in the Cretaceous Sierra Nevada Batholith. If such an approach were adopted to my field example at Merry Widow, 10% limestone assimilation into a 27 km^3 pluton would produce ~3400 Tg CO_2 (Table C7) – orders of magnitude higher than the ~55 Tg CO_2 I calculate from the potentially thin reacted margin (<10 m). These differences attest to the importance of detailed field observations on the actual amount that a pluton interacts with limestone wallrock to produce CO_2. In addition, Lee et al. (2013) likely estimates an even greater masses of generated CO_2, where plutons are assumed to have interacted with carbonate lithologies at great depth within thick (>35 km) crustal sections. In contrast, these estimates have reservoir depths restricted to the well-defined thickness of limestone wallrock in this study. I note this study does not consider stoped blocks of wallrock into magma, however, field evidence and geochemistry at Merry Widow shows wallrock stoping is negligible, similar to other pluton-limestone studies where stoping is not volumetrically significant (Glazner and Bartley, 2006).

I also account for CO_2 produced from limestone assimilation into dikes and sills that extensively intrude the Quatsino limestone, and comprise a significant volume (up to 18%) of exposed outcrop in some regions (Figure 4.8). Calcium-rich boundary melts that form at limestone contacts of basalt dikes and sills within the Bonanza arc, including Merry Widow, can make up 4% of dike or sill magma volumes (Chapter 3). I consider the 4% of reacted magma to

be a liberal estimate, as compositional variation in magmas (i.e., more Si, less H_2O, etc) and flow dynamics (i.e., re-melting of channel walls) will affect the volume reacted. Nonetheless, these boundary melts formed from 20 – 25 wt.% limestone assimilation into basalt (Chapter 3), and are therefore capable of producing 9 – 11 wt.% CO_2. To quantify the volume of reacted margins (i.e., boundary melts) in dikes and sills at Merry Widow, I consider field relations showing they intrude the Quatsino limestone for a distance of up to ~1.5 km (Figure 4.1b). If dikes and sills intrude the wallrock for 1.5 km on all sides of the pluton, this results in 40.5 km^3 of intruded limestone intruded by dikes and sills at Merry Widow. Because dikes and sills can comprise up to 18% of the limestone outcrop volume (Figure 4.8), I calculate approximately 7.3 km^3 of magma (18% of 40.5 km^3) intrudes the Quatsino limestone in the form of m-scale and tabular basalt dikes and sills. If 4% of the volume of these basaltic dikes and sills (assumed density of 2900 kg/m^3) assimilates 20 – 25 wt.% limestone, that would indicate 847 Tg of magma (Table C7) is capable of producing 74 – 93 Tg CO_2 (Table 4.1, Figure 4.7).

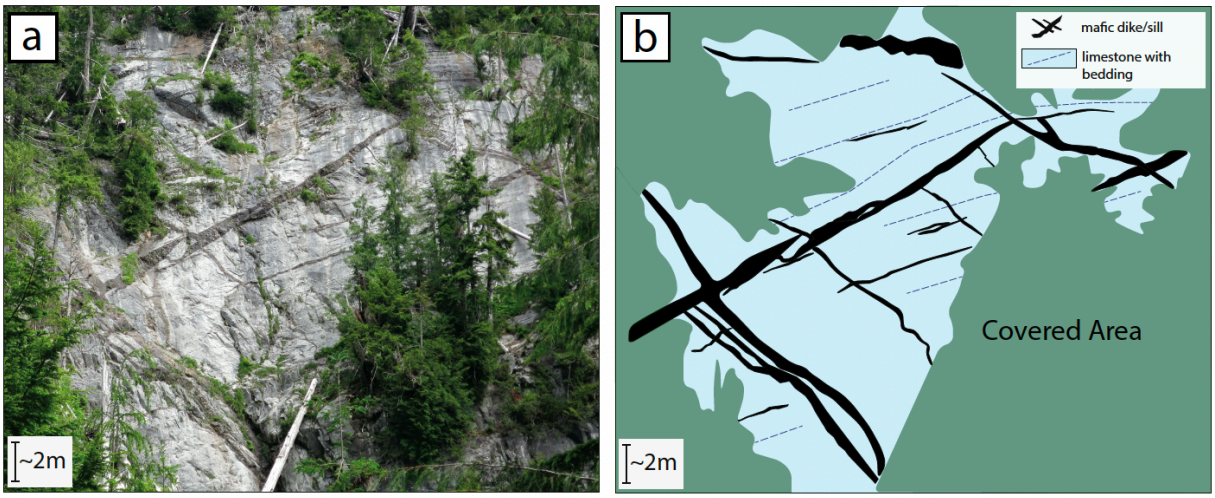

Figure 4.8: **(a)** Field photo of extensive dikes and sills that intrude the limestone at Merry Widow, approximate location shown in Figure 4.1b, and **(b)** a digitized schematic of (a). Image analysis using Fiji software (Image J2 trainable weka segmentation plugin v. 2.9.0 – Schindelin et al., 2012) of digitized outcrops and quantified line lengths of dikes and sills in contact within a given surface area of limestone indicates dikes and sills make up to 18% of the total volume of exposed outcrops in some regions at Merry Widow.

Orbicular dikes (Chapter 2) are a unique expression of dike-limestone reactions at depth, and comprise <1% (0.27 km^3) of total pluton volume, where orbicules account for up to 17% of the orbicular dike volume (0.27 km^3 x 0.17 = 0.05 km^3, Table C7). Using a liberal estimate from Chapter 2 where 25 wt.% limestone into basalt (2900 kg/m^3) produces orbicules, I calculate a contribution of <15 Tg CO_2 using the same calculation methods described above for non-orbicular dikes and sills (total magma reacted = 133 Tg magma, 11 wt.% is CO_2, for a total mass of 15 Tg CO_2) (Table 4.1, Figure 4.7).

From these calculations, I show the perhaps surprising outcome that larger plutons are less efficient at producing and transferring magmatic CO_2 compared to m-scale tabular dikes and sills. These estimates can be extrapolated to the entire Bonanza arc, but I first quantify contributions from metamorphic CO_2.

4.6.2.2 Non-magmatic CO_2 contributions

The ~50 – 150 m wide metamorphic aureole at Merry Widow is dominantly comprised of skarn mineralization (garnet + clinopyroxene + sulphides + calcite), the product of decarbonated and silicified limestone. Considering a ~1 km limestone thickness, the total volume of the aureole varies from 1.1 to 3.2 km^3. For a limestone density of 2700 kg/m^3 this indicates 3.0 – 8.6 x 10^3 Tg of wallrock was decarbonated, producing ~1300 to 3800 Tg of CO_2 (Table 4.1) (Figure 4.7). This value is an order of magnitude greater than the magmatic CO_2 produced from limestone assimilation in dikes and sills (<110 Tg CO_2 – mass includes both orbicular and non-orbicular dikes) or the pluton (<55 Tg CO_2).

In addition to the metamorphic aureole, I consider CO_2 produced from reactive transport of hydrothermal fluids with minor amounts of SiO_2 (<2.5 wt.%) within the Quatsino limestone (Table B1). However, limestone collected ~300 m from the pluton margin has similar $\delta^{18}O$ values to limestone collected ~1 m from dike contacts (>19 ‰, Table C4), where no samples indicate decreased $\delta^{18}O$ values reflective of magmatic fluid infiltration ($\delta^{18}O$ ~ 5.5 – 5.9 ‰; Bindeman, 2008). I therefore consider reactive transport of hydrothermal fluids is limited or negligible.

Finally, comparing both magmatic (total ~144 – 163 Tg) and metamorphic (~1300 – 3800 Tg) CO_2 produced at Merry Widow (Table 4.1), I estimate that ~4 – 11% of crustal-derived CO_2 is produced from magma, and ~89 – 96% from contact metamorphism. Magmatic CO_2 contributions that range from 144 – 163 Tg of CO_2 are calculated from minimum (74 and <55 Tg of CO_2) and maximum (93 and <55 Tg of CO_2) contributions, respectively, in addition to 15 Tg of CO_2 from orbicular dikes. The range of crustal-derived CO_2 percentages (4 – 11%) is calculated from varying magmatic contributions (144 -163 Tg CO_2) divided by total magmatic +

metamorphic CO_2 released. For example, a minimum-crustal to maximum-metamorphic contribution would be: 144/(144+ 3800)*100 = 3.6%; whereas a maximum-crustal to minimum-metamorphic contribution would be: 163/(163+1300)*100 = 11.1% (units in equation to calculate percentages are in Tg CO_2). These figures are comparable to estimates from Ramos et al. (2020) of 13% and 87% for magmatic and metamorphic CO_2, respectively, from a distribution of skarn-marble areas and plutons in a corridor of the Sierra Nevada Batholith.

4.6.2.3 Magmatic CO_2 flux of the Bonanza arc

Volcanic and plutonic rocks of the Bonanza arc cover an areal extent of 6,200 km^2 and 11,600 km^2 respectively on Vancouver Island. Volcanic rocks are approximately 3 km in thickness, and plutonic rocks have a minimum thickness of ~16 km (Canil and Morris, 2023). These thicknesses, combined with areal extents indicates a volume of ~19,000 km^3 for volcanic rocks, and a minimum of ~190,000 km^3 for plutonic rocks. Using a basaltic density of 2900 kg/m^3, I calculate the mass of erupted (volcanic rocks) and intruded (plutonic rocks) magmas to be 5.5 x 10^7 Tg and 5.5 x 10^8 Tg, respectively. Assuming the erupted volcanic rocks were fed by dikes and sills that were 4% contaminated with 20 – 25 wt.% limestone produces 1.9 – 2.4 x 10^5 Tg CO_2 (e.g., considering 4% of 5.5 x 10^7 Tg of magma assimilates limestone, then: (0.04)(5.5 x 10^7 Tg magma) = 2.2 x 10^6 Tg of reacted magma that is 20 wt.% limestone or 9 wt.% CO_2 = 1.9 x 10^5 Tg CO_2 – Table C7). Bonanza plutonic rocks are assumed to have reacted with a range of 0.5 – 1 km limestone thicknesses, therefore amounting to a total volume of 6000 km^3 to 12,000 km^3 (e.g., a 1/16 of the total plutonic rock thickness (16 km) reacting with 1 km of limestone = (0.063 x 190,000 km^3 = ~6000 km^3)). These volumes amount to 1.7 – 3.5 x 10^7 Tg of magma. Similar to Merry Widow, I consider 0.8% of the total plutonic rock volume reacts with the 0.5 –

1 km of limestone along its contact, generating a range of 1.4 – 2.8 x 10^5 Tg of magma that has reacted with the host limestone (Table C7). Considering 20 wt.% limestone assimilation into these reacted magma masses generates 1.3 – 2.5 x 10^4 Tg CO_2 (Table C7).

Integrating these masses of magmatic crustal-derived CO_2 over the timespan of the arc (40 Myr; Canil and Morris, 2023), gives CO_2 fluxes of 4.8 – 6.1 x 10^{-3} Tg CO_2/yr from erupted volcanic rocks and 3.1 – 6.3 x 10^{-4} Tg CO_2/yr from plutons (Table 4.2, Figure 4.9). This amounts to an average of magmatic crustal-derived CO_2 of 5.5 x 10^{-3} ± 6.1 x 10^{-4} Tg CO_2/yr from volcanic rocks and 4.7 x 10^{-4} ± 1.6 x 10^{-4} Tg CO_2/yr from plutonic rocks. These magmatic fluxes over the ~40 Myr timespan of the Jurassic Bonanza arc indicate that erupted volcanic rocks, if fed by dikes and sills, are capable of producing an order of magnitude greater CO_2 in comparison to their plutonic equivalents (Figure 4.9).

In addition, mantle-derived CO_2 needs to be considered when estimating arc fluxes, as it ultimately contributes to the total CO_2 fluxed. To do so, I use a range of conservative (0.3 wt.% – Wallace, 2005) and liberal (1.5 wt.% – Blundy et al., 2010) initial magma CO_2 contents. Considering these CO_2 wt.% ranges within Bonanza arc magma volumes (volcanic rocks ~19,000 km^3, plutonic rocks ~190,000 km^3) converted to magma masses that erupt or stall over the 40 Myrs timespan of the arc produces 0.05 to 0.23 Tg CO_2/yr (e.g., total magma volume = 19,000 km^3 + 190,000 km^3 = 209,000 km^3; considering 2900 kg/m^3 density gives 6.06 x 10^8 Tg magma with 0.3 – 1.5 wt.% CO_2; Table C7). From these values, a calculated average of mantle-derived CO_2 flux is 0.14 ± 0.09 Tg CO_2/yr. These mantle-derived flux rates indicate notably higher contributions than what may be possible from magma-carbonate interactions (Table 4.2, Figure 4.9).

Lithologic Unit	Unit Volume	Volume reacted/assimilated	Limestone assimilated	CO_2 flux	CO_2 transport media
	(km^3)	*(%)*	*(wt.%)*	*(Tg CO_2/yr)*	
plutonic rocks	~6000 – 12000*	< 1	20	**3.1 – 6.3 x 10^{-4}**	magma
volcanic rocks	~19,000	< 4	20	**4.8 – 6.1 x 10^{-3}**	magma
skarn	~50 – 275	100	n/a	**1.5 – 8.1 x 10^{-3}**	metamorphic fluids
mantle-derived	~209,000	n/a	n/a	**0.05 – 0.23**	magma
TOTAL	--	--	--	**0.05 – 0.24**	magma & fluids

Table 4.2: *CO_2 flux (Tg/yr) of Bonanza arc lithologies + mantle-derived CO_2 contributions*
**Note that although total volume of plutonic rocks is ~190,000 km^3, only 0.5 – 1 km of the 16 km plutonic rock thickness is considered to interact with the Quatsino limestone. Calculations for CO_2 flux provided in Table C7.*

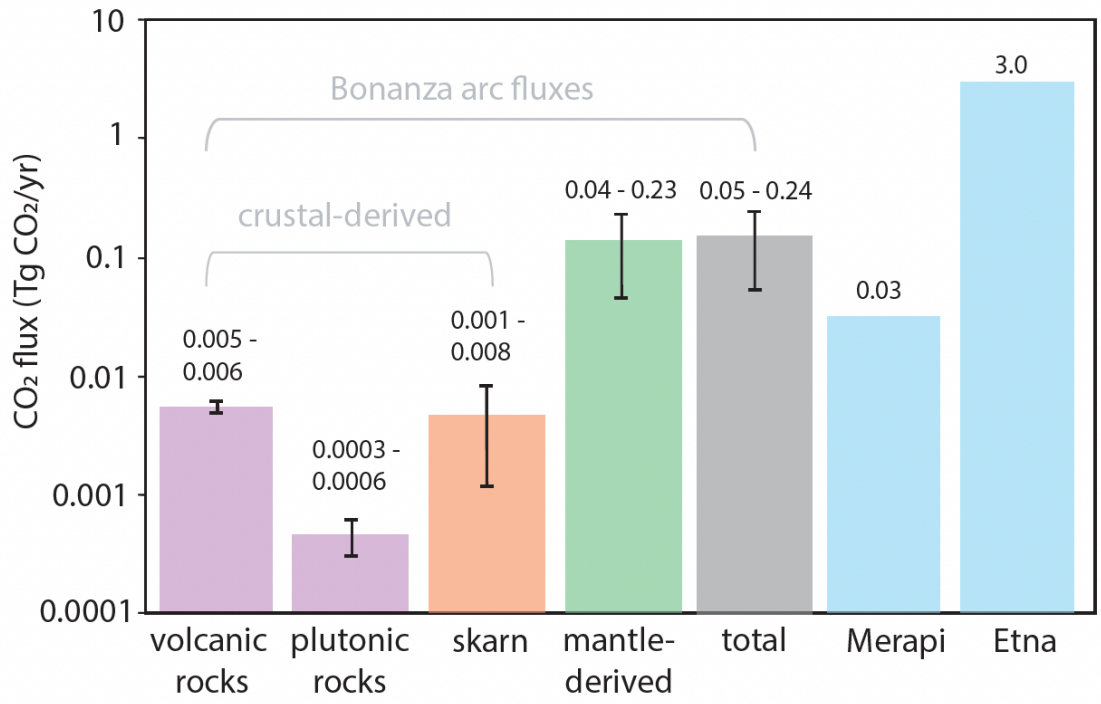

Figure 4.9: CO_2 flux (Tg/yr) from Jurassic Bonanza arc units over the ~40 Myr arc timespan, which includes crustal-derived magmatic CO_2 (volcanic and plutonic rocks) and metamorphic CO_2 (skarn). Erupted volcanic rocks make up ~3 km in thickness, and are assumed to be fed by dikes and sills that are up to 4% contaminated with limestone from interactions at depth, where reacted margins are generally <2 cm within 1 – 2 m wide dikes and sills (Chapter 3). Plutonic rocks show any potential of a reacted margin is limited to the outermost 10 m of the pluton margin, amounting to <1% of the total pluton volume that may have assimilated limestone (Chapter 4). In addition, plutons are considered to have only interacted with a range of 0.5 – 1 km limestone thickness. Metamorphic CO_2 flux from magma-carbonate interactions is indicated by skarn production (wallrock decarbonation). Mantle-derived CO_2 flux for the Bonanza arc is calculated based on a range of conservative (0.3 wt.% – Wallace, 2005) to liberal (1.5 wt.% – Blundy et al., 2010) values. Total CO_2 arc flux of the Bonanza arc indicates most CO_2 contributions are mantle-derived (grey column). A comparison of fluxes from arc volcanoes (Merapi, Etna) that intersect crustal carbonates is also show, based on fluxes compiled by Auippa et al. (2019), which includes both crustal-derived and mantle-derived CO_2. Flux ranges are based on calculations provided in Table C7, and summarized in Table 4.2. Note the y-axis in log scale.

4.6.2.4 Metamorphic CO_2 flux of the Bonanza arc

Finally, to quantify all CO_2 produced from an arc system, I consider the metamorphic CO_2 flux in addition to the magmatic flux. To estimate a metamorphic CO_2 flux produced over the 40 Myr Bonanza arc timespan, I use the current areal extent of the Quatsino limestone on Vancouver Island, in addition to the volume of limestone decarbonized, mineralized and converted to skarn. To estimate the total volume of skarn produced from an original limestone volume, I compare the volume of the skarn produced at Merry Widow (1.1 – 3.2 km^3) to the unreacted volume of limestone remaining (40.5 km^3), giving an original total estimate of 41.6 – 43.7 km^3 of limestone at Merry Widow. Therefore, ~3 – 8% of the original limestone was decarbonized during magma emplacement and metamorphism. I use these estimates for calculating skarn production within the Bonanza arc.

Using an aerial extent of ~3150 km^2, and a range of Quatsino limestone thickness of 0.5 – 1 km, I estimate 3 – 8% of an original volume (~1600 to 3400 km^3) of limestone was decarbonized to produce 49 to 274 km^3 of decarbonated rock now preserved as skarn mineralization within the Bonanza arc. This indicates 1.3 – 7.4 x 10^5 Tg of limestone was decarbonized ± mineralized (assuming 2700 kg/m^3 density), and capable of producing 5.8 x 10^4 to 3.3 x 10^5 Tg of CO_2 (considering limestone decarbonates and produces 44 wt.% CO_2). Integrating this metamorphic CO_2 over the 40 Myr timespan of the arc produces a flux of 1.5 to 8.1 x 10^{-3} Tg CO_2/yr , or an average of 4.8 x 10^{-3} ± 3.3 x 10-3 Tg CO_2/yr (Table 4.2, Figure 4.9). Because reactive transport of fluids with trace amounts (<2.5 wt.%) of SiO_2 in the Quatsino limestone is negligible at Merry Widow, where $\delta^{18}O$ carbonate values do not reflect infiltration of magmatic fluids, I do not consider it as a notable source of CO_2 flux from the Bonanza arc.

Finally, when considering all CO_2 fluxes together: 1) crustal-derived magmatic CO_2 (5.5 – 6.4 x 10^{-3} Tg CO_2/yr); 2) crustal-derived metamorphic CO_2 (1.5 to 8.1 x 10^{-3} Tg CO_2/yr); and 3) mantle-derived CO_2 (0.04 – 0.23 CO_2/yr) produces a total CO_2 flux from the Bonanza arc of 0.05 to 0.24 Tg CO_2/yr (Table 4.2, Figure 4.9). This work quantifies the limited contributions of crustal-derived CO_2, whether magmatic (via assimilation) or metamorphic and highlights that most of the CO_2 fluxed from the Jurassic Bonanza arc would have been mantle-derived.

4.6.3 The validity of carbonate assimilation in 'transcrustal' arc magma systems

The magmatic and metamorphic fluxes for an entire section of the Bonanza arc are lower than some singular modern arc volcanoes built upon crustal carbonates (Etna, Popocatépetl) yet higher than others (Merapi) (Goff et al., 2001; Iacono-Marziano et al., 2009; Auippa et al., 2019, Deegan et al., 2023) and only once mantle-derived CO_2 is considered (Table 4.2, Figure 4.9). The Bonanza arc however, has a much thinner arc crustal section (~ 21 km – Canil and Morris, 2023), with 1 km of carbonate in the crustal stratigraphy, compared to notably greater thickness of carbonate-rich strata beneath these modern volcanoes: ~3 km beneath Popocatépetl in the Trans Mexico Volcanic Belt (Goff et al., 2001), and ~5 – 8 km beneath the Campanian arc in Italy (Iacono-Marziano et al., 2009). A minimum of 0.65 km of limestone beneath Merapi perhaps makes flux estimates for the Bonanza arc more comparable, but sedimentary units within the Central Javan volcanic arc can reach much greater thicknesses of up to 8 – 11 km (Deegan et al., 2023 and references within), so a greater flux is to be expected. Ultimately the thickness of the carbonate that is intruded by plutons is important for how much metamorphic crustal-derived CO_2 is produced, however reasonable depths of reaction need to be considered. Less important is

the thickness of the erupted volcanic strata, which is typically limited to depths of <5 km in thickness at active (Suyehiro et al., 1996) and extinct (Morris et al., 2019) arcs.

Based on these modern volcanoes, and consideration of plutonic rock volumes in ancient arc systems, previous studies have suggested that carbonate-rich lithologies throughout thick (>35 km) arc crust, can be '*vertically extensive, occurring from subvolcanic to uppermost mantle paleodepths'* (Lee and Lackey, 2015), and that intruding magmas could assimilate carbonates throughout the crust to produce enough CO_2 to have driven past greenhouse climates, such as during the Cretaceous (Lee et al., 2013). Consideration of experimental data, however, would suggest that carbonate assimilation is more muted at greater depths in the arc crust. Basalt-carbonate experiments by Carter and Dasgupta (2015) confirm far more carbonate dissolution into silicate melts at lower pressures is capable for a given temperature (Figure 4.10). Other low-pressure (≤ 0.5 GPa) hydrous basalt-limestone reaction experiments at similar temperatures (1050 to 1300°C), as summarized in Chapter 2 (c.f. Figure 2.12), further confirms this trend in carbonate assimilation (Iacono-Marziano et al., 2007, 2008; Freda et al., 2008; Deegan et al., 2010; Mollo et al., 2010). This is an outcome of the pressure dependence of the reaction:

$$CaCO_{3(s)} + SiO_{2(l)} = CaSiO_{3(l)} + CO_{2(g)}$$

In contrast to previous work, this study shows a general lack of carbonate assimilation into stalled arc magma bodies, now preserved as plutons, with only a marginal veneer of the pluton (<1% volume) assimilating at most 20 wt.% of limestone. Slightly more (<4%) assimilation is observed for magma transported in channels (dikes, sills) in the same setting. I therefore suggest that previous considerations of transcrustal assimilation of carbonate into arc magmas may have over-estimated the true volume of plutons interacting with wallrock, where

mid- to lower-crustal carbonates (>0.5 GPa), even at higher temperatures, are not likely significant contributors to crustal-derived CO_2.

From this work, I surmise that active arc volcanoes that intersect carbonate in their substrate with crustal-like C and He isotopic signatures in emitted volcanic gases (i.e., Italy, Indonesia – Mason et al., 2017) are dominantly emitting CO_2 gas produced from metamorphic decarbonation, not by carbonate assimilation. This crustal-derived metamorphic CO_2 would be readily degassed from vents, fumaroles, and hot springs, similar to where gas samples are collected (Mason et al. 2017). Both my estimate and estimates from Ramos et al. (2020) of metamorphic crustal-derived CO_2 from decarbonation in the aureole (>89% and 87%, respectively) support this interpretation.

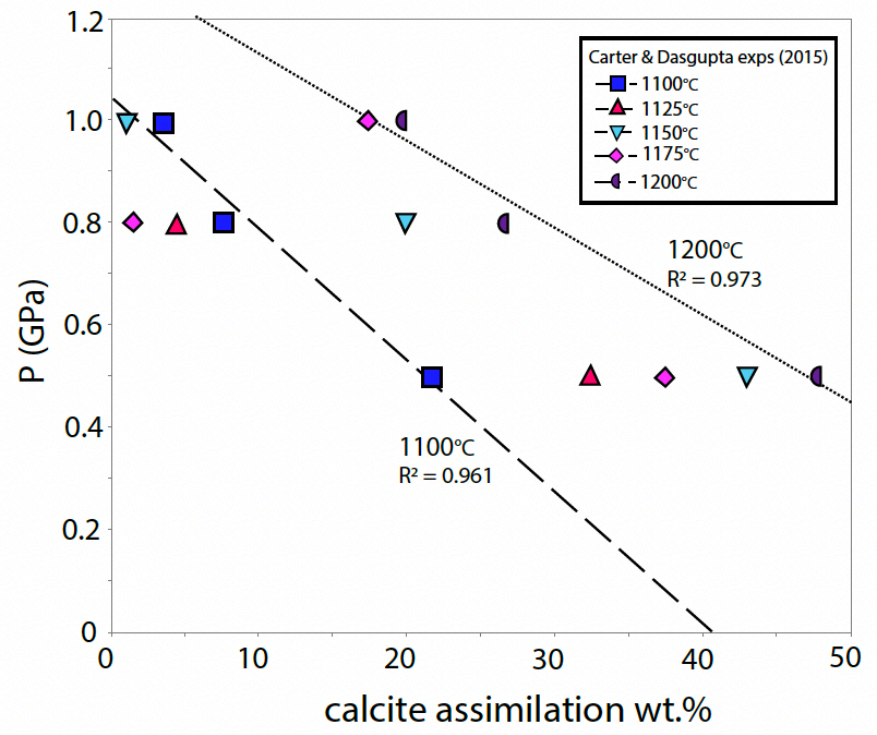

Figure 4.10: Pressure versus percent of calcite assimilated from basalt-carbonate experiments by Carter and Dasgupta (2015) at varying pressures (0.5 – 1 GPa) and temperatures (1100°C – 1200°C), which displays greater calcite assimilation at lower pressure and higher temperatures. Assimilation % is calculated based on calcite remaining versus initial calcite prior to experiments.

4.7 Conclusions

I demonstrate in a detailed field study of a gabbro pluton within the Jurassic Bonanza arc, that only a <2 m chilled margin shows any detectable limestone assimilation from enriched bulk U, Sr, and $^{87}Sr/^{86}Sr$ values. Geochemical modeling of carbonate assimilation and concurrent fractional crystallization suggests that 20 wt.% limestone was assimilated, but only into a reacted margin (<1% of total pluton volume).

A detailed comparison of magma-carbonate reaction within magmas from this study (pluton) and previous work on dikes and sills, shows the latter are more efficient (up to 4% magma reacted) versus a pluton (<1% magma reacted). These estimates indicate that crustal-derived magmatic CO_2 is small, less than 11% of that produced by metamorphism through decarbonized wallrock (now skarn). I therefore surmise that CO_2 outgassed at active arcs with crustal-like signatures (C, He) is dominantly (>89%) metamorphic and produced from wallrock decarbonation.

I extrapolate the CO_2 produced from these magma-carbonate interactions at Merry Widow and calculate CO_2 fluxes from magma-carbonate interactions for the entire Jurassic Bonanza arc that is orders of magnitude smaller than present-day CO_2 fluxes from some singular arc volcanoes intersecting carbonate-rich lithologies (i.e., Etna, Popocatépetl), and only comparable when mantle-derived CO_2 contributions are considered. My lower estimates compared to active systems may be due to thinner (<1 km) carbonate sequences in the Bonanza arc crustal substrate. However, I caution that historical fluxes from magma-carbonate interactions were likely over-estimated, where entire magma chambers do not assimilate a consistent mass fraction of carbonate wallrock. Assimilation into stalled magma bodies in thick transcrustal sections is also restricted to shallow depth. My results provide realistic and quantitative limits on arc-derived CO_2 from upper crustal wallrock sources.

Chapter 5
Conclusions

5.1 Research overview and significance

This dissertation documents the findings from multiple research projects that tested limestone assimilation limits into various scales of arc magma bodies, using a detailed field approached from the Jurassic Bonanza arc, on Vancouver Island, Canada.. Here, I briefly summarize these chapters individually.

In Chapter 2, orbicular dikes display unique textures, mineralogy, and geochemistry that suggest a reaction of basalt with limestone at depths, where two melts (orbicule and host melt) with different viscosities that are not in equilibrium with one another were preserved from rapid cooling. Major and trace element modeling shows orbicular compositions are obtained from binary mixing of 3 – 25% limestone into arc basalt, and that orbicule compositions are similar to hybrid melts formed from low pressure (<0.5 GPa) basalt-limestone reactions in experiments by others. My results from geochemical modeling and comparison to experiments indicates that orbicular dikes are capable of producing >11 wt.% CO_2. Contributions from these dikes estimates a liberal CO_2 flux of Bonanza arc magmas (plutonic + volcanic rock volumes) of up to 1.16 Tg of CO_2/year. Based on subsequent work, this estimate is likely over-estimated, where as mentioned in the proceeding Chapter 4, entire pluton volumes do not react with wallrock lithologies.

Motivated by the orbicular dikes, which indicated that small m-scale intrusions may be significant CO_2 produces in arc systems, I further looked in detail at the contacts of basalt dikes and sills with limestone, and is the work documented in Chapter 3. My detailed examination of basalt-limestone contacts indicates reacted margins (boundary melts) are produced in localized

magmatic margins of dikes and sills, that are distinctly different in colour, texture, and chemistry from more interior melts. Perhaps the most notable and unexpected findings from this work was that boundary melts produce element enrichments above igneous and wallrock values (Sr). A more macro-scale of this work also compared bulk rock margin to interior geochemistry, which showed anomalous Sr enrichments within both dike and sill interiors, far above igneous values (up to 5500 ppm Sr in a basaltic sill). Processes such as uphill diffusion and meltback along channel walls from replenishing melt sources may have driven these extreme enrichments. Nonetheless, the goal of this study was to quantify CO_2 production at basalt-limestone contacts, and from geochemically modeling I determined that assimilation of ~20 – 25 wt.% limestone into basalt (likely a minimum) can produce the boundary melts that account for up to 4% of the dike and sill volumes.

Finally, in the last chapter of this dissertation, I focus on constraining limestone assimilation in plutons, as historical estimates of arc CO_2 flux rates has largely considered plutons (and batholiths) to be the drivers of carbonate assimilation and ultimately the CO_2 producers that may have driven greenhouse events in Earth's history. My work documents a detailed view from drillcore and exposed outcrops of a pluton margin, now in contact with a substantial metamorphic aureole (~50 – 150 m wide). From this study, petrography, and geochemistry of both bulk rock and mineral phases indicates any limestone assimilation must be limited to a thin veneer of the pluton (<10 m wide), where there is no indication of reaction with enriched crustal sources 10 – 1100 m from the margin. In fact, only a <2 m margin shows any indication of limestone assimilation, and similar to dikes and sills – up to 20% limestone, but a lack of data from 2 – 10 m permits me to conclude that the extent of the reacted pluton margin must be <10 m. Nonetheless, a reacted margin of 2 or 10 m wide indicates that limestone

assimilation within these systems is extremely localized, and accounts for <1% of the total pluton volume. This work suggests that historical estimates which considered >10% assimilation of carbonate-rich lithologies into entire plutons that ultimately drove greenhouse events is unlikely. In addition, I again highlighted how former experimental work (by others) implies that reactions into plutons are limited at high P (>0.5 GPa), such as in the mid- to lower-crust where plutonic rocks dominate.

In the final sections of Chapter 4, I calculate CO_2 production from the various magmatic sources at my field site and conclude that dikes and sills are more efficient at assimilating limestone along channel margins, where the surface area of magma within smaller m-scale tabular bodies is greater. In addition, to provide a holistic view of CO_2 production from plutons that intrude carbonate, I calculated a CO_2 production from wallrock decarbonation within the aureole, and find that metamorphic CO_2 dominates (>89% CO_2 produced) over magmatic CO_2 (<11% CO_2 produced) in these systems. This indicates that enriched $\delta^{13}C$ CO_2 from arcs built on carbonate platforms today is likely sourced from metamorphic decarbonation within the wallrock. Extrapolated estimates used to calculate Bonanza arc crustal-derived CO_2 flux shows lower estimates than fluxes from some active arc volcanoes today (i.e., Etna, Popocatépetl), which may be due to a much thinner (<1 km) carbonate source with the Bonanza arc crust.

5.2 Future research directions

The work presented in this dissertation provides a detailed analyses that is focused on a particular area of magma-carbonate reactions within arc crust, yet much work is still needed to understand the processes and variabilities within these complex interactions and settings. For example, the work in this thesis is focused on a well-constrained field approach of limestone assimilation into basalt. Because of this, my study is limited to the compositions that occur within my field setting, which are tholeiitic arc basalts and their gabbroic plutonic equivalent – which represent my magma compositions, and nearly pure limestone as my assimilant – which represents my wallrock compositions. One of the advantages to the work I have done is that I use simple compositions (basalt + limestone) to document reactions extents, however compositions in both the magma and carbonate can vary greatly. Experiments by Carter and Dasgupta (2016) indicate limestone assimilation into more evolved compositions (andesite) may be just as effective as basalt, but drastically drops towards dacitic compositions. Carter and Dasgupta (2018) also performed experiments on the decarbonation of limestone versus dolostone into basalt and dacite, and document that dolostone reacts more readily than limestone, however experimental data on this is limited to only two experiments at mid-crustal pressures (1000°C and 1150°C, both at 0.5 GPa). Because experimental data (i.e., from Carter and Dasgupta, 2015) indicates that reactions progress at low pressure (<0.5 GPa), it would be beneficial to test mafic-carbonate systems with varying carbonate compositions, mimicking the dominantly mafic dikes and sills that transit the shallow crust (<5 km). Testing the effect of carbonate composition would also be useful from a field approach, where if increased dolostone assimilation into magma occurs should we then infer that contact aureole of plutons in dolostone to be larger and wider?

Continuing on the subject of metamorphic versus magmatic CO_2 production within these systems, it is likely – based on the results from my work and as indicated in the dissertation text – that most of the enriched $\delta^{13}C$ gas emitted at active arcs built on carbonate substrate are sourced from decarbonation in the wallrock, or metamorphically. One outstanding question however is – how well do we know that lower $^3He/^4He$ with enriched $\delta^{13}C$ values is indicative of crustal-derived C sources? Are there any cases in which enriched C carried into subductions zone on the slab can flux CO_2 with an enriched crustal-like signature (for C, He)? For example, in two recent papers (Plank and Manning, 2019; Lopez et al., 2023) do not correlate enriched outgassed CO_2 with $\delta^{13}C$ ~0‰ with crustal carbonate in the overlying plate, but instead potentially from altered oceanic crust (AOC) (c.f. Figure 2a in Plank and Manning, 2019; Figure 3a in Lopez et al., 2023). In addition, what C and He signatures might we see for pelagic sediments decarbonized from the slab? Future proxies that better constrain slab- versus crustal-derived carbonate sources are necessary for understanding this, and would have further implications on the global C cycle.

Finally, I suggest focused studies (likely experimental) to inform on how metals might enrich within reacted magmas in these shallow magma-carbonate systems. Although localized to magmatic margins, we do not fully understand the partitioning of elements into these unique Ca-rich and Si-poor magmas. In addition, if wallrock lithologies are more enriched in certain elements and components (i.e., Sr, U) in comparison to their intruding magma, might we use wallrock compositions to further inform on metal enrichment potential in intruding melts.

Bibliography

Ague, J., and Nicolescu, S. (2014), Carbon dioxide released from subduction zones by fluid-mediated reactions: *Nature Geoscience*, 7, p. 355-360. https://doi.org/10.1038/ngeo2143

Andrew, A., Armstrong, R.L., and Runkle, D. (1991), Neodynium-strontium-lead isotope study of Vancouver Island igneous rocks: *Canadian Journal of Earth Science*, 28, p. 1744-1752. https://doi.org/10.1139/e91-156

Auippa, A., Fischer, T.P., Plank, T., Robidoux, P., Di Napoli, R. (2017), Along-arc, inter-arc and arc-to-arc variations in volcanic gas CO_2/S_T ratios reveal dual source of carbon in arc volcanism: *Earth-Science Reviews:* 68, p. 24 – 47. https://doi.org/10.1016/j.earscirev.2017.03.005

Auippa, A., Fischer, T.P., Plank, T., Bani, P. (2019), CO_2 flux emissions from the Earth's most actively degassing volcanoes, 2005 – 2015: *Scientific Reports*, 9, p. 1 – 19. https://doi.org/10.1038/s41598-019-41901-y

Barnes, C.G., Prestvik, T., Barnes, M.A.W., Anthony, E.Y., and Allen, C.M. (2003), Geology of a magma transfer zone: the Hortavær Igneous Complex, north-central Norway: *Norwegian Journal of Geology*, 83, p. 187–208.

Barnes, C.G., Prestivik, T., Sundvoll, B., and Surratt, D. (2005), Pervasive assimilation of carbonate and silicate rocks in the Hortavær igneous complex, north-central Norway: *Lithos*, 80, p. 179–199, https://doi.org/10.1016/j.lithos.2003.11.002

Barnes, C.G., Prestvik, T., Li, Y., McCulloch, L., Yoshinobu, A.S., and Frost, C.D. (2009), Growth and zoning of the Hortavær intrusive complex, a layered alkaline pluton in the Norwegian Caledonides: *Geosphere*, 5, p. 286–301, https://doi.org/10.1130/GES00210.1

Berner, R.A. (1991), A model for atmospheric CO_2 over Phanerozoic time: *American Journal of Science*, 291, p. 339 – 376.

Berner, R.A. (2004), The Phanerozoic carbon cycle: CO_2 and O_2. Oxford University Press, New York.

Bindeman, I. (2008), Oxygen isotopes in mantle and crustal magmas as revealed by single crystal analysis, Mineralogical Society of America, *Reviews in Mineralogy & Geochemistry*, 69, p. 445-478.

Blundy, J., Cashman, K.V., Rust, A., and Witham, F. (2010), A case for CO_2-rich arc magmas, *Earth and Planetary Science Letters*, 290(3-4), p. 289 – 301. https://doi.org/10.1016/j.epsl.2009.12.013

Blythe, L.S., Deegan, F.M., Freda, C., Jolis, E.M., Masotta, M., Misiti, V., Taddeucci, J., and Troll, V.R. (2015), CO_2 bubble generation and migration during magma-carbonate interaction. *Contributions to Mineralogy and Petrology*, 169, https://doi.org/10.1007/s00410-015-1137-4

Brooker, R.A., and Kjarsgaard, B.A. (2011), Silicate-carbonate liquid immiscibility and phase relations in the system SiO_2-Na_2O-Al_2O_3-CaO-CO_2 at 0.1 – 2.5 GPa with applications to carbonatite genesis. *Journal of Petrology*, 52, p. 1281 – 1305. https://doi.org/10.1093/petrology/egq081

British Columbia Geological Survey, (2021), MapPlace GIS internet mapping systems; British Columbia Ministry of Energy, Mines and Petroleum Resources. http://www.MapPlace.ca

British Columbia Geological Survey (BCGS), (2023a), MapPlace GIS internet mapping systems. British Columbia Ministry of Energy, Mines and Petroleum Resources. http://www.MapPlace.ca

British Columbia Geological Survey (BCGS), (2023b), MINFILE Mineral Inventory. British Columbia Ministry of Energy, Mines and Petroleum Resources. http://minfile.gov.bc.ca

Bruce, P.M., and Huppert, H.E. (1989), Thermal controls of basaltic fissure eruptions: *Nature*, 342, p. 665-667, https://doi.org/10.1038/342665a0

Brune, S., Williams, S.E. and Müller, R.D. (2017), Potential links between continental rifting, CO_2 degassing and climate change through time. *Nature Geoscience*, 10, 941–946. https://doi.org/10.1038/s41561-017-0003-6

Busby, C., Fackler-Adams, B., Mattison, J., Deoreo, S. (2006), View of an intact oceanic arc, from surficial to mesozonal levels: Cretaceouos Alisitos Arc, Baja California: *Journal of Volcanology and Geothermal Research*, 149, p. 1 – 46. https://doi.org/10.1016/j.jvolgeores.2005.06.009

Canil, D., Styan, J., Larocque, J., Bonnet, E., and Kyba, J. (2010), Thickness and composition of the Bonanza arc crustal section, Vancouver Island, Canada. *Geological Society of America Bulletin,* 122, p. 1094-1105. https://doi.org/10.1130/B26578.1

Canil, D., Johnston, S.T., Larocque, J.P., Friedman, R., and Heaman, L. (2013), Age, construction and exhumation of intermediate mid-crust of the Jurassic Bonanza arc, Vancouver Island, Canada: *Lithosphere,* 5, p. 92-97. https://doi.org/10.1130/L225.1

Canil, D., and Morris R,A. (2023), Continentalization of an intraoceanic arc as exemplified by the Jurassic Bonanza arc of Vancouver Island, Canada: *Geological Society of America Bulletin*, https://doi.org/10.1130/B36716.1

Cao, W., Lee, C.-T.A., and Lackey, J.S. (2017), Episodic nature of continental arc activity since 750 Ma: A global compilation: *Earth and Planetary Science Letters*, 461, p. 85–95. https://doi.org/10.1016/j.epsl.2016.12.044

Caldiera, K., and Rampino, M.R. (1990) Carbon dioxide emissions from Deccan Volcanism and a K/T boundary Greenhouse Effect: Geophysical Research Letters, 17, https://doi.org/10.1029/GL017i009p01299

Caricchi, L., Sheldrake, T.E., and Blundy, J. (2018), Modulation of magmatic processes by CO_2 flushing. *Earth and Planetary Science Letters*, 491, p. 160-171. https://doi.org/10.1016/j.epsl.2018.03.042

Caricchi, L., Townsend, M., Rivalta, and Namiki, A. (2021), The build-up and triggers of volcanic eruption: *Nature Reviews Earth & Environment*, 2, p. 458 – 476, https://doi.org/10.1038/s43017-021-00174-8

Carter, L.B., and Dasgupta, R. (2015), Hydrous basalt–limestone interaction at crustal conditions: implications for generation of ultracalcic melts and outflux of CO_2 at volcanic arcs: *Earth and Planetary Science Letters*, 427, p. 202–214, https://doi.org/10.1016/j.epsl.2015.06.053

Carter, L.B., and Dasgupta, R. (2016), Effect of melt composition on crustal carbonate assimilation: Implications for the transition from calcite consumption to skarnification and associated CO_2 degassing: *Geochemistry, Geophysics, Geosystem*, 17, p. 3893 – 3916, https://doi.org/10.1002/2016GC006444

Carter, L.B, and Dasgupta, R. (2018), Decarbonation in the Ca-Mg-Fe carbonate system at mid-crustal pressure as a function of temperature and assimilation with arc magmas – Implications for long-term climate: *Chemical Geology*, 492, p. 30 -48. https://doi.org/10.1016/j.chemgeo.2018.05.024

Chadwick, J.P., Troll, V.R., Ginibre, C., Morgan, D., Gertisser, R., Waight, T.E., and Davidson, J.P. (2007), Carbonate assimilation at Merapi Volcano, Java, Indonesia: Insights from

crystal isotope stratigraphy: *Journal of Petrology*, 48, p.1793–1812, https://doi.org/10.1093/petrology/egm038

Charlier, B., and Grove, T.L. (2012), Experiments on liquid immiscibility along tholeiitic liquid lines of descent. *Contributions to Mineralogy and Petrology*, 164, p. 27 – 44. https://doi.org/10.1007/s00410-012-0723-y

Chen, C., Förster, M.W., Foley, S.F. and Shcheka, S.S. (2023), Carbonate-rich crust subduction drives the deep carbon and chlorine cycles: *Nature,* 620, p. 576–581. https://doi.org/10.1038/s41586-023-06211-4

Coogan, L.A., Daëron, M., and Gillis, K.M. (2019), Seafloor weathering and the oxygen isotope ratio in seawater: Insight from whole-rock $\delta^{18}O$ and carbonate $\delta^{18}O$ and Δ_{47} from the Troodos ophiolite. *Earth and Planetary Science Letters,* 508, 41 – 50. https://doi.org/10.1016/j.epsl.2018.12.014

D'Souza, R.J., Canil, D., and Creaser, R. (2016), Assimilation, differentiation, and thickening during the formation of arc crust in space and time: the Jurassic Bonanza arc, Vancouver Island, Canada: *Geological Society of America Bulletin,* 128, p. 543–557, https://doi.org/10.1130/B31289.1

Dasgupta, R., and Hirschmann, M.M. (2010), The deep carbon cycle and melting in Earth's interior: Earth and Planetary Science Letters, 298, p. 1–13.

DeBari, S.M., Anderson, R.G., and Mortensen, J.K. (1999), Correlation among lower to upper crustal components in an island arc: the Jurassic Bonanza arc, Vancouver Island, Canada: *Canadian Journal of Earth Sciences*, 36, p. 1371–1413, https://doi.org/10.1139/e99-029

Deegan, F.M., Troll, V.R., Freda, C., Misiti, V., Chadwick, J.P., McLeod, C.L., and Davidson, J.P. (2010), Magma–carbonate interaction processes and associated CO_2 release at Merapi

volcano, Indonesia: insights from experimental petrology: *Journal of Petrology*, 51, p. 1027–1051, https://doi.org/10.1093/petrology/egq010

Deegan, F.M., Whitehouse, M.J., Troll, V.R., Geiger, H., Jeon, H., le Roux, P., Harris, C., van Helden, M., and González-Maurel, O. (2021), Sunda arc mantle source $\delta^{18}O$ value revealed by intracrystal isotope analysis*: Nature Communications*, 12, https://doi.org/10.1038/s41467-021-24143-3

Deegan, F.M., Troll, V.R., Gertisser, R., and Freda, C. (2023), Magma-Carbonate Interaction at Merapi Volcano, Indonesia, *in* Gertisser, R., Troll, V.R., Walter, T.R., Nandaka, I.G.M.A., and Ratdomopurbo, A., eds., Merapi Volcano: Geology, eruptive activity, and monitoring of a high-risk volcano. Active Volcanoes of the World. Springer, p. 291 – 321, https://doi.org/10.1007/978-3-031-15040-1_10

Del Moro, A., Fulignati, P., Marianelli, P., and Sbrana, A. (2001), Magma contamination by direct wall rock interaction: constraints from xenoliths from the walls of a carbonate-hosted magma chamber (Vesuvius 1944 eruption): *Journal of Volcanology and Geothermal Research,* 112, p. 15–24. https://doi.org/10.1016/s0377-0273(01)00231-1

DePaolo, D.J. (1981), Trace element and isotopic effects of combined wallrock assimilation and fractional crystallization: *Earth and Planetary Science Letters,* 53(2), p. 189-202. https://doi.org/10.1016/0012-821X(81)90153-9

Dufek, J., and Bachmann, O. (2010), Quantum magmatism: Magmatic compositional gaps generated by melt-crystal dynamics: *Geology,* 38(8), p. 687-690, https://doi.org/10.1130/G30831.1

Dyer, B., Lee, C.-T.A., Leeman, W.P., and Tice, M. (2011), Open-system Behavior during Pluton–Wall-rock Interaction as Constrained from a Study of Endoskarns in the Sierra Nevada Batholith, California: *Journal of Petrology*, 52, p. 1987 – 2008. https://doi.org/10.1093/petrology/egr037

Edmonds, M., Tutolo, B., Iacovino, K., and Moussallam, Y. (2020), Magmatic carbon outgassing and uptake of CO_2 by alkaline waters: *American Mineralogist*, 105, p. 28 – 34. https://doi.org/10.2138/am-2020-6986CCBY

Eggins, S.M., Woodhead, J.D., Kinsley, L.P.J., Mortimer, G.E., Sylvester, P., McCulloch, M.T., Hergt, J.M., and Handler, M.R. (1997), A simple method for the precise determination of ≥ 40 trace elements in geological samples by ICPMS using enriched isotope internal standardisation: *Chemical Geology*, 134, p. 311-326. https://doi.org/10.1016/S0009-2541(96)00100-3

Faure, G. (1998), Principles and applications of geochemistry: a comprehensive textbook for geology students: Prentice Hall-Inc., 600 p.

Fecova, K. (2009), *Conuma River and Leagh Creek intrusive complexes: Windows into mid-crustal levels of the Jurassic Bonanza arc, Vancouver Island, British Columbia.* (Masters thesis), Simon Fraser University

Freda, C., Gaeta, M., Misiti, V., Mollo, S., Dolfi, D., Scarlato, P. (2008), Magma–carbonate interaction: an experimental study on ultrapotassic rocks from Alban Hills (Central Italy): Lithos, 101, p. 397–415, https://doi.org/10.1016/j.lithos.2007.08.008

Fulignati, P., Marianelli, P., Santacroce, R., and Sbrana, A. (2004), Probing the Vesuvius magma chamber-host rock interface through xenoliths: *Geological Magazine*, 141, p. 417 – 428. https://doi.org/10.1017/s0016756804009392

Galvez, M.E., and Pubellier, M. (2019), How do subduction zones regulate the carbon cycle? In: Deep Carbon textbook, Chapter 10, p. 276 – 312.

Ganino, C., Arndt, A.T., Zhou, MF., Gaillard, F., and Chauvel, C. (2008), Interaction of magma with sedimentary wall rock and magnetite ore genesis in the Panzhihua mafic intrusion SW China: *Mineralium Deposita,* 43, 677-694. https://doi.org/10.1007/s00126-008-0191-5

Ghiorso, M.S., and Gualda, G.A.R. (2015), An H_2O–CO_2 mixed fluid saturation model compatible with rhyolite-MELTS: *Contributions to Mineralogy and Petrology*, 169, p. 1-30. https://doi.org/10.1007/s00410-015-1141-8

Giordano, D., Russell, J.K., and Dingwell, D.B. (2008), Viscosity of magmatic liquids: a model: *Earth and Planetary Science Letters*, 271, p. 123–134, https://doi.org/10.1016/j.epsl.2008.03.038

Glazner, A.F. (2021), Thermal constraints on the longevity, depth, and vertical extent of magmatic systems: *Geochemistry Geophysics, Geosystems. 22*, e2020GC009459. https://doi.org/10.1029/2020GC009459

Glazner, A.F., and Bartley, J.M. (2006), Is stoping a volumetrically significant pluton emplacement process? GSA Bulletin, 118 (9/10), p. 1185 – 1195.

Goff, F., Love, S.P., Warren, R.G., Counce, D., Obenholzner, J., Siebe, C., & Schmidt, S.C., (2001), Passive infrared remote sensing evidence for large, intermittent CO_2 emissions at Popocatépetl volcano, Mexico: *Chemical Geology,* 177 (1–2), p. 133-156.

Gonzalez, C.M., Gorczyk, W., and Gerya, T. (2015), Decarbonation of subducting slabs : insight from thermomechanical-petrological numerical modelling: *Gondwana Research*, 17, p. 314 – 332. https://doi.org/10.1016/j.gr.2015.07.011

González-Garcia, D., Petrelli, M., Behrens, H., Vetere, F., Fischer, L.A., Morgavi, D., and Perugini, D. (2018), Diffusive exchange of trace elements between alkaline melts: Implications for element fractionation and timescale estimations during magma mixing:

Geochimica et Cosmochimica Acta, 233, p. 95 – 114. https://doi.org/10.1016/j.gca.2018.05.003

Hayes, J.M., and Waldbauer, J.R. (2006), The carbon cycle and associated redox processes through time: Philosophical Transactions B of the Royal Society, 1470, p. 931 – 950.

Heinonen, J.S., Iles, K.A., Heinonen, A., Fred, R., Virtanen, V.J., Bohrson, W.A. and Spera, F.J. (2021), From binary mixing to magma chamber simulator: In crustal magmatic system evolution (eds M. Masotta, C. Beier and S. Mollo). https://doi.org/10.1002/9781119564485.ch7

Iacono-Marziano, G., Gaillard, F., and Pichavant, M. (2007), Limestone assimilation and the origin of CO_2 emissions at the Alban Hills (Central Italy): Constraints from experimental petrology: *Journal of Volcanology and Geothermal Research*, 166, p. 91–105, https://doi.org/10.1016/j.jvolgeores.2007.07.001

Iacono-Marziano, G., Gaillard, F., and Pichavant, M. (2008), Limestone assimilation by basaltic magmas: an experimental re-assessment and application to Italian volcanoes. *Contributions to Mineralogy and Petrology*, 155, p. 719–738, https://doi.org/10.1007/s00410-007-0267-8

Iacono-Marziano, G., Gaillard, F., Scaillet, B., Pichavant, M., and Chiodini, G. (2009), Role of non-mantle CO_2 in the dynamics of volcano degassing: The Mount Vesuvius example: *Geology,* 37, p. 319–322, https://doi.org/10.1130/G25446A.1

Iacono-Marziano, G. (2020). *Interactions between magmas and host sedimentary rocks: a review of their implications in magmatic processes (magma evolution, gas emissions and ore processes).* (Doctoral dissertation), Retrieved from HAL Open Science. Université d'Orléans, 2020, https://insu.hal.science/tel-02966588/document

Isson, T.T., Planavsky, N.J., Coogan, L.A., Stewart, E.M., Ague, J.J., Bolton, E.W., Zhang, S., McKenzie, N.R., and Kump, L.R. (2020), Evolution of the global carbon cycle and climate regulation on Earth: *Global Biogeochemical Cycles*, 34, p. 1-28, https://doi.org/10.1029/2018GB006061

Johnston, F.K.B., Turchyn, A.V., and Edmonds, M. (2011), Decarbonation efficiency in subductionzones: Implications for warm Cretaceous climates: *Earth and Planetary Science Letters*, 303, p. 143–152. https://doi.org/10.1016/j.epsl.2010.12.049

Jolis, E.M., Freda, C., Troll, V.R., Deegan, F.M., Blythe, L.S., McLeod, C.L., and Davidson, J.P. (2013), Experimental simulation of magma–carbonate interaction beneath Mt. Vesuvius, Italy. *Contributions to Mineralogy and Petrology,* 166, p. 1335–1353. https://doi.org/10.1007/s00410-013-0931-0

Kerrick, D. M. (2001), Present and past nonanthropogenic CO_2 degassing from the solid earth: *Reviews of Geophysics*. 39, p. 565–585. https://doi.org/10.1029/2001RG000105

Kerrick, D.M., and Caldeira, K. (1998), Metamorphic CO_2 degassing from orogenic belts: *Chemical Geology*, 145, p. 213–232. https://doi.org/10.1016/S0009-2541(97)00144-7

Kerrick, D., Connolly, J. (2001), Metamorphic devolatilization of subducted marine sediments and the transport of volatiles into ’he Earth's mantle: *Nature,* 411, p. 293–296. https://doi.org/10.1038/35077056

Kinsman, D.J.J. (1969), Interpretation of Sr (super +2) concentrations in carbonate minerals and rocks. *Journal of Sedimentary Research*: 39 (2): p. 486–508. doi: https://doi.org/10.1306/74D71CB7-2B21-11D7-8648000102C1865D

Kuniyoshi, S., and Liou, J.G. (1976), Burial metamorphism of the Karmutsen volcanic rocks, northeastern Vancouver Island, British Columbia: *American Journal of Science*, 276, p. 1096 – 1119. https://doi.org/10.2475/ajs.276.9.1096

Larocque, J. (2008), *The role of amphibole in the evolution of arc magmas and crust: the case from the Jurassic Bonanza arc section, Vancouver Island, Canada,* (Masters thesis). Retrieved from UVicSpace. University of Victoria. http://hdl.handle.net/1828/1309

Larocque, J., and Canil, D. (2010), The role of amphibole in the evolution of arc magmas and crust: the case from the Jurassic Bonanza Arc section, Vancouver Island, Canada: *Contributions to Mineralogy and Petrology,* 159, 475–488. https://doi.org/10.1007/s00410-009-0436-z

Larson, R.L. (1991), Latest pulse of Earth: Evidence for a mid-Cretaceous superplume: *Geology*, 19, p. 547–550. https://doi.org/10.1130/0091-7613(1991)019<0547:LPOEEF>2.3.CO;2

Lee, C.-T.A., Shen, B., Slotnick, B.S., Liao, K., Dickens, G.R., Yokoyama, Y., Lenardic, A., Dasgupta, R., Jellinek, M., Lackey, J.S., Schneider, T., and Tice., M.M. (2013), Continental arc – island arc fluctuations, growth of crustal carbonates, and long-term climate change: *Geosphere*, 9, p. 21–36, https://doi.org/10.1130/GES00 822.1

Lee, C.-T.A., and Lackey, J.S. (2015), Global continental arc flare-ups and their relation to long-term greenhouse conditions: *Elements,*11, p. 125-130s https://doi.org/10.2113/gselements.11.2.125

Lee, C.-T.A., Jiang, H., Dasgupta, R., and Torres, M. (2019), A framework for understanding whole-Earth carbon cycling. In: Deep Carbon textbook, Chapter 11, p. 313 – 357.

Lentz, D, R. (1999), Carbonatite genesis: A reexamination of the role of intrusion-related pneumatolytic skarn processes in limestone melting: *Geology*, 27– p. 335 - 338, http://doi.org/10.1130/0091-7613(1999)027<0335:CGAROT>2.3.CO;2

Lesher, C.E. (1990), Decoupling of chemical and isotopic exchange during magma mixing: Nature*,* 344, p. 235–237, https://doi.org/10.1038/344235a0

Lesher, C.E. (1994), Kinetics of Sr and Nd exchange in silicate liquids: Theory, experiments, and applications to uphill diffusion, isotopic equilibration, and irreversible mixing of magmas: *Journal of Geophysical Research*, 99, p. 9585– 9604, https://doi.org/10.1029/94JB00469

Lester, G.W., Clark, A.H., Kyser, T.K., and Naslund, H.R. (2013), Experiments on liquid immiscibilty in silicate melts with H_2O, P, S, F, and Cl: Implications for natural magmas. *Contributions to Mineralogy and Petrology*, 166, p. 329 – 349. https://doi.org/10.1007/s00410-013-0878-1

Lopez, T., Fischer, T.P., Plank, T., Malinverno, A., Rizzo, A., Rasmussen, D.J., Cottrell, E., Werner, C., Kern, C., Bergfeld, D., Ilanko, T., Andrys, J.L., and Kelley, K.A. (2023), Tracking carbon from subduction to outgassing along the Aleutian-Alaska Volcanic Arc: Science Advances, 9. DOI: 10.1126/sciadv.adf3024

Lund, J.C. (1966), *Structural geology of Empire Mine, Empire Development Limited, Port McNeil, British Columbia*. (Masters thesis), Retrieved from UBC Theses and Dissertations, University of British Columbia.

Mason, E., Edmonds, M., and Turchyn, A.V. (2017), Remobilization of crustal carbon may dominate volcanic arc emissions: *Science*, 357, p. 290– 294, https://doi.org/10.1126/science.aan5049

Massey, N.W.D. (1995a), Geology and mineral resources of the Alberni-Nanaimo lakes sheet, Vancouver Island 92F/1W, 92F/2E, and part of 92F/7E: British Columbia Ministry of Energy, Mines and Petroleum Resources, Paper 1992-2, p. 1-132.

Massey, N.W.D. (1995b) Geology and mineral resources of the Cowichan Lake sheet, Vancouver Island 92C/16: British Columbia Ministry of Energy, Mines and Petroleum Resources, Paper 1992-3, p. 1-112.

Massey, N.W.D. (1995c), Geology and mineral resources of the Duncan sheet, Vancouver Island 92B/13: British Columbia Ministry of Energy, Mines and Petroleum Resources, Paper 1992-4, p. 1-112.

Mattey, D., Lowry, D., and Macpherson, C. (1994), Oxygen isotope composition of mantle peridotite. *Earth and Planetary Science Letters*, 128(3), p. 231–241. https://doi.org/10.1016/0012-821X(94)90147-3

McCarthy, A., and Müntener, O. (2016), Comb layering monitors decompressing and fractionating hydrous mafic magmas in subvolcanic plumbing systems (Fisher Lake, Sierra Nevada, USA): *Journal of Geophysical Research: Solid Earth*, 121, p. 8595-8621. https://doi.org/10.1002/2016JB013489

McKenzie, N. R., Horton, B. K., Loomis, S. E., Stockli, D. F., Planavsky, N. J., and Lee, C.-T. A. (2016), Continental arc volcanism as the principal driver of icehouse-greenhouse variability: *Science*, 352, p. 444–447. doi:10.1126/science.aad5787

Meinert, L.D., Dipple, G. M., and Nicolescu, S. (2005), World skarn deposits: *Economic Geology 100th Anniversary Volume*, p. 299 – 336.

Miyashiro, A. (1974), Volcanic rock series in island arcs and active continental margins. *American Journal of Science,* 274(4), p. 321 – 355.

Mollo, S., Gaeta, M., Freda, C., Di Rocco, T., Misiti, V., and Scarlato, P. (2010), Carbonate assimilation in magmas: a reappraisal based on experimental petrology: *Lithos,* 114, p. 503–514. https://doi.org/10.1016/j.lithos.2009.10.013

Morris, Rebecca (2023). Crustal carbonate assimilation limits and CO_2 production within arc magmas - The Jurassic Bonanza arc, Vancouver Island, Canada (Dissertation Tables). figshare. Dataset. https://doi.org/10.6084/m9.figshare.24884265.v1

Morris, R. A., DeBari, S.M., Busby, C., Medynski, S., and Jicha, B.R. (2019), Building arc crust: Plutonic to volcanic connections in an extensional oceanic arc, the southern Alisitos arc, Baja California: Journal of Petrology, 60, p. 1195 – 1228. doi: 10.1093/petrology/egz029

Morris, R., and Canil, D. (2020), Skarn mineralization along magma-carbonate contacts in the Merry Widow Mountain area, Vancouver Island, British Columbia (NTS 092L); *in* Geoscience BC Summary of Activities 2019: Minerals, Geoscience BC, Report 2020-01: p. 5 – 12.

Morris, R., and Canil, D. (2021), Cryptic magmatic skarn of the Merry Widow deposit, Vancouver Island (NTS 092L); in Geoscience BC Summary of Activities: Minerals, Geoscience BC, Report 2021-01: p. 47 – 54.

Morris, R.A., and Canil, D. (2022), CO_2 transport at shallow depths in arc magmas: Evidence from unique orbicular dikes in the Jurassic Bonanza arc, Vancouver Island, Canada: *Contributions to Mineralogy and Petrology*, 177, https://doi.org/10.1007/s00410-021-01852-y

Morris, R.A., Canil, D., Spence, J. (2023), Magma-carbonate interactions drive CO_2 production and metal enrichment in shallow dikes and sills at volcanic arcs. *Geology*; doi: https://doi.org/10.1130/G51439.1

Muller, J.E. (1977), Evolution of the Pacific Margin, Vancouver Island, and adjacent regions: Canadian Journal of Earth Sciences, 14, p. 2062-2085. https://doi.org/10.1139/e77-176

Nandedkar, R. H., Ulmer, P., and Müntener, O. (2014), Fractional crystallization of primitive, hydrous arc magmas: an experimental study at 0 7 GPa: *Contributions to Mineralogy and Petrology*, 167, p. 1–27.

Nicholls, J., and Russell, J. K. (2016), Igneous rock associations 20. Pearce element ratio diagrams: Linking geochemical data to magmatic processes. *Geoscience Canada*, 43(2), p. 133–146. https://doi.org/10.12789/geocanj.2016.43.095

Nicholson, G. (2006): Assessment report on the diamond drilling on the Merry Widow property, Nanaimo Mining Division, Vancouver Island; BC Ministry of Energy, Mines and Low Carbon Innovation, Assessment Report 28863, https://aris.empr.gov.bc.ca/ArisReports/28863.PDF, accessed December 2023.

Nixon, G.T., and Orr, A.J. (2007), Recent revisions to the early Mesozoic stratigraphy of Vancouver Island and metallogenic implications, British Columbia: British Columbia Ministry of Energy, Mines and Petroleum Resources Geological Fieldwork 2006: p.163–177.

Nixon, G.T., Hammack, J.L., Hamilton, J.V., Jennings, H., Larocque, J.P., Orr, A.J., Friedman, R.M., Archibald, D.A., Creaser, R.A., Orchard, M.J., Haggart, J.W., Tipper, H.W., Tozer, E.T., Cordey, F., and McRoberts, C.A. (2011), Geology, geochronology, lithogeochemistry and metamorphism of the Alice Lake area, northern Vancouver Island, NTS 092L/06 and part of 092L/03: British Columbia Geological Survey Geoscience Map 2011-4, v. 1, scale 1:50000, 1 sheet.

Paton, C., Hellstrom, J., Paul, B.,Woodhead, J. and Hergt, J. (2011), Iolite: Freeware for the visualisation and processing of mass spectrometric data: *Journal of Analytical Atomic Spectrometry*, doi:10.1039/c1ja10172b

Paulson, B.D. (2010). *Magmatic processes in the Jurassic Bonanza Arc: Insights from the Alberni Region of Vancouver Island, Canada* (Masters thesis): Bellingham, Washington, Western Washington University, 121 p.

Pearce, T.H. (1968), A contribution to the theory of variation diagrams: *Contributions to Mineralogy and Petrology*, 19, p.142-157. https://doi.org/10.1007/BF00635485

Pearce, J. A., and Peate, D. W. (1995), Tectonic implications of the composition of volcanic arc magmas: *Annual Review of Earth and Planetary Sciences, 23,* p. 251–286.

Philpotts, A.R. (1982), Compositions of immiscible liquids in volcanic rocks: *Contributions to Mineralogy and Petrology,* 80, p. 201 – 218. https://doi.org/10.1007/BF00371350

Piochi, M., Ayuso, R.A., Vivo, B.D, and Somma, R. (2006), Crustal contamination and crystal entrapment during polybaric magma evolution at Mt. Somma–Vesuvius volcano, Italy: Geochemical and Sr isotope evidence: *Lithos*, 86, p. 303–329. https://doi.org/10.1016/j.lithos.2005.05.009

Plank, T., Kelley, K. A., Zimmer, M. M., Hauri, E. H. & Wallace, P. J. (2013), Why do mafic arc magmas contain 4 wt.% water on average: *Earth and Planetary Science Letters*, 364, p. 168–179.

Plank, T., and Manning, C.E. (2019), Subducting carbon: *Nature*, 574, p. 343–352. https://doi.org/10.1038/s41586-019-1643-z

Poli, S. (2015), Carbon mobilized at shallow depths in subduction zones by carbonatitic liquids. Nature Geoscience, 8. https://doi.org/10.1038/ngeo2464

Ramos, E.J., Lackey, J.S., Barnes, J.D., and Fulton, A.A. (2020), Remnants and rates of metamorphic decarbonation in continental arc: *Geological Society of America Today*, 30, p.1–8, https://doi.org/10.1130/GSATG432A.1

Ratschbacher, B.C., Paterson, S.R., and Fischer, T.P. (2019), Spatial and depth-dependent variations in magma volume addition and addition rates to continental arcs: Application to global CO_2 fluxes since 750 Ma: *Geochemisty, Geophysics, Geosystems*, 20, p. 2997–3018. https://doi.org/10.1029/2018gc008031

Ray, G.E., and Webster, I.C.L. (1991), Geology and mineral occurrences of the Merry Widow skarn camp, northern Vancouver Island: BC Ministry of Energy, Mines and Petroleum Resources, BC Geological Survey, Open File 1991-08, scale 1, p 5000.

Roedder, E. (1951), Low-temperature liquid immiscibility in the system K_2O – FeO – Al_2O_3 – SiO_2: *American Mineralogist*, 35, p. 282–286.

Rollinson, H. R. (1993), Using geochemical data: evaluation, presentation, interpretation. Harlow, Essex, England : New York, Longman Scientific & Technical.

Ryan, W.B.F., Carbotte, S.M., Coplan, J.O., O'Hara, S., Melkonian, A., Arko, R., Weissel, R.A., Ferrini, V., Goodwillie, A., Nitsche, F., Bonczkowski, J., and Zemsky, R. (2009), Global multi-resolution topography (GMRT) synthesis data set: *Geochemistry, Geophysics, Geosystems,* 10:Q03014. https://doi.org/10.1029/2008GC002332

Sangster, D.F. (1964). *The contact metasomatic magnetite deposits of southwestern British Columbia.* (Doctoral Dissertation), Retrieved from UBC Theses and Dissertations, University of British Columbia.https://open.library.ubc.ca/cIRcle/collections/ubctheses/831/items/1.0053070

Schindelin, J., Arganda-Carreras, I., Frise, E., Kaynig, V., Longair, M., Pietzsch, T., Preibisch, S., Rueden, C., Saalfeld, S., Schmid, B., Tinevez, J-Y., White, D.J., Hartenstein, V., Eliceiri, K., Tomancak, P., and Cardona, A. (2012), Fiji: an open-source platform for biological image-analysis: *Nature Methods*, 9, p. 676-682. https://doi.org/10.1038/nmeth.2019

Schmidt, M.W., Green, D.H., and Hibberson, W.O. (2004), Ultra-calcic magmas generated from Ca-depleted mantle: an experimental study on the origin of ankaramites: *Journal of Petrology*, 45, p. 531 – 554. https://doi.org/10.1093/petrology/egg093

Shaw, A.M., Hilton, D.R., Fischer, T.P., Walker, J.A., and Alvarado, G.E. (2003), Contrasting He–C relationships in Nicaragua and Costa Rica: insights into C cycling through

subduction zones: Earth and Planetary Science Letters, 214, p, 499 – 513. https://doi.org/10.1016/S0012-821X(03)00401-1

Shinohara, H. (2013), Volatile flux from subduction zone volcanoes: insights from a detailed evaluation of the fluxes from volcanoes in Japan. Journal of Volcanology and Geothermal Research, 268, p. 46 – 63. https://doi.org/10.1016/j.jvolgeores.2013.10.007

Skora, S., Blundy, J.D., Brooker, R.A., Green, E.C.R., de Hoog, J.C.M., and Connolly, J.A.D. (2015), Hydrous phase relations and trace element partitioning behaviour in calcareous sediments at subduction-zone conditions: *Journal of Petrology*, 56, p. 953–980, https://doi.org/10.1093/petrology/egv024

Spera, F.J., and Bohrson, W.A. (2002), Energy-constrained open-system magmatic processes 3. Energy-Constrained Recharge, Assimilation, and Fractional Crystallization (EC-RAFC): *Geochemisty, Geophysics, Geosystems*, 3, p. 1 – 20. https://doi.org/10.1029/2002GC000315

Stewart, R.J., and Page, R.J. (1973), Zeolite facies metamorphism of the Late Cretaceous Nanaimo Group, Vancouver Island and Gulf Islands, British Columbia: *Canadian Journal of Earth Science*, 11, p. 280 -284.

Sun, S.S., and McDonough, W.F. (1989), Chemical and isotopic systematics of oceanic basalts; implications for mantle composition and processes; magmatism in the ocean basins. In: Saunders, A.D. and Norry, M.J. (eds) Magmatism in the Ocean Basins. *Geological Society, London, Special Publications* 42, p. 313 – 345.

Suyehiro, K., Takahashi, N., Ariie, Y., Yokoi, Y., Hino, R., Shinohara, M., Kanazawa, T., Hirata, N., Tokuyama, H. and Taira, A. (1996), Continental crust, crustal underplating, and low-Q upper mantle beneath an oceanic island arc: *Science*, 272, p. 390–392.

Tamburello, G., Pondrelli, S., Chiodini, G., and Rouwet, D. (2018), Global-scale control of extensional tectonics on CO_2 earth degassing: *Nature Communications*, 9. https://doi.org/10.1038/s41467-018-07087-z

Troll, V. R., Hilton, D. R., Jolis, E. M., Chadwick, J. P., Blythe, L. S., Deegan, F. M., Schwarzkopf, L. M., and Zimmer, M. (2012), Crustal CO_2 liberation during the 2006 eruption and earthquake events at Merapi volcano, Indonesia: *Geophysical Research Letters*, 39, doi:10.1029/2012GL051307.

Troll, V.R., Deegan., Jolis, E.M., Harris, C., Chadwick, J.P., Gertisser, R., Schwarzkopf, L.M., Borisova, A.Y., Bindeman, I.N., Sumarti, S., and Preece, K. (2013), Magmatic differentiation processes at Merapi Volcano: inclusion petrology and oxygen isotopes: *Journal of Volcanology and Geothermal Research*, 261, p. 38 – 49. https://doi.org/10.1016/j.jvolgeores.2012.11.001

Urey, H. C. (1952), On the early chemical history of the Earth and the origin of life: *Proceedings of the National Academy of Sciences*, 38, p. 351–363.

Van Hinsberg, V.J., Berlo, K., Migdisov, A.A., and Williams-Jones, A.E. (2016), CO_2-fluxing collapses metal mobility in magmatic vapour: *Geochemical Perspectives Letters*, 2, p. 169 – 177, doi: 10.7185/geochemlet.1617

Varshneya, A. K., and Cooper, A. R. (1972), Diffusion in the system K_2O-SrO-SiO_2: III, Interdiffusion Coefficients: *Journal of the American Ceramic Society*, 55, p. 312–317. https://doi.org/10.1111/j.1151-2916.1972.tb11293.x

Wallace, P. (2005), Volatiles in subduction zone magmas: Concentrations and fluxes based on melt inclusion and volcanic gas data: *Journal of Volcanology and Geothermal Research,* 140 (1-3), p. 217 – 240. https://doi.org/10.1016/j.jvolgeores.2004.07.023

Werner, C., Fischer, T.P., Auippa, A., Edmonds, M., Cardellini, C., Carn, S., Chiodini, G., Cottrell, E., Burton, M., Shinohara, H., and Allard, P. (2019), Carbon dioxide emissions from subaerial volcanic regions: two decades in review. In: Deep Carbon: Past to Present, eds B. Orcutt, R. Dasgupta, and I. Daniel, Cambridge University Press, p. 188 – 236.

Wesley, R. and Nelson, M. (2008), Diamond drilling, geochemical and geophysical assessment report for the 2007 program at the Merry Widow project, Nanaimo Mining Division, Vancouver Island; BC Ministry of Energy, Mines and Low Carbon Innovation, Assessment Report 30002a, 242 p., https://aris.empr.gov.bc.ca/ArisReports/3000-2A.PDF [accessed December, 2023)

White, W., and Hofmann, A. (1982), Sr and Nd isotope geochemistry of oceanic basalts and mantle evolution: *Nature,* 296, p. 821–825. https://doi.org/10.1038/296821a0

Whitley, S., Gertisser, R., Halama, R., Preece, K., Troll, V.R., and Deegan, F.M. (2019), Crustal CO_2 contribution to subduction zone degassing recorded through calc-silicate xenoliths in arc lavas: *Scientific Reports*, 9, https://doi.org/10.1038/s41598-019-44929-2

Whitley, S., Halama, R., Gertisser, R., Preece, K., Deegan, F.M., Troll, V.R. (2020), Magmatic and metasomatic effects of magma-carbonate interaction recorded in calc-silicate xenoliths from Merapi volcano (Indonesia): *Journal of Petrology*, 60, p. 1 – 38. https://doi.org/10.1093/petrology/egaa048

Zhang, Y., Ni, H., and Chen, Y. (2010), Diffusion data in silicate melts: *Reviews in Mineralogy & Geochemistry*, 72, p. 311 – 408. https://doi.org/10.2138/rmg.2010.72.8

Zhang, J., and Lee, C.-T.A. (2021), Disequilibrium crystallization and rapid crystal growth: a case study of orbicular granitoids of magmatic origin. *International Geology review,* 63, p. 900 – 916, https://doi.org/10.1080/00206814.2020.1734975

Appendices

Appendix A – Chapter 2 Supplemental Material

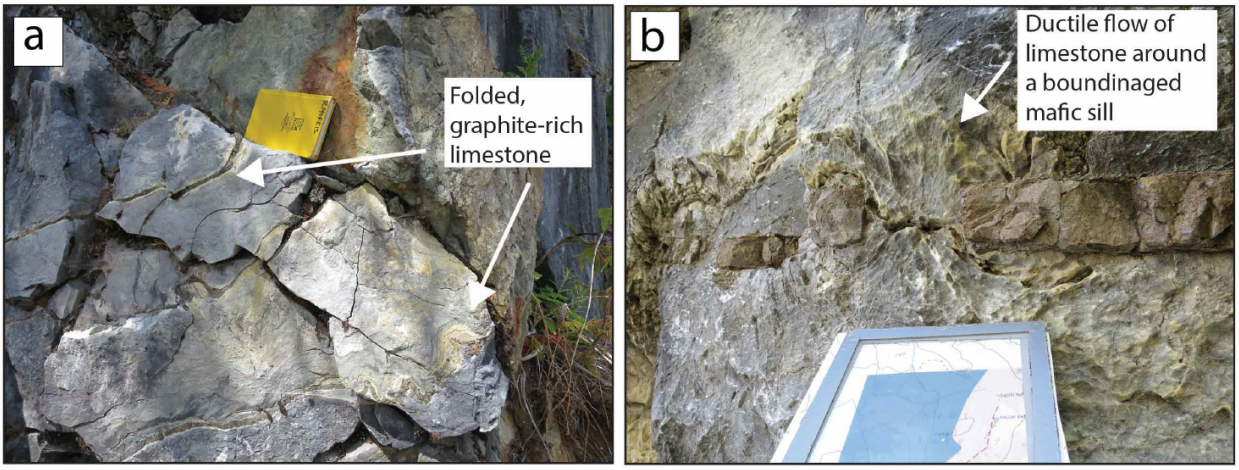

Figure A1: Ductile folding of limestone at Merry Widow occurs on a cm- and m-scale at when in close proximity with magma contacts (i.e., pluton, dikes, sills). **(a)** Folding is evident in graphite-rich layers. Photo taken near dike outcrop RM19-78 with a field book for scale. **(b)** Ductile flow of limestone around a boudinaged mafic sill. Photo taken near outcrop RM19-161. The map board for scale is 20 cm wide.

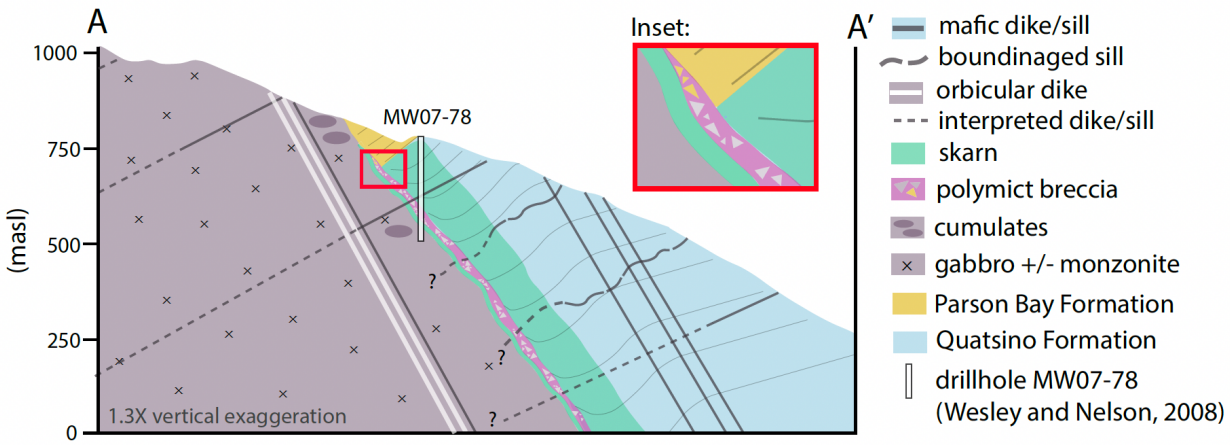

Figure A2: Cross-section A–A' (from Figure 2.2a), representing the field relationships at depth, which are established from extrapolation of exposed bedding and contacts and from publicly available drillhole data (Nicholson, 2006; Wesley and Nelson, 2008). The Parson Bay Formation (dominantly tuffaceous at Merry Widow) is concordant with the underlying Quatsino Formation, where well-defined and exposed bedding was measured at numerous localities (Figure 2.2a). Skarn occurs at the contact of the pluton with the Quatsino Formation, and is exposed from a quarry that has removed overburden (i.e., Parson Bay) or in drillcore and underground audits. The skarn is dominantly clinopyroxene, garnet, massive calcite, massive magnetite, and sulphides. Minor (m-scale) polymict breccias cross-cut the skarn and overlying Parson Bay Formation. No skarn mineralization was observed within the Parson Bay Formation, with the exception of a ~20 cm of hydrothermal alteration (dominantly epidote) at gabbro-Parson Bay contact (RM19-144 in Figure 4.1). Regional faulting not included in cross-section.

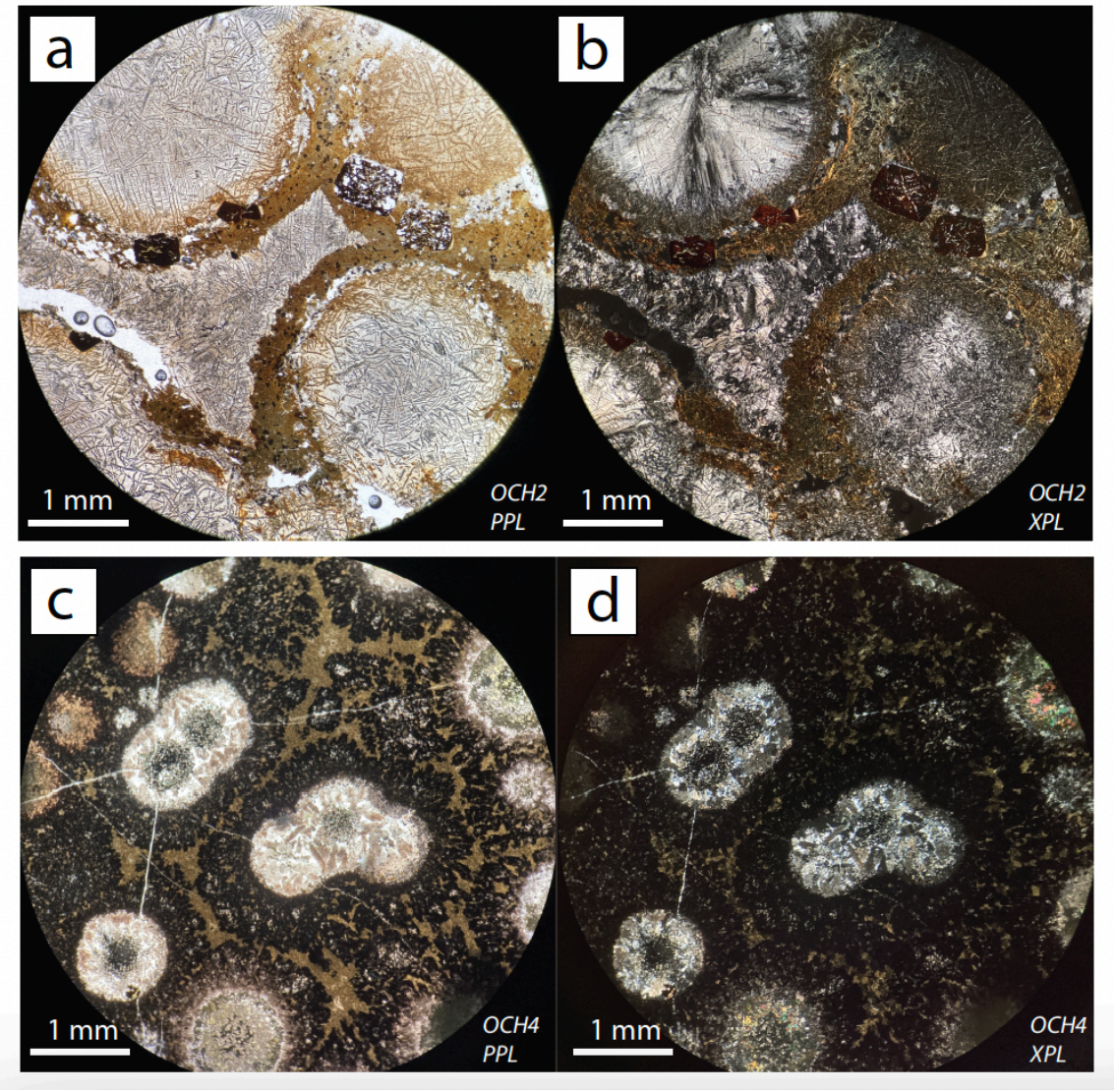

Figure A3: Photomicrographs images of spherulitic lavas. The spherulites are dominantly albite (first order white – grey in Figure A3b) and display partial to full replacement of secondary minerals (epidote, oxides, chlorite, albite).

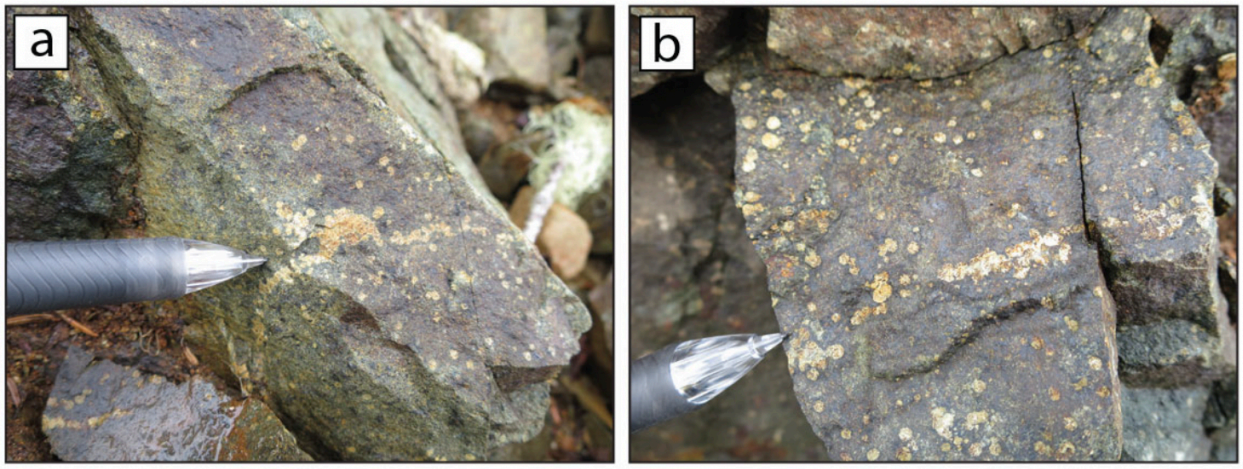

Figure A4: Field photos showing orbicular dikes in outcrop, with light coloured orbicules set in a darker groundmass of host melt. Note the amalgamation of some orbicules. Photos taken at outcrop RM19-120, pen for scale..

Figure A5: Field relationships of the late-stage orbicular dikes cross-cutting earlier mafic dikes and monzonite of the Merry Widow pluton.

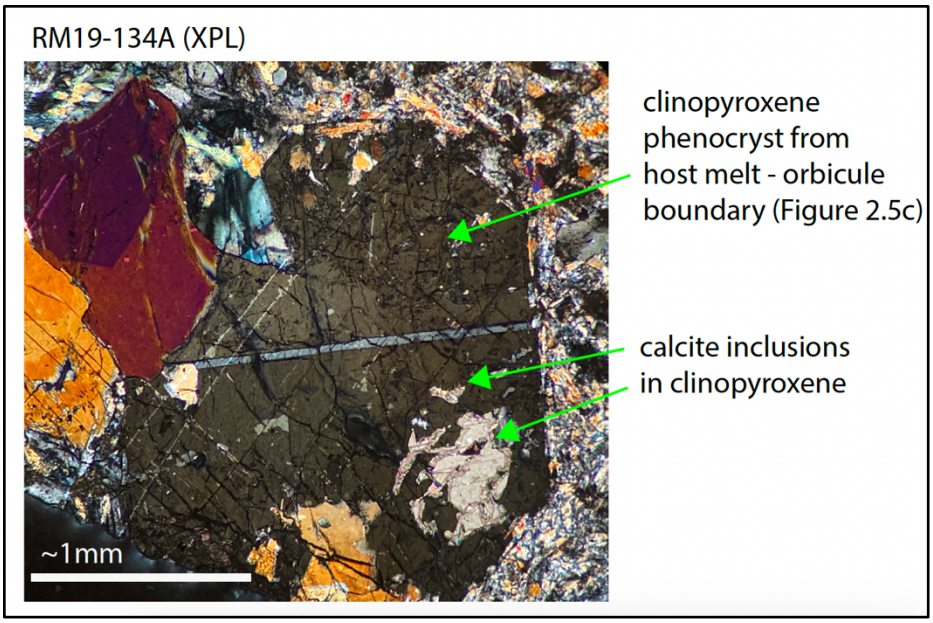

Figure A6: Calcite inclusions in clinopyroxene phenocryst along host melt – orbicule boundary in Figure 2.5c.

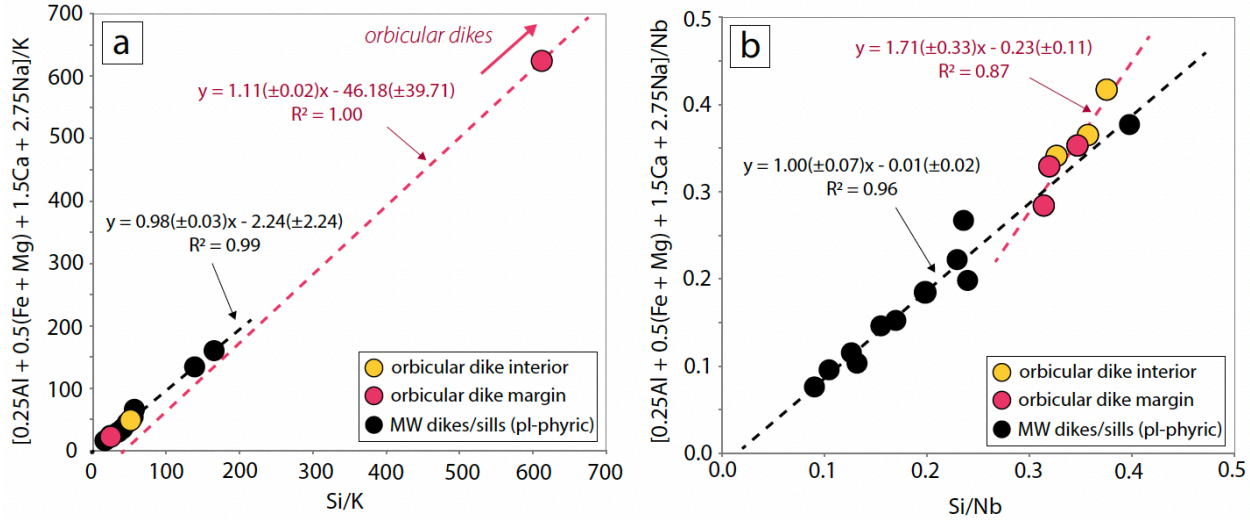

Figure A7: Pearce element ratio diagrams of plagioclase-phyric dikes (black circles) and orbicular dikes (red and yellow circles) using K **(a)** and Nb **(b)** as normalizing elements. A slope of ~1 for dikes indicates that the melts were dominantly controlled by olivine + clinopyroxene + plagioclase 'sorting' (addition and/or fractionation). This also indicates these elements were immobile on the scale of the samples. The disposition of orbicular dikes from a slope of ~1 when normalized to K and Nb indicates the orbicular dikes are part of a separate chemical system with different petrogenetic processes (i.e., crustal assimilation) than closed-system olivine + clinopyroxene + plagioclase addition and/or fractionation.

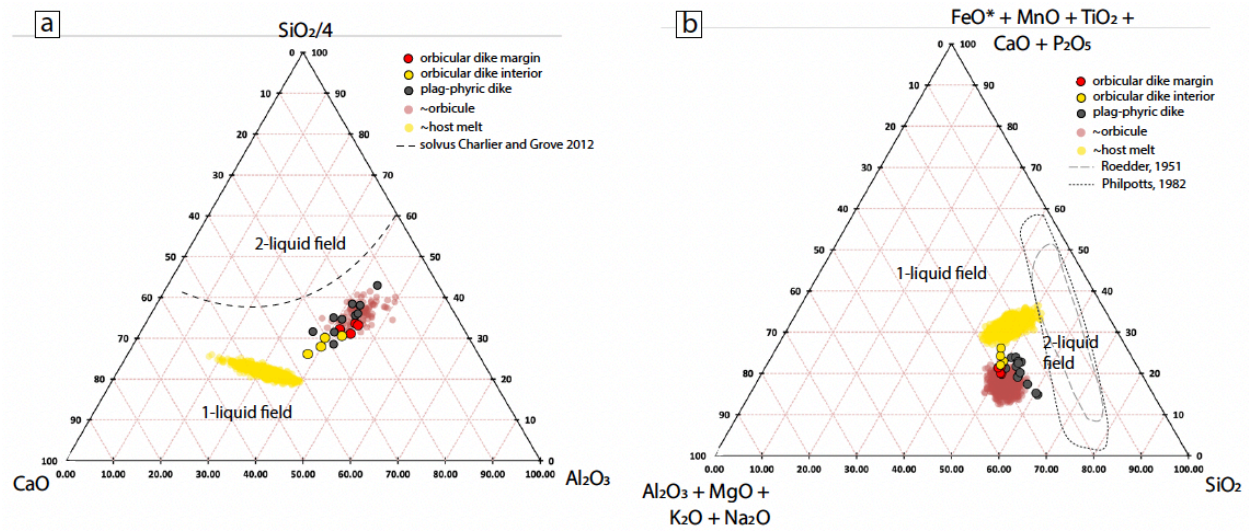

Figure A8: Compositions of orbicule dike margins, interiors, host melt, and orbicules, as well as plagioclase-phyric dikes compared to two-liquid fields (solvi) in the systems **(a)** $SiO_2/4$–CaO–Al_2O_3 (Charlier and Grove 2012) and **(b)** $FeO+MnO+TiO_2+CaO+P_2O_5$–$Al_2O_3+MgO+K_2O+Na_2O$–SiO_2 (Roedder 1951, Philpotts 1982). Note all compositions plot within the one-liquid field when compared with experimentally derived two-liquid solvi.

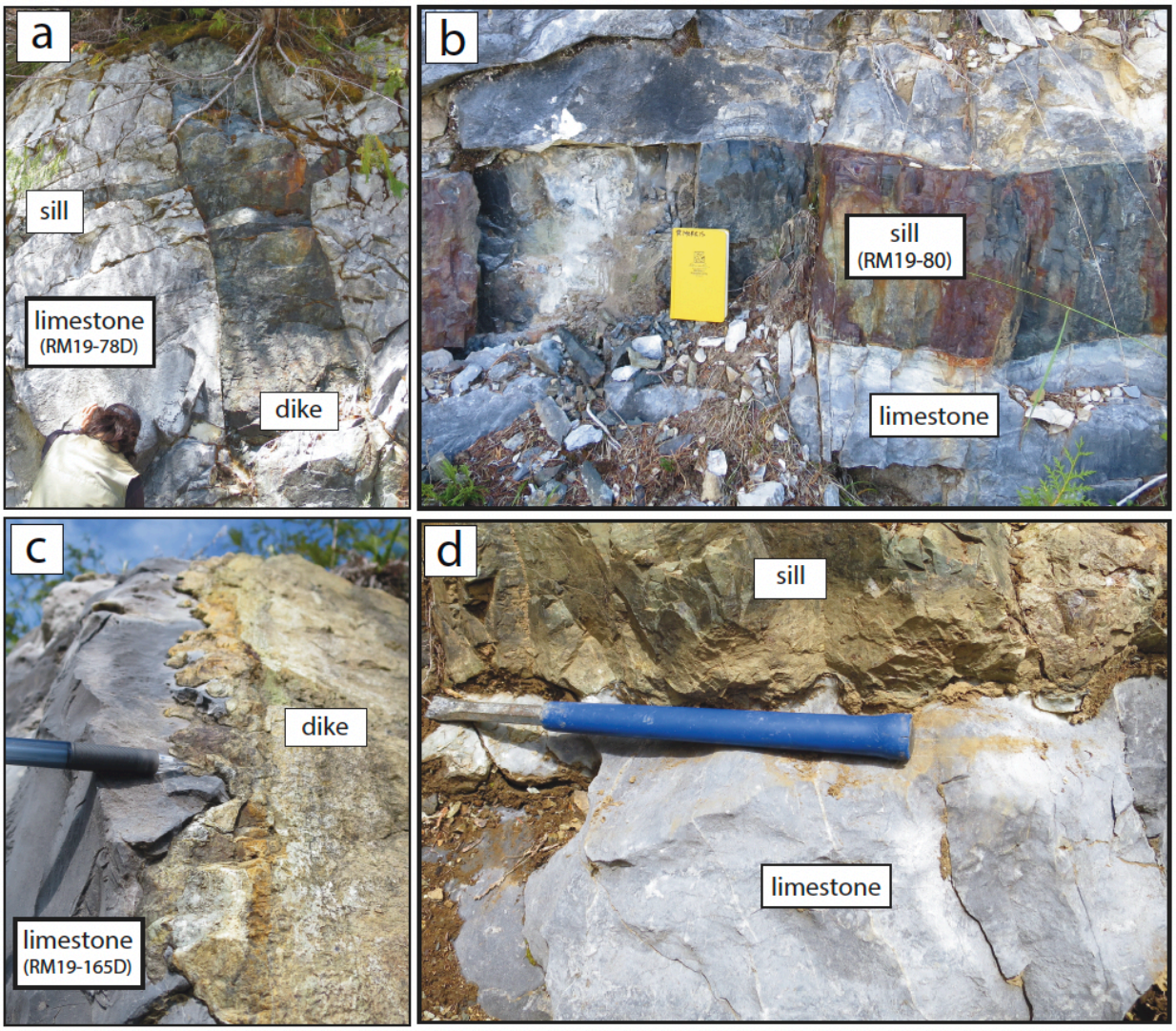

Figure A9: Basalt-limestone outcrop locations at Merry Widow displaying sharp (a,b) and irregular (c,d) contacts.

Tables available at: https://doi.org/10.6084/m9.figshare.24884265.v1

Table A1 - EMPA clinopyroxene compositions

SAMPLE	SPOT	CPX TYPE	SPOT LOCATION	SiO2_pct	TiO2_pct	Al2O3_pct	Cr2O3_pct	FeO_pct	MnO_pct	MgO_pct	CaO_pct	Na2O_pct	TOTAL	Si mol %
134A_75		intergranular - orbicule	mid	51.01	0.67	2.7	0	11.18	0.33	14	19.4	0.19	99.48	48.78
134A_76		intergranular - orbicule	rim	51.46	0.67	2.36	0	11.91	0.4	13.73	19.04	0.19	99.76	49.15
134A_77		intergranular - orbicule	mid	51.59	0.53	2.73	0	9.18	0.26	15.38	19.9	0.18	99.75	48.71
134A_84		phenocryst - interface	core	52.42	0.37	3.09	0.15	5.56	0.13	16.74	21.57	0.14	100.17	48.74
134A_85		phenocryst - interface	mid	52.39	0.36	3.11	0.18	5.49	0.13	16.76	21.4	0.12	99.94	48.83
134A_95		intergranular - host melt	mid	49.8	0.71	5.63	0.18	6.94	0.14	14.41	22.23	0.2	100.24	47.37
134A_96		intergranular - host melt	mid	52.57	0.41	2.65	0.13	6.52	0.17	16.44	21.47	0.12	100.48	48.80
134A_105		phenocryst - orbicule	rim	52.14	0.37	3.3	0.33	5.2	0.12	16.38	22.63	0.15	100.62	48.39
134A_106		phenocryst - orbicule	rim	52.09	0.41	3.06	0.15	5.82	0.15	16.58	22	0.12	100.38	48.38
134A_111		phenocryst - orbicule	core	50.16	0.57	5.19	0.46	5.74	0.12	15.36	22.56	0.15	100.31	47.34
134A_112		phenocryst - orbicule	core	51.98	0.39	3.45	0.12	5.49	0.11	16.23	22.32	0.13	100.22	48.46
134A_114		phenocryst - host melt	core	49.75	0.52	6	0.89	5.39	0.11	15.01	22.4	0.18	100.25	47.30
134A_116		phenocryst - host melt	rim	51.66	0.55	2.99	0.02	7.97	0.19	15.6	21.2	0.14	100.32	48.38
134A_127		phenocryst - glomerocryst	mid	50.03	0.65	5.54	0.2	6.14	0.12	15.03	22.23	0.2	100.14	47.41
134A_128		phenocryst - glomerocryst	rim	47.96	1.24	6.2	0	9.53	0.2	13.3	21.36	0.27	100.06	46.27
134A_136		phenocryst - glomerocryst	mid	51.95	0.44	3.06	0.13	6.51	0.21	16.12	21.67	0.14	100.23	48.49
134A_137		phenocryst - glomerocryst	rim	51.75	0.57	2.73	0.02	10.47	0.3	14.75	19.87	0.17	100.63	48.71
134A_141		phenocryst - glomerocryst	mid	50.74	0.55	4.79	0.13	6	0.12	15.05	22.44	0.19	100.01	47.95
134A_143		phenocryst - glomerocryst	core	49.9	0.48	5.91	0.95	5.06	0.09	15.1	22.2	0.24	99.93	47.54
134B1_156		intergranular - orbicule	rim	49.84	0.79	4.67	0.04	8.67	0.21	15.16	20.43	0.13	99.94	47.36
134B1_157		intergranular - orbicule	rim	49.66	0.82	5.18	0.23	7.62	0.18	15.44	20.62	0.14	99.89	47.21
134B1_167		intergranular - orbicule	rim	47.38	1.38	7.46	0.23	8.26	0.15	13.42	21.19	0.2	99.67	46.07
134B1_168		intergranular - orbicule	rim	46.94	1.49	7.98	0.31	7.79	0.14	13.15	21.97	0.19	99.96	45.64
134B1_169		intergranular - orbicule	rim	49.18	0.88	5.82	0.03	8.69	0.2	14.61	20.44	0.15	100	47.04
134B1_182		intergranular - host melt	rim	51.09	0.46	3.35	0.15	8.72	0.34	13.19	22.75	0.16	100.21	48.54
134B1_183		intergranular - host melt	rim	47.69	1.21	7.25	0.18	8.63	0.17	13.7	20.74	0.24	99.81	46.22
134B1_184		intergranular - host melt	rim	49.28	0.39	4.58	0.09	10.55	0.37	13.4	20.6	0.16	99.42	47.55
134B1_185		intergranular - host melt	rim	47.28	1.32	7.84	0.27	7.53	0.14	13.53	21.81	0.2	99.92	45.84
134B1_186		intergranular - host melt	rim	49.16	0.74	6.58	0.35	7.2	0.13	14.68	21.34	0.19	100.37	46.91
134B1_187		intergranular - host melt	rim	51.07	0.53	3.51	0.14	8.5	0.27	15.24	21.36	0.13	100.75	47.88
134B1_204		intergranular - orbicule	rim	46.17	1.68	7.53	0.03	12.04	0.22	11.03	20.58	0.36	99.64	45.72
134B1_205		intergranular - orbicule	mid	48.36	0.86	7.26	0.22	7.47	0.15	13.93	20.95	0.2	99.4	46.88
134B1_206		intergranular - orbicule	rim	46.23	1.63	8.92	0.13	8.4	0.15	12.31	21.3	0.2	99.27	45.64
134B1_207		intergranular - orbicule	rim	44.56	2.1	9.82	0.05	9.48	0.16	11.46	21.14	0.21	98.98	44.58
134B1_208		intergranular - orbicule	rim	46.21	1.58	9.07	0.24	7.69	0.13	12.81	21.54	0.16	99.43	45.43
134B1_209		intergranular - orbicule	rim	50.58	0.65	4.37	0.08	7.84	0.18	15.69	19.97	0.1	99.46	48.05
134B1_224		intergranular - host melt	rim	48.22	1.13	6.57	0	11.1	0.25	12.41	19.09	0.32	99.09	47.41
134B1_225		intergranular - host melt	rim	46.39	1.59	8.05	0.02	10.91	0.2	11.05	18.96	0.43	97.6	46.94
134B1_226		intergranular - host melt	rim	50.68	0.64	3.46	0	11.09	0.3	15.33	18.49	0.12	100.11	48.03
134B1_194		phenocryst - orbicule	core	51.17	0.42	4.45	0.48	5.16	0.12	15.63	22.07	0.16	99.66	48.36
134B1_195		phenocryst - orbicule	mid	50.26	0.46	5.22	0.56	5.11	0.11	15.29	22.31	0.14	99.46	47.82
134B1_197		phenocryst - orbicule	rim	48.94	0.92	5.04	0.04	10.21	0.24	13.86	19.95	0.15	99.35	47.27
134B1_282		phenocryst - host melt	core	52.33	0.34	3.3	0.51	5.12	0.12	16.18	22.24	0.14	100.28	48.81
134B1_288		phenocryst - host melt	mid	52.31	0.36	3.26	0.49	5.14	0.12	16.24	22.45	0.14	100.51	48.66
134B1_291		phenocryst - host melt	rim	51.11	0.71	3.65	0.03	8.85	0.24	15.07	20.29	0.31	100.26	48.25
134B1_292		phenocryst - host melt	rim	50.79	0.77	3.78	0.02	8.62	0.24	15.06	20.43	0.3	100.01	48.07
134B1_293		phenocryst - host melt	mid	50.37	0.54	4.82	0.34	5.88	0.11	15.4	22.49	0.14	100.09	47.54
134B1_299		phenocryst - host melt	core	50.27	0.66	4.96	0.07	6.61	0.12	15.01	22.68	0.18	100.56	47.34
134B1_300		phenocryst - host melt	core	49.82	0.74	4.97	0.05	7.13	0.12	14.84	22.55	0.22	100.44	47.05
134B1_304		phenocryst - host melt	mid	50.63	0.55	5.11	0.36	5.83	0.13	15.8	22.54	0.19	101.14	47.29
134B1_305		phenocryst - glomerocryst	rim	50.44	0.56	5.9	0.62	5.55	0.11	15.11	22.12	0.16	100.57	47.72
134B1_306		phenocryst - glomerocryst	mid	49.56	0.59	6.31	0.9	5.55	0.11	14.91	21.89	0.18	100	47.35
134B1_308		phenocryst - glomerocryst	mid	50.25	0.47	5.66	0.89	5.04	0.1	15.3	22.1	0.18	99.99	47.74
134B1_309		phenocryst - glomerocryst	mid	50.6	0.43	5.25	0.88	4.9	0.11	15.42	22.42	0.17	100.18	47.86
134B1_310		phenocryst - glomerocryst	mid	49.81	0.55	6.04	0.87	5.43	0.12	14.92	22.13	0.19	100.06	47.48
134B1_311		phenocryst - glomerocryst	mid	50.29	0.47	5.54	0.86	5.24	0.11	14.99	22.49	0.15	100.14	47.75
134B1_312		phenocryst - glomerocryst	mid	51.37	0.38	4.19	0.63	5.11	0.11	15.84	22.23	0.15	100.01	48.32
134B1_313		phenocryst - glomerocryst	mid	50.3	0.48	5.8	0.48	5.42	0.11	15.31	22.15	0.21	100.26	47.61

Notes: Analytical uncertainty was calculated from standard deviations of measured standards: Si ~0.14%; Al ~0.09%; Ca ~0.16%; Fe ~0.18%; Mg ~0.06%; Na ~0.15%; K ~0.03%; Ti ~0.33%; Cr ~0.1%, and Mn ~0.06%. Measured standards included: Cr2O3 chromium oxide Alfa for Cr ka, Fe2SiO4 fayalite Rockport for Fe ka, TiO2 Rutile MTI for Ti ka, CaMgSi2O6 diopside Wakefield for Mg ka, Si ka, Ca ka NaAlSi3O8 albite VA 131705 for Na ka, KAlSi3O8 sanidine Itrongay for Al ka, K ka, and Spessartine Little 3 for Mn ka.

Table A1 - EMPA clinopyroxene compositions (con't)

SAMPLE_SPOT	Ca cation %	Al cation %	Fe cation %	Mg cation %	Ti cation %	Cr cation %	Mn cation %	Na cation %	Total	Mg Number (N	Wo	En	Fs	Aergerine	Jadeite	Diopside	
134A_75	19.88	1.52	8.94	19.96	0.48	0.00	0.27	0.18	99.82	69.06	41.2	41.3	17.5	2.4	-0.7	98.3	
134A_76	19.48	1.33	9.51	19.55	0.48	0.00	0.32	0.18	99.82	67.27	40.1	40.3	19.6	0.0	1.8	98.2	
134A_77	20.13	1.52	7.25	21.65	0.38	0.00	0.21	0.16	99.84	74.91	41.8	44.9	13.4	4.0	-2.3	98.4	
134A_84	21.49	1.69	4.32	23.21	0.26	0.06	0.10	0.13	99.87	84.29	44.4	47.9	7.6	2.9	-1.7	98.8	
134A_85	21.37	1.71	4.28	23.29	0.25	0.07	0.10	0.11	99.89	84.48	44.0	48.0	8.0	1.8	-0.8	99.0	
134A_95	22.65	3.16	5.52	20.43	0.51	0.07	0.11	0.18	99.82	78.73	48.2	43.5	8.4	6.9	-5.3	98.4	
134A_96	21.36	1.45	5.06	22.75	0.29	0.05	0.13	0.11	99.89	81.80	44.0	46.9	9.1	3.0	-2.0	99.0	
134A_105	22.50	1.80	4.04	22.66	0.26	0.12	0.09	0.13	99.87	84.88	46.9	47.2	5.9	5.2	-4.0	98.8	
134A_106	21.89	1.67	4.52	22.96	0.29	0.06	0.12	0.11	99.89	83.55	45.5	47.7	6.8	5.7	-4.7	99.0	
134A_111	22.82	2.89	4.53	21.61	0.40	0.17	0.10	0.14	99.86	82.67	48.4	45.9	5.7	8.0	-6.8	98.8	
134A_112	22.29	1.90	4.28	22.55	0.27	0.04	0.09	0.12	99.88	84.05	46.3	46.8	6.9	4.2	-3.2	99.0	
134A_114	22.82	3.36	4.29	21.27	0.37	0.33	0.09	0.17	99.83	83.23	48.6	45.3	6.0	6.3	-4.9	98.6	
134A_116	21.27	1.65	6.24	21.78	0.39	0.01	0.15	0.13	99.87	77.72	44.2	45.3	10.5	5.5	-4.3	98.8	
134A_127	22.57	3.09	4.87	21.23	0.46	0.07	0.10	0.18	99.82	81.36	48.0	45.1	6.9	7.1	-5.5	98.4	
134A_128	22.08	3.52	7.69	19.13	0.90	0.00	0.16	0.25	99.75	71.33	48.0	41.6	10.4	12.8	-10.6	97.8	
134A_136	21.67	1.68	5.08	22.43	0.31	0.05	0.17	0.13	99.87	81.53	45.0	46.6	8.4	4.8	-3.7	98.8	
134A_137	20.04	1.51	8.24	20.70	0.40	0.01	0.24	0.16	99.84	71.52	41.5	42.9	15.6	3.6	-2.0	98.5	
134A_141	22.72	2.67	4.74	21.20	0.39	0.05	0.10	0.17	99.83	81.72	47.8	44.6	7.6	4.8	-3.3	98.5	
134A_143	22.66	3.32	4.03	21.45	0.34	0.36	0.07	0.22	99.78	84.18	48.3	45.7	6.0	5.3	-3.3	98.1	
134B1_156	20.80	2.61	6.89	21.47	0.56	0.02	0.17	0.12	99.88	75.71	44.0	45.4	10.6	9.0	-7.8	98.9	
134B1_157	21.00	2.90	6.06	21.88	0.59	0.09	0.14	0.13	99.87	78.32	44.6	46.4	9.0	8.5	-7.3	98.8	
134B1_167	22.08	4.27	6.72	19.45	1.01	0.09	0.12	0.19	99.81	74.33	47.8	42.1	10.1	9.1	-7.4	98.3	
134B1_168	22.89	4.57	6.33	19.06	1.09	0.12	0.12	0.18	99.82	75.06	49.9	41.5	8.6	10.3	-8.7	98.5	
134B1_169	20.95	3.28	6.95	20.83	0.63	0.01	0.16	0.14	99.86	74.98	44.6	44.4	11.0	8.4	-7.1	98.7	
134B1_182	23.16	1.88	6.93	18.68	0.33	0.06	0.27	0.15	99.85	72.95	48.2	38.9	12.8	3.3	-2.0	98.7	
134B1_183	21.54	4.14	6.99	19.79	0.88	0.07	0.14	0.23	99.77	73.89	46.8	43.0	10.3	10.3	-8.3	97.9	
134B1_184	21.30	2.60	8.51	19.27	0.28	0.03	0.30	0.15	99.85	69.36	45.4	41.1	13.6	10.0	-8.6	98.6	
134B1_185	22.66	4.48	6.11	19.55	0.96	0.10	0.11	0.19	99.81	76.21	49.3	42.6	8.1	10.3	-8.7	98.4	
134B1_186	21.82	3.70	5.75	20.88	0.53	0.13	0.11	0.18	99.82	78.42	46.8	44.8	8.4	8.2	-6.6	98.4	
134B1_187	21.46	1.94	6.66	21.30	0.37	0.05	0.21	0.12	99.88	76.17	45.1	44.8	10.1	8.6	-7.5	98.9	
134B1_204	21.84	4.39	9.97	16.28	1.25	0.01	0.18	0.35	99.65	62.02	48.1	35.9	16.0	11.9	-8.9	96.9	
134B1_205	21.76	4.15	6.06	20.13	0.63	0.08	0.12	0.19	99.81	76.87	46.7	43.2	10.2	5.9	-4.2	98.3	
134B1_206	22.53	5.19	6.94	18.12	1.21	0.05	0.13	0.19	99.81	72.32	49.0	39.4	11.6	7.1	-5.4	98.3	
134B1_207	22.66	5.79	7.93	17.09	1.58	0.02	0.14	0.20	99.80	68.30	50.1	37.8	12.1	10.7	-9.0	98.2	
134B1_208	22.69	5.25	6.32	18.78	1.17	0.09	0.11	0.15	99.85	74.81	49.5	40.9	9.6	8.3	-7.0	98.7	
134B1_209	20.33	2.45	6.23	22.22	0.46	0.03	0.14	0.09	99.91	78.11	42.3	46.3	11.4	3.8	-2.9	99.1	
134B1_224	20.11	3.81	9.13	18.19	0.84	0.00	0.21	0.31	99.69	66.59	43.1	39.0	17.8	3.9	-1.0	97.1	
134B1_225	20.55	4.80	9.23	16.67	1.21	0.01	0.17	0.42	99.58	64.35	44.4	36.0	19.6	0.8	3.2	96.1	
134B1_226	18.78	1.93	8.79	21.66	0.46	0.00	0.24	0.11	99.89	71.13	39.3	45.3	15.4	7.5	-6.3	98.8	
134B1_194	22.35	2.48	4.08	22.02	0.30	0.18	0.10	0.15	99.85	84.37	46.6	45.9	7.5	2.1	-0.8	98.7	
134B1_195	22.74	2.93	4.07	21.69	0.33	0.21	0.09	0.13	99.87	84.21	47.8	45.6	6.5	4.1	-3.0	98.9	
134B1_197	20.64	2.87	8.25	19.95	0.67	0.02	0.20	0.14	99.86	70.76	43.8	42.3	13.9	8.0	-6.6	98.7	
134B1_282	22.23	1.81	3.99	22.50	0.24	0.19	0.09	0.13	99.87	84.92	45.9	46.4	7.7	1.2	-0.1	98.9	
134B1_288	22.38	1.79	4.00	22.52	0.25	0.18	0.09	0.13	99.87	84.92	46.3	46.6	7.1	2.6	-1.5	98.9	
134B1_291	20.53	2.03	6.99	21.21	0.50	0.01	0.19	0.28	99.72	75.22	43.3	44.7	12.0	6.1	-3.4	97.3	
134B1_292	20.72	2.11	6.82	21.25	0.55	0.01	0.19	0.28	99.72	75.69	43.8	44.9	11.3	6.9	-4.3	97.4	
134B1_293	22.74	2.68	4.64	21.67	0.38	0.13	0.09	0.13	99.87	82.36	48.1	45.8	6.2	7.5	-6.4	98.9	
134B1_299	22.88	2.75	5.21	21.07	0.47	0.03	0.10	0.16	99.84	80.19	48.6	44.8	6.6	9.1	-7.7	98.6	
134B1_300	22.82	2.77	5.63	20.89	0.53	0.02	0.10	0.20	99.80	78.77	48.9	44.8	6.3	11.5	-9.8	98.3	
134B1_304	22.56	2.81	4.55	22.00	0.39	0.13	0.10	0.17	99.83	82.85	48.1	46.9	5.0	9.7	-8.2	98.5	
134B1_305	22.42	3.29	4.39	21.31	0.40	0.23	0.09	0.15	99.85	82.91	47.3	44.9	7.8	3.0	-1.7	98.7	
134B1_306	22.41	3.55	4.43	21.24	0.42	0.34	0.09	0.17	99.83	82.73	47.7	45.2	7.2	4.7	-3.2	98.5	
134B1_308	22.50	3.17	4.00	21.67	0.34	0.33	0.08	0.17	99.83	84.40	47.5	45.8	6.7	3.7	-2.2	98.5	
134B1_309	22.72	2.93	3.88	21.74	0.31	0.33	0.09	0.16	99.84	84.87	47.9	45.8	6.3	3.8	-2.5	98.6	
134B1_310	22.60	3.39	4.33	21.20	0.39	0.33	0.10	0.18	99.82	83.04	48.0	45.0	6.9	4.6	-3.1	98.5	
134B1_311	22.88	3.10	4.16	21.22	0.34	0.32	0.09	0.14	99.86	83.60	48.2	44.7	7.1	3.5	-2.3	98.8	
134B1_312	22.40	2.32	4.02	22.21	0.27	0.23	0.09	0.14	99.86	84.68	46.7	46.3	7.0	3.0	-1.8	98.8	
134B1_313	22.46	3.23	4.29	21.60	0.34	0.18	0.09	0.19	99.81	83.43	47.7	45.9	6.4	5.5	-3.8	98.3	

Notes: Analytical uncertainty was calculated from standard deviations of measured standards: Si <0.14%; Al <0.09%; Ca <0.16%; Fe <0.18%; Mg <0.06%; Na <0.15%; K <0.03%; Ti <0.33%; Cr <0.1%, and Mn <0.06%.

Measured standards included: Cr2O3 chromium oxide Alfa for Cr ka, Fe2SiO4 fayalite Rockport for Fe ka, TiO2 Rutile MTI for Ti ka, CaMgSi2O6 diopside Wakefield for Mg ka, Si ka, Ca ka, NaAlSi3O8 albite VA 131705 for Na ka, KAlSi3O8 sanidine Itrongay for Al ka, K ka, and Spessartine Little 3 for Mn ka.

Table A2 - EMPA prehnite compositions

SAMPLE_SPOT	PHASE	SPOT LOCATION	SiO2_pct	TiO2_pct	Al2O3_pct	Cr2O3_pct	FeO_pct	MnO_pct	MgO_pct	CaO_pct	Na2O_pct	H2O_pct	TOTAL	Si cation %	Ca cation %	Al cation %	Fe cation %	Mg cation %	Ti cation %	T
134A_80	prehnite	intergranular - orbicule	43.62	0.04	23.86	0	1.55	0.06	0	26.39	0.06	4.34	99.9	49.91	32.36	16.09	1.48	0	0.03	
134A_81	prehnite	intergranular - orbicule	43.67	0.04	24.65	0	0.66	0.02	0	26.57	0.04	4.36	100.0	50.02	32.61	16.64	0.63	0	0.03	
134A_82	prehnite	intergranular - orbicule	43.33	0.06	23.12	0	2.17	0.04	0	26.36	0.07	4.32	99.5	49.71	32.40	15.63	2.08	0	0.05	
134A_102	prehnite	intergranular - orbicule	43.1	0	24.06	0.03	1.58	0.01	0	26.67	0	4.33	99.8	49.44	32.78	16.26	1.52	0	0.00	
134A_103	prehnite	intergranular - orbicule	43.15	0.02	23.3	0.04	1.97	0.02	0	26.44	0.04	4.33	99.3	49.64	32.59	15.80	1.90	0	0.02	
134A_104	prehnite	intergranular - orbicule	43.21	0.04	23.15	0.04	2.09	0.01	0	26.32	0.04	4.33	99.2	49.74	32.46	15.70	2.01	0	0.03	
134B1_158	prehnite	intergranular - orbicule	43.04	0.15	23.12	0.03	2.15	0.02	0	26.52	0.03	4.32	99.4	49.45	32.65	15.65	2.07	0	0.13	
134B1_159	prehnite	intergranular - orbicule	42.92	0.17	23.16	0.02	2.06	0.02	0	26.53	0	4.32	99.2	49.41	32.73	15.71	1.98	0	0.15	
134B1_160	prehnite	intergranular - orbicule	43.16	0.18	23.16	0	2.09	0.02	0	26.48	0.03	4.32	99.4	49.55	32.57	15.67	2.01	0	0.16	
134B1_170	prehnite	intergranular - orbicule	43.21	0.09	22.67	0	2.71	0.02	0.06	26.46	0.08	4.31	99.6	49.42	32.42	15.28	2.59	0.1023	0.08	
134B1_171	prehnite	intergranular - orbicule	43.59	0.1	23.21	0	2.18	0.03	0	26.54	0.11	4.32	100.1	49.68	32.41	15.59	2.08	0	0.09	
134B1_172	prehnite	intergranular - orbicule	43.4	0.04	22.81	0	2.48	0.07	0	26.35	0.09	4.32	99.6	49.70	32.33	15.39	2.38	0	0.03	
134B1_201	prehnite	intergranular - orbicule	43.29	0.09	22.82	0.04	2.38	0	0	26.45	0.05	4.32	99.4	49.65	32.51	15.42	2.28	0	0.08	
134B1_202	prehnite	intergranular - orbicule	43.12	0.32	22.23	0	2.9	0.02	0.05	26.17	0.04	4.31	99.2	49.53	32.21	15.05	2.79	0.0857	0.28	
134B1_203	prehnite	intergranular - orbicule	43.34	0.1	23.03	0	2.23	0	0	26.24	0.07	4.33	99.3	49.80	32.30	15.59	2.14	0	0.09	
134B1_212	prehnite	intergranular - orbicule	43.28	0.11	23	0	2.1	0.02	0	26.54	0.02	4.32	99.4	49.66	32.63	15.55	2.02	0	0.09	
134B1_213	prehnite	intergranular - orbicule	43.28	0.11	22.94	0	2.24	0.01	0	26.27	0.05	4.33	99.2	49.77	32.37	15.55	2.15	0	0.10	
134B1_214	prehnite	intergranular - orbicule	43.08	0.07	21.71	0	3.66	0	0	26.2	0.07	4.29	99.1	49.45	32.22	14.68	3.51	0	0.06	
134B1_218	prehnite	intergranular - orbicule	42.98	0.1	22.83	0.03	2.51	0.02	0	26.48	0.03	4.31	99.3	49.39	32.60	15.46	2.41	0	0.09	
134B1_219	prehnite	intergranular - orbicule	43.64	0.02	23.79	0	1.83	0.05	0	26.51	0.05	4.33	100.3	49.74	32.37	15.98	1.74	0	0.02	
134B1_220	prehnite	intergranular - orbicule	43.39	0.08	23.03	0.03	2.35	0.02	0	26.39	0.09	4.32	99.7	49.66	32.36	15.53	2.25	0	0.07	
134B1_221	prehnite	intergranular - orbicule	43.2	0.04	24.69	0	0.82	0.03	0	26.62	0.09	4.35	99.9	49.58	32.74	16.70	0.79	0	0.03	
134B1_222	prehnite	intergranular - orbicule	43.73	0.08	23.93	0	1.3	0.02	0	26.52	0.16	4.34	100.1	49.94	32.45	16.10	1.24	0	0.07	
134B1_223	prehnite	intergranular - orbicule	43.87	0.1	24.08	0	1.22	0.02	0	26.39	0.28	4.35	100.3	50.01	32.23	16.18	1.16	0	0.09	

Notes: Analytical uncertainty was calculated from standard deviations of measured standards: Si <0.14%; Al <0.09%; Ca <0.16%; Fe <0.18%; Mg <0.06%; Na <0.15%; K <0.03%; Ti <0.33%; Cr <0.1%, and Mn <0.06%.
Measured standards included: Cr2O3 chromium oxide Alfa for Cr ka, Fe2SiO4 fayalite Rockport for Fe ka, TiO2 Rutile MTI for Ti ka, CaMgSi2O6 diopside Wakefield for Mg ka, Si ka, Ca ka,
NaAlSi3O8 albite VA 131705 for Na ka, KAlSi3O8 sanidine Itrongay for Al ka, K ka, and Spessartine Little 3 for Mn ka.

Table A3 - EMPA titanite compositions

SAMPLE_SPOT	PHASE	SPOT LOCATION	SiO2_pct	TiO2_pct	Al2O3_pct	Cr2O3_pct	FeO_pct	MnO_pct	MgO_pct	CaO_pct	TOTAL	Si cation %	Ca cation %	Al cation %	Fe cation %	Mg cation %	Ti cation %	Total
134A_98	titanite	intergranular - host melt	31.47	31.43	4.56	0.04	1.47	0	0	28.04	97.01	35.32	33.72	3.02	1.38	0	26.54	100.0
134A_99	titanite	intergranular - host melt	32.36	24.74	8.8	0	1.97	0.03	0.24	27.24	95.38	37.03	33.40	5.93	1.89	0.41	21.30	100.0
134A_100	titanite	intergranular - host melt	32.51	24.68	8.88	0	2.03	0.03	0.26	28.25	96.64	36.66	34.13	5.90	1.91	0.44	20.94	100.0
134A_101	titanite	intergranular - host melt	31.54	31.46	4.69	0	1.51	0	0	29.15	98.35	34.86	34.52	3.05	1.40	0	26.16	100.0
134A_78	titanite	intergranular - orbicule	31.94	31.97	4.6	0.07	0.84	0	0	29.24	98.66	35.20	34.53	2.99	0.77	0	26.51	100.0
134A_79	titanite	intergranular - orbicule	34.29	23.24	9.27	0.04	1.98	0	0	28.76	97.58	38.22	34.35	6.09	1.85	0	19.49	100.0
134A_108	titanite	intergranular - orbicule	31.77	31.44	4.96	0.06	0.98	0	0.15	29.1	98.46	35.08	34.43	3.23	0.90	0.25	26.12	100.0
134A_109	titanite	intergranular - orbicule	32	31.99	4.67	0.06	0.94	0	0	29.26	98.92	35.18	34.47	3.03	0.86	0	26.46	100.0
134A_110	titanite	intergranular - orbicule	32.25	30.81	5.05	0.08	0.89	0.02	0	29.24	98.34	35.64	34.62	3.29	0.82	0	25.61	100.0
134A_117	titanite	intergranular - orbicule	31.56	31.57	4.19	0.04	1.3	0	0	29.19	97.85	35.00	34.68	2.74	1.21	0	26.34	100.0
134A_118	titanite	intergranular - orbicule	32.29	30.84	4.94	0.11	1.43	0	0	29	98.61	35.61	34.27	3.21	1.32	0	25.59	100.0
134A_119	titanite	intergranular - orbicule	31.72	32.42	4.13	0.05	1.14	0	0	29.26	98.72	34.92	34.51	2.68	1.05	0	26.85	100.0
134B1_161	titanite	intergranular - orbicule	31.73	30.76	4.42	0.03	1.87	0	0.34	28.36	97.51	35.26	33.76	2.89	1.74	0.56	25.71	99.9
134B1_162	titanite	intergranular - orbicule	33.29	27.26	7.54	0	1.95	0	0.2	28.61	98.85	36.64	33.74	4.89	1.79	0.33	22.57	100.0
134B1_163	titanite	intergranular - orbicule	32.71	29.12	6.1	0	1.91	0	0.24	28.66	98.74	35.97	33.77	3.95	1.76	0.39	24.09	99.9
134B1_173	titanite	intergranular - orbicule	32.71	26.3	7.95	0.03	1.96	0	0.06	29.25	98.26	36.24	34.72	5.19	1.82	0.10	21.92	100.0
134B1_174	titanite	intergranular - orbicule	33.27	25.27	8.35	0	1.97	0.02	0.21	28.66	97.75	37.01	34.16	5.47	1.83	0.35	21.15	100.0
134B1_175	titanite	intergranular - orbicule	31.66	29.78	5.2	0	2.06	0	0.41	28.46	97.57	35.19	33.89	3.41	1.91	0.68	24.90	100.0
134B1_198	titanite	intergranular - orbicule	31.86	29.44	5.91	0	1.67	0	0	29.25	98.13	35.31	34.73	3.86	1.55	0	24.55	100.0
134B1_199	titanite	intergranular - orbicule	33.78	25.05	8.5	0	1.67	0	0.07	28.68	97.75	37.59	34.20	5.57	1.55	0.12	20.97	100.0
134B1_200	titanite	intergranular - orbicule	35.79	19.76	12.75	0	2.15	0.02	0	28.89	99.36	39.35	34.03	8.26	1.98	0	16.34	100.0
134B1_215	titanite	intergranular - orbicule	31.67	30.21	5.5	0	1.8	0	0	29.27	98.45	34.99	34.65	3.58	1.66	0	25.11	100.0
134B1_216	titanite	intergranular - orbicule	31.6	28.85	5.99	0	1.74	0	0	30.14	98.32	34.87	35.64	3.90	1.61	0	23.95	100.0
134B1_217	titanite	intergranular - orbicule	31.89	28.12	6.43	0	2.15	0	0.05	29.35	97.99	35.37	34.88	4.20	1.99	0.08	23.47	100.0

Notes: Analytical uncertainty was calculated from standard deviations of measured standards: Si <0.14%; Al <0.09%; Ca <0.16%; Fe <0.18%; Mg <0.06%; Na <0.15%; K <0.03%; Ti <0.33%; Cr <0.1%, and Mn <0.06%.
Measured standards included: Cr2O3 chromium oxide Alfa for Cr ka, Fe2SiO4 fayalite Rockport for Fe ka, TiO2 Rutile MTI for Ti ka, CaMgSi2O6 diopside Wakefield for Mg ka, Si ka, Ca ka, NaAlSi3O8 albite VA 131705 for Na ka, KAlSi3O8 sanidine Itrongay for Al ka, K ka, and Spessartine Little 3 for Mn ka.

Table A4 - EMPA albite compositions

SAMPLE_SPOT	PHASE	SPOT LOCATION	SiO2_pct	TiO2_pct	Al2O3_pct	Cr2O3_pct	FeO_pct	MnO_pct	MgO_pct	CaO_pct	Na2O_pct	K2O_pct	TOTAL	Si cation %	Ca cation %	Al cation %	Fe cation %	Na_cations (%)	K_cations (%)	Mg cation %	TOTAL
134A_89	albite	intergranular - host melt	68.97	0	19.83	0	0.1	0	0	0.13	11.73	0.02	100.78	74.75	0.15	12.67	0.09	12.33	0.01	0	100.0
134A_90	albite	intergranular - host melt	68.96	0	20	0.02	0.08	)	0	0.28	11.37	0.03	100.74	74.83	0.33	12.79	0.07	11.96	0.02	0	100.0
134A_91	albite	intergranular - host melt	68.61	0	19.75	0	0.12	0	0	0.22	11.37	0.03	100.1	74.88	0.26	12.70	0.11	12.03	0.02	0	100.0
134A_176	albite	intergranular - host melt	68.42	0	20.19	0	0.29	0	0	0.49	11.38	0.06	100.83	74.24	0.57	12.91	0.26	11.97	0.04	0	100.0
134B1_177	albite	intergranular - host melt	68.49	0	20.18	0	0.38	0	0	0.43	11.55	0.06	101.09	74.13	0.50	12.87	0.34	12.12	0.04	0	100.0
134B1_178	albite	intergranular - host melt	68.79	0	19.98	0	0.37	0.01	0	0.19	11.61	0.06	101.01	74.47	0.22	12.75	0.33	12.18	0.04	0	100.0
134B1_188	albite	intergranular - host melt	67.25	0	20.56	0	0.21	0	0	1.05	11.03	0.12	100.22	73.55	1.23	13.25	0.19	11.69	0.08	0	100.0
134B1_189	albite	intergranular - host melt	67.82	0	20.64	0	0.17	0	0	0.94	11.37	0.06	101	73.56	1.09	13.19	0.15	11.96	0.04	0	100.0
134B1_190	albite	intergranular - host melt	67.8	0	20.5	0	0.28	0	0	0.88	11.36	0.07	100.89	73.60	1.02	13.11	0.25	11.96	0.05	0	100.0
134B1_344	albite	intergranular - host melt	67.65	0	20.91	0	0.09	0	0	0.97	10.95	0.2	100.77	73.67	1.13	13.42	0.08	11.56	0.14	0	100.0
134B1_345	albite	intergranular - host melt	67.55	0	20.83	0	0.1	0	0	0.56	11.07	0.29	100.4	73.89	0.66	13.43	0.09	11.74	0.20	0	100.0
134B1_346	albite	intergranular - host melt	67.14	0	21.09	0	0.15	0	0	0.87	10.82	0.38	100.45	73.49	1.02	13.60	0.14	11.48	0.27	0	100.0
134B1_347	albite	intergranular - host melt	67.89	0.02	20.61	0	0.13	0	0	0.98	11.01	0.07	100.71	73.85	1.14	13.21	0.12	11.61	0.05	0	100.0
134B1_227	albite	intergranular - host melt	67.19	0	20.65	0	0.59	0	0.14	0.95	10.93	0.07	100.52	73.26	1.11	13.27	0.54	11.55	0.05	0.23	100.0
134B1_228	albite	intergranular - host melt	66.27	0.02	20.94	0	0.8	0	0.32	0.98	10.65	0.26	100.24	72.58	1.15	13.51	0.73	11.31	0.18	0.52	100.0
134B1_229	albite	intergranular - host melt	67.43	0.02	20.51	0	0.3	0	0	1.07	10.94	0.07	100.34	73.63	1.25	13.20	0.27	11.58	0.05	0	100.0

Notes: Analytical uncertainty was calculated from standard deviations of measured standards.: Si <0.14%; Al <0.09%; Ca <0.16%; Fe <0.18%; Mg <0.06%; Na <0.15%; K <0.03%; Ti <0.33%; Cr <0.1%, and Mn <0.06%.

Measured standards included: Cr2O5 chromium oxide Alfa for Cr ka, Fe2SiO4 fayalite Rockport for Fe ka, TiO2 Rutile MTI for Ti ka, CaMgSi2O6 diopside Wakefield for Mg ka, Si ka, Ca ka, NaAlSi3O8 albite VA 131705 for Na ka, KAlSi3O8 sanidine Itrongay for Al ka, K ka, and Spessartine Little 3 for Mn ka.

Table A5 - EMPA chlorite compositions

SAMPLE_SPOT	PHASE	SPOT LOCATION	SiO2_pct	TiO2_pct	Al2O3_pct	Cr2O3_pct	FeO_pct	MnO_pct	MgO_pct	CaO_pct	Na2O_pct	K2O_pct	H2O_pct	TOTAL	Si cation %	Ca cation %	Al cation %	Fe cation %	Mg cation %	Ti cation %	TOTAL
134A_92	chlorite	intergranular - host melt	29.86	0.04	16.69	0	21.18	0.25	19.23	0.21	0.03	0.03	11.77	99.29	34.48	0.26	11.36	20.46	33.11	0.03	99.7
134A_93	chlorite	intergranular - host melt	29.68	0.03	17.07	0	21.53	0.26	19.39	0.2	0.03	0.04	11.74	99.97	34.05	0.25	11.54	20.66	33.16	0.03	99.7
134A_94	chlorite	intergranular - host melt	30.1	0.03	17.09	0	20.78	0.26	18.86	0.2	0.08	0.04	11.81	99.25	34.91	0.25	11.68	20.15	32.61	0.03	99.6
134A_120	chlorite	intergranular - host melt	29.14	0	16.83	0.04	21.83	0.26	18.94	0.27	0	0.01	11.72	99.04	33.86	0.34	11.52	21.21	32.81	0	99.7
134A_121	chlorite	intergranular - host melt	27.83	0	18.27	0.02	23.32	0.31	17.05	0.42	0	0	11.62	98.84	33.04	0.53	12.78	23.15	30.18	0	99.7
134A_122	chlorite	intergranular - host melt	28.4	0	17.69	0	23.16	0.28	18.1	0.26	0	0	11.63	99.52	33.14	0.33	12.17	22.60	31.49	0	99.7
134A_129	chlorite	intergranular - host melt	29.22	0.02	15.98	0.02	21.38	0.25	19.83	0.28	0.04	0.01	11.73	98.76	33.72	0.35	10.87	20.63	34.12	0.02	99.7
134A_130	chlorite	intergranular - host melt	29.67	0	17.55	0	21.62	0.25	18.7	0.23	0	0	11.75	99.77	34.33	0.29	11.97	20.92	32.25	0	99.8
134A_131	chlorite	intergranular - host melt	29.68	0	17.1	0	22.15	0.26	19.61	0.17	0	0	11.7	100.67	33.76	0.21	11.46	21.07	33.25	0	99.7
134B1_179	chlorite	intergranular - host melt	28.88	0	16.33	0	22.87	0.27	18.29	0.19	0.05	0.03	11.65	98.56	33.82	0.24	11.27	22.40	31.93	0	99.7
134B1_180	chlorite	intergranular - host melt	28.03	0	18.89	0	24.34	0.35	16.57	0.11	0	0.01	11.58	99.88	33.12	0.14	13.15	24.05	29.18	0	99.6
134B1_181	chlorite	intergranular - host melt	29.49	0.02	17.07	0	22.76	0.27	18.43	0.15	0.04	0.02	11.67	99.92	34.09	0.19	11.63	22.00	31.76	0.02	99.7
134B1_191	chlorite	intergranular - host melt	29.14	0	16.74	0	22.64	0.26	18.24	0.2	0.04	0.04	11.68	98.98	34.03	0.25	11.52	22.11	31.75	0	99.7
134B1_192	chlorite	intergranular - host melt	29.23	0.02	16.92	0	22.97	0.27	18.23	0.22	0	0.03	11.65	99.54	33.95	0.27	11.58	22.31	31.57	0.02	99.7
134B1_193	chlorite	intergranular - host melt	30.24	0.33	16.46	0	22.66	0.29	18.4	1	0	0.03	11.64	101.05	34.40	1.22	11.03	21.56	31.20	0.28	99.7
134B1_210	chlorite	intergranular - host melt	28.3	0.02	18.44	0	24.36	0.3	16.93	0.12	0	0	11.58	100.05	33.23	0.15	12.76	23.92	29.63	0.02	99.7
134B1_211	chlorite	intergranular - host melt	28.51	0.02	16.76	0	22.92	0.26	17.61	0.16	0.03	0	11.66	97.93	33.84	0.20	11.72	22.75	31.16	0.02	99.7
134B1_230	chlorite	intergranular - host melt	28.12	0.02	18.46	0	24	0.34	17.39	0.15	0	0	11.58	100.06	32.91	0.19	12.73	23.49	30.34	0.02	99.7

Notes: Analytical uncertainty was calculated from standard deviations of measured standards: Si <0.14%; Al <0.09%; Ca <0.16%; Fe <0.18%; Mg <0.06%; Na <0.15%; K <0.03%; Ti <0.33%; Cr <0.1%, and Mn <0.06%.

Measured standards included: Cr2O3 chromium oxide Alfa for Cr ka, Fe2SiO4 fayalite Rockport for Fe ka, TiO2 Rutile MTI for Ti ka, CaMgSi2O6 diopside Wakefield for Mg ka, Si ka, Ca ka, NaAlSi3O8 albite VA 131705 for Na ka, KAlSi3O8 sanidine Itrongay for Al ka, K ka, and Spessartine Little 3 for Mn ka.

Table A6 - EMPA epidote compositions

SAMPLE_SPOT	PHASE	SPOT LOCATION	SiO2_pct	TiO2_pct	Al2O3_pct	Cr2O3_pct	FeO_pct	MnO_pct	MgO_pct	CaO_pct	Na2O_pct	K2O_pct	H2O_pct	TOTAL	Si cation %	Ca cation %	Al cation %	Fe cation %	Mg cation %	Ti cation %	TOTAL
134B_164	epidote	intergranular - host melt	37.7	0.11	24.22	0	10.86	0.15	0.08	23.05	0	0	1.9	98.07	43.80	28.69	16.58	10.55	0.14	0.10	99.85
134B_165	epidote	intergranular - host melt	37.42	0.06	23.93	0	11.1	0.12	0.64	22.26	0	0	1.9	97.43	43.64	27.81	16.44	10.82	1.11	0.05	99.88
134B_166	epidote	intergranular - host melt	37.82	0.09	24.86	0	10.41	0.15	0	23	0.06	0	1.9	98.29	43.94	28.63	17.02	10.11	0	0.08	99.78

Notes: Analytical uncertainty was calculated from standard deviations of measured standards: Si <0.14%; Al <0.09%; Ca <0.16%; Fe <0.18%; Mg <0.06%; Na <0.15%; K <0.03%; Ti <0.33%; Cr <0.1%, and Mn <0.06%.
Measured standards included: Cr2O3 chromium oxide Alfa for Cr ka, Fe2SiO4 fayalite Rockport for Fe ka, TiO2 Rutile MTI for Ti ka, CaMgSi2O6 diopside Wakefield for Mg ka, Si ka, Ca ka, NaAlSi3O8 albite VA 131705 for Na ka, KAlSi3O8 sanidine Itrongay for Al ka, K ka, and Spessartine Little 3 for Mn ka.

Table A7: Mean phase compositions and standard deviations

Location	phase	value	SiO2_wt.%	CaO_wt.%	Al2O3_wt.%	FeO*_wt.%	MgO_wt.%	TiO2_wt.%	Cr2O3_wt.%	MnO_wt.%	Na2O_wt.%	K2O_wt.%	Total
orbicule	intergranular	mean	48.51	20.61	6.13	9.02	13.72	1.12	0.11	0.20	0.19	–	99.62
		std dev	*2.28*	*0.82*	*2.52*	*1.58*	*1.47*	*0.50*	*0.11*	*0.08*	*0.06*	–	
orbicule	prehnite	mean	43.32	26.43	23.26	2.05	0.00	0.09	–	–	–	–	95.16
		std dev	*0.25*	*0.13*	*0.70*	*0.65*	*0.02*	*0.07*	–	–	–	–	
orbicule	titanite	mean	32.49	29.03	6.32	1.62	0.09	28.71	–	–	–	–	98.26
		std dev	*1.11*	*0.41*	*2.17*	*0.45*	*0.13*	*3.34*	–	–	–	–	
host melt	intergranular	mean	49.38	20.80	5.41	8.88	13.94	0.83	0.14	0.23	0.21	–	99.82
		std dev	*1.88*	*1.40*	*1.97*	*1.76*	*1.50*	*0.41*	*0.11*	*0.09*	*0.09*	–	
host melt	chlorite	mean	29.08	0.25	17.24	22.58	18.32	0.03	–	–	–	–	87.51
		std dev	*0.74*	*0.20*	*0.81*	*1.06*	*0.93*	*0.08*	–	–	–	–	
host melt	albite	mean	67.89	0.69	20.45	0.26	0.03	–	–	–	11.20	0.12	100.63
		std dev	*0.76*	*0.35*	*0.41*	*0.20*	*0.09*	–	–	–	*0.31*	*0.11*	
host melt	epidote	mean	37.65	22.77	24.34	10.79	0.24	0.08	–	–	–	–	95.86
		std dev	*0.21*	*0.44*	*0.48*	*0.35*	*0.35*	*0.02*	–	–	–	–	
host melt	titanite	mean	31.97	28.17	6.73	1.75	0.13	28.08	–	–	–	–	96.82
		std dev	*0.54*	*0.78*	*2.43*	*0.30*	*0.14*	*3.89*	–	–	–	–	

Appendix B – Chapter 3 Supplemental Material

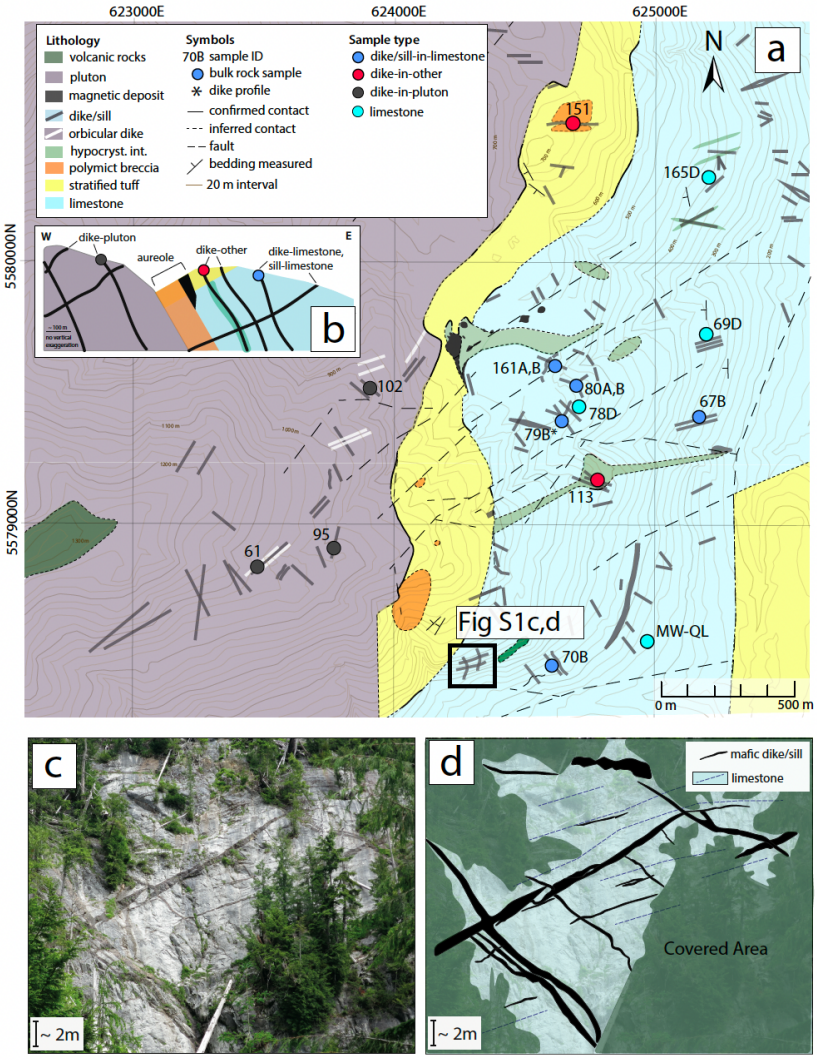

Figure B1: **(a)** Bedrock geology and sample locations collected at the Merry Widow location, modified after Sangster (1964), Lund (1966), Ray and Webster (1991), and Nixon et al. (2011). Unit labelled as 'hypocryst. int' is a less prolific but earlier swarm of wide (up to ~100 m in diameter) xenolith-rich hypocrystalline andesite dikes with near-vertical flow banding that are cross-cut by later mafic dikes. **(b)** Cross-section schematic displaying the naming scheme for the various dikes at the Merry Widow location. A generalized 'aureole' (skarn including magnetite ore + breccia) is also displayed. **(c)** Field photo demonstrating the extensive network of dikes and sills that intrude the limestone, and **(d)** a digitized schematic representing (B1c).

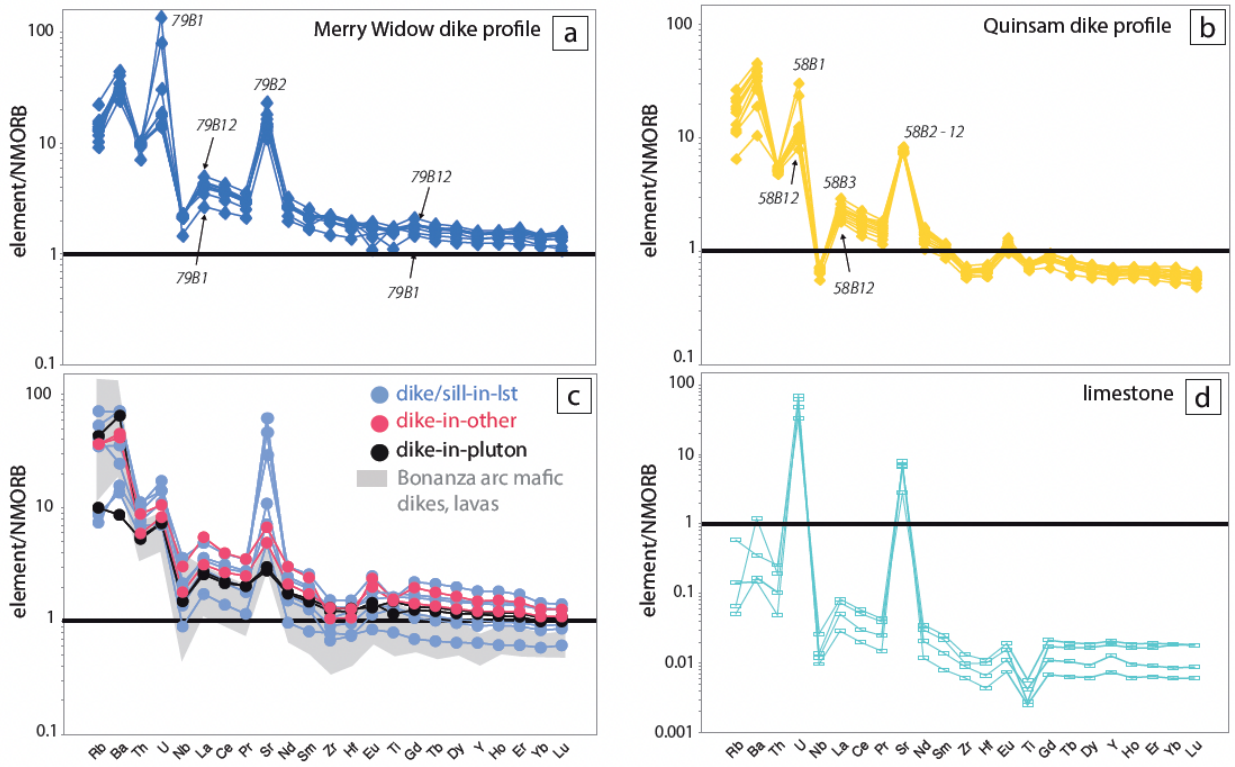

Figure B2: N-MORB normalized extended trace element plots (Sun and McDonough, 1989) for dike profiles **(a)** 79B and **(b)** 58B show elevated U and Sr peaks; **(c)** dikes at the Merry Widow location, including dike-in-limestone and sill-in-limestone samples show elevated U and Sr peaks. Dike-in-pluton samples display similar trends to basaltic Bonanza arc dikes and lavas from other localities (DeBari et al., 1999; Canil and Morris, 2023). Limestone **(d)** displays low concentrations (<1 ppm) in most trace elements, with the exception of U, Sr, Ba, Ti, and V (not shown – Table B1).

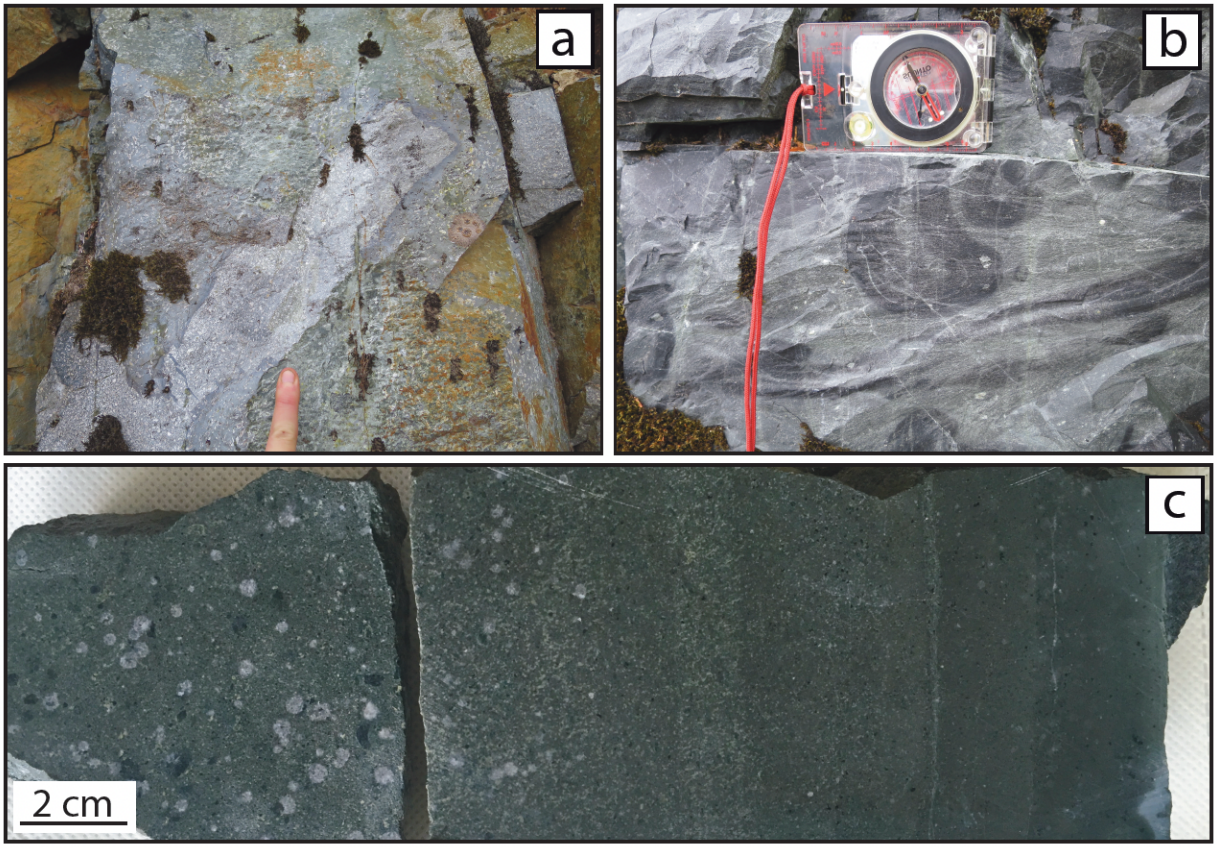

Figure B3: Multiple intrusions of magma is evident in dikes in the form of **(a)** earlier xenoliths entrained in host magma of similar composition and texture, and **(b,c)** flow banding. Images (a) and (b) from dikes near (a) or at (b) sample 151 locality (Figure B1). Image (c) is an orbicular dike (RM19-134) from Chapter 2 (Morris and Canil, 2022).

Table B1 Bulk rock major element (wt.%) and trace element (ppm) composition for silicate and carbonate samples

	dike-in-limestone						*sill-in-limestone*		*dike-in-pluton*			*dike-in-other*		*limestone*			
Sample	*67B*	*70B*	*79B*	*89B*	*161B*	161A	*80B*	80A	*102*	*61*	*95*	*113*	*151*	69D	78D	165D	MW-QL
Location/interval sampled	margin	margin	margin	margin	margin	interior	margin	interior	interior	interior	interior	interior	interior	n/a	n/a	n/a	n/a
Latitude	50.3536	50.3451	50.3536	50.3476	50.3556	50.3556	50.3547	50.3547	50.3547	50.3484	50.3491	50.3514	50.3638	50.3562	50.3538	50.3617	50.3453
Longitute	-127.2401	-127.2480	-127.2474	-127.2517	-127.2482	-127.2482	-127.2466	-127.2466	-127.2580	-127.2639	-127.2599	-127.2456	-127.2468	-127.2395	-127.2470	-127.2393	-127.2432
SiO_2	49.9	52.7	53.0	56.1	50.5	51.2	51.0	–	50.1	57.8	48.3	49.7	53.6	–	–	–	–
TiO_2	1.01	1.99	1.78	1.85	1.68	1.62	2.07	–	1.89	1.24	1.47	1.92	1.98	0.0054	0.0032	0.0073	0.0035
Al_2O_3	18.5	16.9	16.1	15.0	14.5	15.4	14.2	–	14.1	14.9	14.2	16.1	16.3	–	–	–	–
FeO*	6.58	7.19	9.08	6.87	8.24	8.23	10.08	–	12.67	7.85	10.05	9.92	8.56	–	–	–	–
MnO	0.14	0.15	0.16	0.13	0.18	0.17	0.17	–	0.21	0.22	0.21	0.18	0.08	0.0065	0.0084	0.0085	0.0023
MgO	6.06	3.11	3.36	2.30	3.78	4.13	4.20	–	3.91	1.65	3.97	4.75	3.31	0.89	0.49	5.07	7.92
CaO	12.89	8.40	7.64	7.45	12.89	10.72	9.54	–	6.32	4.36	8.53	10.97	7.92	53.74	55.64	50.64	45.69
Na_2O	2.65	4.72	5.05	4.83	4.95	4.24	3.57	–	3.50	5.43	4.07	3.13	4.88	–	–	–	–
K_2O	0.28	0.89	0.75	2.60	0.69	0.93	1.72	–	0.91	1.29	0.23	0.92	1.13	–	–	–	–
P_2O_5	0.17	0.69	0.34	0.63	0.27	0.22	0.31	–	0.21	0.44	0.18	0.27	0.68	–	–	–	–
LOI	1.73	2.02	1.77	2.06	1.92	1.88	1.39	1.63	4.33	3.78	7.85	1.61	1.22	–	–	–	–
Total	99.9	98.7	99.1	99.8	99.6	98.7	98.2	1.6	98.1	99.0	99.0	99.5	99.7	54.6	56.1	55.7	53.6
Ni	28.8	3.7	0.6	0.8	5.2	8.8	12.4	8.4	3.9	0.3	10.7	18.1	1.7	–	–	–	–
Cr	82.2	4.5	2.4	3.8	17.4	24.1	24.1	28.3	1.2	2.1	24.1	22.1	2.4	0.7	0.7	0.8	1.4
V	227	125	183	84	329	338	399	410	371	30	284	349	119	1.8	2.6	2.1	11.3
Sc	32	24	29	28	37	39	44	45	39	17	36	38	27	0.2	0.1	0.3	0.2
Co	18	6	23	24	18	24	27	16	36	10	31	22	12	–	–	–	–
Cu	12	6	19	109	16	14	63	34	13	9	57	28	13	–	–	–	–
Nb	2.1	8.4	5.7	10.4	3.6	3.2	5.0	4.5	3.5	7.3	3.5	4.2	7.1	0.03	0.02	0.06	0.03
Pb	0.5	1.0	1.1	2.6	1.4	1.2	10.5	2.6	1.6	4.5	2.3	1.3	1.4	0.15	0.06	0.52	0.05
Rb	4.9	19.5	12.8	43.4	4.1	23.2	39.8	29.8	24.1	28.3	5.6	20.5	20.4	0.03	0.08	0.33	0.04
Sr	439	2624	1472	895	645	981	4159	5553	270	252	252	442	606	602	720	622	252
Th	0.67	1.34	0.90	2.24	0.92	0.82	1.27	1.12	0.66	1.66	0.64	0.71	1.06	0.013	0.006	0.031	0.02
U	0.33	0.66	0.41	0.97	0.52	0.34	0.81	0.67	0.35	0.86	0.34	0.39	0.50	2.25	2.93	1.53	3.31
Cs	0.92	0.64	0.16	0.21	4.06	3.16	1.22	0.84	0.18	0.10	0.15	0.51	0.92	0.005	0.011	0.025	0.01
Y	18	51	36	61	28	25	40	41	33	53	32	34	42	0.4	0.2	0.6	0.5
Zr	58	113	61	182	67	50	98	78	97	202	91	97	78	0.7	0.5	1.0	0.7
Ba	86	223	229	600	99	154	439	449	410	277	55	283	261	1.1	0.9	2.2	7.5
Hf	1.55	3.13	1.79	4.86	1.97	1.52	2.71	2.50	2.66	5.30	2.48	2.64	2.19	0.014	0.009	0.023	0.020
Ta	0.13	0.53	0.35	0.64	0.22	0.20	0.32	0.29	0.22	0.46	0.22	0.26	0.44	0.001	0.001	0.004	0.005
La	4.3	12.3	11.0	17.3	7.1	7.0	8.6	9.1	6.5	13.8	6.8	7.9	13.7	0.126	0.072	0.209	0.185
Ce	10.5	29.4	25.5	44.6	17.1	16.2	21.9	23.6	16.2	33.7	16.8	20.1	29.8	0.226	0.149	0.438	0.385
Pr	1.53	4.62	4.01	7.16	2.64	2.38	3.55	3.65	2.70	5.19	2.68	3.30	4.65	0.033	0.020	0.057	0.052
Nd	7.1	22.1	18.2	32.6	12.3	11.1	16.8	18.0	13.1	23.9	12.7	15.5	22.0	0.151	0.087	0.260	0.220
Sm	2.13	6.82	5.12	9.05	3.64	3.34	5.09	5.32	4.13	6.94	3.90	4.57	6.38	0.036	0.021	0.066	0.057
Eu	0.86	2.55	1.78	2.67	1.40	1.16	1.59	1.84	1.34	2.31	1.48	2.04	2.43	0.011	0.008	0.019	0.016
Gd	2.56	8.14	5.79	9.96	4.24	3.92	5.91	6.26	4.92	7.97	4.62	5.26	7.27	0.040	0.025	0.079	0.064
Tb	0.45	1.43	0.98	1.66	0.73	0.68	1.03	1.09	0.88	1.38	0.82	0.91	1.20	0.007	0.004	0.013	0.011
Dy	2.94	9.08	6.20	10.41	4.73	4.38	6.71	7.04	5.71	8.92	5.31	5.83	7.51	0.043	0.028	0.086	0.076
Ho	0.62	1.85	1.28	2.18	0.99	0.93	1.41	1.50	1.20	1.88	1.12	1.23	1.54	0.010	0.006	0.019	0.017
Er	1.82	5.10	3.65	6.30	2.88	2.68	4.12	4.22	3.49	5.56	3.24	3.57	4.35	0.027	0.019	0.057	0.049
Tm	0.28	0.72	0.53	0.93	0.43	0.40	0.61	0.62	0.52	0.84	0.48	0.53	0.63	0.004	0.003	0.008	0.008
Yb	1.78	4.41	3.29	5.90	2.77	2.54	3.88	3.97	3.26	5.44	3.02	3.35	3.90	0.026	0.018	0.058	0.056
Lu	0.28	0.64	0.47	0.89	0.42	0.39	0.58	0.58	0.49	0.84	0.45	0.50	0.58	0.004	0.003	0.008	0.008

Notes:

Major and trace element data for samples italicized: *67B, 70B, 79B, 89B, 161B, 80B, 102, 61, 95, 113,* and *151* are from Morris and Canil (2022), included here for completeness, where sample names are shortened (i.e., *67B* refers to RM19-67B from Morris and Canil, 2022).

Major element total includes LOI. FeO* is total FeO, calculated from $Fe_2O_{3(total)}$*0.8995. See methods section for data accuracy and precision details. En dash (–) indicates element not analyzed;

Major element oxides are reported in weight percent (wt.%), trace element concentrations are in parts per million by weight (ppm).

*RM19-144 is a gabbro from the Merry Widow pluton, only included here as an external check comparing EMPA and ICP-OES methods for major element analyses.

References:

Morris, R.A., Canil, D., 2022, CO2 transport at shallow depths in arc magmas: Evidence from unique orbicular dikes in the Jurassic Bonanza arc, Vancouver Island, Canada: Contributions to Mineraloly and Petrology, v. 177, https://doi.org/10.1007/s00410-021-01852-y

Table B1 Bulk rock major element (wt.%) and trace element (ppm) composition for silicate and carbonate samples (con't)

dike profile

Sample	58B-1	58B-2	58B-3	58B-4	58B-5	58B-6	58B-7	58B-8	58B-9	58B-10	58B-11	58B-12	79B-1	79B-2	79B-3	79B-4	79B-5	79B-6	79B-7	79B-8	79B-10	79B-12
Location/interval sampled	0 - 3 mm	3 - 7 mm	7 - 12 mm	12 - 16 mm	16 - 21 mm	21 - 25 mm	25 - 29 mm	29 - 33 mm	33 - 38 mm	38 - 43 mm	43 - 46 mm	46 - 51 mm	5 - 9 mm	9 - 14 mm	14 - 20 mm	20 - 25 mm	25 - 30 mm	30 - 35 mm	35 - 40 mm	40 - 45 mm	50 - 55 mm	60 - 65 mm
Latitude	49.8483	49.8483	49.8483	49.8483	49.8483	49.8483	49.8483	49.8483	49.8483	49.8483	49.8483	49.8483	50.3536	50.3536	50.3536	50.3536	50.3536	50.3536	50.3536	50.3536	50.3536	50.3536
Longitute	-125.5102	-125.5102	-125.5102	-125.5102	-125.5102	-125.5102	-125.5102	-125.5102	-125.5102	-125.5102	-125.5102	-125.5102	-127.2474	-127.2474	-127.2474	-127.2474	-127.2474	-127.2474	-127.2474	-127.2474	-127.2474	-127.2474
SiO_2	46.7	48.0	51.0	51.2	51.3	51.7	51.5	52.0	52.1	51.5	51.2	51.7	37.0	45.5	46.6	48.4	48.8	49.8	50.3	50.5	50.4	49.4
TiO_2	0.99	0.90	0.95	0.96	0.88	0.91	0.95	0.98	0.96	0.93	0.91	0.89	1.42	2.15	2.02	1.99	1.93	2.01	2.01	2.05	2.10	2.18
Al_2O_3	18.1	18.7	19.3	19.1	19.1	19.7	19.4	19.6	20.2	20.1	19.6	19.8	9.3	15.5	14.6	14.5	14.5	14.6	14.7	14.9	15.1	14.6
FeO*	8.63	8.23	8.65	8.95	8.98	8.37	8.85	8.43	8.15	8.50	9.08	8.18	24.96	10.76	13.74	12.77	12.44	11.49	11.11	10.56	10.29	11.39
MnO	0.20	0.16	0.18	0.17	0.17	0.16	0.18	0.16	0.15	0.16	0.17	0.18	0.41	0.39	0.37	0.34	0.31	0.29	0.29	0.28	0.27	0.29
MgO	3.54	3.63	3.70	3.56	3.51	3.38	3.55	3.37	3.20	3.24	3.57	3.57	3.31	3.43	3.59	3.67	3.78	3.92	3.95	3.83	3.82	3.89
CaO	20.74	18.94	11.90	11.34	11.17	10.94	10.89	10.34	10.31	10.59	10.85	11.04	20.99	19.24	14.20	12.87	12.54	12.17	12.05	11.93	12.00	11.93
Na_2O	0.65	1.22	3.47	3.64	3.64	3.71	3.65	3.91	3.95	3.77	3.62	3.63	0.37	1.28	2.54	3.34	3.46	3.73	3.77	3.87	3.86	3.73
K_2O	0.17	0.33	0.52	0.52	0.57	0.69	0.67	0.77	0.67	0.61	0.62	0.49	0.30	0.63	0.75	0.61	0.64	0.71	0.73	0.71	0.77	0.77
P_2O_5	0.17	0.16	0.14	0.15	0.16	0.15	0.15	0.15	0.16	0.15	0.15	0.14	0.23	0.35	0.32	0.31	0.32	0.32	0.33	0.33	0.34	0.42
LOI	<dl	<dl	<dl	0.34	<dl	<dl	<dl	0.53	0.48	0.54	0.61	0.28	6.20	1.41	0.61	0.33	0.56	0.38	0.13	0.36	0.22	0.46
Total	100.0	100.2	99.8	99.9	99.5	99.7	99.7	100.3	100.3	100.2	100.4	99.8	104.5	100.7	99.3	99.1	99.3	99.4	99.4	99.4	99.2	99.1
Ni	1.4	1.3	2.2	2.4	2.3	1.9	2.3	4.1	2.4	2.8	2.5	2.2	23.9	2.5	4.7	5.7	5.7	5.7	5.8	6.0	5.8	5.9
Cr	1.8	1.7	1.7	1.9	1.3	1.1	1.3	1.2	0.9	1.4	1.1	1.4	8.0	7.4	8.0	7.5	8.1	8.0	7.5	8.4	7.0	7.4
V	226	233	232	237	231	225	225	237	238	235	238	223	261	296	335	314	320	327	317	320	326	329
Sc	23	22	23	22	23	22	22	24	23	24	23	22	29	42	41	39	39	40	36	40	40	40
Co	11	10	15	19	19	16	17	17	19	21	20	14	157	18	17	16	17	16	16	16	16	18
Cu	32	10	13	28	38	27	30	35	45	50	40	22	165	12	12	13	14	11	9	10	13	17
Nb	1.7	1.5	1.6	1.7	1.6	1.5	1.5	1.7	1.7	1.7	1.6	1.3	3.5	5.4	5.0	5.1	5.3	5.1	5.2	5.3	5.3	5.1
Pb	–	–	–	–	–	–	–	–	–	–	–	–	–	–	–	–	–	–	–	–	–	–
Rb	3.7	6.3	6.5	7.5	9.6	12.7	12.8	15.1	12.0	10.2	10.8	6.8	5.3	12.8	7.6	5.9	6.8	7.7	8.1	7.4	8.6	9.1
Sr	751	758	664	662	673	687	692	700	713	702	674	678	1007	2132	1394	1208	1270	1308	1322	1367	1527	1683
Th	0.68	0.68	0.64	0.58	0.66	0.63	0.62	0.69	0.65	0.63	0.62	0.60	0.87	1.20	1.25	1.17	1.27	1.19	1.14	1.23	1.22	1.18
U	1.44	1.13	0.48	0.52	0.60	0.50	0.57	0.55	0.47	0.48	0.44	0.38	6.65	3.85	1.47	0.90	0.85	0.71	0.69	0.66	0.69	0.71
Cs	–	–	–	–	–	–	–	–	–	–	–	–	–	–	–	–	–	–	–	–	–	–
Y	17	17	19	20	20	18	17	20	18	19	18	16	35	38	42	42	43	42	39	43	43	45
Zr	51	47	48	46	49	48	48	55	50	51	49	44	112	169	161	158	163	158	145	165	158	146
Ba	67	121	180	205	221	262	260	292	248	224	227	169	265	287	187	155	190	222	224	197	205	187
Hf	1.45	1.34	1.35	1.24	1.42	1.36	1.37	1.58	1.43	1.48	1.45	1.24	2.87	4.11	4.03	3.94	4.02	3.97	3.47	4.03	3.90	3.64
Ta	–	–	–	–	–	–	–	–	–	–	–	–	–	–	–	–	–	–	–	–	–	–
La	5.8	5.7	7.4	6.7	6.1	5.9	5.6	5.6	5.3	5.0	4.9	4.6	6.8	8.9	10.4	10.5	11.2	11.1	10.9	10.5	9.9	12.7
Ce	14.9	14.8	17.4	15.5	15.0	14.3	13.4	13.6	12.9	12.2	11.4	10.4	18.0	23.4	26.8	27.4	29.3	28.5	28.9	27.2	26.5	32.6
Pr	2.41	2.30	2.49	2.25	2.17	2.12	1.94	2.03	1.94	1.85	1.71	1.55	2.86	3.43	3.90	4.07	4.18	4.06	4.13	3.91	3.92	4.79
Nd	12.0	11.3	11.7	11.0	10.8	10.4	9.5	10.4	9.7	9.1	8.6	7.7	14.8	16.5	19.6	20.1	20.8	20.4	20.0	19.2	19.8	23.9
Sm	3.12	2.89	3.06	3.08	3.03	2.90	2.59	3.05	2.83	2.74	2.58	2.31	4.49	4.68	5.56	5.77	5.92	5.73	5.58	5.74	5.87	6.83
Eu	1.05	0.99	1.23	1.36	1.27	1.20	1.11	1.21	1.08	1.03	1.02	1.01	1.57	1.14	1.47	1.75	1.86	1.90	1.78	1.75	1.75	2.01
Gd	3.28	3.19	3.58	3.48	3.45	3.31	3.03	3.49	3.15	3.27	3.13	2.65	5.49	5.72	6.71	6.82	6.89	6.73	6.35	6.79	6.83	7.86
Tb	0.51	0.51	0.55	0.55	0.56	0.51	0.48	0.56	0.51	0.52	0.49	0.42	0.90	0.98	1.12	1.11	1.14	1.11	1.04	1.11	1.16	1.26
Dy	3.07	3.04	3.40	3.52	3.37	3.24	2.91	3.48	3.23	3.24	3.02	2.68	5.88	6.42	7.36	7.44	7.57	7.59	7.04	7.65	7.71	8.11
Ho	0.65	0.65	0.71	0.74	0.73	0.69	0.62	0.74	0.69	0.69	0.66	0.59	1.27	1.42	1.56	1.52	1.58	1.55	1.43	1.58	1.60	1.65
Er	1.80	1.84	2.00	2.17	2.10	1.94	1.81	2.09	1.89	2.00	1.87	1.65	3.66	4.07	4.46	4.65	4.75	4.66	4.28	4.89	4.93	5.13
Tm	0.25	0.27	0.30	0.31	0.31	0.29	0.28	0.33	0.28	0.30	0.29	0.24	0.55	0.57	0.66	0.65	0.69	0.68	0.59	0.67	0.68	0.68
Yb	1.67	1.79	2.01	2.24	2.07	1.91	1.77	2.03	1.82	1.86	1.83	1.61	3.61	3.67	4.23	4.35	4.42	4.43	4.06	4.52	4.54	4.59
Lu	0.22	0.26	0.27	0.29	0.28	0.28	0.26	0.30	0.26	0.28	0.26	0.24	0.54	0.50	0.62	0.66	0.68	0.66	0.63	0.73	0.70	0.67

Notes:

Major and trace element data for samples italicized: *67B, 70B, 79B, 89B, 161B, 80B, 102, 61, 93, 113,* and *151* are from Morris and Canil (2022), included here for completeness, where sample names are shortened (i.e., *67B* refers to RM19-67B from Morris and Canil, 2022).

Major element total includes LOI. FeO* is total FeO, calculated from $Fe_2O_{3(total)}$*0.8995. See methods section for data accuracy and precision details. En dash (–) indicates element not analyzed;

Major element oxides are reported in weight percent (wt.%), trace element concentrations are in parts per million by weight (ppm).

*RM19-144 is a gabbro from the Merry Widow pluton, only included here as an external check comparing EMPA and ICP-OES methods for major element analyses.

References:

Morris, R.A., Canil, D., 2022, CO2 transport at shallow depths in arc magmas: Evidence from unique orbicular dikes in the Jurassic Bonanza arc, Vancouver Island, Canada: Contributions to Mineraloly and Petrology, v. 177, https://doi.org/10.1007/s00410-021-01852-y

Table B1 **Table S1** Bulk rock major element (wt.%) and trace element (ppm) composition for silicate and carbonate samples (con't)

	duplicates					*repeats (from Morris & Canil, 2022)*			*external method check*		*standards (ICP-OES, Actlabs)*					*standards (solutions ICP-MS, UVic)*
Sample	79B_Dup	61_Dup	165D_DUP	79B-3_DUP	161A_Dup	80B_R	161B_R	95_R	RM19-144*_EMPA	RM19-144*_ICPOES	DNC-1	GBW 07113	W-2a	SY-4	BIR-1a	JLs-1
Location/interval sampled	margin	interior	n/a	14 - 20 mm	interior	margin	margin	interior	n/a	n/a	n/a	n/a	n/a	n/a	n/a	n/a
Latitude	50.3536	50.3484	50.3617	50.3536	50.3556	50.3547	50.3556	50.3491	50.3619	50.3619	n/a	n/a	n/a	n/a	n/a	n/a
Longitute	-127.2474	-127.2639	-127.2393	-127.2474	-127.2482	-127.2466	-127.2482	-127.2599	-127.2503	-127.2503	n/a	n/a	n/a	n/a	n/a	n/a
SiO_2	53.3	58.0	–	–	–	–	–	–	49.1	50.2	47.1	73.9	53.4	50.7	48.3	–
TiO_2	1.77	1.25	0.007	–	–	–	–	–	1.52	1.55	0.48	0.28	1.10	0.29	0.97	–
Al_2O_3	16.2	14.9	–	–	–	–	–	–	17.7	17.0	18.26	12.7	15.5	21.03	15.34	–
FeO*	9.07	7.92	–	–	–	–	–	–	10.53	10.21	8.55	2.91	10.31	5.59	9.81	–
MnO	0.15	0.22	0.008	–	–	–	–	–	0.2	0.2	0.15	0.14	0.16	0.11	0.17	–
MgO	3.36	1.68	5.09	–	–	–	–	–	5.25	5.16	10.02	0.14	6.29	0.5	9.61	–
CaO	7.61	4.44	51.6	–	–	–	–	–	11.44	11.61	11.41	0.58	10.92	7.99	13.59	–
Na_2O	5.10	5.45	–	–	–	–	–	–	2.94	2.90	1.89	2.5	2.26	7.01	1.82	–
K_2O	0.76	1.29	–	–	–	–	–	–	0.42	0.41	0.22	5.39	0.63	1.68	0.02	–
P_2O_5	0.34	0.45	–	–	–	–	–	–	0.13	0.10	0.08	0.03	0.12	0.12	0.04	–
LOI	–	–	–	–	–	–	–	–	–	–	–	–	–	–	–	–
Total	–	–	–	–	–	–	–	–	–	–	–	–	–	–	–	–
Ni	–	–		4.5	8.6	11.6	4.8	10.0	–	–	–	–	–	–	–	–
Cr	–	–	1	8	24	24	16	23	–	–	–	–	–	–	–	2.86
V	–	–	2	325	341	394	326	286	–	–	–	–	–	–	–	3.30
Sc	–	–	0	39	39	44	38	36	–	–	–	–	–	–	–	0.04
Co	–	–	–	16	24	26	17	31	–	–	–	–	–	–	–	–
Cu	–	–	–	9	13	59	14	53	–	–	–	–	–	–	–	–
Nb	–	–	0.1	4.9	3.2	4.9	3.5	3.4	–	–	–	–	–	–	–	0.02
Pb	–	–	0.6	0.7	1.1	9.6	1.3	2.1	–	–	–	–	–	–	–	0.08
Rb	–	–	0.3	7.5	21.8	38.7	3.8	5.1	–	–	–	–	–	–	–	0.11
Sr	–	–	625	1311	1030	4123	652	256	–	–	–	–	–	–	–	311
Th	–	–	0.03	1.08	0.86	1.27	0.93	0.71	–	–	–	–	–	–	–	0.02
U	–	–	1.54	1.25	0.38	0.82	0.54	0.37	–	–	–	–	–	–	–	1.74
Cs	–	–	–	–	3.37	1.27	4.29	0.16	–	–	–	–	–	–	–	0.02
Y	–	–	1	41	27	41	29	34	–	–	–	–	–	–	–	0.23
Zr	–	–	1	92	57	93	67	102	–	–	–	–	–	–	–	0.23
Ba	–	–	2	186	156	435	100	55	–	–	–	–	–	–	–	484
Hf	–	–	0.02	2.76	1.72	2.67	2.04	2.81	–	–	–	–	–	–	–	0.005
Ta	–	–	–	–	0.21	0.31	0.22	0.22	–	–	–	–	–	–	–	0.002
La	–	–	0.2	10.2	6.8	8.3	6.9	6.6	–	–	–	–	–	–	–	0.097
Ce	–	–	0.4	26.4	16.5	22.9	17.8	17.5	–	–	–	–	–	–	–	0.171
Pr	–	–	0.06	3.84	2.42	3.52	2.65	2.68	–	–	–	–	–	–	–	0.021
Nd	–	–	0.3	18.4	11.8	17.5	12.9	13.3	–	–	–	–	–	–	–	0.083
Sm	–	–	0.07	5.32	3.51	5.22	3.78	4.03	–	–	–	–	–	–	–	0.021
Eu	–	–	0.02	1.42	1.20	1.59	1.42	1.48	–	–	–	–	–	–	–	0.039
Gd	–	–	0.08	6.29	4.22	6.28	4.51	4.90	–	–	–	–	–	–	–	0.022
Tb	–	–	0.01	1.09	0.74	1.10	0.79	0.87	–	–	–	–	–	–	–	0.003
Dy	–	–	0.09	6.99	4.73	7.05	5.01	5.70	–	–	–	–	–	–	–	0.019
Ho	–	–	0.02	1.47	1.01	1.50	1.07	1.22	–	–	–	–	–	–	–	0.004
Er	–	–	0.06	4.11	2.83	4.22	3.02	3.45	–	–	–	–	–	–	–	0.013
Tm	–	–	0.01	0.60	0.42	0.62	0.45	0.51	–	–	–	–	–	–	–	0.002
Yb	–	–	0.06	3.88	2.72	4.02	2.91	3.30	–	–	–	–	–	–	–	0.012
Lu	–	–	0.01	0.57	0.41	0.59	0.44	0.49	–	–	–	–	–	–	–	0.002

Notes:

Major and trace element data for samples italicized: *67B, 70B, 79B, 89B, 161B, 80B, 102, 61, 95, 113,* and *151* are from Morris and Canil (2022), included here for completeness, where sample names are shortened (i.e., *67B* refers to RM19-67B from Morris and Canil, 2022).

Major element total includes LOI. FeO* is total FeO, calculated from $Fe_2O_{3(meas)}$*0.8995. See methods section for data accuracy and precision details. En dash (–) indicates element not analyzed;

Major element oxides are reported in weight percent (wt.%), trace element concentrations are in parts per million by weight (ppm).

*RM19-144 is a gabbro from the Merry Widow pluton, only included here as an external check comparing EMPA and ICP-OES methods for major element analyses.

References:

Morris, R.A., Canil, D., 2022, CO2 transport at shallow depths in arc magmas: Evidence from unique orbicular dikes in the Jurassic Bonanza arc, Vancouver Island, Canada: Contributions to Mineraloly and Petrology, v. 177, https://doi.org/10.1007/s00410-021-01852-y

Table B2 $^{87}Sr/^{86}Sr$ isotope compositions for bulk rock powder

	dike-in-limestone						*sill-in-limestone*		*dike-in-pluton*			*dike-in-other*	
Sample	67B	70B	79B	89B	161B	161A	80B	80A	102	61	95	113	151
Location/interval sampled	margin	margin	margin	margin	margin	interior	margin	interior	interior	interior	interior	interior	interior
Latitude	50.3536	50.3451	50.3536	50.3476	50.3556	50.3556	50.3547	50.3547	50.3547	50.3484	50.3491	50.3514	50.3638
Longitute	-127.2401	-127.2480	-127.2474	-127.2517	-127.2482	-127.2482	-127.2466	-127.2466	-127.2580	-127.2639	-127.2599	-127.2456	-127.2468
$^{87}Rb/^{86}Sr$	0.032	0.022	0.025	0.140	0.018	0.068	0.028	0.016	0.258	0.325	0.064	0.134	0.097
$^{87}Sr/^{86}Sr_{measured}$	0.7053	0.7072	0.7079	0.7068	0.7051	0.7068	0.7081	0.7081	0.7052	0.7046	0.7035	0.7049	0.7057
2 SE	0.0006	0.0006	0.0006	0.0006	0.0006	0.0006	0.0006	0.0011	0.0006	0.0006	0.0006	0.0006	0.0006
$^{87}Sr/^{86}Sr_{197Ma}$	0.7052	0.7071	0.7078	0.7064	0.7051	0.7066	0.7080	0.7080	0.7044	0.7037	0.7034	0.7045	0.7055
$^{87}Sr/^{86}Sr_{230Ma}$	–	–	–	–	–	–	–	–	–	–	–	–	–
Rb (ppm)	4.9	19.5	12.8	43.4	4.1	23.2	39.8	29.8	24.1	28.3	5.6	20.5	20.4
Sr (ppm)	439	2624	1472	895	645	981	4159	5553	270	252	252	442	606

Notes:

2 SE =analytical uncertainty reported as two standard deviations, except for sample 78D where repeat/duplicate analyses reported precision > analytical uncertainty;

Rb and Sr concentrations are from Table B1. En dash (–) indicates age not applicable for sample;

$^{87}Sr/^{86}Sr_{measured}$ indicates present-day ratio measured; $^{87}Sr/^{86}Sr_{197Ma}$ and $^{87}Sr/^{86}Sr_{230Ma}$ indicates calculated initial ratios based on ages of 197 Ma (silicates) and 230 Ma (carbonates), respectively.

Initital ratios for duplicate samples use non-duplicate Rb and Sr values from the same sample. 'Dup' refers to a duplicate analyses of digested sample (already in solution), whereas 'R' (i.e., 95_R) is a full procedural repeat from powder to solution.

Table B2 $^{87}Sr/^{86}Sr$ isotope compositions for bulk rock powders (con't)

	limestone				*dike profile*									
Sample	69D	78D	165D	MW-QL	58B-1	58B-2	58B-3	58B-4	58B-7	58B-11	79B-1	79B-2	79B-3	79B-4
Location/interval sampled	n/a	n/a	n/a	n/a	0 - 3 mm	3 - 7 mm	7 - 12 mm	12 - 16 mm	25 - 29 mm	43 - 46 mm	5 - 9 mm	9 - 14 mm	14 - 20 mm	20 - 25 mm
Latitude	50.3562	50.3538	50.3617	50.3453	49.8483	49.8483	49.8483	49.8483	49.8483	49.8483	50.3536	50.3536	50.3536	50.3536
Longitute	-127.2395	-127.2470	-127.2393	-127.2432	-125.5102	-125.5102	-125.5102	-125.5102	-125.5102	-125.5102	-127.2474	-127.2474	-127.2474	-127.2474
$^{87}Rb/^{86}Sr$	0.0001	0.0003	0.002	4.6E-04	0.014	0.024	0.028	0.033	0.054	0.046	0.015	0.017	0.016	0.014
$^{87}Sr/^{86}Sr_{measured}$	0.7079	0.7089	0.7081	0.7075	0.7061	0.7064	0.7044	0.7048	0.7051	0.7047	0.7067	0.7073	0.7067	0.7071
2 SE	0.0011	0.0013	0.0011	0.0011	0.0011	0.0011	0.0011	0.0011	0.0011	0.0011	0.0011	0.0011	0.0011	0.0011
$^{87}Sr/^{86}Sr_{197Ma}$	–	–	–	–	0.7061	0.7063	0.7043	0.7047	0.7050	0.7046	0.7066	0.7072	0.7066	0.7071
$^{87}Sr/^{86}Sr_{230Ma}$	0.7079	0.7089	0.7081	0.7075	–	–	–	–	–	–	–	–	–	–
Rb (ppm)	0.03	0.08	0.33	0.04	3.7	6.3	6.5	7.5	12.8	10.8	5.3	12.8	7.6	5.9
Sr (ppm)	602	720	622	252	751	758	664	662	692	674	1007	2132	1394	1208

Notes:

2 SE =analytical uncertainty reported as two standard deviations, except for sample 78D where repeat/duplicate analyses reported precision > analytical uncertainty;

Rb and Sr concentrations are from Table B1. En dash (–) indicates age not applicable for sample;

$^{87}Sr/^{86}Sr_{measured}$ indicates present-day ratio measured; $^{87}Sr/^{86}Sr_{197Ma}$ and $^{87}Sr/^{86}Sr_{230Ma}$ indicates calculated initial ratios based on ages of 197 Ma (silicates) and 230 Ma (carbonates), respectively.

Initital ratios for duplicate samples use non-duplicate Rb and Sr values from the same sample. 'Dup' refers to a duplicate analyses of digested sample (already in solution), whereas 'R' (i.e., 95_R) is a full procedural repeat from powder to solution.

Table B2 $^{87}Sr/^{86}Sr$ isotope compositions for bulk rock powders (con't)

	dike profile (con't)		*duplicates & procedural repeats*										
Sample	79B-7	79B-10	67B_Dup	80B_Dup	113_Dup	69D_Dup	78D_Dup	79B-3_Dup	161A_Dup	161B_Dup	80A_Dup	80B_R	95_R
Location/interval sampled	35 - 40 mm	50 - 55 mm	margin	margin	interior	n/a	n/a	14 - 20 mm	interior	margin	interior	margin	interior
Latitude	50.3536	50.3536	50.3536	50.3547	50.3514	50.3562	50.3538	50.3536	50.3556	50.3556	50.3547	50.3547	50.3491
Longitute	-127.2474	-127.2474	-127.2401	-127.2466	-127.2456	-127.2395	-127.2470	-127.2474	-127.2482	-127.2482	-127.2466	-127.2466	-127.2599
$^{87}Rb/^{86}Sr$	0.018	0.016	0.032	0.028	0.134	0.0001	0.0003	0.016	0.068	0.018	0.016	0.028	0.064
$^{87}Sr/^{86}Sr_{measured}$	0.7071	0.7072	0.7057	0.7080	0.7048	0.7079	0.7079	0.7062	0.7060	0.7059	0.7083	0.7075	0.7036
2 SE	0.0011	0.0011	0.0006	0.0006	0.0006	0.0011	0.0013	0.0011	0.0011	0.0011	0.0011	0.0011	0.0011
$^{87}Sr/^{86}Sr_{197Ma}$	0.7071	0.7071	0.7056	0.7079	0.7044	–	–	0.7062	0.7058	0.7059	0.7082	0.7074	0.7034
$^{87}Sr/^{86}Sr_{230Ma}$	–	–	–	–	–	0.7079	0.7079	–	–	–	–	–	–
Rb (ppm)	8.1	8.6	4.9	39.8	20.5	0.03	0.08	7.6	23.2	4.1	29.8	39.8	5.6
Sr (ppm)	1322	1527	439	4159	442	602	720	1394	981	645	5553	4159	252

Notes:

2 SE =analytical uncertainty reported as two standard deviations, except for sample 78D where repeat/duplicate analyses reported precision > analytical uncertainty;

Rb and Sr concentrations are from Table B1. En dash (–) indicates age not applicable for sample;

$^{87}Sr/^{86}Sr_{measured}$ indicates present-day ratio measured; $^{87}Sr/^{86}Sr_{197Ma}$ and $^{87}Sr/^{86}Sr_{230Ma}$ indicates calculated initial ratios based on ages of 197 Ma (silicates) and 230 Ma (carbonates), respectively.

Initital ratios for duplicate samples use non-duplicate Rb and Sr values from the same sample. 'Dup' refers to a duplicate analyses of digested sample (already in solution), whereas 'R' (i.e., 95_R) is a full procedural repeat from powder to solution.

Table B3 SN ICP-MS vs LA-ICP-MS concentrations on repeat samples

Sample	Lab	Method	Ni (ppm)	Cr (ppm)	V_ppm	Sc_ppm	Co_ppm	Cu_ppm	Nb_ppm	Rb_ppm	Sr_ppm	Th_ppm	U_ppm	Y_ppm	Zr_ppm
RM19-58B-1	UVic	solutions ICP-MS	1.7	0.38	225	23	11	34	1.6	3.9	725	0.66	1.39	17	48
RM19-58B-1	UVic	LA-ICP-MS	1.38	1.76	226	23.0	11.30	31.70	1.74	3.69	751	0.68	1.44	16.9	51.0
RPD			*10.10*	*-64.79*	*-0.25*	*-0.96*	*-1.50*	*2.82*	*-2.76*	*3.10*	*-1.76*	*-1.32*	*-1.80*	*1.34*	*-3.38*
RM19-58B-2	UVic	solutions ICP-MS	1.6	0.11	235	22	10	6	1.5	7.2	749	0.68	1.13	18	36
RM19-58B-2	UVic	LA-ICP-MS	1.29	1.68	233	22	10.17	9.96	1.51	6.33	758	0.68	1.13	17.4	47.3
RPD			*9.32*	*-88.23*	*0.41*	*0.01*	*-0.49*	*-27.64*	*0.49*	*6.48*	*-0.57*	*-0.14*	*-0.03*	*1.43*	*-13.10*
RM19-58B-3	UVic	solutions ICP-MS	1.9	0.58	234	22	15	9	1.6	6.5	651	0.64	0.40	20	35
RM19-58B-3	UVic	LA-ICP-MS	2.17	1.67	232	22.5	14.64	13.46	1.63	6.52	664	0.64	0.48	18.9	47.8
RPD			*-5.83*	*-48.50*	*0.38*	*-0.63*	*-0.22*	*-19.87*	*-0.49*	*-0.07*	*-1.02*	*-0.54*	*-9.72*	*2.75*	*-15.61*
RM19-58B-4	UVic	solutions ICP-MS	2.4	1.27	232	22	18	30	1.7	7.5	648	0.61	0.49	21	39
RM19-58B-4	UVic	LA-ICP-MS	2.39	1.94	237	21.9	18.68	27.74	1.69	7.51	662	0.58	0.52	20.0	45.8
RPD			*-0.08*	*-20.87*	*-1.01*	*0.96*	*-1.95*	*4.37*	*-0.99*	*-0.30*	*-1.07*	*2.86*	*-3.68*	*2.96*	*-8.43*
RM19-58B-7	UVic	solutions ICP-MS	2.0	0.49	217	21	17	33	1.5	13.1	673	0.62	0.43	17	36
RM19-58B-7	UVic	LA-ICP-MS	2.34	1.26	225	22.2	16.81	30.17	1.55	12.85	692	0.62	0.57	17.0	47.8
RPD			*-7.60*	*-44.53*	*-1.75*	*-3.59*	*-0.08*	*5.02*	*-1.18*	*0.97*	*-1.35*	*0.57*	*-13.99*	*1.01*	*-13.88*
RM19-58B-11	UVic	solutions ICP-MS	2.5	0.40	227	22	19	48	1.5	11.4	665	0.59	0.35	17	31
RM19-58B-11	UVic	LA-ICP-MS	2.51	1.11	238	23.3	20.37	40.25	1.58	10.78	674	0.62	0.44	18.2	49.2
RPD			*-0.10*	*-46.55*	*-2.42*	*-3.09*	*-2.44*	*8.81*	*-2.62*	*2.93*	*-0.66*	*-2.14*	*-11.38*	*-2.62*	*-22.32*
RM19-79B-1	UVic	solutions ICP-MS	20.4	6.14	220	23	155	208	3.1	7.6	853	0.77	5.95	32	99
RM19-79B-1	UVic	LA-ICP-MS	23.9	8.00	261	28.9	157.37	165.11	3.48	5.26	1007	0.87	6.65	35.1	112.0
RPD			*-7.86*	*-13.17*	*-8.59*	*-10.54*	*-0.89*	*11.42*	*-5.34*	*18.09*	*-8.28*	*-6.13*	*-5.57*	*-4.95*	*-6.04*
RM19-79B-2	UVic	solutions ICP-MS	2.7	8.73	286	40	18	11	5.2	14.3	1886	1.12	3.44	38	136
RM19-79B-2	UVic	LA-ICP-MS	2.53	7.36	296	41.8	18.41	11.63	5.44	12.76	2132	1.20	3.85	37.9	168.6
RPD			*3.28*	*8.48*	*-1.62*	*-2.32*	*-0.56*	*-1.15*	*-1.99*	*5.84*	*-6.11*	*-3.64*	*-5.67*	*0.09*	*-10.54*
RM19-79B-3	UVic	solutions ICP-MS	4.5	8.24	318	38	16	9	4.9	7.5	1309	1.08	1.26	40	96
RM19-79B-3	UVic	LA-ICP-MS	4.67	7.99	335	40.7	16.90	11.81	5.02	7.61	1394	1.25	1.47	41.8	161.4
RPD			*-1.46*	*1.51*	*-2.51*	*-3.56*	*-1.81*	*-11.47*	*-1.29*	*-0.77*	*-3.15*	*-7.49*	*-7.72*	*-1.79*	*-25.46*
RM19-79B-4	UVic	solutions ICP-MS	5.2	8.12	305	37	15	8	4.9	5.5	1171	1.08	0.72	43	83
RM19-79B-4	UVic	LA-ICP-MS	5.69	7.51	314	38.8	15.91	13.42	5.07	5.92	1208	1.17	0.90	42.2	158.0
RPD			*-4.63*	*3.88*	*-1.49*	*-1.75*	*-1.86*	*-24.41*	*-1.35*	*-3.37*	*-1.59*	*-4.31*	*-10.82*	*0.47*	*-31.12*
RM19-79B-7	UVic	solutions ICP-MS	5.2	8.00	316	38	16	8	5.1	8.0	1272	1.08	0.56	43	78
RM19-79B-7	UVic	LA-ICP-MS	5.85	7.55	317	36.4	16.16	8.93	5.22	8.10	1322	1.14	0.69	38.6	145.1
RPD			*-6.09*	*2.95*	*-0.11*	*2.02*	*-0.99*	*-8.52*	*-1.39*	*-0.33*	*-1.96*	*-2.72*	*-10.29*	*4.97*	*-30.30*

Notes:
SN-ICP-MS indicates sample was obtained by solution nebulisation inductively coupled plasma mass spectrometry;
LA-ICP-MS indicates sample was obtained by laser ablation inductively coupled plasma mass spectrometry;
RPD indicates relative percent difference where values >10% are shown in red text.
Concentrations (ppm) are parts per million by weight.

Appendix B - Supplementary Material Text

METHODS

Sample collection

Bulk rock samples for geochemical analyses (Table B1) were collected from the following lithologies: four limestone samples from various stratigraphic levels collected >1 m away from intrusive contacts (sample 'D'); five dikes and one sill in contact with limestone sampled at margins ('B') and interiors ('A'), referred to as 'dike-in-limestone' or 'sill-in-limestone' samples; three dikes that cross-cut the pluton, referred to as 'dike-in-pluton' samples; and two dikes that cross-cut stratified tuff or an andesite intrusion, referred to as 'dike-in-other' samples. An illustration of this naming scheme is presented in Figure B1b.

Dike-in-limestone margins from both the Merry Widow and Quinsam locality were micro-sampled at mm-scale increments from a visible limestone contact inwards through the boundary melt to the dike interior, and are herein referred to as 'dike profiles' (Figure 3.3). To obtain dike profile samples, contacts of dike with limestone were sawed into a 1 cm thick slab that was then micro-sectioned normal to the dike-in-limestone interface with a diamond saw in ~ 5 mm thick intervals, numbered with increasing distance to the contact (Figure 3.3). Each 5 mm thick segment in the profile was then crushed to a powder in an agate mortar and pestle. In total, 12 micro-samples were obtained from both dike profiles (79B1 to 79B12 and 58B1 to 58B12). Notable sulphides visible at the contact in 79B1 were avoided during sample collection (Figure 3.3). Sampled intervals 1 and 2 from dike profiles (i.e., 79B1,2 and 58B1,2) were collected from the boundary melt (Figure 3.3).

Major element analyses

Bulk rock analyses of major elements for dikes and sills were analyzed by inductively coupled plasma optical emission spectrometry (ICP-OES) by Activation Laboratories Ltd (Actlabs). Samples were prepared by powdering fresh rock chips in a planetary agate ball mill. Analyses by ICP-OES measured 10 major element oxides (SiO_2, TiO_2, Al_2O_3, $Fe_2O_{3(T)}$, MnO, MgO, CaO, Na_2O, K_2O, and P_2O5) (Table B1). Data accuracy was estimated by calculating differences between known and measured values of certified reference materials (DNC-1, GBW 07113, W-2A, SY-4, and BIR-1a). Differences were <2.5% or within 0.1% (i.e., the latter for minor amounts of MnO, K_2O, P_2O_5), with the exception of two $Fe_2O_{3(T)}$ measured differences of 4.7% (DNC-1) and 3.2% (W-2A). Precision estimates measured by Actlabs between repeat unknown samples (61 and 79B) were <3.7%.

Bulk rock analyses of major elements for dike profiles were analyzed by electron micro probe microanalysis (EMPA) using a five-wavelength spectrometer Cameca SX-100 at the University of Alberta on homogenized glass beads made from rock powders. Sample powders were prepared by hand pulverizing fresh rock chips in an agate mortar and pestle. The powders were mounted on Pt wire loops and melted in air at 1300°C for 24 hours and quenched into homogenized glass beads. Analyses by EMPA measured 10 major elements (SiO_2, TiO_2, Al_2O_3, FeO, MnO, MgO, CaO, Na_2O, K_2O, and P_2O5) (Table B1). Data accuracy was estimated by calculating differences between known and measured values of certified reference materials of basaltic glasses (BHVO-2G: in Jochum et al., 2005; IOB: ‘Glass, Basaltic, Indian Ocean’ in Jarosewich et al., 1980; Grimsvotn: in Jude-Eton et al., 2012; Hawaii: ‘Glass, Basaltic, Makopuhi Lava Lake, HI’ in Jarosewich et al., 1980, JDF: ‘Glass, Basaltic, Juan de Fuca Ridge in Jarosewich et al., 1980; and Laki: in Kuehn et al., 2011), where differences were <2% or

within 0.2% (i.e., the latter for minor amounts of MnO, Na_2O, K_2O, P_2O_5). Precision estimates were measured from repeat analyses on standards (three repeats) and all unknown samples (five repeats) and were within 0.8 wt.% (2σ) for all oxides. An external sample (RM19-144* - Table B1) was submitted separately as a method check to compare ICP-OES vs EMPA major element analyses, where oxide differences were <3.8% or within 0.1 wt.% (P_2O_5).

Bulk rock analyses of CaO, MgO, TiO_2, and MnO wt.% in limestone samples was obtained by solution nebulisation inductively coupled plasma mass spectrometry (SN ICP-MS) using an Agilent 8800 ICP-MS at the University of Victoria (Table B1). Limestone samples were prepared by hand pulverizing fresh rock chips in an agate mortar and pestle. Digestion of carbonates is described in detail below. Major element analyses by SN ICP-MS measured CaO, MgO, TiO_2, and MnO using calibration techniques, where a certified reference material with known values (JLs-1) was analysed along with samples. Data precision was estimated from comparison of repeat analyses on an unknown sample (165D), where measured differences were <0.3% for MgO, <0.9% for CaO, <3.0% for TiO_2, and <0.6% for MnO.

Trace element analyses by SN ICP-MS

Methods for trace element compositions by solutions ICP-MS (SN ICP-MS) for bulk rock analyses are described in Morris and Canil (2022), with the exception of a sampled sill and dike interior (80A, 161A), dike profiles, and limestones that were analyzed in this study (Table B1). Three samples from Morris and Canil (2022) were also analyzed as procedural repeat analyses (80B, 161B, and 95 – Table B1). The same powders used for silicate and carbonate major element analyses were used for trace element analyses. The digestion of rock powders varied for silicates (dike profiles, 80A, 161A) versus carbonates (limestone). For silicates,

samples were prepared by digesting ~100 mg of bulk rock powder in concentrated acids (1 ml of 16 M HNO_3 followed by 1.5 ml of 28 M HF) at 125°C for 24 hrs. Digested solutions were uncapped and dried at 125°C for 2 hrs until a gel-like state was reached. A second acid digestion (4 ml of 8 M HNO_3) at 125°C for 12 hrs was completed, dried down, followed by third and final acid digestion (4 ml of 8 M HNO_3), which was capped until final solutions were ready to be made. For limestone powders, samples were prepared by digesting ~100 mg of bulk rock powder into 0.5 ml of deionized H_2O followed by a 'drop-by-drop' addition of 0.5 ml of 16 M HNO_3, which was then left to sit for >1 hr before adding by 1.5 ml of 28M HF at 125°C for 24 hrs. Digested solutions were uncapped and dried at 125°C for 2 hrs until a gel-like state was reached. A second acid digestion (2 ml of 8 M HNO_3) at 125°C for 2 hrs was completed, dried down, followed by third digestion (4 ml of 8 M HNO_3), also dried down, followed by a fourth and final acid digestion (4 ml of 8 M HNO_3), which was capped until final dilutions were ready to be made. Final solutions for both silicate and limestone samples were prepared by diluting digested samples in ~125 ml of deionized water. I note that Anachemia Environmental Grade Nitric Acid (HNO_3), Anachemia Environmental Grade Hydrofluoric Acid (HF), and 18.2 MΩ-cm water (made in house) was used for sample preparation and digestions, and that digestions and dilutions were performed inside a class 100 total exhaust fume hood.

Analyses by SN ICP-MS measured 14 rare earth elements (REE), as well as Cr, V, Sc, Nb, Pb, Rb, Sr, Th, U, Cs, Y, Zr, Ba, Hf and Ta. For silicate samples, Ni, Co, and Cu were also analyzed. Limits of detection for all elements was <0.5 ppb, well below the detection of low element concentrations in specific samples (i.e., REEs in carbonates). Data correction methods were adapted from Cheatham et al. (1993), using ^{115}In as an internal standard. Drift was observed in specific elements (Cr, Ni, Cu, Rb, Sr, Ba, and U) and was corrected for by a third order

polynomial function unique to the specific element drift. The corrected data was converted from counts per second (CPS) to concentration by calibration with analyzed silicate standards (BCR-2, BHVO-2, BIR-1a, and DNC-1) forced through an intercept (0,0). Using the calibration curve set by silicate standards, the limestone standard (JLs-1) was analyzed as an internal check and reported values within 10% of known standard values for all elements analyzed with the exception of Sc, Hf, Ta, and Er. Precision on measured differences between duplicate (161A, 79B-3, 165D) and procedural repeat (95, 161B, 80B) samples was within 10% with the exception of Cu, Zr, and Hf for one duplicate sample (79B-3) (Table B1).

Trace element analyses of glass beads by LA-ICP-MS

Fused glass beads were analysed by laser ablation ICP-MS (LA-ICP-MS) on dike profile samples to confirm concentrations obtained by SN ICP-MS analysis (Table B3), and to obtain remaining dike profile concentrations on samples not yet analyzed. Analyses were conducted using a 213 nm Nd-YAG laser (Cetac-Teledyne LSX-213 G2+ HelEx) interfaced to an Agilent 8800 ICP-MS (LA-ICP-MS) at the University of Victoria. The laser was set at a repetition rate of 10 Hz and fluence of 7 J/cm^2 ablating 100 micron diameter spot sizes in <2.5 mm homogenized glass beads. The 100 micron laser was rastered along 300 µm lines at 10 µm/s for a total count time of 60 s. Background count rates were measured for 30 s prior to firing the laser. Analyzed elements and their respective averaged detection limits (in ppm) include: ^{60}Ni (0.34), ^{52}Cr (0.40), ^{51}V (0.05), ^{45}Sc (0.15), ^{59}Co (0.06), ^{63}Cu (0.21), ^{93}Nb (<0.01), ^{85}Rb (0.04), ^{88}Sr (0.06), ^{232}Th (<0.01), ^{238}U(<0.01), ^{89}Y(<0.01), ^{90}Zr(<0.01), ^{137}Ba(0.07), ^{178}Hf (<0.01) and 14 rare earth elements (REE), all with detection limits <0.01 ppm with the exception of ^{153}Eu (0.02) and ^{157}Gd (0.05). Data reduction was completed at the University of Victoria using the Iolite^{TM} (V4.8)

software package (Paton et al., 2010). Data was calibrated using three external standards (BCR2G, KL2G, and ML3B) and with ^{42}Ca as internal standard using concentrations measured by EMPA. The trace element abundances in dike profile samples analyzed by both SN ICP-MS and LA-ICP-MS were within 10% for all elements except for Ni, Cr, Sc, Cu, Rb, U, Zr, and Hf (Table B3). Both Cu and Rb are volatile and lost during glass bead synthesis in air (Scholtysik and Canil, 2018). For this study, I report LA-ICP-MS results for dike profile samples (Table B1).

$^{87}Sr/^{86}Sr$ analyses by tandem ICP-MS

$^{87}Sr/^{86}Sr$ ratios were measured using the University of Victoria's Agilent 8800 ICP-MS/MS following the method of Bolea-Fernandez et al. (2016). Samples analyzed included dikes (11) a sill (2), limestone (4), and dike profiles (12). The analysis method uses the Agilent 8800's tandem MS configuration (tandem quadrupole mass filters bracketing an octopole reaction cell) to measure $^{87}Sr/^{86}Sr$ ratios free from ^{87}Rb interference. To achieve on-line separation of Sr from Rb, 10% CH_3F and 90% He is used as the reaction cell gas, and the 8800 is run in "mass shift" mode, where Q2 is set 19 atomic mass units greater than Q1. Sr^+ reacts with CH_3F to form SrF^+, while Rb^+ does not react with CH_3F. Q1 allows ions to enter the cell only one atomic mass unit at a time, which ensures unwanted reaction products do not interfere with the results. $^{86}Sr^+$, $^{87}Sr^+$, $^{88}Sr^+$ react quantifiably to form $^{105}SrF^+$, $^{106}SrF^+$, and $^{107}SrF^+$ which are transmitted one at a time through Q2 and detected. Rb^+ does not react with the cell gas and is rejected by Q2. The detector dead time, which is specific to the instrument used and necessary for correcting count rates, was determined to be 35 ns based on the measurement of mass-shifted $^{88}Sr/^{86}Sr$ ($^{107}SrF+/^{105}SrF+$) count ratio from solutions containing 4, 8, 12, and 16 ppb Sr.

Aliquots of the solutions previously used for SN ICP-MS trace element analysis were diluted in 0.32 M HNO_3 so that all had 10 ppb Sr. I chose to run all of the samples with consistent 10 ppb Sr concentration in order to ensure all signals were collected with the detector in pulse counting mode. As well, running all at the same Sr concentration minimizes any needed dead time correction. Two 'runs' of samples were completed: one in December 2021 (dikes and a sill margin; 12 samples) and one in July 2022 (dike profiles, a sill interior, limestone, and repeat 2021 samples; 17 samples + 4 repeats from 2021). For both runs, samples were bracketed by NIST SRM 987 ('bracket solution'), a strontium carbonate with a known and certified isotopic ratio ($^{87}Sr/^{86}Sr = 0.71034 \pm 0.00026$), which was required for external mass discrimination calculations (Bolea-Fernandez et al., 2016).

For the December 2021 run, reference materials included BHVO-2, BCR-2, DNC-1, and BIR-1a. For the July 2022 run, reference materials included silicate standards (BHVO-2, BCR-2, and BIR-1a), and a carbonate standard (JLs-1). Analytical uncertainty measured from repeat analyses of a 10 ppb Sr solution that was prepared by combining ~4 ml from each unknown sample was ± 0.0006 (2σ, n = 6) for the December 2021 run, and ± 0.0011 (2σ, n = 10) for the July 2022 run. Data accuracy was estimated by comparison of measured versus preferred and/or published values of certified reference materials, where the absolute differences were near or within analytical uncertainty (December 2021 absolute differences: BHVO 0.0003 – 0.0008; DNC-1 0.0004 – 0.0008; BCR-2 0.0005; BIR-1A 0.0004; July 2022 absolute differences: JLs-1 0.0009; BHVO 0.0001 – 0.0004), with the exception of the BCR-2 and BIR-1a solutions run in July 2022, where BCR-2 (n=4) consistently reported lower $^{87}Sr/^{86}Sr$ (0.002 – 0.003) than the *preferred* value (BCR2: 0.70492 ± 0.00055; Jochum et al., 2016) and BIR-1a (n=2) reported slightly higher $^{87}Sr/^{86}Sr$ (0.001 – 0.002) than *published* values (0.70307 – 0.70311 ± 0.00025;

Fourny et al., 2016). I note that matrix effects may have resulted in variable errors in the measured $^{87}Sr/^{86}Sr$ ratios related to the variable dilution factors. I suggest that some uncertainty induced by variable matrix effects between unknown samples and the bracket solution could be minimized using a matrix matched bracket solution. Precision on duplicate and repeat samples analyzed (December 2021: n = 3; July 2022: n = 8) were within analytical uncertainty (± 0.0006 in December 2021 run; ± 0.0011 in July 2022 run) with the exception of one limestone sample (78D) with ± 0.0013 uncertainty (2σ) (Table B2). $^{87}Sr/^{86}Sr$ ratios were further calculated to initial values, based on the following ages: 197 Ma for magmatic rocks (Nixon et al., 2011), and 230 Ma (Carnian to Early Norian) for the limestone (Nixon and Orr, 2007).

Appendix B Bibliography

Bolea-Fernandez, E., Balcaen, L., Resano, M., and Vanhaecke, F. (2016), Tandem ICP-mass spectrometry for Sr isotopic analysis without prior Rb/Sr separation: *Journal of Analytical Atomic Spectrometry*, 31, p. 303–310.

Canil, D., and Morris, R.A. (2023), Continentalization of an intraoceanic arc as exemplified by the Jurassic Bonanza arc of Vancouver Island, Canada: *Geological Society of America Bulletin*, https://doi.org/10.1130/B36716.1

Cheatham, M.M., Sangrey, W.F., and White, W.M. (1993), Sources of error in external calibration ICP-MS analysis of geological samples and an improved non-linear drift correction procedure: *Spectrochimica Acta*, 48B (3), p. E487-E506, https://doi.org/10.1016/0584-8547(93)80054-X

DeBari, S.M., Anderson, R.G., and Mortensen, J.K. (1999), Correlation among lower to upper crustal components in an island arc: the Jurassic Bonanza arc, Vancouver Island, Canada: *Canadian Journal of Earth Sciences*, 36, p. 1371–1413, https://doi.org/10.1139/e99- 029

Fourny, A., Weis, D., and Scoates, J. S. (2016), Comprehensive Pb-Sr-Nd-Hf isotopic, trace element, and mineralogical characterization of mafic to ultramafic rock reference materials: *Geochemistry, Geophysics, Geosystems*, 17, p. 739– 773, https://doi.org/10.1002/2015GC006181

Jarosewich, E., Nelen, J.A. and Norberg, J.A. (1980), Reference Samples for Electron Microprobe Analysis: *Geostandards Newsletter*, 4, p. 43 – 47, https://doi.org/10.1111/j.1751-908X.1980.tb00273.x

Jochum, K.P., Willbold, M., Raczek, I., Stoll, B. and Herwig, K. (2005), Chemical Characterisation of the USGS Reference Glasses GSA-1G, GSC-1G, GSD-1G, GSE-1G, BCR-2G, BHVO-2G and BIR-1G Using EPMA, ID-TIMS, ID-ICP-MS and LA-ICP-MS: *Geostandards and Geoanalytical Research,* 29, p. 285 – 302, https://doi.org/10.1111/j.1751-908X.2005.tb00901.x

Jochum, K.P., Weis, U., Schwager, B., Stoll, B., Wilson, S.A., Haug, G.H., Andreae, M.O. and Enzweiler, J. (2016), Reference Values Following ISO Guidelines for Frequently Requested Rock Reference Materials: *Geostandards and Geoanalytical Research,* 40, p. 333-350, https://doi.org/10.1111/j.1751-908X.2015.00392.x

Jude-Eton, T.C., Thordarson, T., Gudmundsson, M.T., and Oddsson, B. (2012), Dynamics, stratigraphy and proximal dispersal of supraglacial tephra during the ice-confined 2004 eruption at Grímsvötn Volcano, Iceland: *Bulletin of Volcanology,* 74, p.1057–1082, https://doi.org/10.1007/s00445-012-0583-3

Kuehn, S.C., Froese, D.G., and Shane, P.A.R. (2011), The INTAV intercomparison of electron-beam microanalysis of glass by tephrochronology laboratories: Results and recommendations, *Quaternary International*, 246, p. 19 – 47, https://doi.org/10.1016/j.quaint.2011.08.022

Lund, J.C., (1966), *Structural geology of Empire Mine, Empire Development Limited, Port McNeil, British Columbia* (Masters thesis), Vancouver, University of British Columbia, 61 p.

Morris, R., and Canil, D. (2022), CO_2 transport at shallow depths in arc magmas: evidence from unique orbicular dikes in the Jurassic Bonanza arc, Vancouver Island, Canada: *Contributions to Mineralogy and Petrology*, 177, https://doi.org/10.1007/s00410-021-01852-y

Morris, R.A., Canil, D., and Spence, J., (2023a), Major element, trace element, and $^{87}Sr/^{86}Sr$ isotope compositions for dikes, sills, dike profiles, and carbonates at Merry Widow and Quinsam, Vancouver Island, Canada. figshare. https://doi.org/10.6084/m9.figshare.23285321

Morris, R.A., Canil, D., Spence, J. (2023b), Magma-carbonate interactions drive CO_2 production and metal enrichment in shallow dikes and sills at volcanic arcs. *Geology*; doi: https://doi.org/10.1130/G51439.1

Nixon, G.T., Hammack, J.L., Hamilton, J.V., Jennings, H., Larocque, J.P., Orr, A.J., Friedman, R.M., Archibald, D.A., Creaser, R.A., Orchard, M.J., Haggart, J.W., Tipper, H.W., Tozer, E.T., Cordey, F., and McRoberts, C.A. (2011), Geology, geochronology, lithogeochemistry and metamorphism of the Alice Lake area, northern Vancouver Island, NTS 092L/06 and part of 092L/03: British Columbia Geological Survey Geoscience Map 2011-4, v. 1, scale 1:50000, 1 sheet.

Paton, C., Hellstrom, J., Paul, B.,Woodhead, J. and Hergt, J. (2011), Iolite: Freeware for the visualisation and processing of mass spectrometric data: *Journal of Analytical Atomic Spectrometry,* 26, p. 2508 – 2518.

Ray, G.E., and Webster, I.C.L. (1991), Geology and mineral occurrences of the Merry Widow skarn camp, northern Vancouver Island: British Columbia Ministry of Energy, Mines and Petroleum Resources: BC Geological Survey, Open File 1991-08, scale 1:5000, 1 sheet.

Sangster, D.F. (1964), *The contact metasomatic magnetite deposits of southwestern British Columbia* (Doctoral dissertation), Vancouver, University of British Columbia, 266 p. https://open.library.ubc.ca/cIRcle/collections/ubctheses/831/items/1.0053070

Scholtysik, R., and Canil, D. (2018), Condensation behaviour of volatile trace metals in laboratory benchtop fumarole experiments: *Chemical Geology*, 492, pp. 49 -58. https://doi.org/10.1016/j.chemgeo.2018.05.006

Appendix C – Chapter 4 Supplemental Material

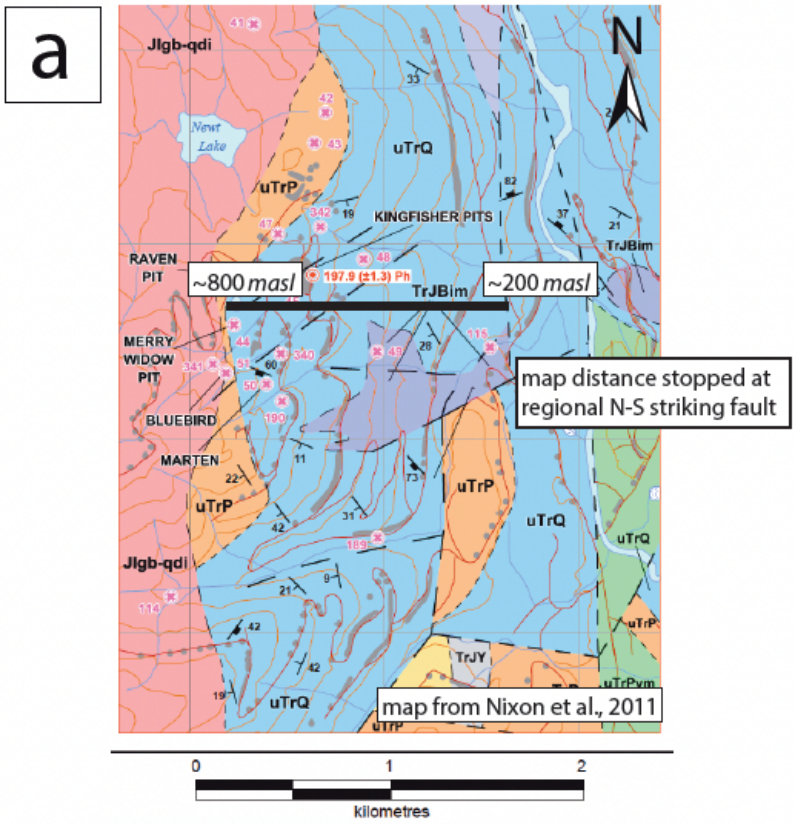

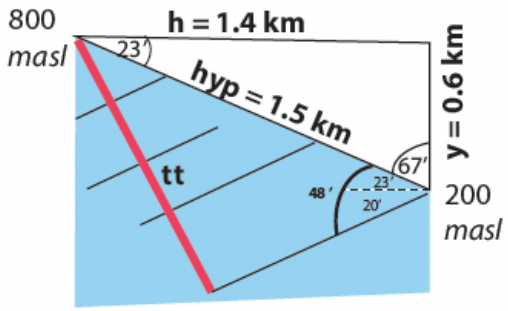

Quatsino dips 20′

sin (43′) = tt/hyp

sin (43′)*1.5 km = tt

tt = 1.0 km

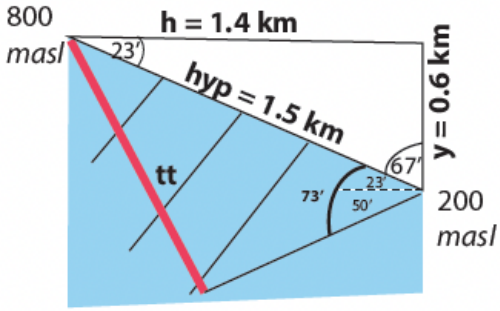

Quatsino dips 50′

sin (73′) = tt/hyp

sin (73′)*1.5 km = tt

tt = 1.4 km

Note: These thicknesses are similar to Ray & Webster (1991) estimates of ~1 km for Quatsino Limestone at Merry Widow. Regional Quatsino Limestone dips ranging from 20 - 50′ are used to calculate true thicknesses (Ray & Webster, 1991).

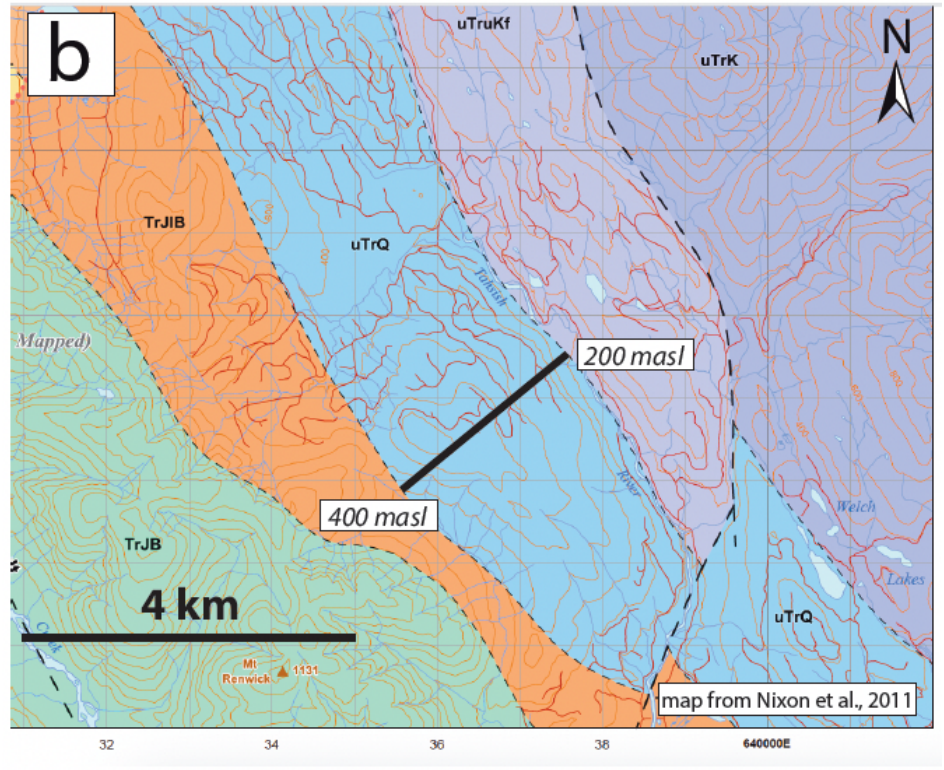

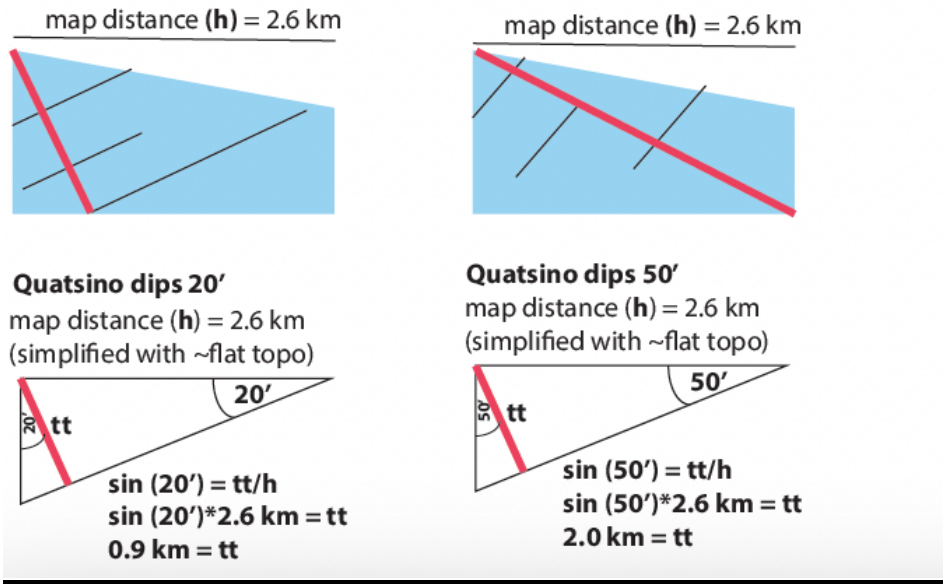

Figure C1: True thickness of the Quatsino Formation from (a) Merry Widow site, where faulting may have offset true thickness, however range of thickness is similar to others (Ray and Webster, 1991). (b) Southeast of Merry Widow, where horizontal map distance suggests thickest regions of exposed Quatsino Formation, with no apparent offset faulting. Map insets are from Nixon et al., 2011. Regional dip of Quatsino Formation ranges from 20 – 50°

(Ray and Webster, 1991). For this dissertation, Quatsino Formation dips of 20 – 25° are used based on field measurements at Merry Widow.

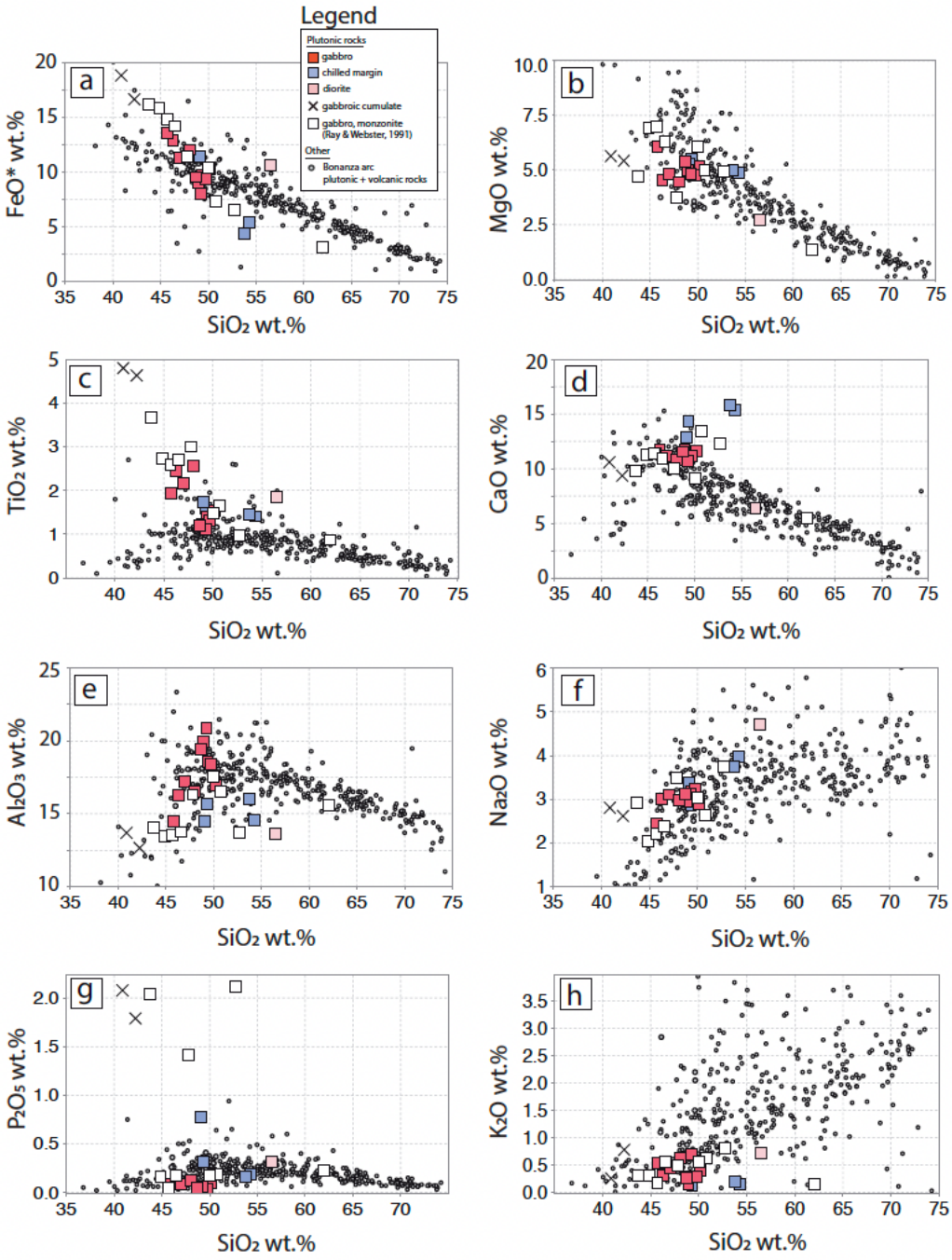

Figure C2: Bulk rock major element bivariate diagrams for Merry Widow magmatic rocks, including plutonic rocks from this study and others (Ray and Webster, 1991) in comparison to Bonanza arc rocks (Massey 1995a, b, c; DeBari et al., 1999; Larocque 2008; Fecova 2009; Larocque and Canil 2010; Paulson 2010; D'Souza et al., 2016; Canil and Morris, 2023). Merry Widow magmatic rocks generally display enriched trends in TiO_2, CaO, Na_2O, FeO*, and ± P_2O_5 and lower in K_2O, MgO, and ± Al_2O3 in comparison to Bonanza arc rock trends.

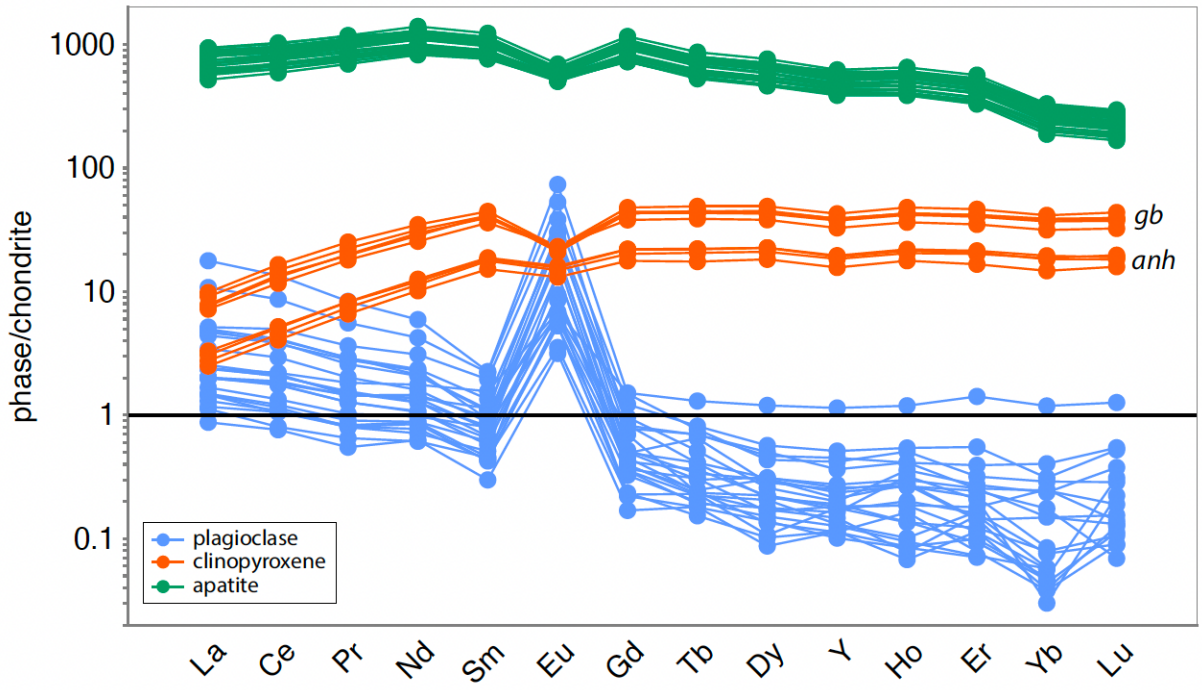

Figure C3: Chondrite normalized rare earth element (REE) plots (Sun and McDonough, 1989) for select phases from gabbro (clinopyroxene, plagioclase) and cumulates (apatite). Italicized 'gb' and 'anh' refers to 'granoblastic' clinopyroxene in finer-grained gabbro and 'anhedral' clinopyroxene in coarser grained gabbro, respectively (textures displayed in Figure 4.2de).

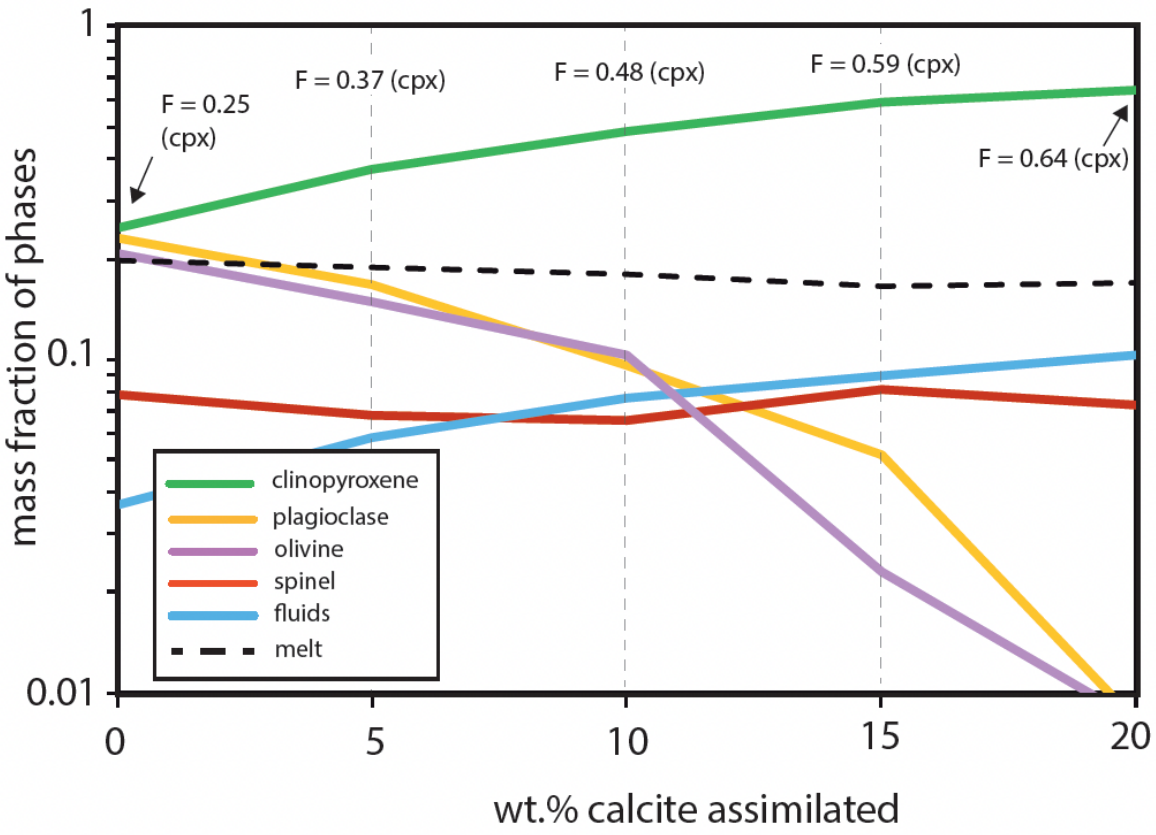

Figure C4: Mass fraction of phases crystallized from a primitive Bonanza arc basalt (JL06-027; Larocque and Canil, 2010) that has assimilated varying amounts (0 – 20%) of calcite using rhyolite-MELTS v.1.2.0 (Ghiorso and Gualda, 2015). No data is provided >20% assimilation due to software failure. Modeled results show final assemblage after crystallizing basalt (unbuffered) until a melt fraction of ~0.2 is reached. Temperatures to achieve a melt fraction of ~0.2 vary from 840°C for pure FC (0% calcite) to 1055°C for 20% calcite assimilation.

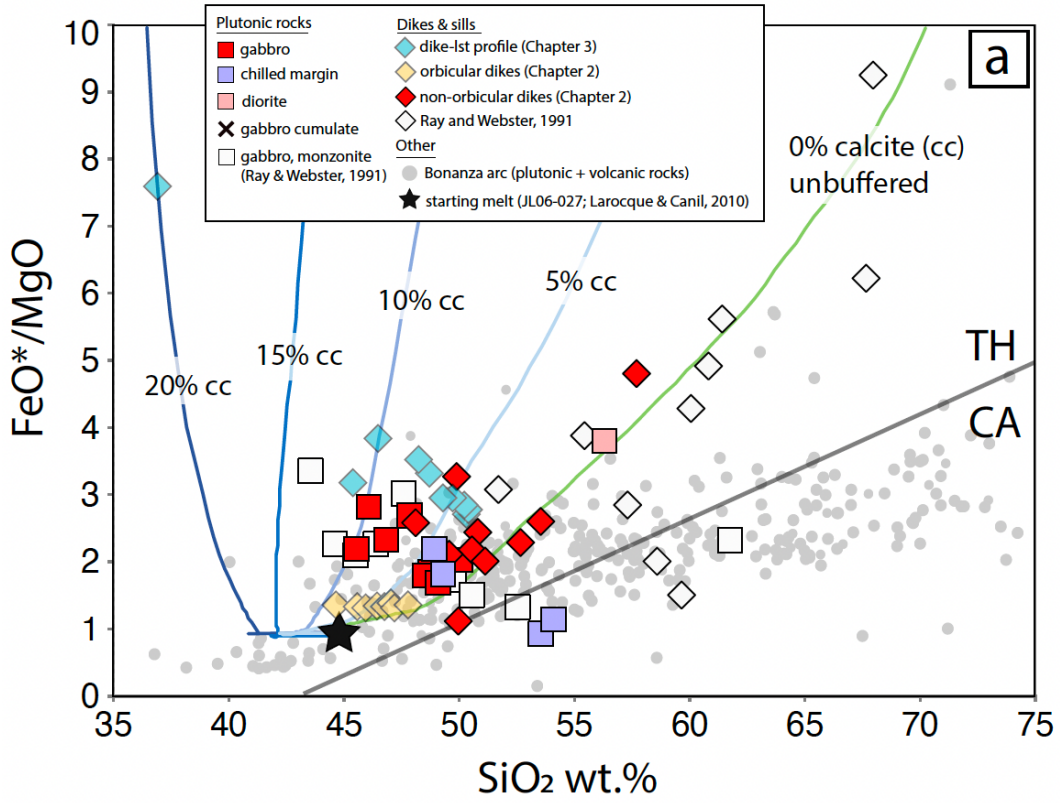

Figure C5: Plot is identical to Figure 4.5a, but here includes dikes and sills from Merry Widow that are known to have assimilated limestone via binary mixing (not AFC), such as orbicular dikes from Chapter 2 (Morris and Canil, 2022), and dike-profile sample RM19-79B1 through 79B12 from Chapter 3. Binary mixing modeling of orbicular dikes (yellow diamonds) suggests 3 – 10 wt.% limestone assimilation from major element chemistry, and up to 25% limestone assimilation for dike-limestone boundary melts (blue diamonds) from trace element and isotope chemistry. Remaining figure details can be found in Figure 4.5a.

Table C1 Bulk-rock major element (wt.%) and trace element (ppm) composition for hand samples

	chilled margin (gabbro)				*gabbro*										*diorite*	*quartz monz*
Sample	MW21-11-96.0	MW21-11-96.3	MW21-11-97.1	MW21-11-97.5	RM19-37	RM19-64A	RM19-84	RM19-107	RM19-114	RM19-132	RM19-135	MW21-12-137	RM19-144	RM19-174	RM19-119	RM19-160
from contact w:	at contact	0.3	1.1	1.5	36	180	103	60	1070	40	42	50	45	9	500	167
Lat_DD	50.3568	50.3568	50.3568	50.3568	50.3556	50.3493	50.3654	50.3545	50.3452	50.3560	50.3542	50.3568	50.3619	50.3551	50.3482	50.3528
Long_DD	-127.2527	-127.2527	-127.2527	-127.2527	-127.2553	-127.2596	-127.2485	-127.2562	-127.2732	-127.2555	-127.2560	-127.2527	-127.2503	-127.2548	-127.2647	-127.2593
Lab_Method	³A) UVic (trace	³A) UVic (trace	³A) UVic (trace	³A) UVic (trace)	Uvic (trace - s	Uvic (trace - s	Uvic (trace - s	Uvic (trace - s	Uvic (trace - s	Uvic (trace - s	Uvic (trace - s	³A) UVic (trace)	Uvic (trace - s	Uvic (trace - s	Uvic (trace - se	only - solution
SiO2	54.3	53.7	49.3	49.1	49.7	48.0	49.3	46.3	45.8	49.4	47.0	48.7	50.2	48.9	56.5	–
TiO2	1.41	1.45	1.58	1.72	1.31	2.55	1.12	2.45	1.93	1.40	2.16	1.19	1.55	1.23	1.84	–
Al2O3	14.6	16.0	15.7	14.5	18.4	16.6	20.9	16.2	14.5	18.6	17.2	19.4	17.0	19.9	13.6	–
FeO*	5.37	4.38	9.68	11.36	9.17	11.82	7.90	12.51	13.05	9.62	11.00	9.48	10.21	8.97	10.30	–
MnO	0.18	0.16	0.26	0.29	0.16	0.25	0.12	0.18	0.25	0.18	0.18	0.17	0.19	0.15	0.25	–
MgO	4.90	4.99	5.52	5.29	4.77	4.46	4.84	4.52	6.06	4.93	4.84	5.41	5.16	5.00	2.75	–
CaO	15.33	15.76	14.33	12.83	11.16	10.76	10.65	11.70	11.33	11.33	11.11	11.55	11.61	11.74	6.33	–
Na2O	3.97	3.75	2.85	3.38	3.24	2.99	3.13	3.01	2.43	3.19	3.11	3.13	2.90	2.96	4.72	–
K2O	0.15	0.19	0.12	0.28	0.28	0.63	0.69	0.31	0.53	0.28	0.44	0.26	0.41	0.15	0.71	–
P2O5	0.19	0.16	0.31	0.78	0.04	0.12	0.06	0.09	0.09	0.06	0.08	0.04	0.10	0.03	0.31	–
LOI	0.30	1.03	–	–	0.61	0.80	1.03	0.50	1.44	0.66	1.31	–	0.38	0.39	0.86	–
Total	100.7	101.6	99.6	99.5	98.9	99.0	99.7	97.8	97.3	99.6	98.4	99.4	99.7	99.4	98.2	–
Ni	16.0	13.4	24.6	2.5	11.4	6.6	19.7	22.4	16.8	11.4	19.9	10.6	23.6	9.9	1.6	0.5
Cr	69.7	25.2	46.9	26.2	22.6	2.9	20.2	9.8	36.4	22.7	10.9	27.6	54.6	23.2	1.3	0.3
V	238	309	265	25	364	410	297	653	537	351	697	368	494	363	229	21
Sc	45	41	54	54	35	46	22	48	56	35	51	33	47	35	30	18
Co	10	8	24	20	36	34	34	38	52	37	37	37	37	37	23	10
Cu	4	5	28	27	8	107	19	18	96	10	20	9	45	9	14	7
Ga	–	–	–	–	–	–	–	–	–	–	–	–	–	–	–	–
Nb	3.8	2.9	0.7	0.5	0.5	0.9	1.3	1.3	2.0	0.7	1.1	0.4	1.6	0.3	6.8	8.2
Pb	0.4	1.1	0.5	1.1	0.4	0.8	1.1	1.0	1.1	0.6	0.8	0.4	1.2	0.3	4.0	0.8
Rb	1.1	2.3	1.8	5.3	5.5	12.8	20.8	6.6	11.1	5.2	11.8	5.5	10.1	1.7	12.6	27.0
Sr	718	781	437	456	383	366	434	343	239	391	339	377	310	396	256	206
Th	0.66	0.43	0.05	0.19	0.07	0.13	0.31	0.19	0.39	0.09	0.13	0.03	0.49	0.02	1.60	2.04
U	0.81	0.69	0.04	0.14	0.04	0.07	0.15	0.10	0.17	0.05	0.08	0.03	0.19	0.01	0.77	0.86
Cs	0.52	0.59	0.46	0.38	0.20	0.28	0.41	0.38	0.17	0.57	0.25	0.72	0.79	0.18	0.27	0.07
Y	47	30	29	30	10	16	13	15	21	12	15	9	20	8	55	68
Zr	66	73	30	25	17	28	21	32	36	21	30	13	31	11	171	53
Ba	91	67	66	91	84	176	92	78	123	80	92	66	104	46	240	373
Hf	1.94	2.14	1.14	0.81	0.54	0.87	0.74	1.02	1.20	0.66	0.97	0.44	0.97	0.39	4.39	2.55
Ta	0.20	0.18	0.06	0.04	0.04	0.07	0.08	0.09	0.14	0.04	0.08	0.03	0.11	0.02	0.44	0.51
La	13.7	11.6	3.4	4.8	1.3	2.0	2.8	2.3	3.3	1.6	2.1	1.3	3.7	0.9	13.2	16.9
Ce	31.9	26.6	10.2	14.5	3.5	5.7	7.1	5.9	8.9	4.4	5.2	3.4	9.4	2.5	33.3	44.3
Pr	4.54	3.45	1.86	2.49	0.60	0.96	1.07	0.96	1.40	0.74	0.90	0.54	1.46	0.44	4.94	6.65
Nd	20.9	14.7	10.8	14.5	3.3	5.3	5.2	5.0	7.2	4.0	4.9	2.9	7.4	2.5	23.4	31.6
Sm	6.47	4.00	3.76	4.73	1.16	1.87	1.57	1.68	2.37	1.39	1.68	1.01	2.31	0.92	6.82	8.87
Eu	3.32	2.38	1.70	2.20	0.88	1.20	0.77	0.93	0.99	0.95	0.93	0.75	0.98	0.72	2.23	2.74
Gd	7.92	4.71	4.80	5.92	1.52	2.41	1.90	2.17	2.99	1.78	2.19	1.34	2.88	1.20	8.08	10.29
Tb	1.40	0.81	0.82	0.94	0.27	0.42	0.33	0.39	0.54	0.32	0.39	0.24	0.51	0.22	1.43	1.80
Dy	8.74	5.10	5.14	5.59	1.77	2.74	2.18	2.51	3.54	2.09	2.53	1.58	3.35	1.44	9.32	11.52
Ho	1.74	1.07	1.05	1.10	0.38	0.57	0.46	0.53	0.75	0.44	0.53	0.34	0.72	0.30	2.00	2.46
Er	4.63	3.00	2.77	2.82	1.04	1.58	1.32	1.46	2.07	1.23	1.48	0.92	2.02	0.82	5.73	7.03
Tm	0.64	0.44	0.38	0.37	0.15	0.23	0.19	0.21	0.30	0.18	0.21	0.13	0.30	0.12	0.86	1.05
Yb	3.84	2.77	2.41	2.21	0.98	1.46	1.28	1.35	1.93	1.15	1.36	0.86	1.95	0.75	5.69	6.75
Lu	0.53	0.40	0.35	0.33	0.15	0.22	0.19	0.20	0.29	0.17	0.20	0.13	0.29	0.11	0.85	0.99

Notes:

Major element total includes LOI. FeO* is total FeO, calculated from $Fe_2O_{3(total)}$*0.8995. See methods section for data accuracy and precision details. En dash (–) indicates element not analyzed;

Major element oxides are reported in weight percent (wt.%), trace element concentrations are in parts per million (ppm).

Table C1 cont'd Bulk-rock major element (wt.%) and trace element (ppm) composition for hand samples

onite	cumulate	external method check (E standards (ICP-OES, Actlabs)							duplicates			
Sample	RM19-64B	MW21-12-91	M19-144*_EMI	M19-144*_ICPC	DNC-1	GBW 07113	W-2a	SY-4	BIR-1a	RM19-144_DUP	RM19-119_DUP	MW21-12-91_DUP	RM19-64B_DUP
from contact w	180	4	n/a	n/a	n/a	n/a	n/a	n/a	n/a	45	500	4	180
Lat_DD	50.3493	50.3568	50.3619	50.3619	n/a	n/a	n/a	n/a	n/a	50.3619	50.3482	50.3568	50.3493
Long_DD	-127.2596	-127.2527	-127.2503	-127.2503	n/a	n/a	n/a	n/a	n/a	-127.2503	-127.2647	-127.2527	-127.2596
Lab_Method	) Uvic (trace - s	A) UVic (trace	A (majors - EM	s (majors - ICP	s (majors - ICP	s (majors - ICP	s (majors - ICP	s (majors - ICP	s (majors - ICP	ors) Uvic (trace - solutions)	Uvic (trace - solut	EMPA) UVic (trace - s	ors) Uvic (trace - solutions ICPMS)
SiO2	42.2	40.9	49.1	50.2	47.1	73.9	53.4	50.7	48.3	–	–	–	–
TiO2	4.63	4.80	1.52	1.55	0.48	0.28	1.10	0.29	0.97	–	–	–	–
Al2O3	12.7	13.7	17.7	17.0	18.26	12.7	15.5	21.03	15.34	–	–	–	–
FeO*	15.95	18.82	10.53	10.21	8.55	2.91	10.31	5.59	9.81	–	–	–	–
MnO	0.34	0.35	0.2	0.2	0.15	0.14	0.16	0.11	0.17	–	–	–	–
MgO	5.43	5.65	5.25	5.16	10.02	0.14	6.29	0.5	9.61	–	–	–	–
CaO	9.35	10.58	11.44	11.61	11.41	0.58	10.92	7.99	13.59	–	–	–	–
Na2O	2.62	2.81	2.94	2.90	1.89	2.5	2.26	7.01	1.82	–	–	–	–
K2O	0.78	0.26	0.42	0.41	0.22	5.39	0.63	1.68	0.02	–	–	–	–
P2O5	1.79	2.08	0.13	0.10	0.08	0.03	0.12	0.12	0.04	–	–	–	–
LOI	1.59	–	–	–	–	–	–	–	–	–	–	–	–
Total	97.4	99.9	–	–	–	–	–	–	–	–	–	–	–
Ni	2.4	0.4	–	–	–	–	–	–	–	23.6	1.62	0.35	2.43
Cr	0.4	<d.l	–	–	–	–	–	–	–	55.2	1.29	<d.l	0.54
V	354	58	–	–	–	–	–	–	–	503	231	60.2	348
Sc	36	30	–	–	–	–	–	–	–	47	30	29	38
Co	50	32	–	–	–	–	–	–	–	37	23	32	50
Cu	125	23	–	–	–	–	–	–	–	44	14	24	122
Ga	–	–	–	–		–	–	–	–	–	–	–	–
Nb	5.5	2.2	–	–	–	–	–	–	–	1.7	6.7	2.3	5.6
Pb	1.8	1.1	–	–	–	–	–	–	–	1.2	3.9	0.9	1.8
Rb	18.3	6.3	–	–	–	–	–	–	–	10	13	6	18
Sr	336	406	–	–	–	–	–	–	–	311	253	392	336
Th	0.50	0.27	–	–	–	–	–	–	–	0.45	1.48	0.27	0.54
U	0.28	0.21	–	–	–	–	–	–	–	0.19	0.74	0.21	0.27
Cs	0.49	0.92	–	–	–	–	–	–	–	0.79	0.27	0.92	0.49
Y	53	47	–	–	–	–	–	–	–	20	54	47	55
Zr	69	35	–	–	–	–	–	–	–	27	175	37	69
Ba	220	71	–	–	–	–	–	–	–	104	240	72	228
Hf	1.95	0.98	–	–	–	–	–	–	–	0.88	4.41	1.04	1.95
Ta	0.35	0.17	–	–	–	–	–	–	–	0.11	0.42	0.18	0.36
La	11.7	9.4	–	–	–	–	–	–	–	3.66	13.14	9.38	11.62
Ce	33.4	28.7	–	–	–	–	–	–	–	9.39	34.10	28.81	32.73
Pr	5.32	4.92	–	–	–	–	–	–	–	1.45	4.94	4.93	5.45
Nd	28.6	28.1	–	–	–	–	–	–	–	7.25	23.39	28.28	29.02
Sm	8.51	8.70	–	–	–	–	–	–	–	2.30	6.78	8.74	8.68
Eu	2.61	3.10	–	–	–	–	–	–	–	0.98	2.20	3.10	2.66
Gd	10.31	10.63	–	–	–	–	–	–	–	2.88	7.98	10.70	10.39
Tb	1.61	1.58	–	–	–	–	–	–	–	0.51	1.42	1.59	1.63
Dy	9.54	9.02	–	–	–	–	–	–	–	3.32	9.18	9.08	9.66
Ho	1.92	1.76	–	–	–	–	–	–	–	0.71	1.97	1.77	1.95
Er	4.98	4.32	–	–	–	–	–	–	–	2.01	5.66	4.40	5.03
Tm	0.66	0.53	–	–	–	–	–	–	–	0.30	0.85	0.54	0.67
Yb	3.95	3.07	–	–	–	–	–	–	–	1.93	5.60	3.11	4.03
Lu	0.57	0.43	–	–	–	–	–	–	–	0.29	0.84	0.43	0.58

Notes:

Major element total includes LOI. FeO* is total FeO, calculated from $Fe_2O_{3(total)}$*0.8995. See methods section for data accuracy and precision details. En dash (–) indicates element not analyzed;
Major element oxides are reported in weight percent (wt.%), trace element concentrations are in parts per million (ppm).

Table C2 $^{87}Sr/^{86}Sr$ isotope compositions for bulk rock powders

	chilled margin (gabbro)		***gabbro***					***diorite***
Sample	MW21-11-96.0	MW21-11-96.3	RM19-64A	RM19-84	RM19-107	RM19-114	RM19-174	RM19-119
stance from contact with wa	at contact	0.3	180	103	60	1070	9	500
Lat_DD	50.3568	50.3568	50.3493	50.3654	50.3545	50.3452	50.3551	50.3482
Long_DD	-127.2527	-127.2527	-127.2596	-127.2485	-127.2562	-127.2732	-127.2548	-127.2647
87Rb/86Sr	0.004	0.009	0.101	0.139	0.056	0.134	0.012	0.142
87Sr/86Sr0	0.7058	0.7061	0.7033	0.7026	0.7041	0.7028	0.7035	0.7027
2 SE	0.0011	0.0011	0.0011	0.0011	0.0011	0.0011	0.0011	0.0011
87Sr/86Sr197Ma	0.7057	0.7061	0.7030	0.7022	0.7039	0.7024	0.7034	0.7023
Rb (ppm)	1.1	2.3	12.8	20.8	6.6	11.1	1.7	12.6
Sr (ppm)	718	781	366	434	343	239	396	256

Notes:

2 SE =analytical uncertainty reported as two standard deviations.

Rb and Sr concentrations are from Table C1.

$^{87}Sr/^{86}Sr_{measured}$ indicates present-day ratio measured; $^{87}Sr/^{86}Sr_{197Ma}$ indicates calculated initial ratios based on ages of 197 Ma.

Table C3 Oxygen isotope ($d^{18}O$ ‰ VSMOW) compositions for bulk rock powders and clinopyroxene

					$d^{18}O$ ‰ VSMOW silicate powders						$d^{18}O$ ‰ VSMOW clinopyroxene					
Sample	Sample Description	Lat_DD	Long_DD	~distance to contact	powder1	powder2	powder3	powder4	internalstd_2SD	precision on repeat	cpx1	cpx2	cpx3	average	internalstd_2SD	precision on repeat_2SD
RM19-174	gabbro	50.3551	-127.2548	9	8.72	4.69	4.89	5.97	0.23	3.71	–	–	–	–	–	–
RM19-37	gabbro	50.3556	-127.2553	36	4.85	6.07	–	–	0.23	1.73	–	–	–	–	–	–
RM19-132	gabbro	50.3560	-127.2555	40	4.94	5.58	–	–	0.23	0.91	4.60	5.14	4.37	4.70	0.26	0.79
RM19-144	gabbro	50.3619	-127.2503	45	4.78	3.9	–	–	0.23	1.24	5.45	5.50	5.28	5.41	0.26	0.24
RM19-105	gabbro	50.3555	-127.2565	73	4.84	4.08	–	–	0.23	1.07	4.94	4.90	4.98	4.94	0.26	0.08
RM19-84	gabbro	50.3654	-127.2485	103	5.43	4.54	–	–	0.23	1.26	4.76	4.75	4.40	4.64	0.26	0.41
RM19-104	gabbro	50.3558	-127.2579	138	5.89	4.59	–	–	0.23	1.84	–	–	–	–	–	–
RM19-160	quartz monzonite	50.3528	-127.2593	167	6.82	6.58	–	–	0.23	0.34	–	–	–	–	–	–
RM19-64A	gabbro	50.3493	-127.2596	180	13.33	–	–	–	0.23	–	–	–	–	–	–	–
RM19-64B	cumulate	50.3493	-127.2596	180	5.75	–	–	–	0.23	–	4.05	3.18	4.24	3.82	0.26	1.14
RM19-114	gabbro	50.3452	-127.2732	1070	3.81	1.81	3	–	0.23	2.01	2.36	2.57	2.51	2.48	0.26	0.22

Notes:

VSMOW refers to the Vienna standard mean ocean water

d in $d^{18}O$ refers to the delta notation

Table C4 Carbon ($d^{13}C$ ‰ VPDB) and isotope ($d^{18}O$ ‰ VSMOW) compositions for Quatsino limestone

Sample	Sample Description	Latitude	Longitude	$d^{13}C$ (‰ VPDB)	$d^{18}O$ (‰ VSMOW)
RM19-MW-QL	dolomitic limestone*, distal (>300 m) from exposed intrusions	50.3453	-127.2432	3.15	22.51
RM19-78D	high calcium limestone*, sampled >1 m from dike	50.3538	-127.2470	3.91	23.45
RM19-69D	high calcium limestone*, sampled >1 m from dike	50.3562	-127.2395	4.22	22.22
RM19-165D	magnesian limestone*, sampled >1m from dike	50.3617	-127.2393	3.49	19.51

Notes:

*Major element chemistry from Table B1 (Chapter 3)

VSMOW refers to the Vienna standard mean ocean water

VPDB refers to the Vienna Pee Dee Belemite Standard

Table C5 **EMPA data for major element chemistry of phases**

Amphibole	phase	SiO_2	TiO_2	Al_2O_3	V_2O_3	Cr_2O_3	FeO	NiO	MnO	MgO	CaO	Na_2O	K_2O	Cl	H_2O	TOTAL	*subclassifications*
RM19-107_amph_142	amphibole	41.3	0.91	9.30	0.224	b.d	23.9	0.011	0.29	6.57	11.0	2.06	0.94	1.94	1.43	99.9	hastingsite
RM19-107_amph_143	amphibole	41.4	0.65	8.44	0.271	0.018	25.8	0.012	0.29	5.45	10.9	1.86	1.17	2.72	1.21	100.3	hastingsite
RM19-107_amph_144	amphibole	42.0	1.40	8.70	0.190	0.007	23.5	0.009	0.29	6.76	11.0	2.12	0.72	1.84	1.46	100.0	hastingsite
RM19-107_amph_145	amphibole	41.6	0.84	8.72	0.243	b.d	24.9	b.d	0.29	6.03	11.0	1.90	1.03	2.25	1.34	100.1	hastingsite
RM19-107_amph_146	amphibole	41.5	1.14	8.27	0.223	0.010	25.0	0.004	0.25	5.76	11.2	1.86	1.09	2.23	1.33	99.9	hastingsite
RM19-107_amph_147	amphibole	41.6	0.81	8.47	0.231	0.003	24.9	0.009	0.29	6.07	10.9	1.94	0.97	2.35	1.31	99.8	hastingsite
RM19-107_amph_148	amphibole	43.8	0.84	7.35	0.242	b.d	24.3	0.006	0.29	7.03	10.9	1.68	0.73	1.39	1.60	100.1	ferro-ferri hornblende
RM19-107_amph_149	amphibole	42.3	0.71	7.12	0.259	0.026	26.4	0.004	0.29	5.67	10.7	1.76	1.21	2.61	1.23	100.3	hastingsite
RM19-107_amph_150	amphibole	36.0	0.04	12.30	0.008	b.d	30.6	b.d	0.28	1.16	11.1	1.90	1.56	4.29	0.72	99.9	chloro-hastingsite
RM19-107_amph_161	amphibole	42.5	1.30	8.12	0.184	b.d	23.1	0.014	0.26	6.81	11.1	1.91	0.84	1.78	1.47	99.5	hastingsite
RM19-107_amph_162	amphibole	36.5	0.04	13.61	b.d	0.020	27.7	0.005	0.23	2.34	11.2	2.05	1.47	4.09	0.80	100.1	ferro-chloro pargasite
RM19-132_amph_204	amphibole	42.6	3.11	9.34	0.127	0.005	15.4	0.011	0.24	11.54	10.9	2.23	0.67	0.25	1.21	96.3	magnesio-hastingsite
RM19-132_amph_205	amphibole	40.3	2.69	9.50	0.075	0.034	20.1	b.d	0.29	11.44	8.5	1.61	0.51	0.20	1.34	96.6	magnesio-hastingsite

Notes:

Amphibole species and corresponding H2O wt% calculate as per the methods of Hawthorne et al. (2012)

Hawthorne et al. (2012) Nomenclature of the amphibole supergroup, American Mineralogist, v (97), p.p 2031–2048

Table C5 **EMPA data for major element chemistry of phases (con't)**

Biotite	**SiO_2**	**TiO_2**	**Al_2O_3**	**V_2O_3**	**Cr_2O_3**	**FeO**	**NiO**	**MnO**	**MgO**	**CaO**	**Na_2O**	**K_2O**	**Cl**	**H_2O**	**TOTAL**	*subclassifications*		
RM19-84_bio_91	36.1	5.57	13.28	0.104	0.014	20.8	0.039	0.10	10.34	0.0	0.28	10.05	0.52	3.67	100.7			
RM19-84_bio_92	36.0	5.78	13.39	0.058	0	20.2	0.022	0.11	10.60	0.0	0.27	9.18	0.46	3.70	99.8			
Clinopyroxene																*Wo*	*En*	*Fs*
RM19-107_cpx_167	51.3	0.93	2.50	0.057	b.d	10.6	0.011	0.32	13.57	20.5	0.34	b.d	–	–	100.2	43.1	39.6	17.3
RM19-107_cpx_168	51.1	0.94	2.58	0.054	0.009	9.4	0.006	0.26	14.24	20.8	0.40	b.d	–	–	99.7	43.3	41.4	15.3
RM19-107_cpx_169	50.9	0.94	2.59	0.061	0.022	10.2	0.002	0.28	13.65	20.8	0.38	b.d	–	–	99.8	43.5	39.7	16.7
RM19-107_cpx_170	51.1	0.93	2.55	0.054	0.004	9.4	0.011	0.26	14.10	20.9	0.36	0.003	–	–	99.6	43.7	41.0	15.3
RM19-107_cpx_171	51.0	0.96	2.59	0.069	0.032	9.5	0.003	0.26	14.31	20.9	0.38	0.002	–	–	100.0	43.3	41.3	15.4
RM19-107_cpx_172	51.0	0.93	2.60	0.070	0.005	9.6	0.017	0.25	14.28	20.7	0.39	b.d	–	–	99.8	43.1	41.4	15.6
RM19-107_cpx_176	50.8	1.17	2.46	0.102	0.004	11.2	0.016	0.38	13.07	20.3	0.35	0.004	–	–	99.9	43.0	38.5	18.6
RM19-107_cpx_177	50.8	0.95	2.30	0.093	0.063	10.7	b.d	0.37	13.36	20.6	0.33	0.004	–	–	99.5	43.3	39.1	17.5
RM19-107_cpx_178	50.7	1.24	2.62	0.082	0.032	11.1	0.006	0.37	13.09	20.5	0.36	b.d	–	–	100.0	43.2	38.5	18.3
RM19-132_cpx_185	51.4	0.81	1.80	0.056	0.001	11.1	0.002	0.40	13.33	20.6	0.32	0.001	–	–	99.9	43.1	38.8	18.1
RM19-132_cpx_186	51.1	0.92	1.94	0.049	0.026	11.5	b.d	0.38	13.29	20.1	0.35	b.d	–	–	99.7	42.3	38.9	18.8
RM19-132_cpx_187	51.7	0.70	1.52	0.032	b.d	11.6	0.013	0.39	13.46	20.0	0.33	b.d	–	–	99.7	41.8	39.2	19.0
RM19-132_cpx_188	51.3	0.71	1.79	0.070	0.023	10.6	0.005	0.37	13.54	20.6	0.29	b.d	–	–	99.4	43.2	39.4	17.4
RM19-132_cpx_200	51.7	0.73	1.62	0.050	0.019	11.8	0.002	0.41	13.52	19.9	0.29	b.d	–	–	100.0	41.5	39.3	19.2
RM19-132_cpx_201	51.0	0.86	1.73	0.066	b.d	11.4	b.d	0.38	13.24	20.2	0.31	b.d	–	–	99.2	42.5	38.8	18.8
RM19-132_cpx_202	50.9	0.87	2.00	0.051	0.016	11.6	b.d	0.39	13.27	20.0	0.33	b.d	–	–	99.4	42.1	38.9	19.0
RM19-132_cpx_203	53.1	0.11	0.51	0.018	0.016	10.6	b.d	0.41	13.20	22.1	0.16	b.d	–	–	100.2	45.3	37.7	17.0
RM19-132_cpx_219	51.8	0.75	1.57	0.026	b.d	11.4	b.d	0.39	13.66	20.1	0.34	b.d	–	–	100.1	41.9	39.5	18.6
RM19-132_cpx_220	51.5	0.85	1.77	0.044	0.016	11.7	0.003	0.40	13.70	20.0	0.33	0.006	–	–	100.2	41.5	39.6	18.9
RM19-132_cpx_221	51.7	0.71	1.59	0.037	0.011	11.7	0.010	0.40	13.64	20.2	0.32	b.d	–	–	100.3	41.8	39.3	18.9
RM19-132_cpx_222	51.3	0.91	2.00	0.066	b.d	11.6	0.005	0.40	13.23	20.2	0.31	b.d	–	–	100.1	42.3	38.6	19.1
RM19-132_cpx_223	51.1	0.69	1.70	0.044	0.018	12.1	0.009	0.40	13.49	19.8	0.32	b.d	–	–	99.7	41.3	39.1	19.6
RM19-132_cpx_224	51.2	0.82	1.71	0.054	b.d	11.5	0.007	0.35	13.38	20.2	0.32	b.d	–	–	99.6	42.3	39.0	18.7
RM19-84_cpx_104	50.3	1.26	2.78	0.113	0.010	10.0	0.002	0.28	13.46	20.8	0.41	b.d	–	–	99.4	43.9	39.6	16.5
RM19-84_cpx_105	50.4	1.14	2.57	0.107	0.016	9.1	b.d	0.28	13.22	22.1	0.40	0.001	–	–	99.4	46.4	38.6	15.0
RM19-84_cpx_106	50.9	1.13	2.59	0.108	0.024	9.7	0.001	0.27	13.34	21.2	0.42	b.d	–	–	99.6	44.8	39.2	16.0
RM19-84_cpx_107	51.8	0.92	2.11	0.100	0.025	10.1	0.005	0.30	14.41	20.1	0.33	b.d	–	–	100.3	41.8	41.7	16.5
RM19-84_cpx_126	51.5	0.78	1.60	0.058	0.002	11.7	0.001	0.34	14.47	18.4	0.32	b.d	–	–	99.1	38.6	42.2	19.1
RM19-84_cpx_127	51.1	0.90	1.95	0.072	0.000	9.9	b.d	0.33	13.71	20.0	0.32	b.d	–	–	98.4	42.7	40.7	16.6
RM19-84_cpx_138	51.4	1.12	2.17	0.071	0.023	11.3	0.008	0.33	14.66	18.6	0.33	b.d	–	–	100.0	38.9	42.7	18.4
RM19-84_cpx_139	52.1	0.70	1.64	0.072	0.002	9.7	0.009	0.31	14.08	21.0	0.31	0.003	–	–	99.8	43.6	40.7	15.7

Notes:

b.d indicates oxide is below detection limits

Table C5 **EMPA data for major element chemistry of phases (con't)**

Orthopyroxene	**SiO_2**	**TiO_2**	**Al_2O_3**	**V_2O_3**	**Cr_2O_3**	**FeO**	**NiO**	**MnO**	**MgO**	**CaO**	**Na_2O**	**K_2O**	**Cl**	**H_2O**	**TOTAL**	*subclassifications*		
RM19-84_opx_112	52.7	0.32	0.94	0.003	0.020	21.2	0.005	0.57	21.96	1.3	0.014	b.d	–	–	99.1	2.7	63.1	34.2
RM19-84_opx_113	52.3	0.26	1.17	0.011	b.d	21.3	0.003	0.58	21.79	1.2	0.007	0.03	–	–	98.7	2.5	63.0	34.5
RM19-84_opx_114	52.6	0.39	0.92	0.007	0.005	21.2	0.001	0.58	21.89	1.6	0.016	b.d	–	–	99.2	3.3	62.7	34.1
RM19-84_opx_115	52.9	0.34	0.85	0.009	0.017	21.3	b.d	0.58	21.80	1.6	0.023	b.d	–	–	99.4	3.3	62.5	34.3
RM19-84_opx_136	52.6	0.25	0.76	0.019	0.022	22.0	0.005	0.60	21.02	1.5	0.017	b.d	–	–	98.8	3.1	61.0	35.9
RM19-84_opx_137	52.8	0.26	0.75	b.d	b.d	21.2	0.001	0.59	21.80	1.4	0.026	b.d	–	–	98.9	2.9	62.8	34.3
Olivine																*Fo*	*Fa*	
RM19-107_ol_173	35.5	0.04	0.02	0.008	0.011	38.7	0.002	0.82	24.39	0.07	b.d	–	–	–	99.5	52.9	47.1	
RM19-107_ol_174	35.4	0.05	0.02	0.001	b.d	37.0	0.009	0.77	25.93	0.07	0.009	–	–	–	99.3	55.5	44.5	
RM19-107_ol_175	35.4	0.05	0.01	b.d	b.d	37.0	0.017	0.79	26.19	0.07	0.023	–	–	–	99.6	55.8	44.2	
RM19-132_ol_182	35.1	0.06	0.01	b.d	0.016	39.4	0.015	0.80	24.25	0.06	0.010	–	–	–	99.7	52.3	47.7	
RM19-132_ol_183	35.2	0.02	0.01	0.015	0.003	39.3	b.d	0.82	24.24	0.06	b.d	–	–	–	99.6	52.4	47.6	
RM19-132_ol_184	35.0	0.04	0.01	b.d	0.001	40.3	0.017	0.82	23.28	0.09	b.d	–	–	–	99.6	50.7	49.3	
RM19-132_ol_197	34.6	0.03	0.01	b.d	b.d	41.5	0.017	0.84	22.29	0.06	0.017	–	–	–	99.4	48.9	51.1	
RM19-132_ol_198	34.6	0.03	0.01	0.004	0.007	41.3	0.003	0.81	22.17	0.03	0.040	–	–	–	99.0	48.9	51.1	
RM19-132_ol_199	34.7	0.02	0.01	b.d	b.d	41.2	0.006	0.83	22.45	0.06	b.d	–	–	–	99.3	49.3	50.7	
RM19-132_ol_215	34.8	0.05	0.02	b.d	b.d	40.6	0.006	0.84	23.12	0.11	0.006	–	–	–	99.5	50.4	49.6	
RM19-132_ol_216	35.0	0.02	0.01	b.d	b.d	40.7	0.010	0.83	22.94	0.05	b.d	–	–	–	99.6	50.1	49.9	
RM19-132_ol_217	34.8	0.04	0.00	0.011	0.005	40.2	0.001	0.82	23.29	0.07	0.008	–	–	–	99.3	50.8	49.2	
RM19-132_ol_218	35.1	0.04	0.01	0.011	b.d	39.8	b.d	0.80	23.78	0.07	b.d	–	–	–	99.6	51.6	48.4	
RM19-84_ol_95	36.3	0.03	b.d	b.d	0.009	33.9	0.022	0.57	28.83	0.06	b.d	–	–	–	99.8	60.2	39.8	
RM19-84_ol_96	36.3	0.02	0.02	0.003	0.001	33.9	0.017	0.59	28.98	0.05	b.d	–	–	–	99.9	60.4	39.6	
RM19-84_ol_97	36.3	0.04	0.01	b.d	0.013	33.9	0.019	0.60	28.62	0.06	b.d	–	–	–	99.6	60.0	40.0	
RM19-84_ol_98	36.1	0.02	0.01	b.d	b.d	33.9	0.014	0.60	28.63	0.06	0.006	–	–	–	99.4	60.1	39.9	
RM19-84_ol_99	36.2	0.04	b.d	b.d	0.005	33.8	0.018	0.58	28.70	0.07	0.005	–	–	–	99.4	60.2	39.8	
RM19-84_ol_108	35.9	0.00	b.d	0.012	0.005	36.7	0.028	0.65	26.21	0.07	b.d	–	–	–	99.5	56.0	44.0	
RM19-84_ol_109	35.7	0.01	b.d	b.d	b.d	36.8	0.016	0.65	26.27	0.06	b.d	–	–	–	99.5	56.0	44.0	
RM19-84_ol_110	35.7	0.04	0.01	0.024	b.d	37.1	0.016	0.64	25.95	0.06	0.008	–	–	–	99.5	55.5	44.5	
RM19-84_ol_111	35.7	0.02	b.d	b.d	0.013	36.9	0.012	0.64	25.91	0.06	0.007	–	–	–	99.2	55.6	44.4	
RM19-84_ol_124	35.9	0.04	0.01	0.001	0.005	35.8	0.022	0.63	26.96	0.05	b.d	–	–	–	99.4	57.3	42.7	
RM19-84_ol_125	35.7	0.04	0.01	b.d	0.014	35.8	0.025	0.64	26.84	0.08	0.005	–	–	–	99.1	57.2	42.8	
RM19-84_ol_135	35.8	0.03	0.01	b.d	b.d	36.2	0.002	0.66	26.62	0.08	0.019	–	–	–	99.4	56.7	43.3	

Notes:

b.d indicates oxide is below detection limits

Table C5 EMPA data for major element chemistry of phases (con't)

Plagioclase	SiO_2	TiO_2	Al_2O_3	V_2O_3	Cr_2O_3	FeO	NiO	MnO	MgO	CaO	Na_2O	K_2O	TOTAL	*An*	*Ab*	*Or*	*location*
RM19-107_plag_163	53.7	0.08	28.94	b.d	b.d	0.39	0.006	0.01	0.04	11.7	5.03	0.18	100.1	55.8	43.2	1.0	rim
RM19-107_plag_164	53.3	0.07	28.84	0.002	0.026	0.38	0	0.01	0.04	11.8	5.01	0.18	99.7	55.9	43.1	1.0	rim
RM19-107_plag_165	53.3	0.08	28.80	b.d	b.d	0.42	0.003	b.d	0.04	11.9	4.74	0.18	99.5	57.6	41.3	1.0	rim
RM19-107_plag_166	53.5	0.08	28.61	b.d	0.016	0.40	0.005	b.d	0.05	11.7	5.02	0.19	99.6	55.8	43.2	1.1	rim
RM19-107_plag_179	54.6	0.08	27.43	b.d	0.009	0.40	0.007	0.01	0.04	10.7	5.31	0.23	98.8	51.9	46.7	1.3	rim
RM19-107_plag_180	53.4	0.08	28.61	0.002	b.d	0.45	b.d	b.d	0.05	11.8	4.83	0.18	99.4	56.8	42.2	1.0	rim
RM19-107_plag_181	54.8	0.09	27.76	0.010	0.006	0.38	0.011	0.01	0.05	10.6	5.35	0.22	99.4	51.6	47.1	1.3	rim
RM19-132_plag_189	46.0	0.02	33.70	b.d	b.d	0.34	0.014	0.01	0.03	17.4	1.84	0.06	99.4	83.7	16.0	0.4	core
RM19-132_plag_190	46.3	0.04	33.37	b.d	b.d	0.34	0.010	b.d	0.02	17.1	1.97	0.03	99.3	82.6	17.2	0.2	core
RM19-132_plag_191	54.1	0.09	27.79	b.d	b.d	0.35	b.d	0.02	0.03	10.7	5.49	0.21	98.8	51.2	47.6	1.2	rim
RM19-132_plag_192	56.2	0.07	26.94	b.d	0.027	0.34	b.d	b.d	0.04	9.4	6.10	0.29	99.4	45.3	53.0	1.7	rim
RM19-132_plag_206	55.8	0.09	26.95	b.d	b.d	0.37	0.001	b.d	0.02	9.5	5.77	0.25	98.8	47.0	51.5	1.5	rim
RM19-132_plag_207	54.2	0.07	28.06	b.d	b.d	0.42	b.d	b.d	0.06	10.9	5.16	0.20	99.1	53.2	45.6	1.2	rim
RM19-132_plag_208	55.9	0.10	27.16	b.d	0.003	0.40	0.008	b.d	0.08	9.7	5.99	0.23	99.6	46.5	52.2	1.3	rim
RM19-132_plag_225	46.9	0.04	33.13	0.006	0.012	0.34	0.005	b.d	0.02	16.7	2.07	0.05	99.3	81.5	18.2	0.3	core
RM19-132_plag_226	55.7	0.06	26.95	b.d	0.017	0.27	0.012	b.d	0.03	9.6	5.98	0.19	98.8	46.6	52.4	1.1	rim
RM19-132_plag_227	55.4	0.06	27.22	b.d	0.005	0.39	b.d	b.d	0.02	9.9	5.75	0.21	99.0	48.3	50.5	1.2	rim
RM19-132_plag_228	46.3	0.05	33.27	0.003	b.d	0.29	b.d	b.d	0.01	17.3	1.91	0.06	99.2	83.1	16.5	0.3	core
RM19-132_plag_229	55.4	0.07	27.37	b.d	b.d	0.24	0.001	0.01	0.02	10.1	5.86	0.23	99.3	48.0	50.6	1.3	rim
RM19-132_plag_230	55.8	0.08	27.10	0.002	b.d	0.31	0.002	0.01	0.03	9.7	6.02	0.26	99.3	46.5	52.0	1.5	rim
RM19-132_plag_231	55.8	0.07	27.03	b.d	b.d	0.31	0.001	0.01	0.03	9.6	5.93	0.27	99.1	46.6	51.9	1.6	rim
RM19-132_plag_232	55.4	0.05	27.65	b.d	0.012	0.54	b.d	b.d	0.02	10.1	5.83	0.25	99.8	48.2	50.4	1.4	rim
RM19-132_plag_233	46.2	0.02	33.38	0.006	0.005	0.32	b.d	0.01	0.02	17.3	1.81	0.06	99.1	83.8	15.8	0.3	core
RM19-84_plag_100	52.9	0.09	29.30	0.006	0.008	0.31	0.007	b.d	0.04	12.2	4.79	0.15	99.8	57.9	41.2	0.9	rim
RM19-84_plag_101	54.5	0.09	27.74	0.011	0.002	0.26	b.d	b.d	0.03	10.5	5.66	0.24	99.1	49.9	48.7	1.4	rim
RM19-84_plag_102	52.4	0.09	28.92	b.d	b.d	0.30	0.000	b.d	0.05	12.3	4.71	0.23	98.9	58.3	40.4	1.3	rim
RM19-84_plag_103	47.3	0.05	32.39	b.d	0.004	0.30	0.009	b.d	0.02	16.4	2.38	0.08	98.9	78.8	20.7	0.4	core
RM19-84_plag_116	47.6	0.04	32.36	b.d	b.d	0.34	0.003	b.d	0.02	16.2	2.37	0.08	99.1	78.8	20.8	0.5	core
RM19-84_plag_117	53.1	0.08	28.50	b.d	0.013	0.31	0.001	0.01	0.03	11.7	4.81	0.26	98.8	56.4	42.0	1.5	rim
RM19-84_plag_118	47.1	0.06	32.70	0.015	0.007	0.33	0.009	0.01	0.01	16.5	2.22	0.06	99.0	80.1	19.5	0.4	core
RM19-84_plag_119	55.7	0.07	26.90	b.d	b.d	0.35	0.010	0.01	0.02	9.7	6.01	0.16	98.9	46.6	52.5	0.9	rim
RM19-84_plag_128	52.9	0.08	28.80	b.d	0.005	0.32	0.010	b.d	0.03	11.9	4.68	0.17	98.8	57.8	41.2	1.0	rim
RM19-84_plag_129	51.0	0.10	29.65	b.d	0.002	0.28	b.d	b.d	0.03	13.0	3.93	0.20	98.3	63.9	34.9	1.2	rim
RM19-84_plag_140	53.2	0.09	28.67	b.d	b.d	0.36	b.d	b.d	0.04	11.7	4.63	0.33	99.0	57.1	41.0	1.9	rim
RM19-84_plag_141	51.7	0.09	29.09	b.d	b.d	0.30	0.008	b.d	0.02	12.6	4.27	0.19	98.2	61.2	37.6	1.1	rim

Notes:
b.d indicates oxide is below detection limits

Table C5 **EMPA data for major element chemistry of phases (con't)**

Ilmenite	TiO_2	Al_2O_3	V_2O_3	Cr_2O_3	FeO	NiO	MnO	MgO	TOTAL
RM19-107_ilm_151	51.20	0.01	b.d	b.d	45.9	0.018	1.58	0.07	98.8
RM19-107_ilm_152	50.55	0.01	b.d	0.009	46.2	0.005	1.68	0.05	98.6
RM19-107_ilm_155	50.94	0.01	b.d	b.d	45.5	b.d	2.18	0.04	98.7
RM19-107_ilm_156	50.74	0.02	b.d	0.006	45.8	0.007	1.92	0.02	98.5
RM19-107_ilm_159	49.55	0.03	0.044	b.d	46.6	0.011	1.44	0.09	97.8
RM19-107_ilm_160	49.04	0.04	0.035	0.029	47.0	0.004	1.46	0.08	97.7
RM19-132_ilm_193	51.11	0.04	b.d	0.019	45.3	0.010	0.97	1.24	98.7
RM19-132_ilm_194	51.31	0.04	b.d	0.017	44.5	0.009	0.86	1.88	98.6
RM19-132_ilm_209	51.00	0.03	b.d	0.050	45.1	b.d	0.85	1.47	98.6
RM19-132_ilm_210	50.82	0.03	b.d	b.d	45.0	b.d	0.82	1.60	98.3
RM19-132_ilm_211	51.02	0.05	b.d	0.004	45.1	b.d	0.87	1.46	98.6
RM19-84_ilm_132	50.53	0.04	0.017	b.d	45.4	0.002	1.04	1.28	98.3
RM19-84_ilm_133	50.69	0.02	0.006	0.016	45.6	b.d	1.20	0.93	98.5
RM19-84_ilm_122	50.48	0.04	0.067	0.010	45.4	0.018	1.08	1.13	98.2
RM19-84_ilm_123	50.47	0.03	0.005	b.d	45.2	0.015	0.88	1.51	98.1
RM19-84_ilm_93	49.76	0.01	0.086	0.025	46.3	0.029	1.64	0.33	98.2
RM19-84_ilm_94	50.25	0.01	b.d	b.d	46.1	0.015	1.73	0.32	98.5
Magnetite									
RM19-84_mag_120	2.12	1.38	1.49	0.070	86.6	0.027	0.10	0.21	92.0
RM19-84_mag_121	2.50	1.20	1.43	0.069	86.1	0.041	0.08	0.16	91.7
RM19-84_mag_130	4.76	2.62	1.57	0.054	82.8	0.019	0.30	0.30	92.4
RM19-84_mag_131	1.93	0.98	1.53	0.058	86.8	0.016	0.09	0.13	91.6
RM19-107_mag_153	10.29	1.00	1.78	0.010	79.2	0.014	0.44	0.02	92.9
RM19-107_mag_154	8.40	1.39	1.71	b.d	80.9	0.011	0.37	0.01	92.8
RM19-107_mag_157	8.42	3.68	0.87	0.021	78.4	0.014	0.36	0.43	92.3
RM19-107_mag_158	7.56	4.85	1.00	0.019	78.4	0.001	0.35	0.07	92.3
RM19-132_mag_195	8.59	3.02	1.00	0.060	79.5	0.022	0.32	0.59	93.2
RM19-132_mag_196	9.88	3.28	0.89	0.059	78.1	0.015	0.46	0.42	93.2
RM19-132_mag_212	8.26	3.09	0.98	0.039	79.9	0.013	0.31	0.38	93.0
RM19-132_mag_213	10.24	3.19	0.96	0.066	77.8	0.012	0.42	0.45	93.2
RM19-132_mag_214	7.56	3.36	1.01	0.050	79.7	0.015	0.30	0.28	92.4

Notes:
b.d indicates oxide is below detection limits

Table C6 LA-ICP-MS data for trace element chemistry of phases

Plagioclase	spot location	Ti49_ppm	Rb85_ppm	Sr88_ppm	Y89_ppm	Zr90_ppm	Ba137_ppm	La139_ppm	Ce140_ppm	Pr141_ppm	Nd146_ppm	Sm147_ppm	Eu151_ppm	Gd157_ppm	Tb159_ppm	Dy163_ppm	Ho165_ppm	Er166_ppm	Tm169_ppm	Yb172_ppm	Lu175_ppm
132_pl_2	mid	321	16.91	638	0.392	0.022	159	0.478	1.150	0.137	0.682	0.146	0.492	0.101	0.024	0.072	0.016	0.024	0.003	0.007	0.003
132_pl_3	rim	635	2.92	806	0.284	0.048	148	1.178	2.536	0.274	1.101	0.206	1.550	0.143	0.009	0.057	0.011	0.019	0.003	0.010	b.d
132_pl_5	rim	615	3.38	754	0.299	0.261	138	1.157	2.309	0.266	1.068	0.141	1.496	0.171	0.015	0.055	0.008	0.015	0.005	0.008	b.d
132_pl_1	core	150	1.15	442	0.178	0.075	19	0.207	0.466	0.052	0.293	0.046	0.183	0.035	0.007	0.022	0.009	b.d	b.d	0.006	0.002
132_pl_4	core	201	13.56	550	0.333	0.048	162	0.278	0.649	0.076	0.361	0.066	0.800	0.080	0.009	0.077	0.015	0.024	0.002	b.d	0.004
144_pl_7	mid	359	0.84	519	0.180	0.080	41	0.353	0.742	0.086	0.412	0.094	0.393	0.048	0.006	0.026	0.004	0.019	0.004	0.007	0.003
144_pl_10	mid	311	0.66	495	0.231	0.064	39	0.346	0.704	0.076	0.396	0.065	0.343	0.082	0.009	0.044	0.004	0.026	0.003	0.010	b.d
144_pl_1	rim	397	1.45	427	0.708	0.472	37	0.470	1.108	0.138	0.645	0.174	0.380	0.160	0.026	0.119	0.023	0.065	0.008	0.069	0.014
144_pl_4	mid	313	1.02	448	0.199	0.066	34	0.309	0.666	0.076	0.333	0.078	0.306	0.067	0.007	0.038	0.005	0.012	b.d	0.010	b.d
144_pl_5	rim	734	1.49	702	0.407	0.386	140	0.815	1.793	0.192	0.749	0.134	1.169	0.103	0.011	0.079	0.015	0.040	0.006	0.030	0.002
144_pl_8	rim	573	2.17	575	0.286	0.329	107	0.602	1.316	0.139	0.640	0.118	0.809	0.075	0.011	0.042	0.011	0.030	0.002	0.043	0.004
144_pl_2	core	209	1.30	458	0.430	0.180	30	0.397	0.821	0.097	0.455	0.122	0.369	0.102	0.015	0.079	0.017	0.042	0.007	0.042	0.005
144_pl_3	core	735	4.60	495	1.792	4.674	46	0.567	1.347	0.174	0.824	0.239	0.397	0.311	0.049	0.305	0.067	0.235	0.027	0.202	0.032
144_pl_6	core	155	0.67	462	0.278	0.068	29	0.345	0.645	0.079	0.410	0.070	0.307	0.047	0.009	0.027	0.008	0.020	b.d	0.013	0.003
144_pl_9	core	135	0.09	484	0.159	0.010	17	0.265	0.492	0.062	0.287	0.069	0.205	0.045	0.007	0.035	b.d	0.012	0.003	b.d	b.d
64A_pl_1	rim	607	0.32	614	0.206	0.044	58	0.476	1.072	0.121	0.494	0.099	0.543	0.073	0.008	0.052	0.006	0.027	0.004	b.d	b.d
64A_pl_3	rim	600	1.99	691	0.269	0.046	87	0.569	1.263	0.148	0.598	0.103	1.220	0.087	0.014	0.056	0.011	0.027	0.003	0.013	0.002
64A_pl_4	core	567	0.32	606	0.177	0.044	56	0.481	1.082	0.121	0.502	0.088	0.546	0.093	0.009	0.034	0.005	0.016	0.002	0.008	0.008
64A_pl_5	rim	667	1.96	775	0.372	4.508	132	1.042	2.359	0.246	0.971	0.166	1.761	0.107	0.013	0.077	0.015	0.036	0.005	0.014	b.d
64A_pl_6	rim	655	0.34	663	0.256	0.061	78	0.561	1.279	0.144	0.590	0.125	1.049	0.073	0.007	0.045	0.018	0.035	b.d	0.005	0.006
64A_pl_2	core	906	3.02	1048	0.314	0.507	196	1.104	2.482	0.278	0.987	0.170	1.730	0.198	0.019	0.065	0.020	0.045	0.014	0.040	0.010
64B_pl_1	rim	564	23.19	1302	0.659	0.084	687	4.210	8.260	0.792	2.770	0.345	4.268	0.306	0.029	0.110	0.029	0.053	0.003	0.049	0.007
64B_pl_2	rim	726	50.42	1116	0.804	2.731	589	1.222	3.045	0.346	1.445	0.298	2.228	0.251	0.030	0.144	0.031	0.091	0.011	0.053	0.013
64B_pl_3	core	596	31.05	1254	0.572	0.065	680	2.561	5.304	0.529	1.978	0.338	3.074	0.169	0.026	0.128	0.023	0.042	0.008	0.025	0.003

Table C6 LA-ICP-MS data for trace element chemistry of phases (con't)

Clinopyroxene	spot location	V51_ppm	Cr52_ppm	Ni60_ppm	Sr88_ppm	Y89_ppm	Zr90_ppm	Ba137_ppm	La139_ppm	Ce140_ppm	Pr141_ppm	Nd146_ppm	Sm147_ppm	Eu151_ppm	Gd157_ppm	Tb159_ppm	Dy163_ppm	Ho165_ppm	Er166_ppm	Tm169_ppm	Yb172_ppm	Lu175_ppm
132_cpx_1	n/a (granoblastic)	414	31.0	16.4	25.3	60.9	53.5	b.d	2.16	9.11	2.12	14.76	6.28	1.31	9.11	1.65	11.43	2.43	6.90	1.00	6.61	1.00
132_cpx_2	n/a (granoblastic)	445	27.6	15.3	25.8	51.4	39.4	b.d	1.71	7.13	1.71	11.92	5.51	1.34	7.81	1.45	9.67	2.06	5.79	0.80	5.36	0.82
132_cpx_3	n/a (granoblastic)	360	15.3	16.5	23.7	59.0	49.1	b.d	1.80	8.01	1.90	13.86	6.08	1.28	8.85	1.62	10.85	2.36	6.68	0.93	6.28	0.95
132_cpx_4	n/a (granoblastic)	347	18.8	15.9	23.3	61.3	53.7	b.d	1.86	8.30	b.d	b.d	6.30	1.21	8.79	1.68	11.25	2.42	6.87	0.99	6.48	0.99
132_cpx_5	n/a (granoblastic)	455	77.8	14.8	25.6	66.9	67.5	6.11	2.33	10.12	2.39	16.26	6.82	1.33	9.83	1.83	12.44	2.71	7.68	1.07	7.03	1.11
144_cpx_1c	core	809	13.0	41.2	18.5	28.9	15.8	0.10	0.65	2.76	0.71	5.31	2.71	0.86	4.15	0.77	5.33	1.16	3.34	0.45	3.17	0.50
144_cpx_1r	rim	769	1.9	36.7	19.8	30.7	17.1	0.08	0.73	3.11	0.78	5.64	2.79	0.91	4.52	0.82	5.74	1.24	3.53	0.49	3.32	0.48
144_cpx_2c	core	780	139.3	55.4	20.7	24.6	14.4	0.11	0.59	2.48	0.63	4.75	2.32	0.76	3.64	0.65	4.63	1.00	2.75	0.39	2.51	0.40
144_cpx_2r	rim	985	91.1	48.7	23.9	30.1	19.3	0.32	0.78	3.18	0.78	5.88	2.87	0.93	4.53	0.83	5.74	1.21	3.43	0.46	3.11	0.46

Table C6 LA-ICP-MS data for trace element chemistry of phases (con't)

Fe-Ti oxides	phase	spot location	Sc45_ppm	V51_ppm	Cr52_ppm	Ni60_ppm	Cu65_ppm	Zn66_ppm	Ga71_ppm	Co59_ppm	Zr90_ppm	Nb93_ppm	Mo95_ppm	Sn118_ppm
132_mag_1	magnetite	n/a	11.1	8033	476	79	11.0	753	66	202	25	b.d	1.9	4.4
132_mag_2	magnetite	n/a	14.7	8642	502	80	2.0	765	67	210	12	b.d	1.5	3.6
132_mag_3	magnetite	n/a	13.2	8730	486	77	3.0	673	70	197	26	b.d	2.3	5.2
144_mag_1	magnetite	n/a	9.7	14760	b.d	201	2.6	2467	98	236	b.d	b.d	4.4	9.8
144_mag_2	magnetite	n/a	11.9	17495	90	199	3.6	1185	86	264	b.d	b.d	2.2	4.6
144_mag_3	magnetite	n/a	9.0	12728	38	161	1.7	890	71	203	b.d	b.d	2.2	4.8
144_ilm_4	ilmenite	n/a	56.4	947	b.d	37	3.5	81	b.d	147	112	49	b.d	2.1
64A_ilm_1	ilmenite	n/a	25.6	897	b.d	b.d	5.8	38	b.d	52	343	41	b.d	1.4
64A_mag_2	magnetite	n/a	9.3	6507	38	31	8.8	1894	60	80	34	b.d	2.2	4.1
64A_ilm_3	ilmenite	n/a	84.4	853	b.d	b.d	3.5	100	b.d	50	467	41	b.d	1.3
64A_ilm_4	ilmenite	n/a	93.7	718	b.d	b.d	3.3	103	b.d	48	441	33	b.d	b.d
64A_ilm_5	ilmenite	n/a	92.6	988	b.d	b.d	3.2	197	b.d	50	414	41	b.d	b.d
64A_ilm_6	ilmenite	n/a	90.4	1034	b.d	b.d	2.9	203	b.d	50	452	41	b.d	b.d
64B_ilm_1	ilmenite	n/a	75.4	789	b.d	b.d	3.4	166	b.d	52	789	49	1.4	3.7
64B_ilm_2	ilmenite	n/a	73.9	777	b.d	b.d	3.3	127	b.d	53	725	56	1.5	3.5
64B_ilm_3	ilmenite	n/a	78.7	867	b.d	b.d	3.3	161	b.d	57	808	42	b.d	3.4
64B_mag_4	magnetite	n/a	7.7	6306	b.d	b.d	25.1	3382	66	70	32	b.d	4.2	6.0
64B_ilm_5	ilmenite	n/a	75.1	1225	b.d	b.d	9.4	117	b.d	56	738	49	1.3	3.5
64B_ilm_6	ilmenite	n/a	77.5	1161	b.d	b.d	4.6	127	b.d	57	896	53	1.5	3.7

Table C6 LA-ICP-MS data for trace element chemistry of phases

Apatite	spot location	Sr88_ppm	Y89_ppm	Zr90_ppm	Ba137_ppm	La139_ppm	Ce140_ppm	Pr141_ppm	Nd146_ppm	Sm147_ppm	Eu151_ppm	Gd157_ppm	Tb159_ppm	Dy163_ppm	Ho165_ppm	Er166_ppm	Tm169_ppm	Yb172_ppm	Lu175_ppm
64B-3_ap_1	n/a	464	647	4.8	4.5	135	415	74	403	119	30	149	20	120	23	59	6.6	35	4.7
64B-3_ap_3	n/a	463	632	5.1	5.5	139	435	77	417	123	30	151	20	121	23	58	6.5	34	4.6
64B-3_ap_4	n/a	477	621	4.4	4.5	135	422	75	414	122	31	150	20	119	23	57	6.4	34	4.5
64B-3_ap_5	n/a	485	872	8.1	5.2	200	567	103	578	166	36	207	28	167	32	82	9.2	48	6.5
64B-3_ap_6	n/a	451	881	6.4	5.8	193	539	97	537	155	34	190	26	160	31	81	9.5	52	7.1
64B-3_ap_7	n/a	449	958	5.6	5.8	222	630	110	593	169	35	205	29	173	33	87	10.1	55	7.3
64B-3_ap_8	n/a	461	744	5.7	5.0	165	472	85	470	137	30	170	23	138	26	67	7.8	42	5.7
64B-3_ap_9	n/a	477	868	8.6	5.1	198	558	101	577	168	36	212	29	171	33	83	9.3	49	6.6
64B-3_ap_10	n/a	482	873	8.4	4.7	199	567	102	587	170	36	214	29	170	33	83	9.3	49	6.6
64B-3_ap_11	n/a	459	739	6.8	4.2	168	484	89	510	148	33	187	25	148	28	71	7.8	41	5.5
64B-3_ap_13	n/a	471	879	8.7	5.4	205	576	105	604	174	37	217	29	176	33	84	9.4	50	6.7
64B-3_ap_14	n/a	471	765	7.3	4.8	176	492	90	514	150	32	189	25	151	29	73	8.1	43	5.8
64B-3_ap_16	n/a	464	815	9.7	5.1	190	534	98	564	163	35	206	28	165	31	80	8.9	47	6.4
64B-3_ap_17	n/a	468	795	6.7	4.5	189	525	95	543	156	33	199	27	159	30	77	8.5	45	6.0
64B-3_ap_18	n/a	463	852	9.4	8.5	191	530	96	544	157	35	199	27	163	31	80	9.1	49	6.6
64B-3_ap_19	n/a	463	811	7.2	4.3	194	534	95	536	155	33	196	26	158	30	76	8.5	45	6.1
64B-3_ap_20	n/a	457	673	4.9	5.9	142	410	75	425	127	29	158	21	128	24	62	7.0	39	5.2
64B-3_ap_21	n/a	486	860	66.4	8.1	194	539	99	571	166	36	205	28	168	32	81	9.1	49	6.5
64B-3_ap_22	n/a	483	817	8.1	4.9	198	545	99	571	164	35	207	28	166	31	79	8.8	46	6.1
64B-3_ap_23	n/a	464	746	5.8	5.0	150	426	78	450	136	32	171	23	138	26	67	7.7	43	5.7
64B-3_ap_24	n/a	470	736	5.6	4.8	146	417	77	441	133	32	168	23	137	26	67	7.7	42	5.7
64B-3_ap_25	n/a	470	678	4.7	4.0	137	390	72	419	126	30	161	22	129	24	61	6.8	37	4.9
64B-3_ap_26	n/a	484	979	9.3	5.0	221	617	112	653	189	40	239	32	194	37	93	10.5	56	7.5
64B-3_ap_27	n/a	474	935	8.4	5.2	213	587	105	604	172	37	218	30	180	34	88	10.1	54	7.2
64B-3_ap_28	n/a	479	895	8.5	4.6	207	590	106	605	173	37	220	30	178	34	86	9.6	51	6.9
64B-3_ap_29	n/a	487	711	7.6	5.6	158	458	82	463	137	31	173	23	139	26	66	7.4	40	5.4
64B-3_ap_30	n/a	485	608	4.6	4.5	123	361	66	385	117	30	150	20	117	22	54	6.0	32	4.2
64B-3_ap_31	n/a	462	849	8.3	5.8	200	584	103	571	164	36	205	28	166	32	81	9.0	48	6.4
64B-3_ap_32	n/a	480	909	8.8	4.7	210	582	106	605	176	38	224	30	179	34	87	9.7	52	6.9
64B-3_ap_33	n/a	484	692	6.8	4.6	146	417	75	438	131	31	167	22	132	25	62	6.8	36	4.8
64B-3_ap_34	n/a	470	656	4.6	4.7	134	386	69	397	119	29	153	20	120	23	56	6.5	34	4.6
64B-3_ap_35	n/a	486	828	7.8	4.5	177	508	92	522	155	34	201	27	160	30	76	8.3	44	5.9

Table C7 CO_2 mass and flux calculations

Location	unit	notes	cted (assimilated lim	density_kg/m3	Limestone thick	volume_km3*	volume_m3	mass_kg	mass_Tg	ailated or decarbonated (reacte	CO2_wt.%	'O2 mass fractio	Mass CO2_Tg	40 Myr flux_Tg CO2/yr
Merry Widow	pluton	10 m margin	0.8	2900	1	0.21	2.10E+08	6.08E+11	608	20	9	0.09	54.7	n/a
Merry Widow	pluton	2 m margin	0.2	2900	1	0.04	4.20E+07	1.22E+11	122	20	9	0.09	11.0	n/a
Merry Widow	pluton	entire pluton	100	2900	1	27	2.70E+10	7.83E+13	78300	10	4	0.044	3445.2	n/a
Merry Widow	dikes and sills in limestone	4% of dike or sill volume assimilates 20 wt.% limestone	4	2900	1	0.29	2.92E+08	8.47E+11	847	20	9	0.088	74.5	n/a
Merry Widow	dikes and sills in limestone	4% of dike or sill volume assimilates 25 wt.% limestone	4	2900	1	0.29	2.92E+08	8.47E+11	847	25	11	0.11	93.1	n/a
Merry Widow	orbicular dikes	orbicular dike <1% of pluton volume (0.27 km3), up to 17%	17	2900	1	0.05	4.59E+07	1.33E+11	133	25	11	0.11	14.6	n/a
Merry Widow	metamorphic aureole 150 m	aureole is 150 m wide	100	2700	1	3.2	3.20E+09	8.64E+12	8640	100	44	0.44	3802	n/a
Merry Widow	metamorphic aureole 50 m	aureole is 50 m wide	100	2700	1	1.1	1.10E+09	2.97E+12	2970	100	44	0.44	1307	n/a
Bonanza Arc	erupted volcanic rocks	4% of erupted bonanza volcanic rocks assimilate 20% limest	4	2900	n/a	19000	1.90E+13	5.51E+16	2.20E+06	20	8.8	0.088	1.9E+05	4.8E-03
Bonanza Arc	erupted volcanic rocks	4% of erupted bonanza volcanic rocks assimilate 25% limest	4	2900	n/a	19000	1.90E+13	5.51E+16	2.20E+06	25	11	0.11	2.4E+05	6.1E-03
Bonanza Arc	emplaced plutons interact with 1 km of lime	0.8% of emplaced Bonanza arc plutonic rocks assimilate 20 %	0.8	2900	1	12000	1.20E+13	3.48E+16	2.78E+05	20	9	0.09	2.5E+04	6.3E-04
Bonanza Arc	emplaced plutons interact with 0.5 km of lir	0.8% of emplaced Bonanza arc plutonic rocks assimilate 20 %	0.8	2900	0.5	6000	6.00E+12	1.74E+16	1.39E+05	20	9	0.09	1.3E+04	3.1E-04
Bonanza Arc	metamorphic aureole 150 m	92% of Quatsino Limestone left (8% decarbonated), 1 km in	100	2700	1	274	2.74E+11	7.40E+14	7.40E+05	100	44	0.44	3.26E+05	8.1E-03
Bonanza Arc	metamorphic aureole 50 m	92% of Quatsino Limestone left (3% decarbonated), 0.5 km	100	2700	0.5	49	4.90E+10	1.32E+14	1.32E+05	100	44	0.44	5.82E+04	1.5E-03
Bonanza Arc	reaction transport of Quatsino Limestone	~2.5 wt.% of silica in Quatsino Limestone reacts with fluids	100	2700	1	79	7.88E+10	2.13E+14	2.13E+05	100	44	0.44	9.36E+04	2.3E-03
Bonanza Arc	reaction transport of Quatsino Limestone	~2.5 wt.% of silica in Quatsino Limestone reacts with fluids	100	2700	0.5	39	3.94E+10	1.06E+14	1.06E+05	100	44	0.44	4.68E+04	1.2E-03
Bonanza Arc	mantle derived CO2 - wallace	0.3 wt.% of basalt = CO2	0.3	2900	n/a	209000	2.09E+14	6.06E+17	6.06E+08	n/a	n/a	n/a	1.82E+06	4.5E-02
Bonanza Arc	mantle derived CO2 - Babsy	1.5 wt.% of basalt = CO2	1.5	2900	n/a	209000	2.09E+14	6.06E+17	6.06E+08	n/a	n/a	n/a	9.09E+06	2.3E-01

Notes: *volume for plutonic rocks based on thickness of Quatsino Limestone (column H)
not used in dissertation, but included here for completeness and/or interest

Appendix C - Supplementary Material Text

DETAILED PETROGRAPHY

Gabbro of the Merry Widow pluton is heterogeneous, displaying layering of coarse- and fine-grained textures proximal (<100 m) to the pluton-wallrock margin. The coarse-grained gabbro is hypidiomorphic and consists of plagioclase (50 – 55%), clinopyroxene (25 – 30%), hornblende (5 – 10%), oxides (5 – 10%), olivine (<10%), apatite (<5%), ± orthopyroxene (<3%), and ± biotite (<5%) (Figure 4.2b). Orthopyroxene typically occurs as oxy-symplectites that form between oxides and olivine (Figure 4.2b). Intergrowths of amphibole (hastingsite) and plagioclase are also common between oxides and plagioclase, similar Type I-b symplectites described in Keevil et al. (2020). Clinopyroxene and plagioclase often display 'eagles beak' textures (Holness et al., 2011). Fine-grained gabbro has abundant plagioclase (45 – 65%) with discrete granoblastic clinopyroxene (15 – 35%), olivine (5 – 10%), amphibole (5 – 10%), and oxides (5 – 10%) (Figure 4.2c), where primocrysts of plagioclase can reach diameters of 0.5 cm, often with sericitized interiors. This granoblastic clinopyroxene gabbro can have an anorthosite-like appearance in outcrop due to the high modal abundance of coarser plagioclase (generally 0.1 – 0.5 cm) with finer-grained (<0.5 mm) granoblastic clinopyroxene along plagioclase boundaries, not visible to the unaided eye. Granoblastic clinopyroxene within the fine-grained gabbro (<0.5 mm) is distinctly different from the larger (2 – 5 mm) clinopyroxene that occurs interstitially (anhedral) in the coarse-grained gabbro (Figure 4.2a,b,c).

The chilled margin of the pluton, as observed in drillcore, consists of a thin veneer (<1.5 m thickness) of very fine-grained (<100 μm) gabbro with clinopyroxene (55 – 60%) and plagioclase (40 – 45%), displaying an annealed-like granoblastic texture in both clinopyroxene

and plagioclase grains (Figure 4.2d,e). This margin is in contact with a heterogeneous metamorphic aureole of dominantly skarn mineralization with polymict intrusive breccias.

Less abundant phases within the gabbro include rare but discrete pegmatitic gabbro cumulates that are spheroidal (~10 to 30 cm in diameter) in outcrop, and notably more resistant to weathering. These cumulates consist of plagioclase (45 – 55%), amphibole (15-20%), clinopyroxene (5 – 10%), olivine (<10%), oxides (15 – 20%), apatite (5 - 10%), ± biotite (<5%), and ± titanite (<1%), where amphibole and clinopyroxene are commonly chloritized and plagioclase is often sericitized. Apatite grains within these cumulates are euhedral, reaching up to 2 mm in diameter and commonly have melt and fluid inclusions. Subhedral titanite typically forms on edges of apatite. Less common occurrences within the pluton include regions with up to 35% Fe-oxides of exsolved ilmenite with magnetite. Regions within the pluton that are 'dioritic' in composition (i.e., RM19-119) modally consist of plagioclase and clinopyroxene, where plagioclase is presumed to be more albitic due to the higher Si-content.

Quartz monzonite of the Merry Widow pluton is the dominant phase within the interior regions of the pluton, close to the Merry Widow mountain summit (Figure 4.1a), and consists of plagioclase feldspar to albite (50 – 70%), quartz (20 – 30%), hornblende (<10%), and oxides (<10%). Graphic intergrowths between quartz and feldspar is common. Minor apophyses of the quartz monzonite intrude or mingle with the marginal gabbro, and also intrude the proximal (<100 m) wallrock.

METHODS

Major element analyses on bulk rock

Bulk rock analyses of major elements for outcrop plutonic rocks (11) were analyzed by inductively coupled plasma optical emission spectrometry (ICP-OES) by Activation Laboratories Ltd (Actlabs). Samples were prepared by powdering fresh rock chips in a planetary agate ball mill. Analyses by ICP-OES measured 10 major element oxides (SiO_2, TiO_2, Al_2O_3, $Fe_2O_{3(T)}$, MnO, MgO, CaO, Na_2O, K_2O, and P_2O5) (Table C1). Data accuracy was estimated by calculating differences between known and measured values of certified reference materials (DNC-1, GBW 07113, W-2A, SY-4, and BIR-1A). Differences were <2.5% or within 0.1% (i.e., the latter for minor amounts of MnO, K_2O, P_2O_5), with the exception of two $Fe_2O_{3(T)}$ measured differences of 4.7% (DNC-1) and 3.2% (W-2A). Precision estimates measured by Actlabs between repeat unknown samples was <3.7%.

Bulk rock analyses of major elements for drillcore plutonic rocks (6) were analyzed by electron micro probe microanalysis (EMPA) using a five-wavelength spectrometer Cameca SX-100 at the University of Alberta on homogenized glass beads made from rock powders. Sample powders were prepared by hand pulverizing fresh rock chips in an agate mortar and pestle. The powders were mounted on Pt wire loops and melted in air at 1300°C for 24 hours and quenched into homogenized glass beads. Analyses by EMPA measured 10 major elements (SiO_2, TiO_2, Al_2O_3, FeO, MnO, MgO, CaO, Na_2O, K_2O, and P_2O5) (Table C1). Data accuracy was estimated by calculating differences between known and measured values of certified reference materials of basaltic glasses (BHVO-2G, IOB, Grimsvotn, Hawaii, JDF, and Laki), where differences were <0.3%. Precision estimates were measured from five repeat analyses on all samples and were within 1.6 wt.% (2σ) for all oxides. Additionally, a plutonic rock (RM19-144) that was analyzed

for majors via ICP-OES (Actlabs) was analyzed using the EMPA glassbeads method as an external duplicate. The relative differences between ICP-OES vs EMPA analyses was <4% for all oxides (Table C1).

Trace element analyses by SN ICP-MS on bulk rock

Trace elements for outcrop (12) and drillcore (6) plutonic rocks were determined using solution nebulisation inductively coupled plasma mass spectrometry (SN ICP-MS) on bulk rock powders using an Agilent 8800 ICP-MS at the University of Victoria (Table C1). Samples were prepared by digesting ~100 mg of bulk rock powder in concentrated acids (1 ml of 16 M HNO_3 followed by 1.5 ml of 28 M HF) at 125°C for 24 hrs. Digested solutions were uncapped and dried at 125°C for 2 hrs until a gel-like state was reached. A second acid digestion (4 ml of 8 M HNO_3) at 125°C for 12 hrs was completed, dried down, followed by third and final acid digestion (4 ml of 8 M HNO_3), which was capped until final solutions were ready to be made. Final solutions were prepared by diluting digested samples in ~125 ml of deionized water.

Analyses by SN ICP-MS measured 14 rare earth elements (REE), as well as Cr, Co, Ni, Cu, V, Sc, Nb, Pb, Rb, Sr, Th, U, Cs, Y, Zr, Ba, Hf and Ta. Limits of detection for all elements was <0.5 ppb. Data correction methods followed Cheatham et al. (1993), using ^{115}In as an internal standard. Drift was observed in specific elements (Cr, Ni, Cu, Rb, Sr, Ba, and U) and was corrected for via a third order polynomial fuction unique to the specific element drift. The corrected data was converted from counts per second (CPS) to concentration by calibration with analyzed silicate standards (BCR-2, BHVO-2, BIR-1A, and DNC-1) forced through an intercept (0,0). Precision on measured differences between procedural duplicate samples was <5%, with

the exception of Pb in MW21-12-91 (8.5%), Cr in RM19-64B (9.1%), and Zr in RM19-144 (6.7%).

$^{87}Sr/^{86}Sr$ analyses by tandem ICP-MS on bulk rock

$^{87}Sr/^{86}Sr$ ratios were measured from outcrop (7) and drillcore (2) plutonic rock samples were measured using the University of Victoria's Agilent 8800 Q3 ICP-MS/MS in tandem mass spectrometry configuration with a collision cell following the methods of Bolea-Fernandez et al. (2016), and as outlined in Chapter 2 – Appendix B (Table C2). Aliquots of the solutions previously used for SN ICP-MS trace element analysis were diluted in 0.32 M HNO_3 to 10 ppb Sr. Reference materials included silicate standards (BHVO-2, BCR-2, and BIR-1a) and one carbonate standard (JLS-1). Analytical uncertainty measured from repeat analyses of a 10 ppb Sr solution that was prepared by combining ~4 ml from each unknown sample was ± 0.0011 (2σ, n = 10). Data accuracy was estimated by comparison of measured versus preferred and/or published values of certified reference materials, where the absolute differences were within analytical uncertainty with the exception of the BCR-2 and BIR-1a, where BCR-2 (n=4) consistently reported lower $^{87}Sr/^{86}Sr$ (0.002 – 0.003) than the *preferred* value (0.70492 ± 0.00055; Jochum et al., 2016), and BIR-1a (n=2) reported slightly higher $^{87}Sr/^{86}Sr$ (0.001 – 0.002) than the *published* values (0.70307 – 0.70311 ± 0.00025; Fourny et al., 2016). The authors note that matrix effects may have resulted in variable errors in the measured $^{87}Sr/^{86}Sr$ ratios related to the variable dilution factors, and uncertainty induced by variable matrix effects could be minimized using a matrix matched bracket solution. Precision on a duplicate sample analyzed (RM19-174) was within analytical uncertainty (absolute difference of 0.00003).

$^{87}Sr/^{86}Sr$ ratios were further calculated to initial values based on an age of 197 Ma (Nixon et al., 2011).

$\delta^{18}O$ isotopes of bulk rock powders and minerals

Bulk rock powders from outcrop plutonic rocks including gabbro (9), monzonite (1), and a cumulate (1) were analyzed for $\delta^{18}O$ by laser fluorination at the University of Oregon Stable Isotope Laboratory, following the methods of Watts et al. (2019) (Table C3). In addition to bulk rock powders, fresh clinopyroxene was hand-picked from five gabbro and one cumulate for $\delta^{18}O$ analyses (Table C3). Gabbro was selected based on a low (and/or no) degree of alteration of clinopyroxenes, identified by the presence chlorite, with the exception of chloritized clinopyroxene from a cumulate (RM19-64B), which was analyzed as a 'worst-case' sample. For each analysis, ~2 mg of bulk rock powder or ~2 mg of clinopyroxene was required. Data accuracy was estimated by repeat analyses on an internal University of Oregon standard (Gore Mountain garnet, UOG) with a known $\delta^{18}O$ of 6.52 ‰, and was within 0.23‰ (2σ) for bulk rock powders and 0.26‰ (2σ) for clinopyroxene. However, precision on repeat analyses on bulk rock powders was much larger, ranging from 0.34 to 3.71 ‰ (2σ, Table C4). Precision on repeat analyses (n=4) on a gabbro (RM19-174) proximal (<10 m) to the pluton-wallrock contact with minimal alteration (i.e., only slight serictization in plagioclase cores, LOI = 0.4%) reported the highest uncertainty 3.71 ‰ (2σ) (Table C4). Precision on repeat analyses (n=3) on a gabbro (RM19-114) collected distally (>1 km) from the pluton-wallrock contact also reported relatively high uncertainty of 2.01 ‰ (2σ) (Table C4). The high uncertainty on some bulk rock powders suggests the ~2 mg of powder may have been too coarse-grained and /or too heterogeneous for a representative 'bulk-rock' analyses. Precision on repeat analyses (n=3) on clinopyroxene grains

from six plutonic rock samples varied from 0.08 to 1.14 ‰ (2σ) (Table C3). The highest variability (1.14 ‰) was from the 'worst-case' chloritized clinopyroxene sampled from a cumulate. I report corresponding $\delta^{18}O$ on bulk rock samples with clinopyroxene for five plutonic samples, as no bulk rock $\delta^{18}O$ analysis was completed on the cumulate due to the obvious alteration in hand sample. For additional accuracy estimates, a sample external to this study (olivine gabbro #935-1-35) with a well-known value ($\delta^{18}O = 4.57 \pm 0.41$ ‰; personal communication with K.Gillis) reported a result of $\delta^{18}O$ 4.88 ‰.

$\delta^{18}O$ and $\delta^{13}C$ isotopes on carbonates

Four limestone samples from Merry Widow were analyzed for $\delta^{18}O$ and $\delta^{13}C$ at the University of Victoria using isotope-ratio mass spectrometry (IRMS). Methods for limestone $\delta^{18}O$ and $\delta^{13}C$ analyses involved heating sample powders (<1.0 mg) and standards (IAEA-603, IAEA-CO-8, internal standard VTS) at 90°C overnight in borosilicate reaction vials to remove volatiles. Vials were placed in a heated block and samples were dissolved with ~15 drops of 100% H_3PO_4 and allowed to react for a minimum of 1 hour. The resulting CO_2 gas was measured on a Sercon Ltd. 20-22 gas-source continuous-flow mass spectrometer with a Gas Box 2 front end. Results for $\delta^{18}O$ and $\delta^{13}C$ are respectively reported relative to Vienna Standard Mean Ocean Water (VSMOW) and Vienna Pee Dee Belemnite (VPDB). Precision, based upon measurement of the internal standard (VTS), is within 0.4‰ (2σ) for $\delta^{18}O$ and within 0.2‰ (2σ) for $\delta^{13}C$, and replicate measurements of RM19-MW-QL were within these uncertainties.

Major element analyses by EMPA on minerals

Clinopyroxene, plagioclase, olivine, magnetite, ilmenite, amphibole or biotite, and ± orthopyroxene in gabbro were analyzed for major element chemistry by electron probe micro-analyses (EMPA) using a five-wavelength spectrometer Cameca SX-100 at the University of Alberta (Table C5). All minerals were measured using a 20 kV accelerating potential and a 30 nA beam current. A focused beam diameter of <1 μm was set for Fe-oxides (magnetite and ilmenite) and set to 2 μm for all other phases (plagioclase, olivine, pyroxene, amphibole, biotite) for better stability under the electron bombardment. Element peaks and backgrounds were counted at 20 s for all elements. Analytical uncertainty was calculated from standard deviations of measured standards: SiO_2 <0.38%; Al_2O_3 <0.24%; CaO <0.05%; FeO <0.11%; MgO <0.23%; Na2O <0.18%; K2O <0.04%; TiO2 <0.17%; Cr2O3 <0.22%; V2O3 <0.27%; NiO <0.27%; MnO <0.10%; and Cl <0.02%.

Trace element analyses by EMPA on minerals

Clinopyroxene, plagioclase, magnetite, ilmenite, and apatite (cumulate only) in gabbro and a cumulate were analyzed for trace element chemistry via laser ablation inductively coupled mass spectrometry (LA-ICP-MS) at the University of Victoria. All analyses were conducted using an Agilent 8800 Q3 ICP-MS coupled to a Teledyne CETAC LSX-213 G2+ laser ablation system, using a helium flow-through sample cell. For clinopyroxene and plagioclase the laser was set at a repetition rate of 10 Hz and fluence of 6.12 Jcm^{-2}, ablated spot sizes were 65 um in diameter along 200 um raster lines. Similar conditions were employed for Fe-oxides, but with a longer raster line of 400 um. For apatite the laser was set at a repetition rate of 10 Hz and fluence of 4.08 Jcm^{-2}, ablated spot sizes were 100 um in diameter along 200 um raster lines.

Data reduction was completed at the University of Victoria using the Iolite^{TM} (v.4.8.6) software package (Paton et al., 2011). Plagioclase from three gabbro and a cumulate were analyzed using NIST 615 as the external standard and known Ca wt.% from EMPA analyses as the internal standard (Table C6). The authors note that plagioclase analyzed from the cumulate was heavily sericitized, and these regions were best avoided during laser ablation. Clinopyroxene from two gabbro was analyzed using NIST 613 as an external standard and known Si wt.% from EMPA analyses as an internal standard (Table C6). Magnetite and ilmenite were analyzed from three gabbro and one cumulate using BCR2G as an external standard and known Fe wt.% from SEM-EDX (Scanning Electron Microscopy-Energy Dispersive X-ray) analysis at the University of Victoria, which was used as an internal standard (Table C6). Apatite from a cumulate was analyzed using NIST 610 as an external standard and known Ca wt.% from an analyzed Durango standard as the internal standard (Table C6). Data reduction on apatite avoided fluid and crystalline inclusions as best as possible.

Appendix C Bibliography

Bolea-Fernandez, E., Balcaen, L., Resano, M., and Vanhaecke, F. (2016), Tandem ICP mass spectrometry for Sr isotopic analysis without prior Rb/Sr separation: *Journal of Analytical Atomic Spectrometry,* 31, p. 303–310.

Cheatham, M.M., Sangrey, W.F., and White, W.M. (1993), Sources of error in external calibration ICP-MS analysis of geological samples and an improved non-linear drift correction procedure: *Spectrochimica Acta,* 48B (3), E487-E506. https://doi.org/10.1016/0584-8547(93)80054-X

Fourny, A., Weis, D., and Scoates, J. S. (2016), Comprehensive Pb-Sr-Nd-Hf isotopic, trace element, and mineralogical characterization of mafic to ultramafic rock reference materials: *Geochemistry, Geophysics, Geosystems,* 17, p. 739– 773, https://doi.org/10.1002/2015GC006181

Ghiorso, M.S., and Gualda, G.A.R. (2015), An H_2O–CO_2 mixed fluid saturation model compatible with rhyolite-MELTS: *Contributions to Mineralogy and Petrology,* 169, p. 1–30. https://doi.org/10.1007/s00410-015-1141-8

Holness, M.B., Stripp, G., Humphreys, M.C.S., Veksler, I.V.V., Nielsen, T.F.D., and Tegner, C. (2011), Silicate Liquid Immiscibility within the Crystal Mush: Late-stage Magmatic Microstructures in the Skaergaard Intrusion, East Greenland: *Journal of Petrology*, 52 (1), p. 175–222. https://doi.org/10.1093/petrology/egq077

Jochum, K.P., Weis, U., Schwager, B., Stoll, B., Wilson, S.A., Haug, G.H., Andreae, M.O. and Enzweiler, J. (2016), Reference Values Following ISO Guidelines for Frequently Requested Rock Reference Materials: *Geostandards and Geoanalytical Research,* 40, p. 333-350. https://doi.org/10.1111/j.1751-908X.2015.00392.x

Keevil, H.A., Namur, O., and Holness, M.B. (2020), Microstructures and Late-Stage Magmatic Processes in Layered Mafic Intrusions: Symplectites from the Sept Iles Intrusion, Quebec, Canada: *Journal of Petrology*, 61(7), https://doi.org/10.1093/petrology/egaa071

Morris, R., and Canil, D. (2022), CO_2 transport at shallow depths in arc magmas: evidence from unique orbicular dikes in the Jurassic Bonanza arc, Vancouver Island, Canada. *Contributions to Mineralogy and Petrology, 177*, https://doi.org/10.1007/s00410-021-01852-y

Paton, C., Hellstrom, J., Paul, B.,Woodhead, J. and Hergt, J. (2011), Iolite: Freeware for the visualisation and processing of mass spectrometric data. *Journal of Analytical Atomic Spectrometry,* 26, p. 2508 – 2518.

Schindelin, J., Arganda-Carreras, I., Frise, E., Kaynig, V., Longair, M., Pietzsch, T., Preibisch, S., Rueden, C., Saalfeld, S., Schmid, B., Tinevez, J-Y., White, D.J., Hartenstein, V., Eliceiri, K., Tomancak, P., and Cardona, A. (2012), Fiji: an open-source platform for biological image-analysis: *Nature Methods*, 9, p. 676-682. https://doi.org/10.1038/nmeth.2019